Annual Report 2008

Center for Nuclear Study,
Graduate School of Science, the University of Tokyo

Editors
   Shin'ichiro Michimasa
   Yuko Soma

Center for Nuclear Study

Annual Report
2008

Center for Nuclear Study,
Graduate School of Science, the University of Tokyo

Preface

This is the annual report of the Center for Nuclear Study (CNS), Graduate School of Science, the University of Tokyo, for the fiscal year 2008 (April 2008 through March 2009). In the CNS, during this period, a large number of scientific activities in various fields of nuclear physics have been carried out and a wide variety of fruitful results have been obtained. This report presents a report of such activities. Some highlights of the report are mentioned here.

Light neutron-rich nuclei have been studied by using nucleon transfer and inelastic scattering where the final states are identified by measuring de-excited gamma-rays. A low-lying proton intruder state has been found for the first time, which shows importance of a deformation effect in N∼8 neutron-rich nuclei. New high-spin states in $^{49-51}$Ti populated by fusion reactions of an RI beam have been found, which gives information on the N=28 shell gap and the single particle energies in the fp-shell. Upgrade of the readout system of the CNS GRAPE has started, where digital pulse data taken by sampling ADCs are analyzed by FPGAs on boards.

Research programs with CRIB continued in nuclear physics as well as nuclear astrophysics, together with the AVF upgrade project that enhances the capability of CRIB facility. The research programs include investigations of α-induced stellar reactions on ^{7}Li, ^{14}O and ^{21}Na. The beta decay of ^{46}Cr was also studied to learn the Gamow-Teller Transitions. Some beam developments were made for new RI beams, and an active target was also designed for studies of stellar reactions with low-cross sections. Some technological development for the beam line as well as for the Wienfilter of CRIB were made in the past year.

A new heavy ion ECR source of CNS that use super-conducting magnet was successfully installed to the AVF cyclotron, and has been used to provide a variety heavy ion beams. Two CNS ECR sources now provide all the beams for the AVF cyclotron and support not only CRIB experiments but also a large number of RIBF experiments. A charge-breeding ECR source is also under development.

A new central module of the AVF cyclotron will be made following the design in 2009. The second is a successful acceleration of heavy ion beams up to 11 Mev/u which was about 9.5 MeV/u before. Following the detailed simulation studies of the heavy ion beams through the cyclotron, beam acceleration tests were successfully performed for ^{16}O and ^{6}Li beams. These beams will be provided to new experimental projects at CRIB. A non-destructive beam monitor was also successfully developed and installed just in front of the CRIB production target. It showed a sensitivity of about a few nA. This new beam monitor will become a powerful tool for all the RIBF facility.

Development of the polarized solid proton target is being proceeded. We have examined how the proton polarization rate depends on pulse structure of excitation light and found that the polarization rate can be doubled for a duty factor of 20% and a repetition rate of 7.5 kHz, compared with the previous settings of 5% and 2.5 kHz. Higher proton polarization can be expected with this new settings.

Construction of the SHARAQ spectrometer and the dedicated high-resolution beamline has completed. The magnetic field distribution in dipole magnets, D1 and D2, were precisely measured with the search coil method. A major part of the beamline has been constructed. Cathode readout drift chambers for tracking detectors at the SHARAQ focal plane have been fabricated in GANIL and installed to SHARAQ in December 2008. It was also found that Low-pressure multiwire drift chambers (LP-MWDC) developed for beamline tracking detectors works well under pressure as low as 10 kPa with an isobuthane gas. In March 2009, the commissioning run has been performed. The first RI beam has reached to the final focal plane of the SHARAQ. Lateral dispersion matching transport was partly achieved by using 250A-MeV ^{14}N beam.

Main goal of the CNS quark physics group is to understand the properties of hot and dense nuclear matter created by colliding heavy nuclei at relativistic energies. The group has been involved in the PHENIX experiment at Relativistic Heavy Ion Collider (RHIC) at Brookhaven National Laboratory,

and has also started active participation in the ALICE experiment at Large Hadron Collider (LHC) at CERN. As for the RHIC PHENIX experiment, the group has been concentrating on the physics analysis with leptons and photons, which include study of charm and bottom production with the non-photonic single electrons, measurement of direct photon yield at low transverse momentum in p+p and A+A collisions using the virtual-gamma method, and determination of neutral pion yield as a function of azimuthal angle from the reaction plane in Au+Au collisions. As for the LHC ALICE experiment, the group has been playing roles in the construction of the Transition Radiation Detector (TRD), and commissioning and calibration of Time Projection Chamber (TPC). R & D of gas electron multiplier (GEM) and related techniques has been continuing. The major activities are; development of 2D-imaging prototype, and performance study of the thick-GEM prototypes with several different hole sizes.

The nuclear theory group has been promoting the RIKEN-CNS collaboration project on large-scale nuclear structure calculations since 2001 and maintaining its parallel computing cluster. In 2008, we developed the effective interactions of various mass region based on the large-scale shell model calculation technique and discussed the "shell evolution" and the role of tensor force quantitatively in exotic nuclei, such as ^{17}C, ^{48}Ca, N=50 isotones, Sm isotopes and so on.

The 7th CNS-EFES International Summer School (CNS-EFES08) has been organized in August 2008 with 9 lecturers including 4 foreign distinguished physicists. There were 115 participants from 14 countries from all over the world.

Finally, I thank Ms. M. Hirano and other administrative staff members for their heartful contributions throughout the year.

<div align="right">
Takaharu Otsuka
Director of CNS
</div>

Table of Contents

1a. Experimental Nuclear Physics: Low and Intermediate Energies

1b. Experimental Nuclear Physics: PHENIX Experiment at BNL-RHIC & ALICE Experiment at CERN-LHC

2. Accelerator and Instrumentation

3. Theoretical Nuclear Physics

4. Other Activities

Appendices

Experimental Nuclear Physics:
Low and Intermediate Energies

Spin dependent momentum distribution of proton in ³He **studied via proton induced exclusive knockout reaction**

Y. Shimizu, T. Uesaka, T. Kawabata, M. Dozono[a], K. Hatanaka[b], K. Itho[c], T. Kawahara[d],
Y. Maeda[e], H. Matsubara[b], T. Noro[a], H. Okamura[b], S. Sakaguchi, H. Sakai[f], Y. Sasamoto,
M. Sasano[f], A. Tamii[b], H. Tokieda, T. Wakasa[a], T. Wakui[g], K. Yako[f], Y. Yamada[a], and
H.P. Yoshida[g]

Center for Nuclear Study, Graduate School of Science, University of Tokyo
[a]Department of Physics, Kyushu University
[b]Research Center for Nuclear Physics, Osaka University
[c]Department of Physics, Saitama University
[d]Department of Physics, Faculty of Science, Toho University
[e]Department of Applied Physics, Faculty of Engineering, University of Miyazaki
[f]Department of Physics, The University of Tokyo
[g]Cyclotron and Radioisotope Center, Tohoku University

1. Introduction

In recent years, there has been a renewed interest in detailed experimental investigations of the ³He system, due to the availability of Faddeev calculations of the ³He ground state wave function. It is predicted from Faddeev calculations of the three-body bound state that three contributions dominate the ³He ground state wave function: 1) a S state in which two protons are coupled in a spin singlet state; 2) a D state, due to the tensor force, where the three nucleon spins are dominantly oriented opposite to the ³He nuclear spin; 3) a mixed-symmetry configuration of the nucleons, the S' state. All other components are expected to be negligibly small. In Faddeev calculations, the S and the S' state contributions to the spectral function are expected to be a maximum for small nucleon momentum while the D state contribution is greatest for large momentum.

Since the D state contribution becomes large in the high momentum region, measurement of the spin observables sensitive to the D state is needed. For the S state contribution only in the ³He ground state wave function, one can find the proton polarization of the d-p cluster in the ³He has a constant value of $-\frac{1}{3}$ independently of the proton momentum. The proton polarization deviate from above value due to the D state contribution. Therefore, the proton polarization of the d-p cluster in the ³He might provide an opportunity to study the ³He in the high momentum region. In the previous experiments [1, 2, 3], however, the poor resolution could not allow the separation of the ³He($p, 2p$) events into the two final-state channels, *i.e.*, the deuterium ground state and the pn unbound state. In the present work, in order to determine the proton polarization of the d-p cluster in the ³He, the high resolution measurement was achieved by making full use of the double-arm spectrograph.

2. Experiment

The measurements of the $³\vec{\mathrm{He}}(\vec{p}, 2p)$ were performed at Research Center for Nuclear Physics (RCNP), Osaka University. Polarized protons produced in an atomic beam polarized ion source [5] were accelerated by the $K = 140$ MeV AVF (Azimuthally Varying Field) cyclotron up to 64.2 MeV. The proton beam was then accelerated up to 392 MeV by the $K = 400$ MeV Ring cyclotron. The outgoing protons were momentum analyzed with two-arm spectrometer system consisting of the Grand Raiden (GR) [6] and the Large Acceptance Spectrometer (LAS) [7]. The setting angle of the GR was fixed at 45.0 degrees. The angle of the LAS and the magnetic fields of both the spectrometers were set so that the recoil momentum of the residual nucleus were 0 and 100 MeV/c. The layout of the system is shown in Fig. 1. In order to measure a reaction point along the target chamber, multi-wire drift chambers were placed at the front of each spectrometers. The beam was transported in a beamline downstream of the polarized ³He targets and focused by quadrupole magnets into the beam stop and a Faraday cup embedded in the shielding wall. Typical beam intensity was 60 nA, limited by acceptable counting rates in the detectors. The beam polarization was monitored by two beam line polarimeters in the West Experimental hall. During the measurements, the beam polarization was typically 0.55.
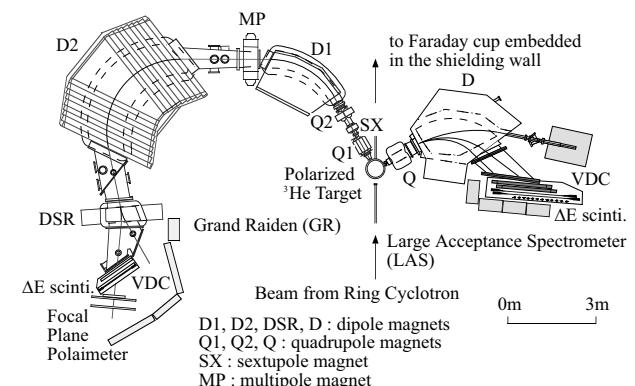
Figure 1. Schematic layout of the RCNP dual spectrometer consisting of the GR and the LAS.

A spin exchange polarized ³He target [8] was used to perform the spin correlation measurements. Detailed descriptions of the polarized ³He target can be found in

Refs. [9, 10, 11]. Here we present only salient details for the present experiment. The target cell contained the ^{3}He gas with a density of 9.8×10^{19} atoms/cm^3 together with a small amount of N$_2$ gas and Rb vapor. During the spin correlation measurements, the ^{3}He polarization was monitored for 40 seconds every one and a half hours by the Adiabatic Fast Passage NMR method [12]. The direction of the polarization was revered every single experimental run. The NMR signals gave relative values of the polarization. The absolute value of the target polarization was determined by a calibration using the $^3\vec{\text{He}}(\vec{p}, \pi^+)^4$He reaction. In the special case of this reaction with spin parities of $\frac{1}{2}^+ + \frac{1}{2}^+ \rightarrow 0^- + 0^+$, where the parity changes, one can show that the spin correlation parameter C_{yy} has a constant value of $+1$ [13]. The measured target polarization was typically $p_y^T = 0.09$.

3. Result

Assuming that the strong interaction is symmetric under parity and time reversal, the spin dependent cross section for a scattering of a spin-$\frac{1}{2}$ projectile by a spin-$\frac{1}{2}$ target is given by [13]

$$\sigma = \sigma_0(1 + p_y A_y + p_y^T A_y^T + p_y p_y^T C_{yy}), \quad (1)$$

where σ_0 is the spin independent cross section, and p_y and p_y^T are the beam and the target polarizations, respectively. In the present experiment, both the beam and the target polarizations were pointed in the vertical direction. The spin correlation parameter C_{yy} is obtained as

$$C_{yy} = \frac{1}{p_y p_y^T} \frac{1 - A}{1 + A}, \quad (2)$$

where

$$A \equiv \frac{Y_{\uparrow\downarrow} + Y_{\downarrow\uparrow}}{Y_{\uparrow\uparrow} + Y_{\downarrow\downarrow}}. \quad (3)$$

Y is the yield where the first and second arrows (up or down) in a subscript indicate the spin directions of the beam and the target, respectively. In the plane wave impulse approximation [14], the spin correlation parameter C_{yy}^{He} for the $^3\vec{\text{He}}(\vec{p}, 2p)$ reaction can be related to that for the pp elastic scattering, C_{yy}^p, extracted from phase shift analyses [15], by

$$P(k) = \frac{C_{yy}^{\text{He}}(k, q)}{C_{yy}^p(q)}, \quad (4)$$

where $P(k)$ is the momentum distribution of the proton polarization in the ^{3}He.

The preliminary results of the momentum distribution of the proton polarization in the ^{3}He are shown in Fig. 2 together with existing data [3]. In the figure, the closed circles and closed squares show the results of the $^3\vec{\text{He}}(\vec{p}, 2p)^2$H reaction and the $^3\vec{\text{He}}(\vec{p}, 2p)pn$ reaction, respectively, and the closed triangles show the results of the sum of two reactions. The open diamonds show the data from Ref. [3]. We see that our results of the sum are consistent with the previous data. The further data analysis is now in progress.
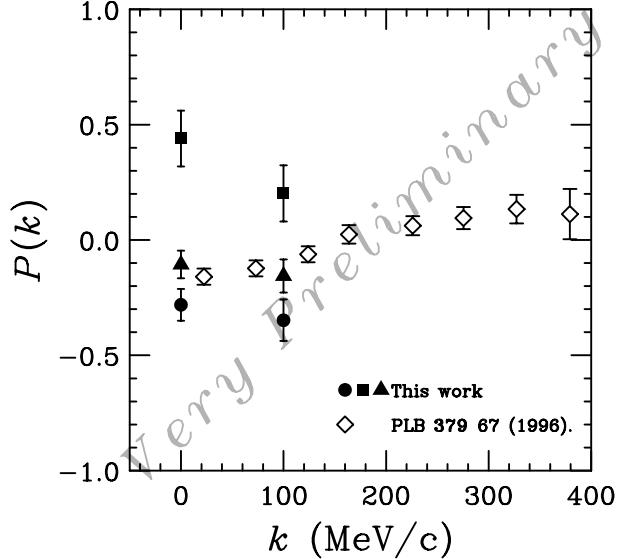
Figure 2. The momentum distribution of the proton polarization in the ^{3}He.

References

[1] A. Rahav *et al.*, Phys. Rev. C **46**, 1167 (1992).
[2] E.J. Brash *et al.*, Phys. Rev. C **47**, 2064 (1993).
[3] R.G. Milner *et al.*, Phys. Lett. **B379**, 67 (1996).
[4] R.b. Wiringa and S.C. Pieper, Phys. Rev. Lett. **89**, 182501 (2002).
[5] K. Hatanaka *et al.*, Nucl. Instrum. Methods Phys. Res. A **384**, 575 (1997).
[6] M. Fujiwara *et al.*, Nucl. Instrum. Methods Phys. Res. A **422**, 484 (1999).
[7] N. Matsuoka *et al.*, RCNP Annual Report 1991, p. 186.
[8] M.A. Bouchiat, T.R. Carver, and C.M. Varnum, Phys. Rev. Lett. **5**, 373 (1960).
[9] Y. Shimizu *et al.*, *in Proceedings of the 11th International workshop on Polarized Sources and Targets*, p. 103.
[10] Y. Shimizu, PhD thesis, Osaka University, 2006.
[11] Y. Shimizu *et al.*, RCNP Annual Report 2003, p. 41.
[12] A. Abragham, *Principles of Nuclear Magnetism* (Oxford University Press, CITY, 1961) pp. 34-36.
[13] G.G. Ohlsen, Rep. Prog. Phys. **35**, 717 (1972).
[14] S. Frullani and J. Mougey, Adv. Nucl. Phys. **14**, 1 (1984).
[15] R.A. Arndt and L.D. Roper, *Scattering Analysis Interactive Dial-In Program* (SAID), Phys. Rev. C **56**, 3005 (1997).

Spin-orbit Potential in Neutron-rich Helium Isotopes

S. Sakaguchi, T. Uesaka, T. Kawabata, T. Wakui[a], N. Aoi[b], Y. Hashimoto[c], Y. Ichikawa[d], K. Itoh[e], M. Itoh[a], H. Iwasaki[d], T. Kawahara[f], Y. Kondo[b], H. Kuboki[b], Y. Maeda[g], K. Miki[d], T. Nakamura[c], T. Nakao[d], Y. Nakayama[c], S. Noji[d], H. Okamura[h], H. Sakai[d], Y. Sasamoto, M. Sasano[d], Y. Satou[c], K. Sekiguchi[b], T. Shimamura[c], Y. Shimizu, M. Shinohara[c], K. Suda[b], D. Suzuki[d], Y. Takahashi[d], A. Tamii[h], K. Yako[d] and M. Yamaguchi[b]

Center for Nuclear Study, Graduate School of Science, University of Tokyo
[a]Cyclotron and Radioisotope Center, Tohoku University
[b]RIKEN (The Institute of Physical and Chemical Research)
[c]Department of Physics, Tokyo Institute of Technology
[d]Department of Physics, University of Tokyo
[e]Department of Physics, Saitama University
[f]Department of Physics, Toho University
[g]Department of Physics, Kyushu University
[h]Research Center for Nuclear Physics, Osaka University

1. Introduction

Recently, renewed interest has been focused on the spin-dependent interaction in unstable nuclei. One of the most direct methods to extract the information on the spin-dependent interaction is the scattering experiment induced by spin-polarized light ions. In order to investigate the unstable nuclei with spin polarization, a polarized proton solid target, which was specially designed for radioactive-ion beam experiments, has been developed at CNS [1, 2]. Making use of this target, we measured the vector analyzing power of the proton elastic scattering from ^{6}He and ^{8}He at 71 MeV/A in 2005 and 2007. The aim of the measurements is to extract the feature of the shape of spin-orbit potentials between protons and ^{6,8}He, and discuss the effect of valence neutrons on the spin-orbit potential. Details of the measurement and the optical model analysis are reported.

2. $\vec{p}+^8$He analyzing power measurement

The experiment was carried out at the RIKEN Nishina Center using the RIKEN Projectile-fragment Separator (RIPS). The energy and the intensity of a ^{8}He beam were 71 MeV/A and 1.5×10^5 pps, respectively. The purity of the beam was 77 %. The material of the secondary target was a single crystal of naphthalene with a thickness of 4.3×10^{21} protons/cm^2. Protons in the crystal were polarized under a low magnetic field of 0.09 T at 100 K by the optical excitation of electrons and the cross-polarization method. The target polarization was 11.0±2.5% on average. Recoil protons were detected using multiwire drift chambers and CsI (Tl) scintillators placed on the left and right sides of the beam line. Leading particles ^{6,8}He were detected using another MWDC and $\Delta E - E$ plastic scintillator hodoscopes.

The measured differential cross sections and analyzing powers are shown in Fig. 1 by closed circles. They are consistent with the previous data of the differential cross section [3] plotted by open circles.
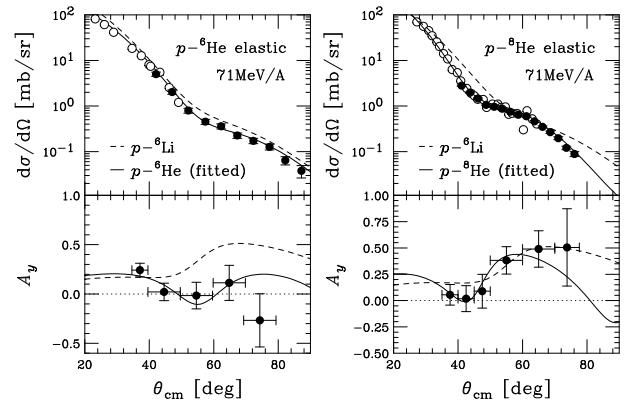
Figure 1. The differential cross sections and the analyzing powers of the $\vec{p}+^{6,8}$He elastic scatteirng at 71 MeV/A.

3. Optical model analysis

In order to extract the global nature of $\vec{p}-^{6,8}$He interactions, the data were phenomenologically analyzed with an optical model potential. For the central and spin-orbit terms, we assumed Woods-Saxon and Thomas type functions, respectively. We searched a parameter set that reproduces the data using a fitting code ECIS79. As an initial potential, a parameter set for $\vec{p}+^6$Li elastic scattering at 72 MeV/A [4] was used. The dashed lines in Fig. 1 show the calculation with initial parameters. Results of the best-fit parameters are presented by solid curves. Both differential cross section and analyzing power data are well reproduced except for the scattering at backward angles.

The potentials obtained are shown in Fig. 2 as a function of radius. The upper panel displays real and imaginary parts of the central term, while the lower one presents a spin-orbit term with error bands resulted from fitting uncertainty. Due to the target polarization uncertainty, there is an additional scale error of 19% for ^{6}He and 22% for ^{8}He in the depth of the spin-orbit potentials.

The shape of the spin-orbit potentials in neutron-rich helium isotopes is discussed here. In order to extract the gross

3
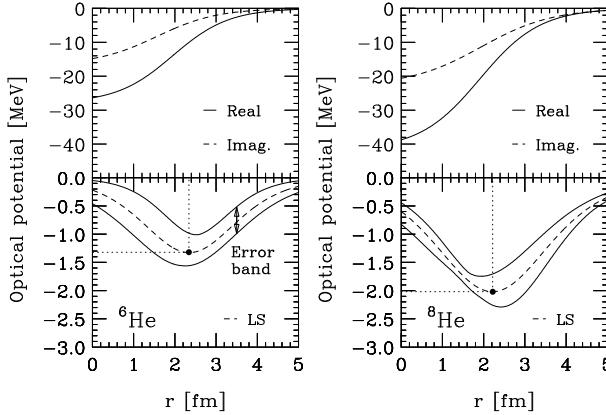
Figure 2. Phenomenological optical potnetials between a proton and ^{6,8}He as a function of radius.

feature of the potentials, we focus on the radius and the amplitude of the peak of spin-orbit potential as shown by the dotted lines in Fig. 2. We call the former "LS radius" and the latter "LS amplitude". Since the spin-orbit potential is usually approximated by the radial derivative of density distribution, LS radius and LS amplitude should be closely related to the radius and the gradient of the density distribution, respectively. The LS radii and LS amplitudes of ^{6}He and ^{8}He are presented in Fig. 3 by closed squares. Those of neighboring even-even stable nuclei [5,6] and a global optical potential [7] are also plotted by closed and open circles. It is clearly demondtrated that the LS amplitudes of ^{6}He and ^{8}He are remarkably smaller than those of stable nuclei. The LS amplitudes of stable nuclei are almost constant and distributed between $4-5.5$ MeV, whereas those of ^{6}He and ^{8}He are as small as 1.3 and 2.0 MeV. It can be concluded that the spin-orbit potentials in neutron-rich helium isotopes are characterized by the significantly shallow shape. This can be intuitively explained from the largely diffused density distribution of ^{6}He and ^{8}He, whose gradient is more than twice as small as that of ^{4}He. Results of more detailed analysis with microscopic optical model calculation will be reported elsewhere.
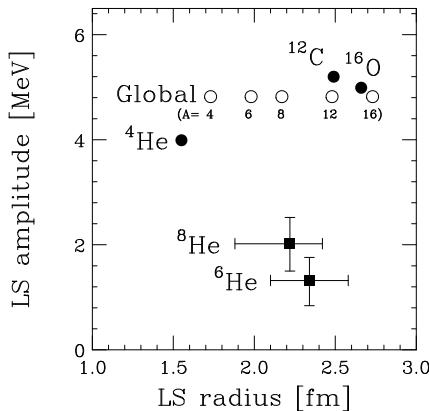
Figure 3. LS radius and LS amplitude of light even-even nuclei.

Here, we discuss the effect of valence neutrons on the spin-orbit potential from the systematics in helium isotopes. For this purpose, an $\alpha + xn$ cluster folding calculation [5]

could be a useful method, since the contribution of an α core and valence neutrons can be separately evaluated. It has been expected from the calculation that the contribution of valence neutrons to the spin-orbit potential is one-order of magnitude smaller than that of an α core. Consequently, the spin-orbit potentials of ^{6,8}He are expected to be related to the spatial distribution of the α core in a nucleus, *i.e.*, the LS radius should increase with the diffuseness of the α core distribution, whereas the LS amplitude should decrease. The LS radius and LS amplitude of helium isotopes are plotted in Fig. 4 as a function of the proton orbital radius, which represents the diffuseness of the α core distribution. Although there are large experimental uncertainties, almost linear relations can be seen. From this we can derive a picture that the valence neutrons affect the spin-orbit potential rather strongly through the $p - \alpha$ interaction than via the direct $p - n$ interaction. The recoil motion of the α core induced by valence neutrons can be important in the explanation of the large difference between spin-orbit potentials in ^{4}He and neutron-rich helium isotopes.
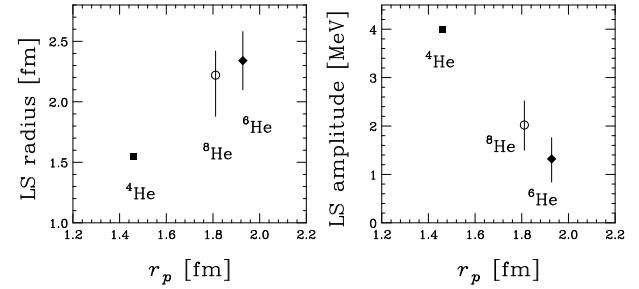
Figure 4. LS radius/amplitude as a function of proton radius.

4. Summary

The vector analyzing power of the proton elastic scattering from ^{6}He and ^{8}He have been measured at 71 MeV/A. We found that the spin-orbit potentials in ^{6}He and ^{8}He are significantly shallower than those in stable nuclei. This shallowness can be naturally explained by the large diffuseness of the neutron-rich helium isotopes. The dominance of $p - \alpha$ core interaction in the $p-^{6,8}$He spin-orbit potentials is also indicated.

References

[1] T. Wakui *et al.*, Nuclear Instruments and Methods in Physics Research A **550** (2005) 521.

[2] T. Uesaka *et al.*, Nuclear Instruments and Methods in Physics Research A **526** (2004) 186.

[3] A. Korsheninnikov, E. Yu. Nikolski, C. A. Bertulani *et al.*, Nuclear Physics A **617** (1997) 45.

[4] R. Henneck *et al.*, Nuclear Physics A **571** (1994) 541.

[5] Y. Iseri *et al.*, Genshikaku Kenkyu **49 No.4** (2005) 53.

[6] H. Sakaguchi *et al.*, Physical Review C **26** (1982) 944.

[7] B.A. Watson *et al.*, Physical Review **182** (1969) 977.

New measurement of alpha resonance scattering on ^{7}Li

H. Yamaguchi, T. Hashimoto, S. Hayakawa, D.N. Binh, D. Kahl, S. Kubono, Y. Wakabayashi[a],
T. Kawabata[b], and T. Teranishi[c]

Center for Nuclear Study, Graduate School of Science, University of Tokyo
[a]*Advanced Science Research Center, JAEA*
[b]*Department of Physics, Kyoto University*
[c]*Department of Physics, Kyushu University*

The exotic cluster structure in ^{11}B and ^{11}C nuclei is attracting much attention in recent years [1]. The $3/2_3^-$ state in ^{11}B at E_{ex}=8.11 MeV is regarded as a dilute cluster state [2], where two α particles and ^{3}He are weakly interacting. In particular, the alpha cluster structure in ^{11}B was studied by measuring its isoscalar monopole and quadrupole strengths in the ^{11}B(d,d') reaction, and the mirror state of the 8.11-MeV state was suggested to have a dilute cluster structure [3,4].

A recent orthogonality-condition-model (OCM) calculation [5] proposed that the $3/2_3^-$ state near the alpha-decay threshold in the A=11 nuclei has a $2\alpha + t$ (^{3}He) dilute cluster structure, but the two α particles are not fully condensed into the lowest s orbit unlike the three α particles in the Hoyle state in ^{12}C. According to the OCM calculation, a fully developed cluster-condensed state emerges near the $2\alpha + t$ (^{3}He) decay threshold with the spin-parity of $1/2^+$ and the isospin of 1/2, but no candidate for this state is reported in the nuclear-data compilation [6]. It is important to search for the unknown $1/2^+$ state and to clarify the cluster structure in ^{11}C and ^{11}B.

In the present study, we used the ^{7}Li+α resonant elastic scattering to investigate the cluster structure. The strength of the resonances are expected to provide information about the alpha-cluster structure.

The ^{7}Li+α system is also related to the astrophysical reaction, ^{7}Li$(\alpha,\gamma)^{11}$B. The resonance parameters studied by the present work should contribute to the precise determination of the ^{7}Li$(\alpha,\gamma)^{11}$B reaction rate at high temperature ($T_9 > 1$). In a low temperature environment such as p-p chain in stars, the ^{7}Li$(p,\alpha)^4$He reaction is usually more important and the ^{7}Li$(\alpha,\gamma)^{11}$B reaction may not take place. However, in some high temperature phenomena, the ^{7}Li$(\alpha,\gamma)^{11}$B reaction should play important roles. In the ν process in supernovae [7], ^{11}B is mainly produced via ^{4}He$(\nu,\nu'p)^3$H$(\alpha,\gamma)^7$Li$(\alpha,\gamma)^{11}$B, but the production can be enhanced with the ^{12}C$(\overline{\nu_e},e^+n)^{11}$B reaction. A precise determination of the ^{7}Li$(\alpha,\gamma)^{11}$B reaction rate would give a good insight into the roles of neutrino reaction and oscillation in the ν process.

The measurement of the ^{7}Li+α elastic scattering was performed at CRIB [8,9], using the thick target method in inverse kinematics [10] to measure the excitation function for excitation energy of 10–13 MeV in ^{11}B. The excited states of ^{11}B in this energy region have been studied by ^{7}Li+α elastic scattering [12,13] or using other methods [14,15,16,17,18,19,20,21], however, some of the res-

onance parameters are still uncertain. Especially, the alpha widths were not determined precisely. Using inverse kinematics, the excitation function at 180 degree in the center-of system, where potential scattering is minimum and the resonances can be observed most clearly, was measured for the first time.

The experimental setup is shown in Fig. 1. The ^{7}Li beam
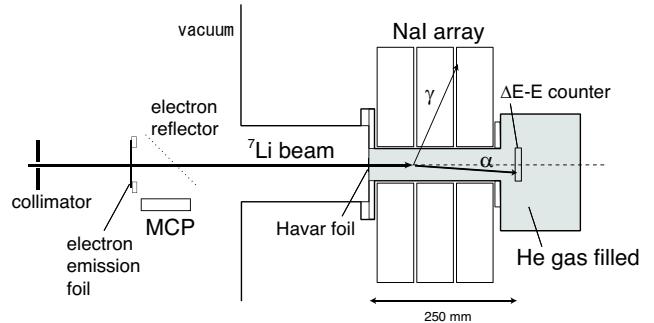
Figure 1. Experimental setup of the measurement of ^{7}Li+α elastic scattering in inverse kinematics.

was accelerated at the AVF cyclotron and transported to the final focal plane (F3) of CRIB. The beam had an energy of 13.7 MeV, and corrimated by a 3×3-mm rectangular aperture at F3.

An MCP was used for the detection of the beam position and timing. A CsI-evapolated 0.7-μm-thick alminum foil was placed on the beam axis for the secondary electron emission. The secondary electrons were reflected by 90 degrees at the biased thin-wire reflector and detected at the MCP with a delay-line readout.

The gas target consisted of a 50-mm-diameter duct and a small chamber. Helium gas at 920 Torr was filled and sealed with a 2.5-μm-thick Havar foil as the beam entrance window. Alpha particles recoiling to the forward angles were detected by the "ΔE-E counter". The counter, consisted of 20-μm- and 480-μm-thick silicon detectors, were placed in the gas chamber. The distance from the beam entrance window to the detector was 250 mm. To measure 478-keV gamma rays from inelastic scattering to the first excited state of ^{7}Li, NaI detectors were placed around the duct. We used ten NaI crystals, each with a geometry of 50 $\times$ 50 $\times$ 100 mm. They covered 20–60% of the total solid angle, depending on the reaction position.

5

Measurement was performed for 2.9×10^{10} particles of ^{7}Li injected into the gas target in 2.5 days. As the gas target was sufficiently thick to stop the ^{7}Li beam, heavier particles were not expected to reach the detector, even if produced. The dominant particle measured was alpha from the elastic scattering, and only small numbers of protons and tritons possibly from ^{7}Li(α,p) reaction and break up of ^{7}Li were observed in the measurement. The background from the contaminating particles in the beam appeared to be negligible, since almost no particles having the energy above 1.5 MeV were detected, when the target gas was replaced to argon of the equivalent thickness. The obtained energy spec-
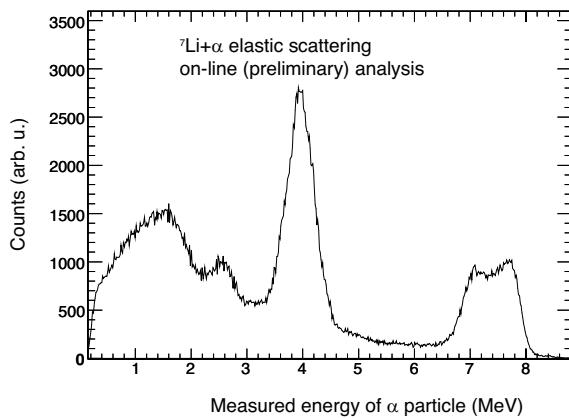
Figure 2. Energy spectrum of the alpha paticles in the measurement. The alpha particles are mostly from ^{7}Li+p elastic scattering.

trum of alpha particle is shown in Fig. 2. A structure having peaks consistent with previous measurements [12, 21] were observed. A low-background measurement was successfully performed, and it is demonstrated that the thick target with inverse kinematics method works for such a light beam particle.

Calculating the kinematics with the consideration of the energy loss in the gas target, the measured energy of the alpha particle can be converted to the excitation energy of ^{11}B, and the excitation fuction for the ^{7}Li+α elastic scattering will be obtained. The excitation function for inelastic scattering can also be obtained by selecting the proton-gamma ray coincident events. The cross section is about two orders of magnitude lower than that for the elastic scattering, and does not affect the spectral shape observed as in Fig. 2.

The resonance parameters to be determined in this study, such as the spin, parity and alpha width (related with the spectroscopic factor of the α-cluster configuration) would provide valuable information for the α-cluster structure in the high excited states, and astrophysical reaction rates in high-temperature phenomena.

References

[1] Y. Kanada-En'yo, Phys. Rev. C **75** 024302 (2007).

[2] A. Tohsaki *et al.*, Phys. Rev. Lett. **87** 192501 (2001).

[3] T. Kawabata *et al.*, Phys. Rev. C **70** 034318 (2004).

[4] T. Kawabata *et al.*, Phys. Lett. B **646** 6 (2007).

[5] T. Yamada, private communication (2007).

[6] D. R. Tilley, J. H. Kelley, J. L. Godwin, D. J. Millener, J. E. Purcell, C. G. Sheu, H. R. Weller, Nucl. Phys. A 745 (2004) 155.

[7] T. Yoshida *et al.*, Phys. Rev. Lett. **96** (2006) 091101.

[8] S. Kubono *et al.*, Eur. Phys. J. A **13** (2002) 217.

[9] Y. Yanagisawa *et al.*, Nucl. Instrum. Methods Phys. Res., Sect. A **539** (2005) 74.

[10] K. Artemov *et al.*, Sov. J. Nucl. Phys. **52** (1990) 408.

[11] H. Yamaguchi *et al.*, Phys. Lett. B **672** (2009) 230–234.

[12] R.Y. Cusson *et al.*, Nucl. Phys. **86** (1966) 481–508.

[13] H. Bohlen *et al.*, Nucl. Phys. A **179** (1972) 504–512.

[14] P. Paul *et al.*, Phys. Rev. **164** (1967) 1332–1342.

[15] G. Schmidt *et al.*, Nucl. Phys. A **173** (1971) 449.

[16] R. Jambunathan and R.K. Hobbie, Phys. Rev. **172** (1968) 1065.

[17] S.L. Hausladen *et al.*, Nucl. Phys. A **217** (1973) 563.

[18] N.R. Fletcher *et al.*, Phys. Rev. C **68** (2003) 024316.

[19] B. Zwieglinski *et al.*, Nucl. Phys. A **389** (1982) 301.

[20] R. Aryaeinejad *et al.*, Nucl. Phys. A **436** (1985) 1.

[21] N. Soić *et al.*, Nucl. Phys. A **742** (2004) 271–290.

Negative parity states in ^{8}B

H. Yamaguchi, Y. Wakabayashi[a], A. Saito, G. Amadio, S. Kubono, H. Fujikawa, J.J. He[b],
T. Teranishi[c], Y.K. Kwon[d], S. Nishimura[e], Y. Togano[f], N. Iwasa[g], K. Inafuku[g], M. Niikura, and
L.H. Khiem[h]

Center for Nuclear Study, Graduate School of Science, University of Tokyo
[a]*Advanced Science Research Center, JAEA*
[b]*Institute of Modern Physics, CAS*
[c]*Department of Physics, Kyushu University*
[d]*Department of Physics, Chung-Ang University*
[e]*RIKEN (The Institute of Physical and Chemical Research)*
[f]*Department of Physics, Rikkyo University*
[g]*Department of Physics, Tohoku University*
[h]*Institute of Physics and Electronics, Vietnam Academy of Science and Technology*

A new measurement of proton resonance scattering on ^{7}Be was performed up to the center-of-mass energy of 6.7 MeV using the low-energy RI beam facility CRIB [1,2,3]. The excitation function of ^{7}Be+p elastic scattering above 3.5 MeV was measured successfully for the first time, providing important information about the resonance structure of the ^{8}B nucleus.

As discussed in [4], a major purpose of this measurement is to observe the unknown broad 2^- resonance around 3 MeV [5,6], which may affect the ^{7}Be$(p,\gamma)^8$B reaction rate in the energy region far below 1 MeV. The astrophysical S-factor $S_{17}(E)$, determined by the ^{7}Be$(p,\gamma)^8$B reaction, is one of the most important parameters in the standard solar model, because its value at the energy of the solar center is directly related to the flux of the ^{8}B neutrino, which is the dominant component of the solar neutrinos detected by some of the major neutrino observatories on earth.

The presence of the 2^- state around 3.5 MeV could not be confirmed because of the limited statistics and energy range in previous experiments [5,6], however, we obtained excitation functions consistent with a presence of the broad 2^- state [4]. Assuming the presence of the 2^- state, we expanded the R-matrix fit to the higher energy region, as illustrated in Fig. 1. The contribution of the inelastic scattering to the first excited state in ^{7}Be is shown in the same figure. A characteristic peak structure was found around the excitation energy of 5 MeV. The peak is considered to be due to a resonance that was not observed in previous studies. R-matrix fits were performed introducing resonance around 5 MeV with all possible combinations of J^π, and only the tail shape in the excitation function between 5.5 and 6.5 MeV was well-reproduced by introducing a 3^+ state, which is known to exist in the mirror nucleus. The calculated excitation functions that fitted to the experimental data for three angular ranges are shown as solid curves in the figure. The parameters for the 2^- resonance are consistent for all the angular ranges within the experimental resolution, as shown by the dashed curves in higher two angular ranges, obtained using the same parameters for the 2^- resonance as the lowest angular range. The 1^- resonance was not ob-

served clearly in the spectra for larger angles, because of the limited energy resolution. The resonance parameters for the newly introduced 3^+ state, which provide best fits were E_{ex}= 6.8–7.5 MeV and Γ =2–4 MeV, depending on the angular range. The fit function shows small, but systematic deviations from the measured data, as seen around 5.5 MeV for the lowest angular range. This may suggest that the excitation function cannot be reproduced by the sets of resonances we assumed. For example, the fit was improved by introducing another 1^+ state at 5.8 MeV, as shown with a dotted curve in the figure.

The resonance parameters determined by the present work and previous studies are summarized in Table 1. The parameters for the 2^- state were determined with improved precision, showing no large discrepancies with previous measurements. Our excitation functions, including the angular dependence and measurement of inelastic scattering, strongly support the existence of the broad 2^- state in ^{8}B nucleus around 3.2 MeV. Excited states of ^{8}B higher than 3.5 MeV were not explored in past measurements, and we discovered new resonance at 5.0 MeV and assigned its J^π as 1^-. A 1^- resonance in the A=8 nuclei was predicted to emerge in the vicinity of a 2^- state by theoretical studies [8,9,10,11]. In [12], a structure due to 1^- level appeared at E_{ex} = 4.1 MeV (E_{proton} = 4.5 MeV) in the calculated S-factor spectrum. The observed resonance might be the first evidence for these predictions in ^{8}B, and could lead to deeper understanding on the structure of the ^{8}B nucleus. We found an indication of resonance at around 7 MeV, but a measurement for higher excitation energy is required to determine its parameters.

In summary, we have studied the proton resonance scattering on ^{7}Be, using a pure ^{7}Be beam produced at CRIB. The excitation function of ^{8}B was measured up to the excitation energy of 6.7 MeV, using the thick-target method and resonance parameters of two negative (non-normal) parity states were determined. The 2^- resonance at 3.2 MeV was reported in two previous measurements, and we determined its energy and width with improved precision. Another resonance at 5 MeV was observed for the first time, and it is

Table 1. Resonance parameters of ^{8}B determined by the present work and previous studies. l is the angular momentum used in the R-matrix calculation.

J^π	l	E_{ex} (MeV)	Γ (MeV)	Reference
1^+	1	0.7695 ± 0.0025	0.0356 ± 0.0006	[7]
3^+	1	2.32 ± 0.02	0.35 ± 0.03	[7]
2^-	0	$3.2^{+0.3}_{-0.2}$	$3.4^{+0.8}_{-0.5}$	present
$(2^-, 1^-)$	0	3	1–4	[5]
2^-	0	3.5 ± 0.5	8 ± 4	[6,7]
1^-	0 or 2	5.0 ± 0.4	0.15 ± 0.10	present
(3^+)	1	~ 7	>2	present

considered to be the 1^- state predicted in theoretical studies.

This work was supported by the Grant-in-Aid for Young Scientists (B) (Grant No. 17740135) of JSPS.

References

[1] S. Kubono et al., Eur. Phys. J. A **13** (2002) 217.

[2] Y. Yanagisawa et al., Nucl. Instrum. Methods Phys. Res., Sect. A **539** (2005) 74.

[3] H. Yamaguchi et al., CNS Annual Report 2005 (2006).

[4] H. Yamaguchi et al., CNS Annual Report 2007 (2009).

[5] V. Gol'dberg et al., *JETP Lett.* **67**, (1998) 1013.

[6] G. Rogachev et al., Phys. Rev. C **64** (2001) 061601(R).

[7] D. R. Tilley, J. H. Kelley, J. L. Godwin, D. J. Millener, J. E. Purcell, C. G. Sheu, H. R. Weller, Nucl. Phys. A 745 (2004) 155.

[8] A. Aswad, H. R. Kissener, H. U. Jäger, R. A. Eramzhia, Nucl. Phys. A 208 (1973) 61–76.

[9] H. D. Knox, D. A. Resler, R. O. Lane, Nucl. Phys. A 466 (1987) 245.

[10] A. van Hees and P. Glaudemans, Z. Phys. A **314** (1983) 323.

[11] A. van Hees and P. Glaudemans, Z. Phys. A **315** (1984) 223.

[12] F. Barker, and A. Mukhamedzhanov, Nucl. Phys. A **673** (2000) 526.

Figure 1. Excitation functions of $p+^7$Be elastic scattering for three angular ranges, fitted with R-matrix calculations. Contributions from inelastic scattering are also shown. The best fit for each angular range with five resonances, including two unknown resonances (1^- at 5.0 MeV and 3^+ at around 7 MeV) are shown with solid curves. The dashed curves for the larger two angular ranges are the calculated functions using the same 2^- resonance parameters as that between 0 and 8 degrees. The dotted curve for 0–8 degrees is a 6-resonance fit with an additional 1^+ state at 5.8 MeV.

Practical Designing of the Direct Measurement of the Astrophysical Reaction $^{11}\mathrm{C}(\alpha,p)^{14}\mathrm{N}$

S. Hayakawa, S. Kubono, T. Hashimoto, H. Yamaguchi, D.N. Binh, D.M. Kahl, Y. Wakabayashi[a],
N. Iwasa[b], N. Kume[b], I. Miura[b], T. Teranishi[c], J.J. He[d], Y.K. Kwon[e], T. Komatsubara[f], S. Kato[g]
and S. Wanajo[h]

Center for Nuclear Study, Graduate School of Science, University of Tokyo
[a]*Japan Atomic Energy Agency*
[b]*Department of Physics, Tohoku University*
[c]*Department of Physics, Kyushu University*
[d]*Institute of Modern Physics*
[e]*Department of Physics, Chung Ang University*
[f]*Department of Physics, University of Tsukuba*
[g]*Department of Physics, Yamagata University*
[h]*Institute for the Physics and Mathematics of the Universe, University of Tokyo*

1. Introduction

Unstable nuclide ^{11}C is considered to locate in the hot *pp*-chain [1] which is an extended *pp*-chain process in metal-poor and high-temperature stars, and at the breakout point from the *pp*-chain region to the CNO cycle region through the $^{11}\mathrm{C}(\alpha,p)^{14}\mathrm{N}$ reaction. Recent simulations of the νp-process [2] in neutrino-driven winds in type II supernovae suggest that this reaction path could considerably affect the nucleosynthesis around mass number $A = 100$ near the end of the process. However, the theoretical predictions related to this reaction could have large uncertainties since the information on its reaction cross section is experimentally unknown except for the ones from the time-reverse reaction studies [3] or some limited information on the resonance parameters [4].

In order to provide more reliable cross section data, a direct measurement is planned to be performed with the CNS Radioactive Isotope Beam separator (CRIB) [5]. The thick-target method [6] is an efficient way to determine the excitation function through a relatively wide center-of-mass energy range (0.4-3 MeV) corresponding to the stellar temperature range (0.5-3 GK) of interest. For the $^{11}\mathrm{C}(\alpha,p)^{14}\mathrm{N}$ reaction, this method can be performed in the inverse kinematics with ^{4}He as the target and ^{11}C as the beam. The difficulties on a thick gas target are to determine the reaction points and to identify the final channels. Even with rather tricky setups, some other (α,p) reaction experiments of the few precedents [7,8] sacrificed the solid angle or limited the detection angle only near 0° against these problems. In this report, a simple setup is proposed with meeting the requirements as discussed below.

2. Experimental Design

The setup consists of two beam profile monitors (2 PPACs or PPAC + MCP), a ^{4}He gas target and ΔE-E silicon detector telescopes at three downstream angles (Fig. 1). Each ΔE layer is position-sensitive. Final states of the $^{11}\mathrm{C}(\alpha,p)^{14}\mathrm{N}$ reaction and background proton events can be distinguished by measuring Time-Of-Flight (TOF) between the first PPAC and the Si detectors. The target density is an important parameter as described in Section 2.1. The beam energy in the gas target should be known to rconstruct the kinematics event by event. Information of the TOF with respect to the RF signal could be useful to derive the beam energy with a reasonable resolution. This time resolution of ~ 3 ns could be improved to 1-2 ns by picking up the γ-rays emitted from the RI beam production target related to the beam bunches timing.
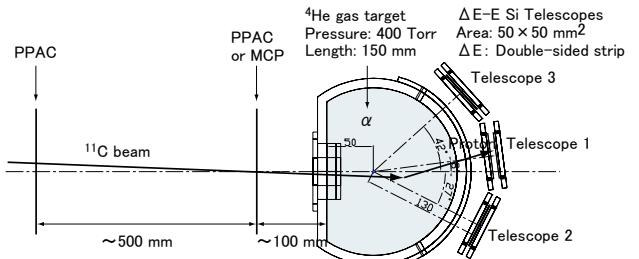
Figure 1. Schematic plan view of the setup.

2.1. Event Identification

A beam at an incident energy of 12 MeV takes about 30 ns to travel and stop in a gas target density at a pressure of 400 Torr and room temperature. This enables the final channels of different excited states of ^{14}N to be separated by 3-5 ns intervals at certain detected proton energies (Fig. 2). It is also possible to distinguish the background protons scattered by the beam particles in the Mylar foil of PPACs by this method. In Fig. 2, (α,p_0) indicates the transition to the ground state of ^{14}N, (α,p_1), (α,p_2) to the first and second excited states, PPAC *a* and *b* the recoil proton events from the two PPACs at upstream. The calculation includes the determination accuracies of time and energy.

2.2. Statistics

From the result of the test experiment [9] the maximum ^{11}C beam rate is expected as high as 5×10^5 pps on target. The yield corresponding to the (α,p_0) channel can be estimated using the cross section derived from the time-reverse reaction data. The cross section increases by two order of magnitude from the center-of-mass energy $E_{\mathrm{CM}} = 1$ to 3
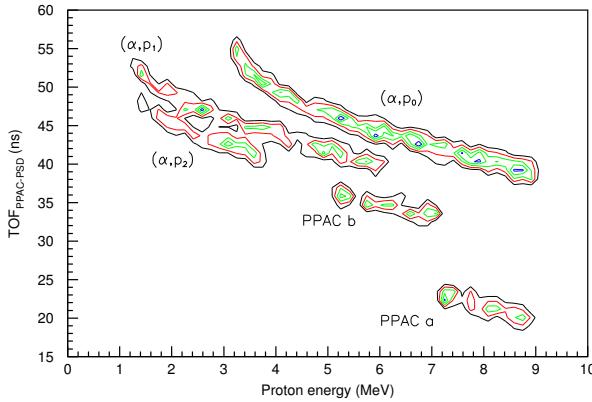
Figure 2. Simulated event identification in a TOF-Energy plot.

MeV at an exponential rate [3]. This redeems the decrease in solid angle at higher energies. the predicted yield of proton per 40-keV-wide bin for a 5-day run is shown in Fig. 3. At the lowest resonance peak which can affect the reaction rate the most, the yield is about 100 of minimally required.
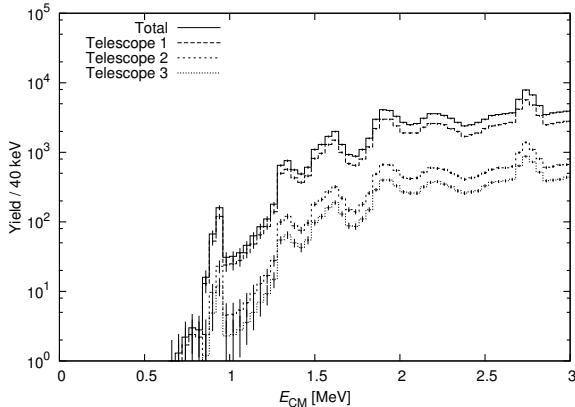
Figure 3. Yield of (α, p_0) protons per 40-keV-wide energy bin.

2.3. Resolutions and Systematic Errors

The determination accuracy of the center-of-mass energy and solid angle are shown in Fig. 4 and Fig. 5 respectively. The position resolution of the beam profile monitors, the accuracy of the beam energy, the energy straggling and the energy and position resolution of the Si detectors are taken into account. The simulation is done at a single proton energy of 4.5 MeV related to the lowest energy events of (α, p_0) with this setup which is of the adversest condition. Two different setups of the beam profile monitors are also assumed, which reflect the different thicknesses and position resolutions. The center-of-mass resolution is estimated to be 50 keV at most which satisfy to observe resonant peaks in the excitation function. An MCP detector can be about 20 times thinner than a PPAC and provide advantages on center-of-mass energy resolution at larger angles and on the solid angle accuracy near the target exit. Although the uncertainty of the solid angle attributed to that of the reaction point is considered as the largest factor for the systematic error, the maximum value is still smaller than the statistical error.
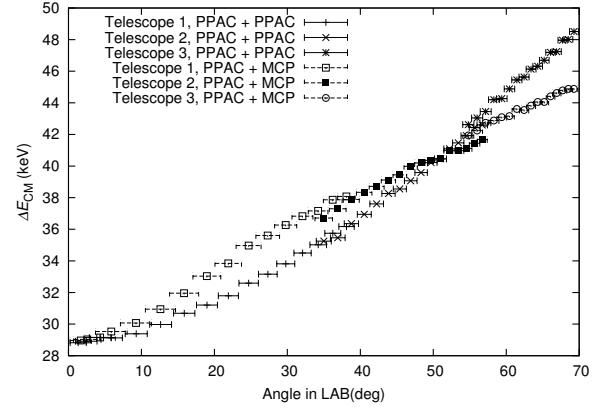
Figure 4. Relation between the scattering angle in laboratory frame and the resolution of center-of-mass energy at proton energy of 4.5 MeV for two different beam monitor setups. Each point is related to the different segments of the double-sided silicon strip detectors.
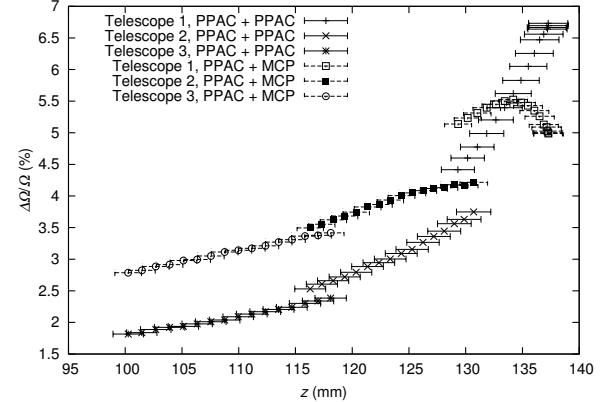
Figure 5. Relation between the uncertainty of the solid angle Ω and the reaction position z along the beam line at proton energy of 4.5 MeV. The origin of z corresponds to the entrance of the target.

3. Conclusions

In this report, proposed is an example of a simple setup, which could overcome the difficulties on the thick-gas-target inverse-kinematics method. Considering event identification, statistics, resolution and systematic errors, this setup could satisfy the required performances with advantages over the past experiments.

The machine time has been already acquired in the 4th RIKEN NP-PAC and scheduled in June, 2009.

References
[1] M. Wiescher *et al.*, APJ, **343**, pp352-, 1989.
[2] S. Wanajo, Astrophys. J. **647**, pp1323-1340, 2006.
[3] P.D. Ingalls *et al.*, Phys. Rev. C **13**, pp524-527, 1976.
[4] F. Ajzenberg-Selove, Nucl. Phys. A **523**, 1, 1991.
[5] Y. Yanagisawa *et al.*, NIM, A **539**, pp74-, 2005.
[6] K.P. Artemov *et al.*, Sov., J., Nucl., Phys., **52**, 480, 1990
[7] D. Goombridge *et al.*, Phys. Rev. C **66**, 055802, 2002
[8] M. Notani *et al.*, Nucl. Phys. A **746**, pp113-117, 2004.
[9] S. Hayakawa, Master's thesis, Dep. of Phys., the Uinv. of Tokyo, 2008.

Study of the ^{14}N$(\alpha,\alpha)^{14}$N, ^{14}N$(\alpha,p)^{17}$O, and ^{14}N$(\alpha,d)^{16}$O reactions using a ^{14}N beam in the inverse kinematics for astrophysics experiments

N.H. Lee[a], S. Kubono[b], H. Yamaguchi[b], T. Hashimoto[b], T. Kawabata[b], Y. Wakabayashi[b], S. Hayakawa[b], Y. Kurihara[b], Dam Nugyen Binh[b], D.M. Kahl[b], T. Ternanishi[c], S. Kato[d], T. Komatsubara[e], M.H. Han[a], A. Kim[a], J.S. Yoo[a], K.I. Hahn[a], Y.W. Kwon[f], B. Guo[g], B.X. Wang[g], and Y.B. Wang[g]

[a]*Ewha Womans University, Korea*
[b]*Center for Nuclear Study, University of Tokyo*
[c]*Kyushu University*
[d]*Yamagata University*
[e]*Tsukuba University*
[f]*Chung-Ang University, Korea*
[g]*CIAE, China*

The cross section of the ^{14}N$(\alpha,p)^{17}$O reaction can be useful as an input for nuclear reaction calculations for some astrophysical conditions related to nuclei with A = 14 ∼ 18. It can also be used for comparing with the ^{14}O$(\alpha,p)^{17}$F reaction, which is an important reaction for understanding the breakout mechanism from the HCNO cycle to the rp process. The excited states in ^{18}F can be studied by the ^{14}N + α experiment, which includes ^{14}N$(\alpha,\alpha)^{14}$N, ^{14}N$(\alpha,p)^{17}$O, and ^{14}N$(\alpha,d)^{16}$O. In addition, the ^{14}N + α experiment can be used as detector calibration for other astrophysically important reactions, especially the ones with radioactive ion beams, by measuring alpha particles and protons.

We performed the ^{14}N + α reaction in inverse kinematics at the CRIB facility of CNS in the RIKEN Accelerator Research Facility [1]. The N+α and O+α experiments were carried out during the same experimental run, where the primary 8.35 MeV/u ^{14}N beam from the AVF cyclotron was used to produce the secondary ^{14}O beam from the ^{14}N(p,n)^{14}O reaction. For this study, we used only ^{14}N beam with the intensity of ∼ 5×10^5 pps, whose purity was 67% for ^{14}N^{+7} and 26% for ^{14}N^{+6} at the F3 focal plane.

All the previous ^{14}N$(\alpha,\alpha)^{14}$N and ^{14}N$(\alpha,p)^{17}$O experiments used alpha particle as a beam and ^{14}N target [2, 3, 4, 5, 6]. We performed these reactions in the inverse kinematics, where a ^{14}N beam bombarded a helium gas target. Therefore, we measured most recoiled alpha and proton from the N+α reaction by the center telescope.

Figure 1 shows the experimental setup at the F3 chamber, where two PPACs, three silicon detector telescopes and a helium gas target were installed for this measurement. The 15 cm long helium gas target has an entrance window of 30 mm diameter and an exit window of 40 mm diameter, covered with a 2.5 μm Havar foil. It contained a 1.43 mg/cm^2 (435 torr, 293 K) helium gas.

While the beam should stop completely in the helium gas or the exit window, the recoiled light particles should be detected by the three sets of the detector telescopes. The center telescope consists of four silicon detectors; a 20 μm silicon strip detector (SSD), a 73 μm position sensitive silicon detector (PSSD), and two 1.5 mm detectors. This sili-
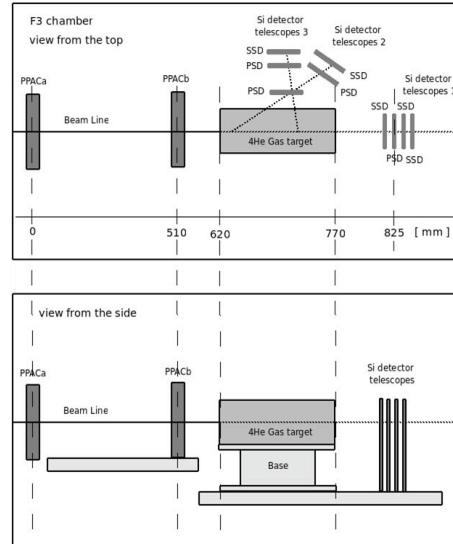
Figure 1. Experimental setup at the F3 chamber viewed from the top (top) and from the side (bottom).

con telescope was placed at zero degrees with respect to the beam direction. The two side-telescopes consist of three layers of 65 μm, 400 μm, and 1.5 mm silicon detectors. The first 65 μm PSSD is shared by the two side telescopes. One of the side telescopes (telescope 3 in Figure 1) was located in perpendicular to the beam direction, and the other telescope (telescope 2 in Figure 1) was rotated forty degrees with respect to the first 65 μm PSSD. The surface area of each detector is 5 cm x 5 cm and each PSSD has 16 x 16 strips.

Because most light particles from the reactions are forward peaked, we only used the events from the center telescope. The second $73\mu m$ silicon and the third 1.5 mm one of the center telescope were used as ΔE and E, respectively for particle identification. Figure 2 shows the particle identification spectrum, where protons, deuterons, ^{3}He and alpha particles were cleanly separated.

From the particle identification spectrum, we can measure simultaneously the cross sections of the ^{14}N$(\alpha,\alpha)^{14}$N, ^{14}N$(\alpha,p)^{17}$O, and ^{14}N$(\alpha,d)^{16}$O reactions from the ^{14}N +α
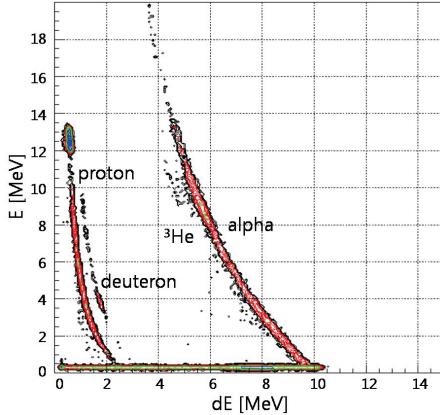
Figure 2. the $\Delta E - E$ spectrum

experiment. The energy of the ^{14}N beam at the helium target just after the entrance Havar foil was 33.9 MeV. This energy allowed us to study the N+α reaction at 3.8 MeV $< E_{cm} < 6.1$ MeV, which corresponds to 8.2 - 10.5 MeV in excited states of ^{18}F.

For calculating the differential cross section, the energy correction due to the reaction point at the target and the detection angle was applied. The corrected energy range measured by the silicon detectors is slightly higher than the raw energy range, because the energy loss by the exit window of the target and the energy loss due to different reaction path were included. The lab energy was then converted to the center of mass energy, and width of the bin was set in the 0.04 MeV interval.

Figure 3 shows the preliminary result of the differential cross section of the ^{14}N$(\alpha,\alpha)^{14}$N. The error bars in Figure 3 represent only statistical errors.
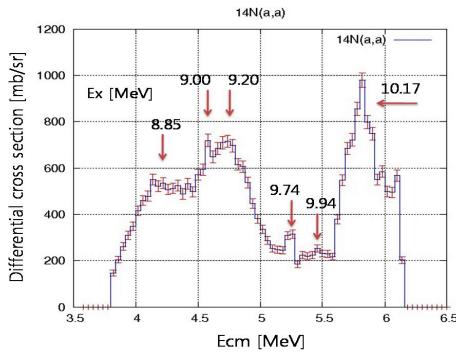
Figure 3. Excitation function for the ^{14}N$(\alpha,\alpha)^{14}$N reaction

Similar to to elastic scattering of ^{14}N + α, we analyzed the data for the ^{14}N$(\alpha,p)^{17}$O reaction and the ^{14}N$(\alpha,d)^{16}$O reaction. Our preliminary results of the differential cross sections of the reactions are shown in Figs. 4 and Figure 5, respectively.

In summary, we studied the ^{14}N$(\alpha,\alpha)^{14}$N, ^{14}N$(\alpha,p)^{17}$O, and ^{14}N$(\alpha,d)^{16}$O reactions at 3.8 MeV $< E_{cm} < 6.1$ MeV in the inverse kinematics. We identified a few excited states of ^{18}F above the ^{14}N + α threshold. Our measured cross sections of ^{14}N$(\alpha,\alpha)^{14}$N, ^{14}N$(\alpha,p)^{17}$O agree with previous other experiments measured using ^{4}He beams. We also measured the cross section of ^{14}N$(\alpha,d)^{16}$O at 3.8 MeV
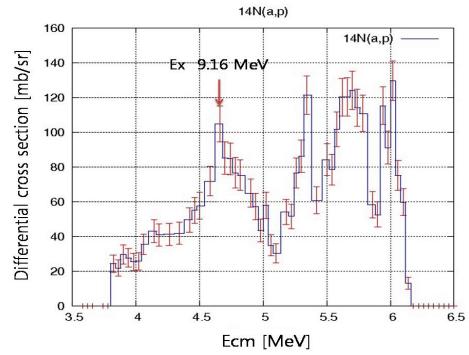
Figure 4. Excitation function for the ^{14}N$(\alpha,$p$)^{17}$O reaction
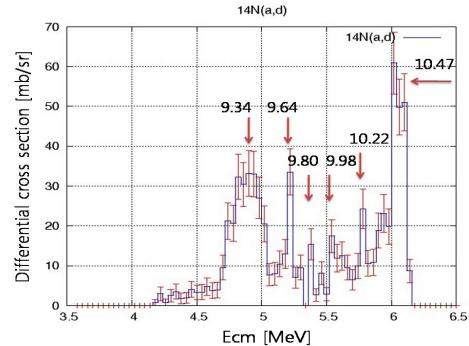
Figure 5. Excitation function for the ^{14}N$(\alpha,$d$)^{16}$O reaction

$< E_{cm} < 6.1$ MeV for the first time. Because of large cross sections of the above reactions and known resonances of ^{18}F, they can be used for energy calibration in other astrophysically important experiments that require radioactive ion beams, such as ^{14}O$(\alpha, p)^{17}$F.

References

[1] Y. Yanagisawa *et al.*, Nucl. Instr. Meth. **A539** (2005) 74.

[2] H. Artigalas *et al.*, Ncul. Instr. and Meth. **B66** (1992) 237.

[3] Feng Ye *et al.*, Ncul. Instr. and Meth. **B94** (1994) 11.

[4] L.A. Foster *et al.*, Ncul. Instr. and Meth. **B79** (1993) 454.

[5] G. Giorginis *et al.*, Ncul. Instr. and Meth. **B113** (1996) 396.

[6] Huizong Xu *et al.*, Ncul. Instr. and Meth. **B149** (1999) 390.

Elastic scattering for 60MeV ^{17}F on ^{12}C target

G. L. Zhang[a], K. J. Liu[a], H. Q. Zhang[b], C. J. Lin[b], C. L. Zhang[b], G. P. An[b], Z. D. Wu[b]

H. M. Jia[b], X. X. Xu[b], F. Yang[b], Z. H. Liu[b], S. Kubono[c]

H. Yamaguchi[c], S. Hayakawa[c], D. N. Binh[c], Y. K. Kwon[d], N. Iwasa[e],

[a]*School of Physics and Nuclear Energy Engineering, Beihang University, Beijing 100191, China*
[b]*China Institute of Atomic Energy, Beijing 102413, China*
[c]*Center of Nuclear Study, University of Tokyo, Japan*
[d]*Department of Physics, Chung-Ang University, Seoul 156-756, South Korea*
[e]*Department of Physics, Tohoku University, Aoba, Sendai, Miyagi 980-8578, Japan*

Our knowledge of nuclei comes mainly from the experiments with nuclei in the valley of the stability. Experiments with nuclei far from the stability-line are expected to provide tests of current nuclear structure models. In particular, light nuclei locating near the drip line may exhibit exotic phenomena, such as manifestations of halo/skin structure. Information on the nuclear structure can be extracted from the reaction data. Among many nuclear reactions, the elastic scattering is a major channel and will provide rich information on reaction mechanism and structures of the nuclei. It also used to determine optical potentials which is important inputs for any reaction studies. However, elastic scattering data for light exotic nuclei are extremely scarce, which raises questions about accuracy and reliability of nuclear structure information extracted from the reaction studies. Because of halo/skin structures and the small binding energy of the last nucleon(s), the light exotic nuclei may behave differently from stable, well-bound nuclei in reactions and reliability of simple-minded extrapolation from the systematics in stable nuclei is open to doubt. Thus, studies of elastic scattering induced by light exotic nuclei are of particular interest.

Study of the ^{17}F elastic scattering is motivated by our interest described above. ^{17}F is a proton drip line nucleus. The study of this nucleus is quite interesting for three reasons: (i) its binding energy is 601 keV. Because of this loose binding, the rms radius is significantly larger than that of 16O core, and is considered to be a nuclear halo state. (ii) it has only one bound state below the breakup threshold, (iii) its first excited state has a halo structure [1, 2]. Many experiments have been performed to explore its structure and reaction mechanisms in recent years. Elastic scattering of ^{17}F+^{208}Pb was measured at 10MeV/nucleon [3], 98MeV and 120 MeV [4], 90.4MeV [5], respectively. Precise data have been obtained for the elastic scattering of ^{17}F on ^{12}C and ^{14}N at 10MeV/nucleon [6].

In most of the above cases, the data are taken for the ^{208}Pb target. The experimental data on light targets are hardly found, except for the data from ^{12}C and ^{14}N at the energy of 10MeV/nucleon [6]. So the experiment was planned to extract the optical potential of the elastic scattering for ^{17}F on light target at energies near Coulomb barrier. We can not only obtain the angular distribution of elastic scattering for ^{17}F on light target at energies near Coulomb barrier, but also know clearly about nuclear interaction for ^{17}F. In the
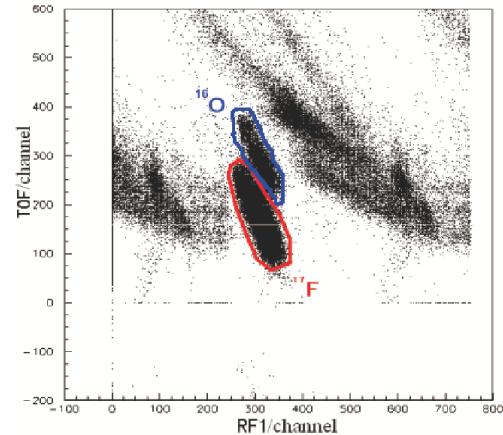
Figure 1. The particle identification before target

theoretical programmes, such as Ptolemy, Double Folding Potential(DFP) and Ecis, etc., one can fit the angular distribution of elastic scattering to extract parameters of the optical potential for nuclear reactions. The optical potential denotes the nuclear interaction between the two nuclei.

In order to obtain the elastic scattering data of ^{17}F on light target nuclei at energies near Coulomb barrier, 60MeV ^{17}F+^{12}C reaction was performed at CNS Radioactive Ion Beam separator (CRIB) in Japan. The beam intensity on the target was about 4×10^5 pps. A $435\mu g/cm^2$-thick ^{12}C target was used for the ^{17}F+^{12}C elastic scattering. Projectile ^{17}F was identified by time of flight (TOF) method before target. Position of ^{17}F are obtained by using two position sensitive PPAC (Parallel Plate Avalanche Counter) along the beam direction, and its position on ^{12}C target can be determined. Six sets of detector telescopes $\triangle$E-E were composed of double sided Silicon strip detectors(50mm×50mm in area)(DSSD) and square silicon detectors(SSD), and covered angle range about $\Theta_{lab} = 5° - 80°$. They were symmetrically positioned around the beam axis in order to measure efficiently the events of ^{17}F elastic scattering. The distance from the target center to the strip detectors are 145 mm, 115 mm and 85 mm depending on the three angle settings. Thin $\triangle$E (DSSD, 65μm thickness) placed in front of 300μm-thick E (SSD). Such detector configuration allowed identification of the Z of the scattered charged
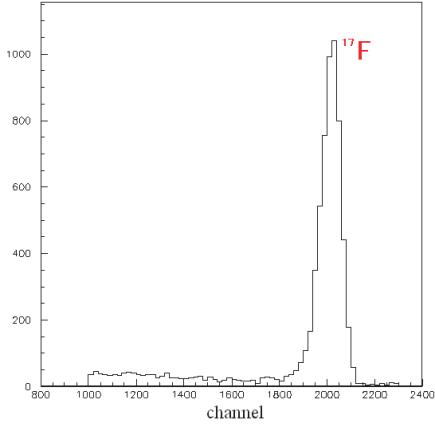
Figure 2. ^{17}F elastic scattering on silicon strip detector

identified clearly from the primary beam, which is a high intensity ^{16}O beam. After target, the silicon strip detectors are used to detect reaction particles.

Figure 2 shows the distribution of ^{17}F on the strip detectors. The elastic peak of ^{17}F is shown clearly. However, the excited state of ^{17}F can not be identified on the strip detectors since the resolution of detectors is not enough yet. The peak should give the quasi-elastic event of ^{17}F. The other continuous distribution could be from the other nuclear reactions, such as breakup, pre-equilibrium, etc. Two PPACs are calibrated from channel to time. The trajectory of ^{17}F is measured by using two PPACs and double strip detectors, then the scattering angle can be obtained. More detailed analyses of elastic scattering for 60MeV ^{17}F+^{12}C are being done.

particles. The emitted angle of ^{17}F can be determined precisely by silicon strip detectors. We will be able to extract precisely the angular distribution of elastic scattering for 60MeV ^{17}F+^{12}C.

Figure 1 shows the particle identification before target by using the method of TOF as well as radio frequency(RF) signal. TOF is obtained by using the time signals of two PPACs before target. It is shown that ^{17}F particles can be

References

[1] R. Morlock et al., Phys. Rev. Lett. **79** (1997) 3837.
[2] M. J. Borge et al., Phys. Lett. B. **217** (1993) 25.
[3] J. F. Liang et al., Phys. Rev. C **65**, (2002) 051603.
[4] J. F. Liang et al., Phys. Rev. C **67**, (2003) 044603.
[5] M. Romoli et al., Phys. Rev. C **69**, (2004) 064614.
[6] J. C. Blackmon et al., Phys. Rev. C **72**, (2005) 034606.

Progress on the ^{18}F+p and ^{18}F+d experiments at CRIB

S. Cherubini[a], C. Spitaleri[a], V. Crucillà[a], M. Gulino[a], M. La Cognata[a], L. Lamia[a],
R.G. Pizzone[a], S. Puglia[a], G.G. Rapisarda[a], S. Romano[a], M.L. Sergi[a], A. Tumino[+]

S. Kubono, H. Yamaguchi, Y. Wakabayashi, S. Hayakawa

N. Iwasa[b], S. Kato[c], H. Komatsubara[d], T. Teranishi[e]

A. Coc[f], F. Hammache[g], De Séreville[g]

[a]*Università di Catania and INFN-LNS, Catania, Italy*

Center for Nuclear Study, Graduate School of Science, University of Tokyo

[b]*Department of Physics, Tohoku University, Sendai, Japan*

[c]*Department of Physics, Yamagata University, Yamagata, Japan*

[d]*Department of Physics, Tsukuba University, Tsukuba, Japan*

[e]*Department of Physics, Kyushu University, Fukuoka, Japan*

[f]*Centre de Spectrométrie Nucléaire et de Spectrométrie de Masse, IN2P3, F-91405 Orsay, France,*

[g]*Institut de Physique Nucléaire, IN2P3, F-91405 Orsay, France*

[+]*Università KORE, Enna, and INFN-LNS, Catania, Italy*

The cross section of the nuclear reaction ^{18}F(p,α)^{15}O is of interest for astrophysics in the energy range 100-500 keV (center of mass). Actually, the first signals coming from a Nova event are the gamma rays emitted in the ^{18}F decay and this is the reason why the knowledge of the cross section of the reaction just mentioned is important [1] and it was widely studied even in recent years, see e.g. [2,3,4,5,6,7,8]. Nonetheless, it still needs to be investigated.

We performed two runs of an experiment aiming at the measurement of the ^{18}F(p,α)^{15}O reaction using a ^{18}F beam produced at the CRIB set-up of the Center for Nuclear Study (CNS) of the University of Tokyo, based at the RIKEN campus in Wako, Japan.

An introduction to our approach to this problem has already been mentioned in previous papers [9, 10]. We will report here on the present status of the experiment and its data analysis.

In the first run, performed in March 2007, we used the thick target method in order to directly measure the cross section of the reaction down to a center of mass energy of roughly 400 keV. As it is well known, this method allows for the investigation of a wide region of the excitation function using a single beam energy.

In the second run, March 2008, we used the Trojan Horse Method (THM) approach (see e.g. [11, 12]) to explore the energy region from roughly 100 keV in the center of mass up to roughly 600 keV so to have an overlap region with our and other direct measurements.

The experimental CRIB set-up is described in ref. [13] and details on the beam production as well as of the detection system are reported in the papers cited above [9, 10].

In the direct measurement experiment, we tuned the CRIB system to get a beam of ^{18}F at roughly 13.5 MeV that was used to bombard a thick (319 μg/cm^2) CH$_2$ target, while in the THM experiment the beam energy was chosen to be around 50 MeV. In this case a set of thin (100-200 μg/cm^2) CD$_2$ target was used.

The main parts of the detection system are a doublet of parallel plate avalanche counters (PPAC) located on the beam line during the measurement, eight bidimensional position sensitive silicon detectors (DPSSD) with a sensitive area of 45 mm by 45 mm each and a pair of double sided multistrip silicon detectors (DSSSD) 48 by 48 mm each. The eight DPSSDs were mounted to form a 3 by 3 squared plane array with a central hole of the dimensions of a single DPSSD. The two DSSSDs were mounted downstream of the DPSSD array to cover part of its central hole.

In the THM experiment, the second PPAC was replaced by a micro channel plate (MCP) system. This allowed for a much lower energy loss of the beam compared with the PPAC, so that the beam production conditions were similar to those of the direct experiment.

The PPACs (or the PPAC-MCP pair) were used to reconstruct the trajectory of each single incident particle. In this way we can correct the measured angles for the intrinsic beam divergence. Also, these detectors were used as part of the time of flight measurement system in order to achieve mass identification.

The DPSSD array and the DSSSD detected the outgoing particles over a large portion of the solid angle ($\phi \simeq 2\pi$ and $\theta \simeq 7-40$ degrees).

The initial phase of the data analysis work was devoted to the writing of a software package that allowed for the convertion of the raw data taken during the experiment into objects readable by the well know ROOT analysis suite.

In spite of the simplicity of this task, much time was devoted to the debugging of the software in order to have a reliable conversion of the data format and to avoid ill-treated events that could bring to artifacts in the data samples. In this software package, routines for the energy and position calibration of the detectors have also been implemented. Special attention was then devoted to the part of software, also embedded in the previous one, that takes care of the transformation of the position information given by the detectors into a correct angular information checking its response to a number of ad hoc generated sample events. Indeed, owing to the intrinsic beam divergence the projectiles do not im-

pinge on the target at zero degrees nor in the central position (as identified by the intersection of the ideal beam direction with the target plane). Instead, they show an incidence angle and position on the target that differ event by event. As the experiments need a relatively high angular resolution, this implies that the zenithal and azimuthal angles have to be calculated taking into account the actual values of the incidence angle and position.

The calibration of the detectors has been performed for
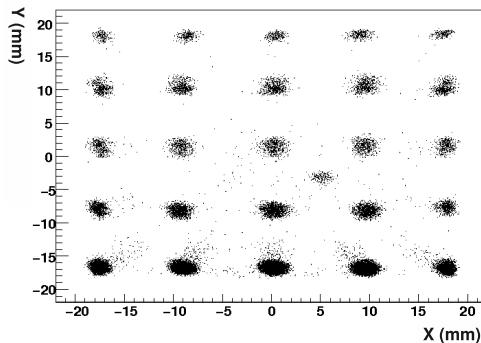
Figure 1. Typical x-y calibration spectrum of a DPSSD. The top panel (x-y matrix) shows the populated regions that correspond to the holes of a calibration grid put in front of the detectors during the calibration runs. The holes had 1 mm diameter. The off-aligned hole was used as a reference for the left-right, up-down orientation. The center of the detector has x=0, y=0 coordinates, the scales are in millimeter. This x-y matrix shows the very little pin-cushion effect suffered by the detector. A gaussian fits of the position peaks show a $\sigma \simeq$ 0.5-0.6 mm, implying a position resolution of the detector better than 1 mm.

both the direct and THM measurements.

The position resolution of the DSSSD is fixed by the strip pitch (3 mm), that of the DPSSDs has been found to be, as declared by the manufacturer, better than 1 mm. Figure 1 shows a typical position pattern obtained from one of the DPSSD. The energy calibration was done using a standard

triple peak alpha source and the elastic scattering of the primary ^{18}O beam on a ^{197}Au target checked against the result for the scattering of the ^{18}F radioactive beam on the same target. The energy resolution of the DSSSD was of the order of 0.5% while the DPSSD ones was somewhat worse, around 1.5%.

The data analysis for the THM experiment is presently being started while that concernig the direct measurement of the ^{18}F+p reaction is more advanced though still not finished yet.

The first goal of this latter analysis is to check the results obtained in this work with those of previous experiments at least in the energy region where they are well estabilished. This comparison is presently being performed.

References

[1] A. Coc et al., A.&A., 357 (2000) 561 and references therein.

[2] M. Wiescher and K.U. Kettner, Astrophys. J. 263 (1982) 891.

[3] K.E. Rehm, M. Paul, A.D. Roberts, et al., Phys. Rev. C52 (1995) R460.

[4] R. Coszach, M. Cogneau, C.R. Bain, et al., Phys. Lett. B353 (1998) 184.

[5] J.S. Graulich, F. Binon, W. Bradfield-Smith, et al., Nucl. Phys. A626 (1997) 751.

[6] J.-S. Graulich, S. Cherubini, R. Coszach, et al.,Phys. Rev. C63 (2001) 011302 and references therein.

[7] R.L. Kozub, D.W. Bardayan, J.C. Batchelder, et al., Phys. Rev. C71 (2005) 032801 (R).

[8] N. De Séreville, A. Coc, C. Angulo, et al., Phys. Rev. C67 (2003) 052801 (R) and references therein.

[9] S. Cherubini et al., *Annual Report 2006* and *Annual Report 2007*, Center fo Nuclear Study, Graduate School of Science, the University of Tokyo

[10] S. Cherubini et al., Perspectives in Nuclear Physiscs, *Proceedings of the 6th Japan-Italy Symposium on Heavy-Ion Physics*,Tokai, Japan, 11-15 November 2008, AIP Conference Proceeedings 1120 (2009) 294

[11] S. Cherubini, V.N. Kondratyev, M. Lattuada , et al., ApJ 457 (1996) 855

[12] C. Spitaleri, S. Typel, R.G. Pizzone, et al. Phys. Rev. C63 (2001) 055801

[13] Y. Yanagisawa, S. Kubono, T. Teranishi, et al., Nucl. Instr. Meth. A 539 (2005) 74

Feasibility study of the ^{18}Ne(α, p)^{21}Na reaction and development of the GEM-MSTPC

T. Hashimoto, S. Kubono, H. Yamaguchi, S. Hayakawa, K. Yamaguchi[a], H. Ishiyama[b],
M.H. Tanaka[b], Y.X. Watanabe[b], H. Miyatake[b], Y. Hirayama[b], N. Imai[b], Y. Fuchi[b], S. C. Jeong[b],
T. Nomura[b], Y. Mizoi[c], S. K. Das[c], T. Fukuda[c], H. Makii[d], and I. Arai[a],

Center for Nuclear Study, Graduate School of Science, University of Tokyo
[a]*Graduate School of Pure and Applied Sciences, University of Tsukuba*
[b]*Institute of Particle and Nuclear Studies (IPNS), High Energy Accelerator Research Organization (KEK)*
[c]*Research Center for Physics and Mathematics, Faculty of Engineering, Osaka Electro-Communication University*
[d]*Advanced Science Research Center, Japan Atomic Energy Agency (JAEA)*

1. Introduction

The ^{18}Ne(α, p)^{21}Na reaction is one of the main possible breakout routes. The reaction lead to the rp-process from the hot-CNO cycle, and convertre the initial CNO elements into heavier elements. It is predicted that the β-decay of ^{18}Ne can be bypassed by the ^{18}Ne(α, p)^{21}Na reaction at $T \geq 0.4$ GK. In particular, at around T = 1.0 GK of which the Gamow energy correspond to 1.5 MeV in center-of-mass energy (E_{cm}), this reaction is considered to dominate the breakout path.

Although several experimental efforts on the ^{18}Ne(α, p)^{21}Na reaction were reported in this energy region [1], the information for the reaction rate is very limited. Presently, there is no direct cross-section measurement of the reaction at the energy of interest. Since the contribution of the reaction to the breakout flow is poorly known, it is very important to measure the cross section of the ^{18}Ne(α, p)^{21}Na reaction accurately for identifying the breakout condition.

We are planning to directly measure the excitation function of the ^{18}Ne(α, p)^{21}Na reaction cross section in the low energies region using a sophisticated active target type detector system, Gas Electron Multiplier – Multiple Sampling and Tracking Proportional Chamber (GEM – MSTPC).

In this report, the feasibility of the experiment is discussed. In addition, the present status of the GEM – MSTPC will be explained.

2. Low-energy ^{18}Ne secondary beam production at CRIB

The required intensity, energy, and purity of the ^{18}Ne beam are 10^5 pps, 3.5 MeV/u, and 80%, respectively. In order to achieve these conditions, we will use the experimental conditions shown in Table 1.

The ^{18}Ne secondary beam particles will be produced using the ^{3}He(^{16}O, ^{18}Ne)n reaction at E(^{16}O) = 6.8 MeV/u and separated by the CNS low-energy Radioactive Ion Beam (CRIB) separator [2]. The cross section of the ^{3}He(^{16}O, ^{18}Ne)n reaction can be roughly estimated to be 1 – 2 mb at E(^{16}O) = 4.5 MeV/u according to a work on the same reaction [3]. Then, the production rate of ^{18}Ne particles may be about $2.0 - 4.1 \times 10^6$ pps. Since the acceptance of CRIB, which calculated by LISE++ [4], is about 5%. The estimated rate of ^{18}Ne is about $1.0 - 2.0 \times 10^5$ pps.

Table 1. The production conditions of ^{18}Ne beam.

Production reaction	^{3}He(^{16}O, ^{18}Ne)n
Energy of primary beam	6.8 MeV/u
Intensity of primary beam	400 pnA
^{3}He gas target	0.46 mg/cm^2
(Cryogenic target)	(Liq. N$_2$ cooled)

One serious concern is the purity of ^{18}Ne beam. We will select ^{18}Ne^{10+} to reject impurities. In this situation, ^{16}O will be stopped in the D1 magnet. In addition, the most of other impurities are swept out by using the Wien Filter and beam stopper in front of the F3 focal plane. Thus, the purity will be achieved higher than 80%. The estimated result satisfied the required condition of the ^{18}Ne beam.

3. Detector system

Figure 1 shows the experimental setup, which consists of a micro-channel plate (MCP), the GEM – MSTPC, and position sensitive silicon detectors (PSDs).
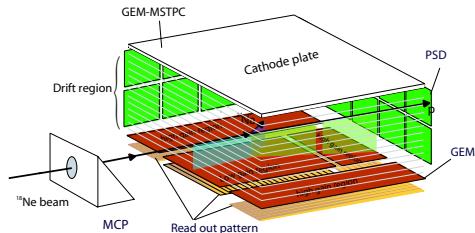
Figure 1. Experimental setup for the ^{18}Ne(α, p)^{21}Na reaction.

The MCP will be set in front of the GEM – MSTPC for the beam monitoring. The beam position and TOF can be measured on an event-by-event basis to identify the nuclide and to determine the absolute energy of beam particle.

The PSD array is set just outside of the gas sensitive area of the GEM -MSTPC in order to measure the energies and directions of protons. The solid angle and the angular range are 15.2% and 0 – 115 degrees, respectively.

The main chamber GEM – MSTPC has a structure based on the MSTPC [5, 6]. The MSTPC can measure the three dimensional trajectories and the energy loss of all relevant charged particle of reaction, which makes it possible to identify the true reaction events. The original MSTPC works well under the the beam injection rate lower than 10^4 pps. However, in the higher injection rate, output signals become unstable due to space charge gain limitation

near the individual anode wire. To overcome this limitation, we adopted a Gas Electron Multiplier (GEM) [7] foil, instead of a multi-wire proportional counter of the MSTPC.

The GEM – MSTPC consists of a drift space region and a proportional region. The drift space region has an active volume of 295 mm long, 278 mm wide 100 mm high. The proportional counter region consists of a low – gain regions for measurement of beam and/or recoil particles, and three high – gain region for measurement of emitted protons. Each region consists of one or more GEM foils and a position sensitive read – out pads.

A Operating gas and its pressure are 90% ^{4}He and 10% CO_2 and 0.2 atm. We studied some properties of the GEM – MSTPC in the low-pressure He +CO_2 (10%) gas using α-rays from a ^{241}Am. The details are shown in Ref. [8].

The experimental requires the gas gain higher than 10^3 for the GEM – MSTPC. We used two kinds of GEM foils for gas gain measurements: One is a standard CERN GEM foil (with 50 μm thickness) [7] and the other one is a 400 μm thick GEM (THGEM) [9]. While the gas gain of CERN GEM is less than 10^3 for single and double GEM configuration, the gain of the THGEM could be higher than 10^3 for a single configuration. In addition, the CERN GEM foil is easy broken, but the THGEM is robust against discharge phenomenon. Therefore, we adopted THGEM as a proportional counter of GEM – MSTPC.

A time dependence of gas gain was found for THGEM. This phenomenon, which comes from charging-up of the insulator between GEM electrodes, depends on the hole structure of the GEM foil [10]. As for the original THGEM, there is a 100 μm bare insulator (rim) from a hole edge. We considered that this rim was related to charging-up phenomenon. The rims were pruned from the original THGEM. After this modification, the pulse height shift disappeared.

It is important for stable position resolution of particle tracks to keep the uniform drift field. The main origin of distorted field is a large amount of positive ions feedback from the GEM foil existing in the drift space [11]. The ion feedback ratio (IFB) is defined as a ratio of total number of feedback positive ions to the one of electrons collected by the anode plate. At beam injection rate of 10^6 pps, this ratio is required to be less than 1%.

The measured IFB for a single THGEM configuration was about 30%. To reduce the IFB, additional two THGEM foils were installed between the drift space and the single THGEM. We have performed systematic search by changing electric voltage of the additional THGEMs and in transfer gaps between the THGEMs. The IFB was found to be less than 2% for this triple THGEM configuration. Further effort to reduce the ion feedback is under progress.

4. Yield estimation

Figure 2 shows estimated number of events per energy bin of 100 keV. The energy-loss process of the beam particle is utilized to scan the center-of-mass (cm) energy (E_{cm})

to deduce the excitation function without changing the secondary beam energy. In the present condition, we can measure the cross sections of the ^{18}Ne(α, p)^{21}Na reaction at $E_{cm} = 0.5 – 4.0$ MeV.

The open squares are calculated by the statistical model [12]. The open circles are calculated results that assumed two resonances together with a statistical calculation. The cross section of resonant reaction was calculated by Breit – Wigner formula. In both cases, we can measure the cross sections at $E_{cm} \geq 1.5$ MeV with a statistical uncertainly better than 20%. This energy region correspond to about $T \geq 1.0$ GK.
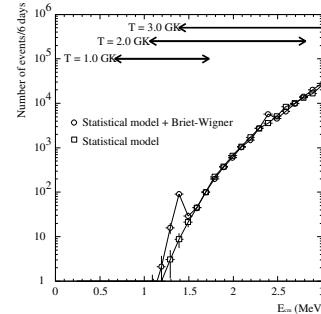
Figure 2. A statistical estimation for the experiment as a function of the reaction energy. Energy region of astrophysical interest are indicated by arrows. The solid lines are eye guide.

5. Summary

We will perform the direct measurement of the excitation function of the ^{18}Ne(α, p)^{21}Na reaction cross section at the low energies region using the GEM – MSTPC. The main problem is the positive ion feed back from the GEM foil. After solving the problem, we can measure the excitation function of the ^{18}Ne(α, p)^{21}Na reaction at $E_{cm} \geq 1.5$ MeV with a statistical uncertainty better than 20%.

References

[1] J. J. He *et al.*, Eur. Phys. J. A **36** (2008) 1, and references therein.
[2] S. Kubono, *et al.*, Nucl. Phys. A **558** (1995) 305.
[3] A. V. Nero *et al.*, Phys. Rev. C **24** (1981) 1864.
[4] O. B. Tarasov and D. Bazin, Nucl. Phys. A **746** (2004) 411.
[5] Y. Mizoi *et al.*, Nucl. Instrum. Meth. A **431** (1999) 112.
[6] T. Hashimoto *et al.*, Nucl. Instrum. Meth. A **556** (2006) 339.
[7] F. Sauli Nucl. Instrum. Meth. A **386** (1997) 531.
[8] K. Yamaguchi *et al.*, Nucl. Instrum Meth A, to be published
[9] C. Shalem *et al.*, Nucl. Imstrum. Meth. A **558** (2006) 475.
[10] J. Benlloch *et al.*, Nucl. Instrum. Meth. A **419** (1998) 418.
[11] F. Sauli *et al.*, Nucl. Instrum. Meth A **560** (2006) 269.
[12] T. Rauscher *et al.*, Atom. Data and Nucl. Data Tables **75** 1.

Alpha Resonant Scattering Measurement Using a ^{21}Na Radioactive Beam

D.N. Binh[a], L.H. Khiem[b], N.T. Tho[b], S. Kubono[a], H. Yamaguchi[a], Y. Wakabayashi[a],
S. Hayakawa[a], D. Kahl[a], T. Hashimoto[a], T. Teranishi[c], S. Kato[d], N. Iwasa[e], N. Kume[e]

[a]Center for Nuclear Study, Graduate School of Science, University of Tokyo
[b]Institute of Physics, Vietnamese Academy for Science and Technology
[c]Department of Physics, Kuyshu University
[d]Physics Department, Yamagata University
[e]Department of Physics, Tohoku University

1. Introduction

The explosive hydrogen burning is thought to be a main source of energy generation in novae and X-ray bursts, and also provides an important route for nucleosynthesis of material up to masses as high as the mass 100 region via rp-process [1]. Nucleosynthesis in the NeNa cycle during nova outbursts leads to the synthesis of the astronomically important ^{22}Na nucleus, the radioactive isotope with a 2.602 yr half-life. Its beta decay leads to the emission of a 1.275 MeV gamma-ray, following population of the first excited state in ^{22}Ne. This gamma-ray is a possible observable for nova events. Observational searches were performed with NASA's COMPTEL on-board CGRO satellite of five ONe novae [2]. Furthermore, ESA satellite INTE-GRAL was launched in April 2002 to attempt to detect this γ ray, but the detection is still quite challenging, since the expected flux is small [3].

The synthesis of ^{22}Na in novae has been extensively investigated in the past two decades (a recent review is found in Ref. [4]). Proton-capture reactions on the seed nuclei "^{20}Ne" are responsible for the synthesis of significant amount of the unstable nucleus ^{21}Na. This is followed by either two possible reaction paths. In the first path (called the "cold" NeNa cycle) ^{21}Na leads to production of ^{22}Na by following reactions, ^{21}Na$(\beta^+)^{21}$Ne$(p,\gamma)^{22}$Na. In the second path, associated with higher temperature (called "hot" NeNa cycle), the proton capture process on ^{21}Na dominates over its β-decay, followed by ^{21}Na$(p,\gamma)^{22}$Mg$(\beta^+)^{22}$Na. There is little net mass flow from ^{22}Mg to ^{23}Al due to the low Q-value for photo disintegration of ^{23}Al. However, the observed ^{22}Na abundance was much smaller than the predicted value by current models of ONe novae. The reduction of the nuclear uncertainties associated with the reactions involved in the synthesis of ^{22}Na is critically important in order to predict how much ^{22}Na can be produced in a typical nova event, and at what distance a nova explosion is expected to provide a detectable flux of γ-rays. One of the main reactions associated with calculating the amount of ^{22}Na in nova outbursts is the ^{21}Na(p,γ) reaction [5]. This reaction study has been recently carried out by TRIUMF-ISAC groupe [6].

At high temperature and density condition, like in X-ray bursts, reaction flow occurs mainly via rp-process, a combination of (p,γ), (α,p) reactions, and β^+ decays, it will be commenced by breakout processes from one cycle to the next. The investigation of the breakout process from the NeNa cycle to the MgAl cycle is also important to understand the early stage of the rp-process [7]. The ^{21}Na$(p,\gamma)^{22}$Mg reaction could be the main link from the NeNa cycle to the MgAl cycle and beyond, and leads the way into rp-process [8]. Since the Q-value of ^{22}Mg(p,γ) is low (Q = 126 keV), it will enter (p,γ)(γ,p) equilibrium with ^{23}Al that prevents the reaction flow, and ^{22}Mg could be a potential waiting point [9].

The predicted ^{22}Na abundance might be reduced by α-induced reactions on ^{21}Na, in particular (α,p). This could be the break-out process from the NeNa cycle and bypassing the production of ^{22}Na, and in the X-ray bursts, it can bridge the waiting point at ^{22}Mg. The other motivation is to advance knowledge of the nuclear level structure in ^{25}Al that was poorly known above the α-threshold. So far, only two levels have been reported above this threshold. They are at 9.275 MeV and 9.415 MeV [11].

2. Experiment

The experiment was performed using a low energy ^{21}Na beam from the CNS Radioactive Ion Beam separator (CRIB) [10]. This is the direct measurement using the thick target method in inverse kinematics. Experimental setup was installed in the F3 chamber at the downstream of the Wien filter as shown in Fig. 1. Two PPACs were set to measure the timing and position of the incoming ^{21}Na beam particles. The timing information was used for making event triggers, and also for particle identification with a time-of-flight (TOF) method. The position of the beam particle and the incident angle at the target were determined by extrapolating the positions measured by the two PPACs. The gas target has a semi-cylindrical shape with a length of 15 cm in the beam line direction. The entrance window was made of a Havar foil of 2.5 μm thickness and the exit window was made of 25 μm thick Mylar foil. The gas cell was filled with Helium gas at 580 Torr.
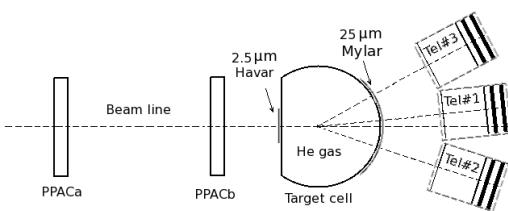
Figure 1. Experiment setup at F3 chamber

There are three multi-layered silicon detector sets, re-

ferred to as $\Delta E - E$ telescopes, were used for measuring the energy and angular distribution of products after the Helium target. The $\Delta E - E$ telescopes consisted of a thin Micron Double-Sided Silicon detector with a thickness of about 70 μm, referred to ΔE detector, followed by a Hamamatsu Silicon detector of 280 μm thickness, and two thick Micron Silicon detectors with thickness of about 1.5 mm. They were placed at 178 mm distant from the center of the gas target.

The ^{21}Na secondary beam was produced via the ^{2}H(^{20}Ne,^{21}Na)n reaction. The ^{20}Ne^{7+} primary beam was accelerated up to 6.23 MeV/u by the AVF cyclotron of RIKEN. The developed cryogenic gas target system [12] was used at F0. Its cell, which has 80 mm length and 20 mm diameter, contained the ^{2}H gas at about 450 Torr and was cooled down to 77 K by liquid nitrogen. The momentum of the ^{21}Na^{11+} secondary beam was analyzed by the dipole magnet D1 and reached the momentum dispersive focal plane F1. The momenta of the particles were selected by a slit at F1 chamber and transported to the achromatical focal plane F2. The particles were clearly identified by the E - TOF method (see Fig. 2 (a)), where TOF implies the time-of-flight between the RF signals from the cyclotron and the Parallel-Plate Avalanche Counters (PPAC), and E indicates the energy measured by a Si detector downstream of the PPAC. There are some other radioactive isotopes produced together with the ^{21}Na beam by some other reactions. The optimum purity of ^{21}Na^{11+} estimated at F2 chamber is 16.1 %. In order to further separate ^{21}Na^{11+} from other contaminant particles, the Wien filter was applied with the high voltages + 72 kV and - 44 kV. After the Wien filter, the ^{21}Na beam is purified about 96 % and has an intensity up to 5×10^5 pps. The beam energy right after the entrance Havar foil is 39 MeV. The beam is fully stopped in the exit Mylar foil. The scanned energy region is from 1 MeV to 6 MeV in the center of mass frame, corresponding to the excitation energy of ^{25}Al compound nucleus from 10.16 MeV to 15.16 MeV.
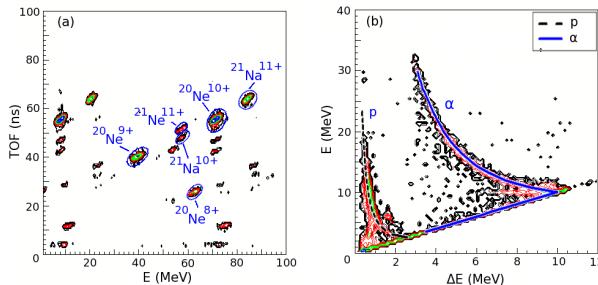
Figure 2. (a) Particle identification at F2, (b) at F3

3. Analysis and preliminary results

The reaction products were detected by the $\Delta E - E$ telescopes. The proton and alpha are distinguished clearly from the other particles as shown in Fig. 2 (b). However, they were produced not only by the (α,p) and alpha scattering reactions in the gas target, but also by other material at upstream of target, such as PPACs. These background can be identified by taking into account the TOF, and subtracted the data of Argon gas measurement. Figure 3 shows preliminary alpha scattering excitation function measured at $0° \sim 10°$ in the laboratory frame, where elastic scattering was assumed for all the α events.
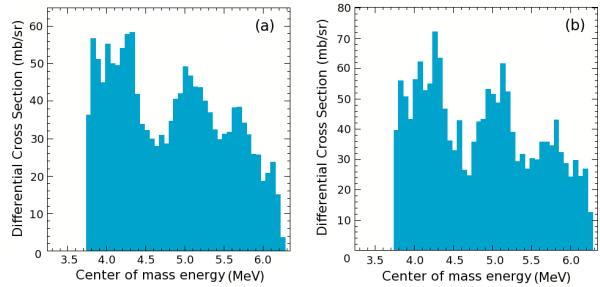
Figure 3. Alpha scattering excitation functions measured at (a) from 0° to 5° and (b) from 5° to 10°

An R-matrix [13] fit to the excitation function will be used to extract physical parameters, such as resonant energies, alpha widths and spin parities in ^{25}Al. These information are crucially important to calculate the reaction rate and to discuss on their implication for astrophysics. The analysis is in progress.

References
[1] W. Bradfield *et al.*, Phys. Rev. C **59** (1999) 3402.
[2] A. F. Iyudin et al., Astron. Astrophys. **300** (1995) 422.
[3] M. Hernanz and J. José, *Udated Prospects for Detectability of Classical Novae with INTEGRAL* (Proc. 5th INTEGRAL Workshop, Germany, 2004) 95.
[4] M. Hernanz, and J. José, *Classical Nova Explosions* (AIP, Melville, NY, 2002).
[5] N. A. Smirnova *et al.*, Phys. Rev. C **62** (2000) 045803.
[6] S. Bishop *et al.*,Phys. Rev. Lett. **90** (2003) 162501-1.
[7] S. Kubono, Nucl. Phys A558 (1995) 305.
[8] J. M. D'Auria et al, Phys. Rev. C69 (2004) 065803
[9] J. L. Fisker, F. K. Thielemann, and M. Wiescher, Astro. J. 608 (2004) 61.
[10] S. Kubono et al., Eur. Phys. J, A **13** (2002) 217.
[11] P. M. Endt, Nucl. Phys. A **633** (1998) 1.
[12] H. Yamaguchi et al Nucl. Instrum. Meth. Phys. Res., Sect. A **589** (2008) 150.
[13] A. M. Lane, and R. G. Thomas, Rev. Mod. Phys. **30** (1958) 257.

Update: study of astrophysically important states in ^{26}Si using the ^{25}Al+p elastic scattering with CRIB

J. Chen[a], A. Chen[a], S. Kubono[b], H. Yamaguchi[b], G. Amadio[b], S. Cherubini[h], M. La .Cognata[h], H. Fujikawa[b], S. Hayakawa[b], N. Iwasa[j], J. J. He[b,1], D. Kahl[a], L. H. Khiem[b], Y. Kurihawa[b], Y. K. Kwon[c], J Y. Moon[c], M. Niikura[b], S. Nishimura[f], A. Odahara[e], J. Pearson[a], R. Pizzone[h], A. Saito[b], C. Signorini[i], T. Teranishi[d], Y. Togano[g], Y. Wakabayashi[b]

[a] *Department of Physics and Astronomy, McMaster University, Canada*
[b] *Center for Nuclear Study, Graduate School of Science, University of Tokyo, Japan*
[c] *Department of Physics, Chung-Ang University, South Korea*
[d] *Department of Physics, Kyushu University, Japan*
[e] *Department of Physics, Nishinippon Institute of Technology, Japan*
[f] *RIKEN(The Institute of Physical and Chemical Research)*
[g] *Department of Physics, Rikkyo University, Japan*
[h] *Department of Physics, University of Catania and INFN, Italy*
[i] *Department of Physics, University of Padova and INFN, Italy*
[j] *Department of Physics, Tohoku University, Japan*

1. Introduction

The astrophysically important states in ^{26}Si have been studied with different reactions [1,2,3,4,5] because of their dominant contributions to the ^{25}Al$(p,\gamma)^{26}$Si reaction rate at nova temperatures. But controversies exist on the spin-parity assignments for some dominant states, such as the 5.912 MeV and 5.946 MeV states, and the level energies and spin-parities of the newly found states from those measurements also need to be confirmed. Furthermore, comparison with the mirror nucleus suggests the possible existence of new states in ^{26}Si, which may contribute strongly to the ^{25}Al$(p,\gamma)^{26}$Si rate at supernova temperatures. To address these issues, we performed an elastic scattering of ^{25}Al+p with CRIB [7] at RIKEN for obtaining information on states in a broad range (E$_x$=5.6 MeV - 8.6 MeV) above the proton threshold [8]. A thick target method [6,9] was used to scan the center-of-mass energy from 0 to 3.38 MeV with the secondary beam of 3.52 MeV/nucleon ^{25}Al impinging on 6.58 mg/cm^2 CH$_2$ target, which corresponds to a range of excited states from 5.515 MeV (^{25}Al+p threshold) to about 8.9 MeV. In this report, we will present the update on the data analysis and the new ^{25}Al$(p,\gamma)^{26}$Si reaction rate based on our result.

2. Data Analysis

After correcting the energy loss of the scattered protons in the target and subtracting the background protons due to the carbon component in the target, we can obtain the final excitation function, as shown in Fig. 2.

Since at low energies (E_R<1.2 MeV) the Coulomb scattering is dominant, no apprarent resonance signature was observed in the excitation function. At the high energy region (E_R>2.5 MeV) in the excitation function, there are several resonance-alike signatures and they are very diffi-

cult to be identified due to the poor statistics. Therefore, we only fit the three prominent resonances in the range from the 1424 keV to 2484 keV using the R-Matrix formalism of the differential cross-section for compound nuclear reactions or scatterings [11].

According to scattering theory, the s-wave (l=0) scattering is dominant and the higher partial waves make less or negligible contributions to the scattering. Therefore, the three resonances can be fitted assuming s-wave scattering, with the best fit shown in Fig. 2. The fitting range corresponds to the level range of 6.942 MeV to 8.002 MeV, which is within the Gamow window (T_9>1). The uncertainty ($\sim$15% , systematic and statistical) for the data is adopted from reference [12] considering the similar experimental set-up. Table 1 lists the resonance parameters for the three resonances extracted from the R-Matrix fit to the data.
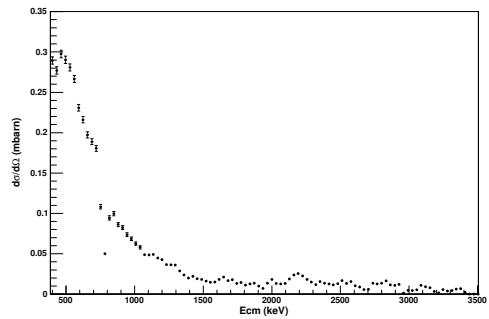
Figure 1. Excitation function at 0° in the center of mass frame after energy loss correction and background subtraction.

Table 1. List of parameters of resonances from a R-Matrix fit to the three resonances in the experimental differential cross section in the energy range 1424 keV — 2484 keV. The pole energy E_λ, the resonance energy E_R and the level energy E_x are in units of MeV and the resonance width Γ_R is in units of keV. The proton separation energy (or proton threshold energy) is S_p=5.518 MeV. Th uncertainties quoted are directly from the fits.

J^π	E_λ	E_R	E_x	Γ_R
2^+	1.882(45)	1.617(76)	7.135(76)	43(10)
2^+	2.018(11)	1.977(15)	7.495(15)	10(3)
3^+	2.251(19)	2.129(28)	7.647(28)	89(15)

Table 2. List of parameters to be used in the calculations of the $^{25}Al(p,\gamma)^{26}Si$ stellar reaction rate. The parameters of the first three resonances are adopted from Ref [4]. The Γ_γ and $\omega\gamma$ for the three resonances from our analysis are estimated by calculating the Weisskopf-unit γ widths of single-particle transitions.

J^π	E_R(keV)	Γ_p (eV)	Γ_γ(eV)	$\omega\gamma$(eV)
1^+	155	1.3×10^{-9}	1.10×10^{-1}	3.25×10^{-10}
3^+	394	2.49	3.30×10^{-2}	1.90×10^{-2}
0^+	428	1.9×10^{-2}	8.80×10^{-3}	5.01×10^{-4}
2^+	1617	4.3×10^{4}	6.98×10^{-2}	2.91×10^{-2}
2^+	1977	1.0×10^{4}	8.93×10^{-2}	3.72×10^{-2}
3^+	2129	8.9×10^{4}	8.01×10^{-7}	4.67×10^{-7}

Figure 2. An R-Matrix fit for the three resonances at $E_R \sim 1.62$ MeV, 1.97 MeV and 2.13 MeV, with s-wave (l=0) scattering for all and J^π=2^+, 2^+ and 3^+, respectively.

3. The ^{25}Al(p,γ)^{26}Si reaction rate

The total resonant reaction rate was calculated using the formula as follows:

$$\langle\sigma v\rangle_{res} = 2.557\times10^{-19}\left(\frac{m_Am_B}{m_A+m_B}T_9\right)^{-3/2}$$
$$\times\sum_i(\omega\gamma)_i exp\left(-\frac{11.605E_{R_i}}{T_9}\right)\ [cm^3s^{-1}]$$

where m_A and m_B are the masses of the reacting nuclei in units of a.m.u., $\omega\gamma$ is the resonance strength in units of eV and E_R is the resonance energy in units of MeV.

Table 2 lists all the input parameter values to be used in the calculation of the $^{25}Al(p,\gamma)^{26}Si$ reaction rate.

The calculated reaction rates are shown in Fig. 3. The rates from the resonances E_R=155 keV ($J^\pi = 1^+$), E_R=394 keV ($J^\pi = 3^+$) and E_R=428 keV ($J^\pi = 0^+$) are directly adopted from Ref [4] and the non-resonant contribution (DC) is is taken directly from Ref. [13].

Figure 3. The ^{25}Al(p,γ)^{26}Si reaction rates from direct capture reaction and individual resonances.

References

[1] D. W. Bardayan *et al.*, Phys. Rev. C **65** (2002) 032801.
[2] J. A. Caggiano *et al.*, Phys. Rev. C **65** (2002) 055801.
[3] Y. Parpottas *et al.*, Phys. Rev. C **70** (2004) 065805.
[4] D. W. Bardayan *et al.*, Phys. Rev. C **74** (2006) 045804.
[5] D. Seweryniak *et al.*, PRC **75** (2007) 062801(R).
[6] S. Kubono, Nucl. Phys. A **693** (2001) 221-248.
[7] S. Kubono *et al.*, EPJ A **13** (2002) 217-220.
[8] J. Chen *et al.*, CNS Annual Reprot (2006) 5.
[9] A. H. Hernández *et al.*, NMB **143** (1998) 569-574
[10] J. C. Thomas *et al.*, Eur. Phys. J.A **21** (2004) 419-435.
[11] A. M. Lane, and R. G. Thomas, Rev. Mod. Phys. **30** (1958) 257.
[12] J. J. He *et al.*, PRC **76** (2007) 055807.
[13] C. Iliadis *et al.*, PRC **53** (1996) 475.

Study of High-Spin States in A∼40 Nuclei

E. Ideguchi, S. Ota, T. Morikawa[a], M. Oshima[b], M. Koizumi[b], Y. Toh[b], A. Kimura[b], H. Harada[b],
K. Furutaka[b], S. Nakamura[b], F. Kitatani[b], Y. Hatsukawa[b], T. Shizuma[b], M. Sugawara[c],
H. Miyatake[d], Y.X. Watanabe[d], Y. Hirayama[d], and M. Oi[e]

Center for Nuclear Study, Graduate School of Science, University of Tokyo
[a]*Department of Physics, Kyushu University*
[b]*Japan Atomic Energy Agency*
[c]*Chiba Institute of Technology*
[d]*Institute of Particle and Nuclear Studies, High Energy Accelerator Research Organization (KEK)*
[e]*Institute of Natural Sciences, Senshu University*

After a systematic investigation of superdeformations in various mass regions [1], a new 'island' of superdeformed (SD) nuclei was found in the nuclear chart around A ∼ 40 (i.e., ^{36}Ar [2], ^{40}Ca [3,4], and ^{44}Ti [5]). These N = Z nuclei are magic and near magic systems whose ground states have a spherical shape. In order to produce the collective degrees of freedom necessary for the formation of SD states, cross-shell excitations involving both *sd* and *fp* shells are necessary. SD shell structure in this mass region plays an important role in forming such large deformed structures. The deformed shell gap at $\beta_2 \sim 0.6$ at N = Z = 20 is associated with the SD band of ^{40}Ca with eight particle eight hole (8p–8h) configuration built on the third 0^+ state. Another deformed shell gap at $\beta_2 \sim 0.5$ at N = Z = 18 is associated with the observed SD band in ^{36}Ar [2] which is built on the second 0^+ state with 4p–4h configuration. The presence of many deformed gaps in this region may imply large deformed structures at high-spin states in A ∼ 40 nuclei. Woods-Saxon single-particle diagram [3] shows the large deformation gaps at $\beta_2 \sim 0.5$ for Z = 18 and N = 22. As a consequence, a SD band structure is expected in ^{40}Ar to be built on the second 0^+ state with 6p–4h configuration, which is similar to those observed in ^{38}Ar [6] and ^{42}Ca [7]. In order to investigate the SD band in ^{40}Ar, we have performed an in-beam γ-ray spectroscopy using a ^{26}Mg(^{18}O, 2p2n)^{40}Ar reaction.

The experiment was performed at the tandem accelerator facility of the Japan Atomic Energy Agency. An ^{18}O beam of 70 MeV was used to irradiate the two stacked ^{26}Mg target foils of 0.47 and 0.43 mg/cm^2 thickness. High-spin states in ^{40}Ar were populated via the ^{26}Mg(^{18}O, 2p2n)^{40}Ar reaction. Gamma rays were detected by the GEMINI-II array [8] comprised of 16 HPGe detectors with BGO Compton suppressor shields, in coincidence with charged particles detected by the Si-Ball [9], a 4π array consisting of 11 ΔE Si detectors of 170 μm thickness. The HPGe detectors were placed at 6 different angles, namely 47° (4 Ge's), 72° (2 Ge's), 90° (2 Ge's), 105° (4 Ge's), 144° (1 Ge) and 147° (1 Ge) with respect to the beam direction, which enables us to perform angular distribution and DCO(Directional Correlations from Oriented states) analyses [10]. The most forward placed Si detector was segmented into five sections and the other Si detectors were segmented into two sections each, giving a total of 25 channels that were used to enhance

the selectivity of multi-charged-particle channels. With a trigger condition of more than two Compton suppressed Ge detectors firing in coincidence with charged particles, a total number of 6.6×10^8 events were collected. Figure 1 shows γ-ray spectra deduced by different charged particle gates; i.e. (a) 2 α, (b) 1 α, (c) 2 proton gates. As clearly seen in the figure, γ rays associated with different evaporation channel were enhanced by the different charged-particle gates.
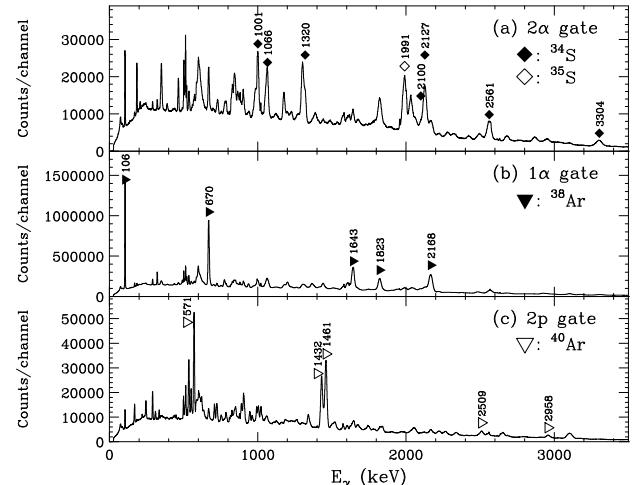
Figure 1. Gamma-ray spectra of the in-band γ transitions of SD band deduced by gating on the different charged-particle channels.

Gamma-gamma coincidence relations were examined by gating on the low-lying known γ-ray transitions, and the previously reported level scheme of ^{40}Ar [11] was confirmed up to the 6.8 MeV level. In addition, two γ-ray cascade transitions of 2268 and 2699 keV were newly identified in coincidence with the 992, 1441 and 1841 keV transitions. These five γ-ray transitions show mutual coincidence relations. Accordingly, these five γ-ray transitions form a rotational band ranging from 2^+ to 12^+ states as shown in Fig. 2.

Spins of the observed levels are assigned on the basis of the DCO ratios of γ rays [10] by analyzing the asymmetric angular correlation matrix. Multipolarities of the in-band transitions and the linking transitions of $4_2^+ \rightarrow 2_1^+$ and $6_2^+ \rightarrow 4_1^+$ are consistent with a stretched quadrupole character. Assuming E2 multipolarity for the stretched quadrupole
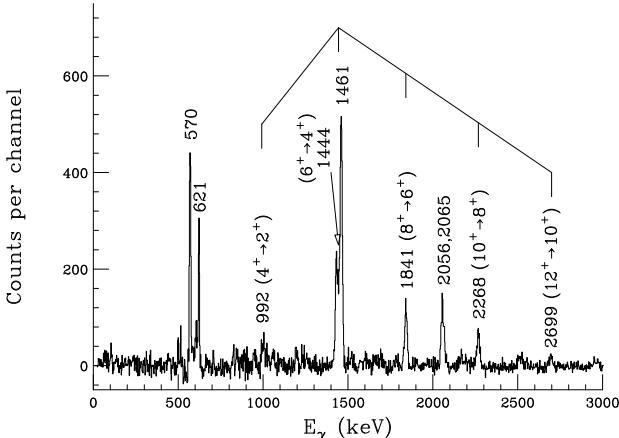
Figure 2. Gamma-ray spectrum created by gating on the in-band γ transitions of SD band in ^{40}Ar.

transitions, the parity of the band was assigned to be positive.
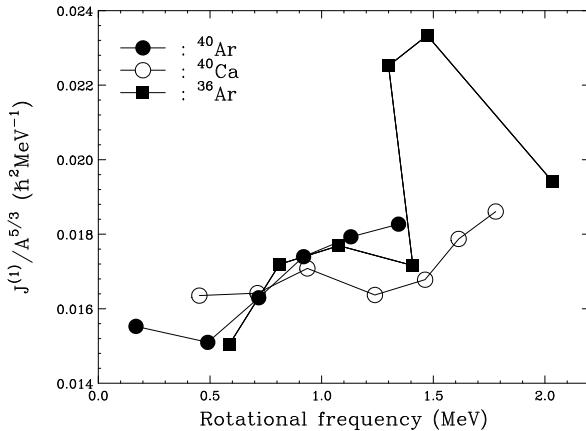
Figure 3. Kinematical moments of inertia $J^{(1)}$ of SD bands in ^{40}Ar (filled circle), ^{36}Ar (filled square) and ^{40}Ca (open circle) scaled by $A^{5/3}$.

In order to compare the high-spin behavior of the rotational band in ^{40}Ar with the SD bands in ^{36}Ar [2] and ^{40}Ca [3], kinematical moments of inertia ($J^{(1)}$) scaled by $A^{5/3}$ for ^{36}Ar, ^{40}Ca and ^{40}Ar are plotted as a function of rotational frequency (Fig. 3). Here, $J^{(1)}$ values are scaled by $A^{5/3}$. Because ^{40}Ar has the similar $J^{(1)}$ values to the one for ^{36}Ar and ^{40}Ca, the size of deformation of the ^{40}Ar rotational band is expected to be as large as the deformation of the SD bands in ^{36}Ar and ^{40}Ca. Unlike ^{36}Ar, no backbending was observed in ^{40}Ar. Its behavior is rather similar to ^{40}Ca. Many theoretical models including the shell model [2, 12, 13, 14] and the several mean-field models [15, 16, 17] were applied to the analyses of ^{36}Ar. All calculations show that the origin of the strong backbending in ^{36}Ar is due to the simultaneous alignment of protons and neutrons in the $f_{7/2}$ orbital.

To determine the deformation of the band, the transition quadrupole moment Q_t was deduced from the residual Doppler shift analysis [18] to be $\sim$1.45 eb [19]. This result indicates the superdeformed shape of the band with the deformation parameter $\beta_2 \sim 0.5$.

Pronounced differences in the high-spin behavior between ^{36}Ar and ^{40}Ar might imply that an addition of four neutrons to ^{36}Ar gives rise to a change on the structure. In order to understand this structural change, the cranked Hatree-Fock-Bogoliubov (HFB) calculations with the P+QQ force [17] were carried out. The evolution of the nuclear shape was treated in a fully self-consistent manner, and the model space of the full sd-fp shell plus the $g_{9/2}$ orbit was employed. The calculation shows that $\beta_2 = 0.57$ at $J = 0\hbar$ and that the deformation gradually decreases to 0.45 at $J = 12\hbar$. The triaxiality component is found to be almost zero ($\gamma \simeq 0°$) throughout this angular momentum range. This result agrees with the experimental Q_t value within the error bars.

Studies of high-spin states in other nuclei produced in the ^{18}O+^{26}Mg fusion reaction are now in progress.

References

[1] B. Singh, R. Zywina, R.B. Firestone, Nucl. Data Sheets **97**, 241-592 (2002).

[2] C.E. Svensson *et al.*, Phys. Rev. Lett. **85**, 2693-2696 (2000).

[3] E. Ideguchi *et al.*, Phys. Rev. Lett. **87**, 222501/1-4 (2001).

[4] C.J. Chiara *et al.*, Phys. Rev. C **67**, 041303(R)/1-5 (2003).

[5] C.D. OfLeary *et al.*, Phys. Rev. C **61**, 064314/1-7 (2000).

[6] D. Rudolph *et al.*, Phys. Rev. C **65**, 034305/1-8 (2002).

[7] M. Lach *et al.*, Eur. Phys. J. A **16**, 309-311 (2003).

[8] M. Oshima *et al.*, J. Radioanal. Nucl. Chem. **278**, 257-262 (2008).

[9] T. Kuroyanagi *et al.*, Nucl. Instrum. Methods Phys. Res. A **316**, 289-296 (1992).

[10] K.S. Krane, R.M. Steffen and R.M. Wheeler, Nucl. Data Tables, **11**, 351–406 (1973).

[11] E. Bitterwolf *et al.*, Z. Phys. A **313**, 123-132 (1983).

[12] E. Caurier, F. Nowacki, and A. Poves, Phys. Rev. Lett. **95**, 042502/1-4 (2006).

[13] E. Caurier, J. Menédez, F. Nowacki, and A. Poves, Phys. Rev. C **75**, 054317/1-11 (2007).

[14] G.-L. Long and Y. Sun, Phys. Rev. C **63**, 021305(R)/1-4 (2001).

[15] T. Inakura *et al.*, Nucl. Phys. A **710**, 261-278 (2002).

[16] M. Bender, H. Flocard, and P.-H. Heenen, Phys. Rev. C **68**, 044321/1-13 (2003).

[17] M. Oi, Phys. Rev. C 76 (2007) 044308/1-15.

[18] B. Cederwall *et al.*, Nucl. Instrum. Methods Phys. Res. Sect. A 354, 591-594 (1995)

[19] E. Ideguchi *et al.*, (to be published).

Beta-decay half life of ^{46}Cr

Y. Wakabayashi[a] H. Yamaguchi[a] T. Hashimoto[a] S. Hayakawa[a] Y. Kurihara[a] D. N. Binh[a,b],

D. Kahl[a], S. Nishimura[c], Y. Gono[c], M. Suga[d], Y. Fujita[d], and S. Kubono[a]

[a]*Center for Nuclear Study, Graduate School of Science, University of Tokyo*
[b]*Institute of Physics and Electronic, Vietnam Academy of Science and Technology*
[c]*RIKEN (The Institute of Physical and Chemical Research)*
[d]*Department of Physics, Osaka University*

1. Introduction

For the rapid proton capture process (*rp*-process) in X-ray burst and the core-collapse stage of supernova, weak interaction processes of proton-rich *pf*-shell nuclei far from stability play important roles [1]. Studies of the β decay and electron capture of these proton-rich *pf*-shell nuclei are of great astrophysical interest. These decays involved in the charged-current processes, e.g., p $\rightarrow$ n + e$^+$ + ν, are predominated by the Fermi and Gamow-Teller (GT) transitions. Thus, these experimental data are required to understand nuclear properties and astrophysical problems.

Information on the GT transitions can be derived directly from β-decay measurements. Recently, studies were performed for several proton-rich *pf*-shell nuclei [2, 3, 4, 5]. However, the GT transition strengths (B(GT)'s) of these proton-rich nuclei far from stability were measured for only a few low-lying states with large uncertainties due to the small production cross sections and short half lives. To determine the B(GT) accurately, it is important to know the feeding ratio and the half life of the β decay accurately.

As for the β decay of ^{46}Cr, one of proton-rich *pf*-shell nuclei, half life has been reported with a large uncertainty; 240(140) [2] ms and 260(60) [6] ms, and only a gamma line of 993 keV was measured with β decay [2].

In this study, the final goal is to measure the properties of ^{46}Cr, namely, i) the half life of the β decay with an accuracy better than 10 %, and ii) the decay branching ratios to the ground state (Fermi transition) and GT states accurately.

2. Experimental procedure

The experiment to measure the half life of ^{46}Cr was performed using the low-energy RI beam separator (CRIB) [7, 8] of the Center for Nuclear Study (CNS), University of Tokyo. The ^{46}Cr nuclei were produced using the ^{36}Ar + ^{12}C fusion reaction. A natural C foil of 0.56 mg/cm^2 was installed as the primary target. The ^{36}Ar primary beam was accelerated to 3.6 MeV/nucleon by the RIKEN AVF cyclotron, and degraded to 3.0 MeV/nucleon by a 2.2-μm-thick Havar foil placed in front of the primary target to maximize production of ^{46}Cr. To separate ^{46}Cr from other nuclei produced in the fusion reaction, a Wien filter (W.F.) was used at high voltages of ± 85 kV. A microchannel plate (MCP) [9, 10] was placed at the final focal plane (F3) to monitor the beam position. We used a 0.7-μm-thick alminized Mylar for the window of the MCP. An ionization chamber (IC) with a 56-mm length was placed behind the

MCP as a ΔE detector. The IC was operated using isobutane gas at 25 Torr. A double-sided Si strip detector (DSSD) with a thickness of 500-μm was placed in the I.C as an E and a β-ray detectors. A Si detector of 1.5-mm thickness was placed behind the DSSD as a β-ray detector. To measure β-delayed γ rays, 3 clover and 1 coaxial Ge detectors were set around the I.C. The primary beam was pulsed to measure the half life of ^{46}Cr. The durations of the beam-on and beam-off periods were 500 and 700 ms, respectively. Non-stop TDC (NSTDC) was used to record absolute time in a pulsed-beam cycle.

3. Experimental results

Figure 1 shows a scatter plot between the ΔE and the time-of-flight (TOF) between the MCP and the RF signals where clean particle identification (PI) is shown. In this experi-
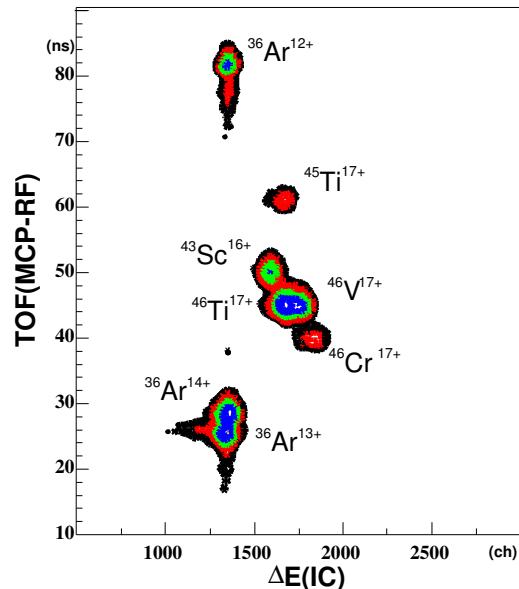
Figure 1. TOF-ΔE spectrum obtained by the I.C and MCP placed at F3.

ment, the purity and the intensity of ^{46}Cr were 2.2 % and 9 particle per second (pps) with the primary beam of 80 particle nA. The purities and intensities of ^{46}Cr and other nuclides in the secondary beam are summarized in Table 1.

Figure 3 shows a decay spectrum of fusion products during beam off. This spectrum was obtained for events with energies greater than 200 keV deposited at DSSD.

Table 1. Purities and intensities of nuclides with the primary beam of 80 particle nA, where the purities and intensities are shown by the unit of % and pps, respectively. Branching ratio indicates the decay branching ratios to the excited states. Half lives are shown by each unit.

Nuclide	$^{46}Cr^{17+}$	$^{46}V^{17+}$	$^{45}Ti^{17+}$	$^{46}Ti^{17+}$	$^{43}Sc^{16+}$	^{36}Ar
Purity (%)	1.8	8.8	2.2	15.6	4.5	50.7
Intensity (pps)	5.6	27.2	6.5	48.6	14.0	157.2
Half life	257 ms	422.4 ms	184.8 m	Stable	3.891 h	Stable
Branching ratio (%)	21.6 [2]	0.019	0.315		22.5	
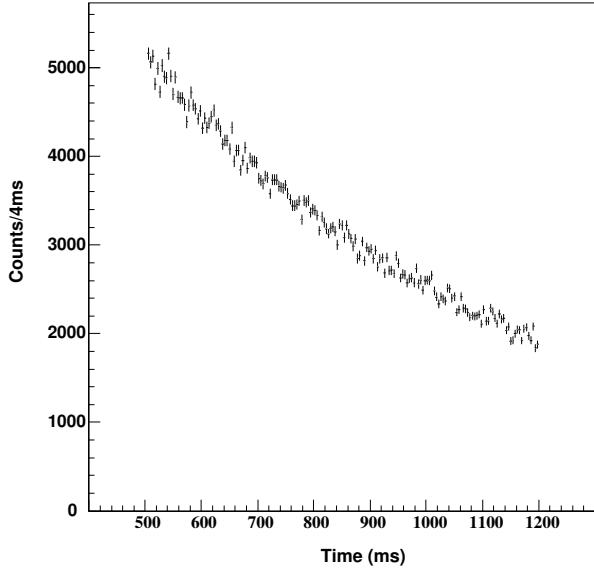
Figure 2. Decay spectrum of fusion products at beam off.

From the PI in Fig. 1, this spectrum have only two decay components of ^{46}V and ^{46}Cr, because ^{46}Ti and ^{36}Ar are stable nuclei and ^{45}Ti and ^{43}Sc have much longer half lives than the duration of beam-off period. The half life of ^{46}Cr was determined as $T_{1/2} = 259\pm40$ ms by fitting this spectrum with a function having two-decay components. This value is consistent with previous data 240 ± 140 ms [2] and 260 ± 60 ms [6]. The half life of ^{46}V was also obtained as $T_{1/2} = 425(4)$ ms. This value is in good agreement with a previous value of $422.50(11)$ ms [11].

Figure 3(a) and (b) show the γ-ray energy spectrum in the energy range of 300 keV to 540 keV and of 540 keV to 1040 keV, respectively. This spectrum was obtained by the β-γ coincidence method during beam off. A 511 keV γ ray in Fig. 3(a) is due to annihilation of positrons emitted from β^+ decay. In Fig. 3(a), a 373 keV β-delayed γ ray of ^{43}Sc is seen. A 993 keV γ ray from β decay of ^{46}Cr [2] is seen in Fig. 3(b).

To discuss the experimental result more in detail, an advanced analysis, using the position information of DSSD, is in progress.

Figure 3. γ-ray energy spectrum at beam off. Figure 3(a) and (b) show spectra for different energy ranges; (a) 300 keV to 540keV, (b) 540 keV to 1040 keV.

References

[1] K. Langanke and G. Martinez-Pinedo, Rev. Mod. Phys. **75**, 819 (2003).
[2] T.K. Onishi et al., Phys. Rev. C **72**, 024308 (2005).
[3] V.T. Koslowsky et al., Nucl. Phys. A **624**, 293 (1997).
[4] I. Reusen et al., Phys. Rev. C **59**, 2416 (1999).
[5] A. Jokinen et al., Eur. Phys. J. A **3**, 271 (1998).
[6] J. Zioni et al., Nucl. Phys. A **181**, 465 (1972).
[7] S. Kubono et al., Eur. Phys. J. A **13**, 217 (2002).
[8] Y. Yanagisawa et al., Nucl. Instrum. Methods Phys. Res. A **539**, 73 (2005).
[9] J.L. Wiza, Nucl. Instrum. Methods **162**, 587 (1979).
[10] D. Shapira et al., Nucl. Instrum. Methods Phys. Res. A **454**, 409 (2000).
[11] Nuclear Data Sheets **91**, 64 (2000).

Experimental Nuclear Physics:
PHENIX Experiment at BNL-RHIC
& ALICE Experiment at CERN-LHC

Systematic study of low p_T direct photons with the virtual photon method at RHIC-PHENIX

Y.L. Yamaguchi, Y. Akiba[a], T. Gunji, K. Ozawa[b], and H. Hamagaki,
for the PHENIX collaboration

Center for Nuclear Study, Graduate School of Science, University of Tokyo
[a] RIKEN (The Institute of Physical and Chemical Research)
[b] Department of Physics, University of Tokyo

1. Introduction

Direct photons are one of the most important probes to investigate properties of the matter created by heavy ion collisions since they leave the medium without strong interaction once they are generated. The direct photons are emitted from every stage of the collisions, and their p_T reflect the temperature of the sources. A special interest is put on direct photons in $1.0 < p_T < 5.0$ GeV/c since primary components are considered to be thermal photons from Quark Gluon Plasma (QGP) and photons produced in jet-medium interactions such as jet-photon conversions and in-medium Bremsstrahlung [1]. Thus, the measurement of the direct photons in $1.0 < p_T < 5.0$ GeV/c provides a deep insight into the created matter, but it is very challenging due to a large background from decays of hadrons, particularly π^0.

In the PHENIX experiment, two different analysis methods, namely, a 'real' photon method and a 'virtual' photon method, have been developed. The 'real' photon method using an electromagnetic calorimeter has been sucessfully used for $p_T > 4.0$ GeV/c both in p+p and Au+Au collisions [2], and the results are in good agreement with the next-to-leading-order perturbative QCD (NLO pQCD) calculation. The method, however, could not produce positive results for $p_T < 4.0$ GeV/c, because of associated large systematic errors primarily from hadron-decay background. On the other hand, the 'virtual' photon method is suitable in $1.0 < p_T < 5.0$ GeV/c. The low p_T direct photons in p+p and Au+Au collisions have been successfully measured with the virtual photon method [3]. Figure 1 shows the direct photon spectra in p+p and Au+Au collisions, and a significant excess over the binary-scaled p+p result is clearly seen in Au+Au collisions in $p_T < 3.0$ GeV/c. However, the observed excess can not be concluded as thermal origin at this moment. The d+Au data is needed to evaluate nuclear effects such as Cronin effect and nuclear shadowing since they may increase or decrease the photon yield in low p_T region. The efforts for measuring the low p_T direct photons in p+p and d+Au collisions with high quality are being made. The current status of the analysis in 200 GeV p+p and d+Au collisions are presented in this report.

2. Virtual Photon Method

In general, any source of real photons can emit virtual photon which convert to low mass e^+e^- pair. A direct photon production process has an associated process in which γ^* instead of γ is emitted, i.e. $q+g \rightarrow q+\gamma^* \rightarrow q+e^+e^-$. The relation between the photon production and the associated e^+e^- production process is expressed by the Kroll-Wada

formula [4],

$$\frac{d^2 n_{ee}}{dm_{ee}} = \frac{2\alpha}{3\pi} \frac{1}{m_{ee}} \sqrt{1 - \frac{4m_e^2}{m_{ee}^2}} \left(1 + \frac{2m_e^2}{m_{ee}^2}\right) S dn_\gamma, \quad (1)$$

where α is the fine structure constant, m_e and m_{ee} are the masses of the electron and the e^+e^- pair, respectively, S is a process-dependent factor and dn_γ is an emission rate of the photons. In the case of π^0 and η Dalitz decays, S is given as $S = |F(m_{ee}^2)|^2 \left(1 - \frac{m_{ee}^2}{m_{hadron}^2}\right)^3$, where F denotes the form factor and m_{hadron} is the mass of the parent hadron. The S factor is obviously zero for $m_{ee} > m_{hadron}$. On the other hand, the S factor becomes unity for $m_{ee}^2 \ll p_T^2$ in the case of virtual direct photon decays. Therefore, it is possible to extract the virtual direct photon component from the e^+e^- pair mass spectrum by utilizing the difference in e^+e^- pair mass dependence of the S factor.

3. Analysis

All combinations between electrons and positrons in the same event are taken. The obtained e^+e^- mass distribution contains several components from different sources, which are listed below.

- Virtual direct photon decays
- Dalitz decays (π^0, η, ω)
- Direct e^+e^- decays of vector mesons
- Photon conversions
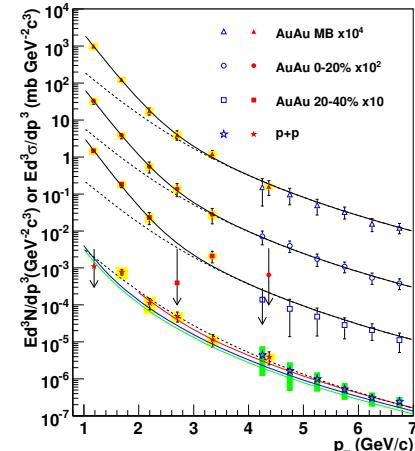
Figure 1. The direct photon spectra in p+p and Au+Au collisions.

- Combinatorial background

- Cross pairs from $\pi^0, \eta \rightarrow 2\gamma$(or γe^+e^-) $\rightarrow$ $e^+e^-e^+e^-$ (Double Dalitz decay)

- Pairs from two independent decays in the same jet or back-to-back jets

The pairs from photon conversions are removed by a cut on the orientation of the pair in the magnetic field, and the combinatorial background is computed with a mixed-event technique. The like-sign pair distributions consist of the combinatorial background pairs, cross pairs and pairs from two independent decays in the same jet or back-to-back jets. Thus, the contributions of these background pairs are evaluated using like-sign pair distributions and a Monte Carlo simulation, and the combinatorial pairs and pairs from jets are subtracted. Finally, the correlated e^+e^- mass distribution, which consists of pairs from known hadron decays and virtual direct photon decay, is obtained.

3.1. p+p Analysis

The data taken in 2006 is used in this analysis and its statistics is about twice as much as the previous p+p data. Figure 2 shows the correlated e^+e^- mass distribution in p+p collisions for $p_T > 1.0$ GeV/c together with a hadronic cocktail calculation. The hadronic cocktail calculation incorporates the individually measured yields of hadrons at the PHENIX experiment, and the corrections such as detector efficiencies, geometrical acceptance and momentum smearing due to a track reconstruction algorithm are incorporated in the cocktail calculation through the GEANT 3 based simulator for the PHENIX detector. The symbol and line show the real data and cocktail calculation, respectively. After correction to obtain the invariant yield of the e^+e^- pairs, the p+p result with higher quality than the existing result will come.
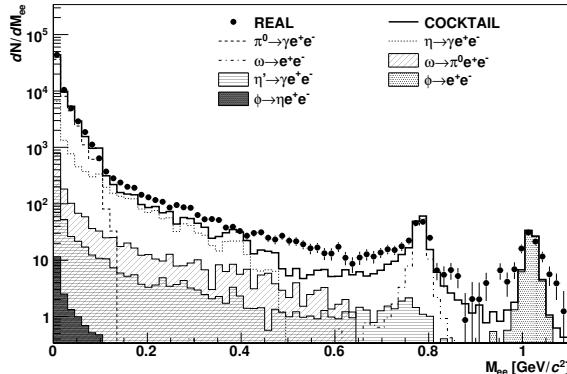
Figure 2. The correlated e^+e^- mass distribution in p+p collisions for $p_T > 1.0$ GeV/c together with a hadronic cocktail calculation.

3.2. d+Au Analysis

Figure 3 shows the correlated e^+e^- mass distribution in d+Au collisions for $p_T > 1.0$ GeV/c. The d+Au data has abundant counting statistics so that even Ψ' is clearly visible at around 3.7 GeV/c^2. Figure 4 shows the p_T sliced e^+e^-

mass spectra in $M_{ee} < 300$ MeV/c^2 in d+Au collisions for $1.0 < p_T < 6.0$ GeV/c. The results up to ~ 6 GeV/c in p_T are expected to be obtained for d+Au collisions. Although some corrections and tuning of the hadronic cocktail calculation will be worked out in order to obtain the direct photon spectrum in d+Au collisions, the d+Au result is promising.
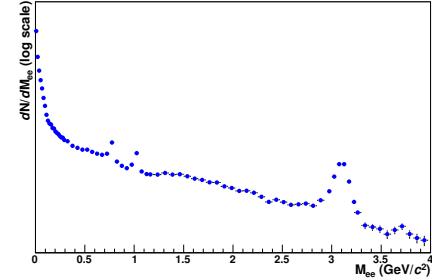
Figure 3. The correlated e^+e^- mass distribution in d+Au collisions for $p_T > 1.0$ GeV/c.
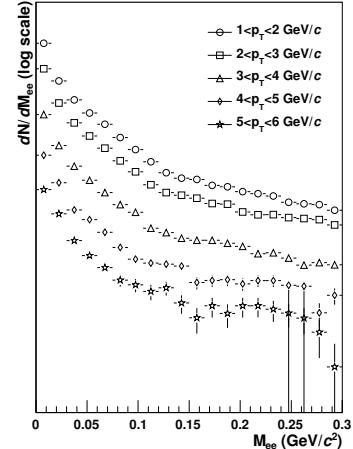
Figure 4. The p_T sliced e^+e^- mass spectra in $M_{ee} < 300$ MeV/c^2 in d+Au collisions for $1.0 < p_T < 6.0$ GeV/c.

4. Summary and Outlooks

In the PHENIX experiment, the two different methods have been employed to measure the direct photons in a wide-ranging p_T region. The virtual photon method has been applied for measuring the low p_T direct photons in p+p and Au+Au collisions, and a significant excess over the binary-scaled p+p result is seen in Au+Au collisions. The d+Au and p+p analysis with higher counting statistics than the existing data are on going to evaluate the contribution of the nuclear effects, which should provide the baseline for Au+Au result with higher accuracy.

References

[1] S. Turbide *et al.,* Phys. Rev. C **69** 014903 (2004).
[2] T. Isobe for the PHENIX collaboration, J. Phys. G: Nucl. Part. Phys. **34** S1015-S1018 (2007).
[3] A. Adare *et al.,* for the PHENIX collaboration, arXiv:0804.4168[nucl-ex].
[4] N.M. Kroll and W. Wada, Phys. Rev. **98** 1355 (1955).

Neutral pion production with respect to the reaction plane in $\sqrt{s_{NN}} = 200$ GeV Au+Au collisions at PHENIX

Y. Aramaki, T. Sakaguchi[a], G. David[a], and H. Hamagaki

Center for Nuclear Study, Graduate School of Science, The University of Tokyo
[a]Physics Department, Brookhaven National Laboratory

1. Introduction

It has been observed in central Au+Au collisions at Relativistic Heavy Ion Collider (RHIC) that the yield of neutral pion at high transverse momentum ($p_T > 5$ GeV/c) is strongly suppressed compared to the expectation from $p+p$ collisions scaled by the number of binary collisions. This suppression is regarded due to the energy loss of hard scattered partons in the hot and dense matter created in heavy ion collisions, and is called as jet quenching.

Dependence of energy loss on path length should provide further insight into the energy loss mechanism. Several theoretical models suggest that LPM effect in QCD plays an important role in radiative energy loss process [1]. These models predict that the magnitude of energy loss is proportional to square of the path length. More precise information on path length can be obtained by measuring the azimuthal angle of emitted particles relative to the reaction plane in non-central collisions. In the case of non-central collision, the matter has a spacial anisotropy, and the reaction plane is defined by the the two vectors representing beam direction and impact parameter. The nuclear modification factor (R_{AA}) and its azimuthal angle dependence have been studied at RHIC.

The R_{AA} is generally expressed using centrality (*cent*) which is associated with both of the impact parameter for collisions and the p_T.

$$R_{AA}(p_T, cent)$$
$$= \frac{\sigma_{pp}^{inel}}{\langle N_{coll}(cent) \rangle} \frac{d^2 N^{AA}(p_T, cent)/dp_T dy}{d^2 \sigma^{NN}/dp_T dy}, \quad (1)$$

where $N^{AA}(cent)$ is the number of neutral pions in a given centrality. σ_{pp}^{inel} is a cross section for inelastic nucleon-nucleon collisions. y is a rapidity. If R_{AA} is equal to one, the particle production in Au+Au collisions can be considered as a superposition of nucleon-nucleon collisions. Furthermore the nuclear modification factor as a function of the azimuthal angle of the detected particle with respect to the reaction plane is expressed by the following equation.

$$R'_{AA}(p_T, cent, \Delta\phi)$$
$$= \frac{N^{AA}(p_T, cent, \Delta\phi)}{\int d\phi N^{AA}(p_T, cent, \Delta\phi)} \times R_{AA}(p_T, cent), \quad (2)$$

here $N^{AA}(p_T, cent, \Delta\phi)$ can be expressed in terms of a Fourier expansion with $\Delta\phi$.

$$N^{AA}(\Delta\phi) \propto 1 + 2 \sum_{n=1}^{\infty} (v_n^{raw} \cos(n\Delta\phi)), \quad (3)$$

where v_n^{raw} is the magnitude of the harmonics of n-th order. The second harmonics (v_2^{raw}) represents the strength of elliptic azimuthal anisotropy. The true azimuthal anisotropy v_2^{corr} is obtained after correcting the reaction plane resolution [2].

$$v_2^{raw} = v_2^{corr} \langle \cos(2\Delta\Psi) \rangle, \quad (4)$$

where $\Delta\Psi$ shows the angular difference between the observed reaction plane and the true one, and its average provides its resolution.

1.1. Azimuthal anisotropy of neutral pion production

The second harmonic term (v_2) shows the magnitude of elliptic anisotropy.

The anisotropy v_2 at low p_T is created by the collective flow, which is an origin of the background in measuring the $R_{AA}(p_T, \Delta\phi)$ for investigating the energy loss. In order to reduce the effect of the collective flow, we measured the yields at higher p_T. Figure 1 shows the anisotropy v_2 of neutral pion as a function of p_T for several centrality classes. These values are non-zero for all centrality classes.

The data are fitted with a constant value or a linear line (a first order polynominal). The fitted results are listed in Table 1 and also shown in Fig. 1.

Table 1 indicate that the anisotropy v_2 of neutral pion in most central and peripheral collisions tends to be constant, while in mid-central collisions it tends to decrease.
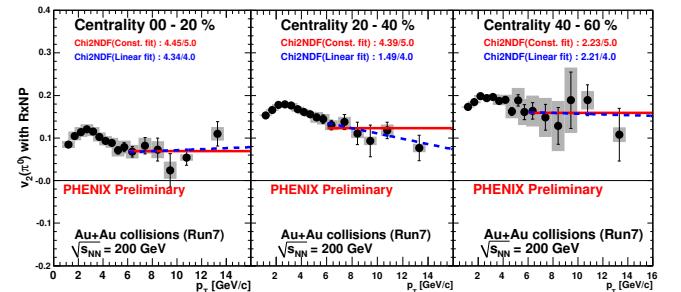
Figure 1. The anisotropy v_2 of neutral pion as a function of p_T for each 20 % centrality class. Solid and dashed lines which are fitted to the data from 6 GeV/c show constant and linear fit function, respectively.

Centrality [%]	Constant (χ^2/NDF)	Linear (χ^2/NDF)
00–20	4.45/5	4.34/4
20–40	4.39/5	1.49/4
40–60	2.23/5	2.21/4

Table 1. Fit results with the two functions for three centrality classes.

1.2. Comparison of the measured $R_{AA}(p_T, \Delta\phi)$ with models

Recently theoretical models (ASW [3], HT [4] and AMY [5]) which involve the space-time evolution of the matter have been proposed to investigate parton energy loss mechanism [6]. Figure 2 shows the calculated R_{AA} results with these models together with the experimental data for two centrality classes. The upper and lower panel show the $R_{AA}(p_T)$ as a function of p_T for centrality $0 - 5$ % and $20 - 30$ %, respectively.

Solid, dashed and long dot dashed lines in the both panels show the results by AMY, HT and ASW, respectively.

These models reproduce the centrality and p_T dependences of R_{AA} well.
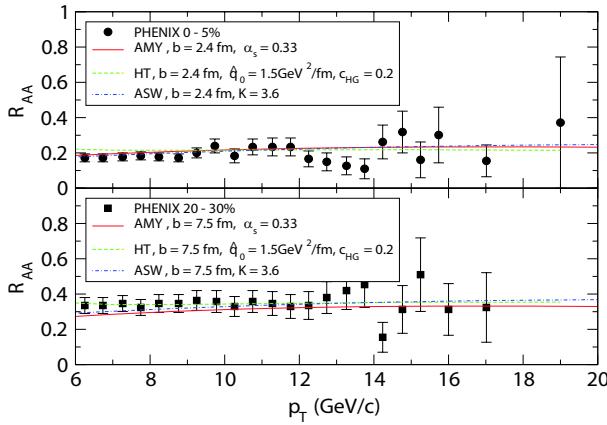
Figure 2. The upper panel shows that $R_{AA}(p_T, cent)$ at centrality 0–5 % as a function of p_T for both of theoretical curves and the data. The lower panel shows that R_{AA} at 20–30 % as a function of p_T for both of three calculations and the data. The continuous, the dashed and the long dashed dotted lines on the both panels show the results by AMY, HT and ASW, respectively.

The measured $R_{AA}(p_T, \Delta\phi)$ as a function of p_T and azimuthal angle from the reaction plane is compared to these models. Figure 3 shows the expected $R_{AA}(p_T, \Delta\phi)$ as a function of the azimuthal angle for these models at centrality 20-30 % and the measured data at PHENIX. Solid circles, triangles and stars represent AMY, HT and ASW at $p_T = 10$ GeV/c. Open circles represent the measured data. The statistical uncertainties are shown as the small bars and

the systematic uncertainties are not still taken into account in this figure.

As shown in Fig. 3, the measured data has strongly dependence on the azimuthal angle and these models are still unable to reproduce its dependence of R_{AA}.
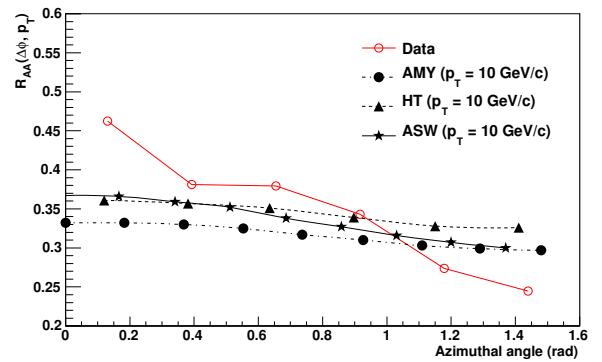
Figure 3. Open circles show $R_{AA}(9 < p_T < 10 GeV/c, \Delta\phi)$ as a function of p_T and azimuthal angle. Solid circles, triangles and stars show AMY, HT and ASW at $p_T = 10$ GeV/c at centrality 20-30 %, respectively.

2. Summary

Study of dependences of R_{AA} on path length and azimuthal angle has been started with the new reaction plane detector. The theretical models are in good agreement with the (azimuthally integrated) measured $R_{AA}(p_T)$. The $R_{AA}(9 < p_T < 10$ GeV/c) as a function of azimuthal angle are compared with these theoretical models. These models could not reproduce the measured azimuthal angle dependence.

The measurement of azimuthal anisotropy v_2 of neutral pion has now been extended to 14 GeV/c. For the most central (0-20%) and peripheral (40-60%) collisions, the elliptic flow tends to be independent from trasnverse momemtum (instead of decreasing monotonically with p_T), while for mid-central collisions (20-40%) we observe a decrease of v_2 with p_T. With the new data we will be able to deduce the dependence of R_{AA} on azimuthal angle up to higher transverse momenta than ever before.

References

[1] M. Gyulassy *et al*., Nucl. Phys. B **571**, (2000) 197-233
[2] J. Barrette *et al*., Phys. Rev. C **55** (1997) 1420.
[3] T. Renk *et al*., Phys. Rev. C**75**, 031902 (2007).
[4] A. Majumder *et al*., Phys. Rev. C**76**, 041902 (2007).
[5] G-Y. Qin *et al*., Phys. Rev. C**76**, 064907 (2007).
[6] S.A. Bass *et al*., J. Phys. G**35**, 104064 (2008).

Measurement of Bottom versus Charm as a Function of Transverse Momentum with Electron-Hadron Correlations in p+p Collisions at $\sqrt{s}$=200 GeV

Y. Morino for the PHENIX Collaboration

Center for Nuclear Study, Graduate School of Science, University of Tokyo

The PHENIX experiment at RHIC has measured single electrons from the semi-leptonic decay of heavy flavor at mid-rapidity in $p + p$ and Au+Au collisions at $\sqrt{s_{NN}} = 200$ GeV [1, 2]. Strong suppression of the single electron yield at high p_T, which include contributions from both charm and bottom decays, was observed in central Au+Au collisions [2]. This effect is conventionally attributed to energy loss by the parent parton in the medium [3]; one also expects the energy loss suffered by bottom quarks to be significantly less than that suffered by charm quarks due to the difference in their masses [4]. Clearly, for both pQCD comparisons and the heavy-ion reference, one wants to disentangle at RHIC energies the separate yields of charm and bottom.

The ratio of the number of electron from bottom (($b \rightarrow e$)) to one from charm and bottom, (($c \rightarrow e$) + ($b \rightarrow e$)) is extracted from the correlation between the heavy flavor electrons and associated hadrons. The extraction is based on partial reconstruction of the $D/\bar{D} \rightarrow e^{\pm}K^{\mp}X$ decay. The invariant mass of unlike charge-sign electron-hadron pairs reveals a correlated signal below the D meson mass of ~ 1.9 GeV/c^2, because of the charge correlation in the D decays. Pairs are formed between a trigger electron ($2.0 < p_T < 7.0$ GeV/c) and an oppositely charged hadron ($0.4 < p_T < 5.0$ GeV/c). $K^{\pm}$ identification is not performed but the mass of all reconstructed hadrons is set to be that of the $K^{\pm}$.

The inclusive reconstructed electron-hadron pairs consist of the following components, according to origin of the trigger electrons: (1) unlike-sign pairs from charm, (2) unlike-sign pairs from bottom and (3) combinatorial background where the electron is a background electron. The main background source is the combinatorial background (3) and almost all background electrons are from e^+e^- pair creation. Like-sign electron-hadron pairs are used to subtract this background. Subtraction using like-sign pairs cancels out completely the combinatorial background where the trigger electron is from e^+e^- pair creation (3). Only the negligibly small (<1%) contribution from K^0_{e3} decay is not canceled out by the subtraction in the background (3). After the subtraction, the reconstructed pairs include a contribution from bottom (2). The reconstructed pairs also contain a signal from partial reconstruction of heavy flavor hadrons and a contribution from a combination of heavy flavor electrons and hadrons from jet fragmentation.

The fraction of bottom contribution to the electrons from heavy flavor is obtained as follows:

$$\frac{(b \rightarrow e)}{((c \rightarrow e) + (b \rightarrow e))} = \frac{\varepsilon_c - \varepsilon_{data}}{\varepsilon_c - \varepsilon_b}, \tag{1}$$

where ε_{data} is the tagging efficiency in real data and $\varepsilon_{c(b)}$ is the tagging efficiency for charm (bottom) production. These are defined as

$$\varepsilon_{data} \equiv \frac{N_{pair}}{N_{e(HF)}} = \frac{N_{c \rightarrow tag} + N_{b \rightarrow tag}}{((c \rightarrow e) + (b \rightarrow e))}, \tag{2}$$

$$\varepsilon_c \equiv \frac{N_{c \rightarrow tag}}{(c \rightarrow e)}, \qquad \varepsilon_b \equiv \frac{N_{b \rightarrow tag}}{(b \rightarrow e)}, \tag{3}$$

where $N_{e(HF)}$ is the number of measured heavy flavor electrons. N_{pair} is the number of background subtracted unlike-sign electron-hadron pairs for invariant mass within $0.4 < M_{eK} < 1.9$ GeV/c^2, which corresponds to the mass range of charmed hadrons. Here, $N_{c(b) \rightarrow tag}$ is the number of reconstructed signals within $0.4 < M_{eK} < 1.9$ GeV/c^2 for charm (bottom) production.

Figure 1 shows the M_{eK} distribution of the reconstructed signals, which is normalized by the yield of heavy flavor electrons ($N_{e(HF)}$) in the range $3 < p_T < 4$ GeV/c (panel a) and $4 < p_T < 5$ GeV/c (panel b). The tagging efficiency in real data, ε_{data}, is determined by the integration of the M_{eK} distribution in Fig. 1 from $M_{eK} = 0.4$ to 1.9 GeV/c^2 as a function of electron p_T.
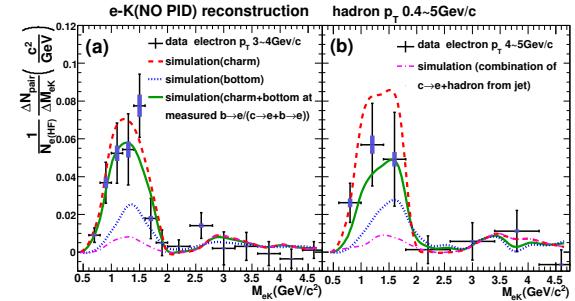
Figure 1. (color online) Comparison of data to a PYTHIA and EvtGen simulation of the invariant mass distributions in PHENIX acceptance for the reconstructed signal. The electron p_T range is 3.0 - 4.0 GeV/c (a) and 4.0 - 5.0 GeV/c (b). The ratios, $(b \rightarrow e)/((c \rightarrow e) + (b \rightarrow e))$, in solid lines are 0.26 (a) and 0.63 (b).

The tagging efficiencies for charm and bottom production, ε_c and ε_b, are calculated with the combination of PYTHIA and EvtGen [6, 7]. PYTHIA is used to simulate charm and bottom production in $p + p$ collisions at $\sqrt{s} = 200$ GeV and is tuned to reproduce heavy flavor hadron ratios. EvtGen, which is a Monte-Carlo simulation suited for decays of D and B hadrons, is used to simulate the semi-leptonic decays. The dashed (dotted) lines in Fig. 1
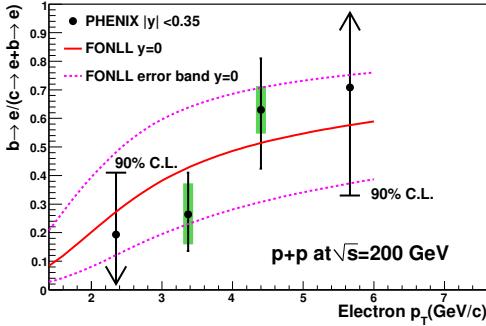
Figure 2. $(b \rightarrow e)/((c \rightarrow e) + (b \rightarrow e))$ as a function of electron p_T compared to a FONLL calculation [8]. The points show the experimental result. The solid line is a FONLL prediction and the dotted lines represent the uncertainty of this FONLL prediction.
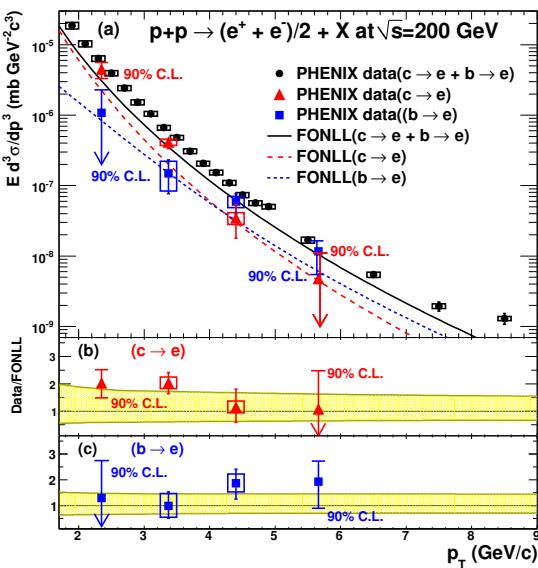
Figure 3. (a): Invariant cross sections of electrons from charm and bottom with the FONLL calculation [8]. (b) and (c): The ratios of data points over the FONLL prediction as a function of electron p_T for charm and bottom. The shaded area shows the uncertainty in the FONLL prediction.

show the M_{eK} distributions of the reconstructed signal for the simulated charm (bottom) production for an electron $3 < p_T < 4$ GeV/c (panel a) and $4 < p_T < 5$ GeV/c (panel b). Since about 85% of the extracted signal comes from partcial reconstruction of heavy flavor hadrons, the tagging efficiency is determined largely by decay kinematics and $\varepsilon_{c(b)}$ can be determined with good precision. The dot-dash lines in Fig. 1 show the contribution from the combination of an electron from charm and hadrons from jet fragmentation for charm production. The solid line in Fig. 1 shows the sum of the M_{eK} distributions for charm and bottom in the simulation with the ratio, $(b \rightarrow e)/((c \rightarrow e) + (b \rightarrow e))$, obtained with Eq. 1.

Figure 2 shows the resulting bottom fraction, $(b \rightarrow e)/((c \rightarrow e) + (b \rightarrow e))$ as a function of electron p_T compared to a fixed-order-plus-next-to-leading-log perturbative QCD calculation (FONLL) [8]. In this figure, the points show the measured $(b \rightarrow e)/((c \rightarrow e) + (b \rightarrow e))$. For the bins with an electron $2 < p_T < 3$ and $5 < p_T < 7$, 90% C.L. and mean values are shown. The solid line shows the central value of the FONLL prediction and the dotted lines show its uncertainty.

In Fig. 3, the single electron spectra for charm and bottom are measured from the ratio, $(b \rightarrow e)/((c \rightarrow e) + (b \rightarrow e))$, and the spectrum of the single electrons. The top panel shows the resulting single electron spectra from charm (triangles) and bottom (squares) compared to the FONLL predictions [8, 9]. The measured spectrum of single electrons (circles) is also shown for reference. The middle (bottom) panel shows the ratio of the measured cross sections to the FONLL calculation for charm (bottom) production. The shaded area shows the uncertainty in the FONLL prediction. These calculations agree with the data for bottom production. The same is true for charm within the theoretical uncertainty with a ratio of data/FONLL of ~2.

The electron spectrum from bottom shown in Fig. 3 is integrated from $p_T = 3$ to 5 GeV/c. This spectrum is then extrapolated to $p_T = 0$ using the shape predicted by pQCD. The extrapolation results in a bottom cross section at midrapidity of $d\sigma_{b\bar{b}}/dy |_{y=0} = 0.92^{+0.34}_{-0.31}(\text{stat})^{+0.39}_{-0.36}(\text{sys})\mu\text{b}$, using a $b \rightarrow e$ total branching ratio of $10 \pm 1\%$. Using pQCD to integrate over rapidity, the total bottom cross section is determined to be $\sigma_{b\bar{b}} = 3.2^{+1.2}_{-1.1}(\text{stat})^{+1.4}_{-1.3}(\text{sys})\mu\text{b}$. FONLL predicts $\sigma_{b\bar{b}} = 1.87^{+0.99}_{-0.67}\mu\text{b}$, in agreement with this result.

In conclusion, the ratio of the yield of electrons from bottom to that from charm has been measured in $p + p$ collisions at $\sqrt{s} = 200$ GeV. The ratio provides the first measurement of the spectrum of electrons from bottom at RHIC. FONLL calculations agree with this result. This result provides an important baseline for the study of heavy quark production in the hot and dense matter created in Au+Au collisions.

References

[1] S. S. Adler *et al.*, Phys. Rev. Lett. **97**, 252002 (2006).
[2] S. S. Adler *et al.*, Phys. Rev. Lett. **98**, 172301 (2007).
[3] M. Gyulassy and M. Plumer, Phys. Lett. **B243**, 432 (1990).
[4] Y. L. Dokshitzer and D. E. Kharzeev, Phys. Lett. **B519**, 199 (2001).
[5] H. van Hees *et al.*, Phys. Rev. Lett. **73**, 192301 (2008).
[6] T. Sjostrand, Comput. Phys. Commun. **82**, 74 (1994).
[7] D. Lange, Nucl. Instrum. Method **A462**, 152 (2001).
[8] M. Cacciari private communication.
[9] M. Cacciari *et al.*, Phys. Rev. Lett **95**, 122001 (2005).

Commissioning of ALICE-TRD and Development of the Detector Control System

T. Gunji, H. Hamagaki, T. Dietel[a], U. Westerhoff[a], K. Oyama[b], K. Schweda[b],
for the ALICE-TRD Collaboration

Center for Nuclear Study, Graduate School of Science, University of Tokyo, Japan
[a] Institut fur Kernphysick, University of Muenster, Germany
[b] Physics Institute des University Heiderberg, Germany

1. Introduction

Ultra-relativistic heavy ion collisions are powerful method to realize the hot and dense QCD medium, composed of de-confined quarks and gluons, called Quark-Gluon-Plasma. A Large Hadron Collider (LHC) at CERN will start its operation in 2009 and first Pb+Pb collisions at the center of mass energy per nucleon ($\sqrt{s_{NN}}$) of 5.5 TeV will be held in 2010 to study the properties of hot and dense QCD matter at extreme high temperature regime.

A Large Ion Collision Experiment (ALICE) is one of the experiments at the LHC and dedicated for the relativistic heavy ion collisions [2]. ALICE detectors are designed to have wide capabilities to measure hadrons, leptons, photons and muons in wide kinematic ranges. ALICE is mainly composed of central barrel detectors and forward muon detectors. In the central barrel, the ALICE is mainly composed of inner tracking system (ITS) with two layers of silicon pixel, two silicon drift and silicon strip detectors, time projection chamber (TPC), transition radiation detectors (TRD), and time of flight detectors (TOF). The primary role of the ALICE-TRD is to provide the identification of the electron with p_T larger than 1 GeV and to enable charged particle tracking for the ALICE [2]. The ALICE-TRD is required to have the pion rejection factor of 100 at the electron identification efficiency of 90% to achieve the feasible measurement of J/ψ and Υ in heavy ion collisions. The ALICE-TRD will cover the wide kinematic region of $|\eta| < 0.9$ in pseudo rapidity and 2π in azimuthal angle. The ALICE TRD is divided into 18 azimuthal sectors, where one sector has 5 longitudinal sections and 6 TRD layers in radial direction [2].

2. ALICE-TRD

The electron identification by the TRD is performed by the measurement of the transition radiation photon in TRD. The ALICE-TRD is composed of the 4 cm thickness radiator (polypropylene's fiber) and the 3 cm thickness MWPC type drift chamber behind the radiator with cathode pad readout. $Xe(85\%)/CO_2(15\%)$ gas mixture is utilized for the detection of transition radiation photons. Front End Electronics (FEE) is mounted behind the ALICE-TRD. The ALICE-TRD FEE is composed of preamplifier and shaper (PASA), 10MHz sampling FADC, and digital circuitry called TRAP, where all of them are assembled in Multi-Chip-Module (MCM) chips. Each MCM processes 18-21 channels and about 120 MCM chips are mounted on one chamber. Digital filters are designed to perform the

nonlinearity, baseline and gain corrections, tail cancellation, and crosstalk suppression. The Tracklet Preprocessor in TRAP is used to perform the online tracking for triggering high-p_T tracks [2, 3]. The readout electronics on one TRD chamber is controlled by Detector Control System Board (DCSB), which contains an FPGA and an ARM core running the Linux operating system. It serves as the master controller of the slow control serial network (SCSN) and configures all of the MCM chips including TRAP chips via redundant daisy chained network. It also controls the voltage regulator shutdown on the Readout Boards (ROB), and distribute clock and trigger signals [2].

3. Commissioning at CERN

The ALICE supper module is composed of 6 layers in radial direction, 5 stacks in beam direction, and 30 TRD chambers in total. The assembly of supper module, check of the gas and cooling tightness, and check the electronics are completed at Muenster University. After the transportation to CERN, supper module is put into the rotator frame and orientated according to the position, where the super module is pulled into in the experiment, as shown in Fig. 1. Similar tests are conducted at the surface before it goes down to the ALICE detector hall. As the TRD uses

Figure 1. TRD super module in rotator frame at CERN

expensive Xe for the transition radiation detection, the leak tightness is very important to ensure the stable operation. There are two ways to estimate the leak rate of the chamber. One is to flush the super-module with gas (Ar/CO_2) at overpressure of 0.5 mbar, then to close the connection and to see the decrease of the pressure. The other is to flush the super module with gas at underpressure, generated by fans at the downstream of the gas system, and to see the increase of the oxygen contamination in the chamber gas, which results in a few mL/h of gas leak at 0.1 mbar. There are several test

items for the front-end electronics to verify the functionality of the readout electronics and the access of the configuration bus. A shutdown test is performed to check the voltage regulation. Network interface test is checked to ensure the data line is not defected. Connection test of the configuration bus is done for the slow control, and the power of the optical fiber for data readout. Long term stress test by sending the trigger with 1 kHz to the electronics and reading out the number of trigger counters in MCMs is done to check the stable operation. Figure 2 shows the RMS of the noise for each channel in one layer of one super module, where 120 MCMs are mounted in total per layer and there are approximately 2000 channels. RMS of 1 corresponds to 1000 electrons and the results are in good fulfillment.
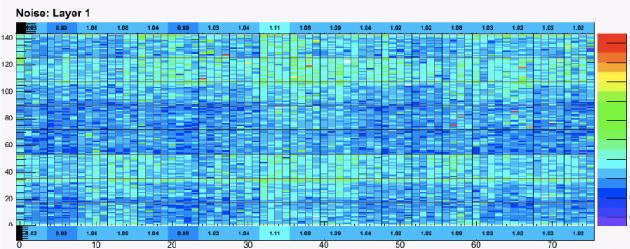
Figure 2. Nose from TRD super module

4. Development of Detector Control System in CNS

All the MCMs are configured through the slow control serial network (SCSN). A requirement of SCSN is to have a redundant architecture with few lines only while it is able to connect all the 65000 MCMs. Therefore, daisy chained network is chosen for this purpose. The network architecture is shown in Fig. 3. There are two rings in the network architecture and two links between slaves (MCMs) and to gain the redundancy, each of the slaves supports bridging as shown in the middle of Fig. 3. In normal operation mode without any defects in slaves, a slave forwards the data to the next slave until it arrives at the master in the same ring. In the bridge mode, the data is sent back on the other ring, breaking up the full duplex ring into two half-duplex rings. The bridge mode allows the network to operate with broken slaves. Figure 4 shows the test setup with two ROBs
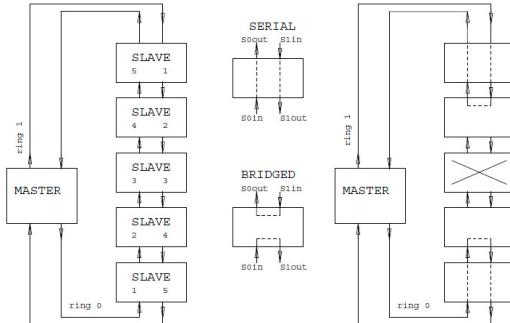
Figure 3. Architecture of SCSN in normal operation (left) and in bridge mode (right)

and one DCS master board to develop the slow control system in CNS [4]. The slow control system is developed for

Figure 4. Two ROBs, one DCSB and test setup at CNS

the case that there are some broken MCMs or the broken lines (network interface) for the data transmission between MCMs. In former case, the network architecture is changed from normal mode to bridge mode and the logic has been implemented in the slow control. It has been tested at both CNS and CERN. For the network interface, there are 12 line as the data transmission between MCMs. Ten bits of them are data, one is for parity and the other is spare bit. If some of the lines for 10 bits data are broken, spare line and parity line are set to be used and the corresponding commands are send to MCMs though the slow control. Graphical front end to check which MCMs have problem on slow control and network interface has been prepared via PVSS software and installed in CERN [4, 5].

5. Summary and Outlook

The ALICE-TRD is one of the main detectors in the central barrel of ALICE. The commissioning of the ALICE-TRD super module is done at the CERN and detail check of the gas leak tightness and front end electronics are performed. Development of the slow control system has been done in CNS to be able to operate the detector even with the defects on MCMs and data lines. It is installed in the CERN and currently it is working without any problems.

References

[1] ALICE Collaboration, Physics Performance Report Vol. 1 J. Phys. **G 30** (2003) 1517.

[2] ALICE Collaboration, "ALICE TRD Technical Design Report", CERN/LHCC 2001-021, ALICE TDR 9, 3 Oct. 2001.

[3] ASICCC: ALICE TRAP User Manual (Darmstadt, Heiderberg, Mannheim, Kaiserslautern) *http://www.kip.uni-heidelberg.de/ti/TRD/doc/trap*

[4] T. Gunji *et al*. CNS Annual Report 2007.

[5] PVSS *http://itcobe.web.cern.ch/itcobe/Services/Pvss*

Production of Photons and Jets in Forward Rapidity at LHC energy and Proposal of Forward Calorimeter in ALICE

T. Gunji, H. Hamagaki, Y. Hori

Center for Nuclear Study, Graduate School of Science, University of Tokyo, Japan

1. Introduction

A Larger Hadron Collider (LHC) at CERN is the largest accelerator in the world and will start operation in 2009. The LHC accelerates proton and heavy ions up to 7 TeV and 2.75 TeV per nucleon, respectively. One of the great interests in heavy ion collisions at the LHC energy is to study the properties of hot and dense QCD matter at extremely high density and temperature.

High energy heavy ion collisions at RHIC give the fruitful results, which suggest the formation of hot and dense QCD medium. One of the interesting experimental results reveals that the medium is quickly thermalized and behaves like perfect liquid not like an ideal gas [1].

To understand the occurrence of the early thermalized system, it is necessary to understand the initial condition of nuclear collisions and the consequences for the thermalization of the system, which is still unclear at RHIC energies and draws great interests at LHC energies.

2. Gluon PDF and Saturation

At the LHC energy, studying the parton distribution functions in proton and its modification in heavy nuclei are interesting subjects. High energy colliding beams can probe small x partons, since the resolving power depends on $\sim 1/\sqrt{s}$, where $\sqrt{s}$ corresponds to the collision energy in center of mass frame. It is well-known from the deep inelastic collisions at HERA that the gluon distribution in proton grows faster at small x than that of valence and sea quarks [3]. Due to the self interactions of gluons, two competing processes between gluon splitting and gluon fusion will be balanced at smaller x. Therefore it is expected that the gluon yield could be saturated at small x. The state of the gluon saturation realized at small x is called as "Color Glass Condensate" [5]. The saturation scale, Q_s, which corresponds to the typical momentum of gluons, is proportional to $A^{1/3}$, $Q_s^2 \propto A^{1/3}$. Due to its "A" dependence, CGC is easily realized in heavy nuclei compared to proton. At the LHC, where x coverage is $x \sim 10^{-4}$, modification of gluon PDF might be important to understand the initial state of nuclei and consequence of the formation of thermalized QCD medium. The physics at forward rapidity is carefully examined to address gluon PDF at small x, some measurement items are discussed, and forward calorimeter is proposed for the LHC-ALICE upgrade [2].

3. Production of photons and jets in forward rapidity

Given that a simple binary collision between two particles (1 and 2) happens and two particles (3 and 4) are emitted after the collisions, the momentum fraction of particle 1 and 2 can be expressed in terms of the rapidity of particle 3

and 4 and its transverse momentum p_T as follows:

$$x_1 = \frac{p_T}{\sqrt{s}}(e^{y_3} + e^{y_4}), \qquad (1)$$

$$x_2 = \frac{p_T}{\sqrt{s}}(e^{-y_3} + e^{-y_4}). \qquad (2)$$

Therefore taking the particle correlation in rapidity is crucial to determine x of colliding partons. The possible measurement items are π^0-jets, di-jet correlation, γ-jet correlation, and heavy quark production. The coverage of x achieved by the correlation measurements was studied using PYTHIA, which is a standard tool for the generation of high energy collisions [6]. The parameters for the generation of physics events are summarized as follows: $p + p$ collisions at $\sqrt{s} = 5.5$ TeV, QCD:Hard Process only, Minimum $\hat{Q}^2 = 20$ GeV^2, and cone jet algorithm utilized with $E_T \leq 20$ GeV and jet cone radius ≤ 0.7. Figure 1 shows the coverage of x_1 (dotted) and x_2 (solid) from the inclusive π^0 measurement (upper left) at forward rapidity ($2 \leq y \leq 4$), where x_2 distribution is broad from 10^{-5} to 10^{-1}. Upper right and bottom left of Fig. 1 show those from π^0-jet measurement, where π^0 is measured at $2 \leq y \leq 4$ and jets are measured at $2 \leq y \leq 4$ and at $-1 \leq y \leq 1$, respectively. By measuring the π^0 at forward rapidity and taking the correlation between π^0 and jets at $2 \leq y \leq 4$ and $-1 \leq y \leq 1$, x_2 can be determined in a narrow region such as $10^{-4} \leq x_2 \leq 10^{-3}$ and $10^{-3} \leq x_2 \leq 10^{-2}$, respectively.
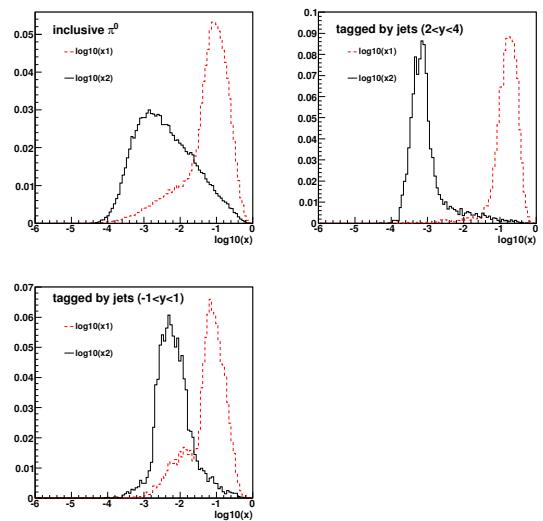
Figure 1. Coverage of x in single π^0 measurement at forward rapidity (upper left), in π^0 measurement tagged by jets at forward rapidity (upper right), and at midrapidity (bottom left).

Another important measurement to reach small x region is the prompt photon production, where the production is

mainly due to $g+q \rightarrow g\gamma$ process. Left and right of Fig. 2 shows the coverage of gluon x achieved by the photon measurement at various rapidity range of photon, where photon p_T is larger than 1 GeV/c and 5 GeV/c, respectively. When the photon is measured at $2 \leq y \leq 4$, x of gluons is achieved to be $10^{-3} \sim 10^{-5}$
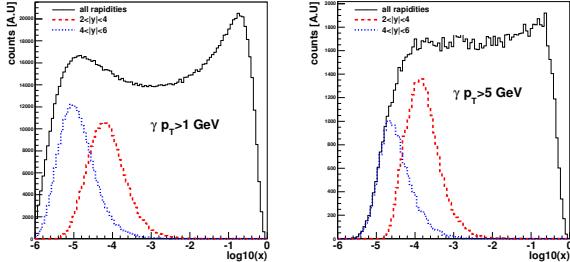
Figure 2. Solid, dashed, and dotted lines correspond to the coverage of x from the photon measurement over the whole rapidity range, at $2 \leq y \leq 4$, and at $4 \leq y \leq 6$, respectively, with the photon $p_T \geq 1$ GeV/c (left) and $p_T \geq 5$ GeV/c (right).

4. Proposal of Forward Calorimeter for the ALICE

Electromagnetic (and hadron) calorimeter is one of the suitable detectors to measure π^0, direct photon, and jets at forward rapidity. One of the key parameters for the calorimeter is the π^0/γ separation power since two γ from high p_T π^0 can merge into a single cluster. Table 1 and Table 2 are the summary of two γ separation at the rapidity of 2 and 3, respectively, for π^0 with p_T of 1, 5 and 10 GeV and longitudinal distance from interaction point of 4 m and 7.5 m.

p_T (GeV/c)	1	5	10
p_{tot} (GeV/c)	10.07	50.33	100.7
$\theta_{2\gamma}^{min}$	0.028	0.0056	0.0028
Δl(at z=4 m)	11 cm	2.2 cm	1.1 cm
Δl(at z=7.5 m)	21 cm	4.2 cm	2.1 cm

Table 1. Kinematics of 2γ from π^0 at y=3.

p_T (GeV/c)	1	5	10
p_{tot} (GeV/c)	3.76	18.81	37.6
$\theta_{2\gamma}^{min}$	0.074	0.0015	0.0074
Δl(at z=4 m)	30 cm	6.0 cm	3.0 cm
Δl(at z=7.5 m)	56 cm	11.2 cm	5.6 cm

Table 2. Kinematics of 2γ from π^0 at y=2.

If we aim to measure up to 10 GeV/c π^0, fine granularity with a small Moliere radius ($r \leq 3.0$ cm) is necessary as the calorimeter material. PbWO$_4$ crystal calorimeter with 2.2 cm Moliere radius and Tungsten(W)+Si tracking calorimeter with spatial resolution of 2 mm could be the good candidates as the forward calorimeter. Especially, a W+Si tracking calorimeter has been proposed in the detector upgrade for the PHENIX experiment at RHIC [7]. The detector is composed of 21 W layers with 4 mm thickness (1.1 X_0), where first 4-5 layers are attached with the Si strip readout and the others are attached to the Si pad sensor. Si strip layer with 500μm strip pitch serves as the position determination of the tracks. The size of Si pad sensor is 1.5 cm $\times$ 1.5 cm and these pads play a role of the energy measurement. We started to participate in this R&D efforts of W+Si calorimeter project for PHENIX. Beamtest experiment has been conducted at CERN-PS and CERN-SPS in June 2009. The performance evaluation is on going and will be reported in near future.

5. Summary and Outlook

Gluon distribution in small x region and the occurrence of color glass condensate are quite attracting subjects in nuclear physics. It plays an important role in understanding the early thermalization of the hot and dense QCD medium. LHC energy is suitable to study small x gluon distribution in proton and its modification in nuclei. π^0-jets correlation and direct photon measurement at forward rapidity are useful and powerful items to address this subject at LHC energy. To achieve π^0 and photon measurement at forward rapidity at ALICE, the W+Si calorimeter is one of the strong candidates, which expects to meet the requirement for two γ separation to be less than 1 cm so as to achieve γ/π^0 separation up to 10 GeV/c in p_T at y=3. We started to participate in the R&D effort of W+Si calorimeter for PHENIX, and the experience and technology will be utilized in the ALICE forward calorimeter.

References

[1] K. Adcox *et al.* (PHENIX Collaboration), Nucl. Phys. **A 757** (2005) 184-283. J. Adams *et al.* (STAR Collaboration), Nucl. Phys. **A 757** (2005) 102-183. I. Arsene *et al.* (BRAHMS Collaboration), Nucl. Phys. **A 757** (2005) 1-27. B. B. back *et al.* (PHOBOS Collaboration), Nucl. Phys. **A 757** (2005) 28-101.

[2] ALICE Collaboration, Physics Performance Report Vol. 1 J. Phys. **G 30** (2003) 1517.

[3] S. Eidelman *et al.* [Particle Data Group], Phys. Lett. **B. 592**, (2004), 1.

[4] K. J. Eskola *et al.*, JHEP 0807 102, 2008, arXiv:0802.0139v2 [hep-ph].

[5] L. D. McLerran, Lect. Notes Phys. 583: 291-334, 2002 (arXiv:hep-ph/0104285).

[6] PYTHIA 8.1 *http://home.thep.lu.se/˜torbjorn/Pythia.html*

[7] PHENIX FoCAL *https://www.phenix.bnl.gov/WWW/p/upgrades/focal/*

Calibration of ALICE-TPC with the laser calibration system

S. Sano, M. Ivanov[a], J. Wiechula[a], H. Hamagaki, T. Gunji, for ALICE-TPC collaboration

Center for Nuclear Study, Graduate School of Science, University of Tokyo
[a]Gesellschaft fur Schwerionenforschung mbH, Darmstadt, Germany

1. Introduction

ALICE (A Large Ion Collider Experiment) is an experiment at the Large Hadron Collider (LHC) optimized for the study of heavy-ion collisions, at a centre-of-mass energy of 5.5 TeV. The prime aim of the experiment is to probe nonperturbative aspects of QCD such as deconfinement and chiral symmetry restoration [1].

As a main tracking detector in the central barrel of ALICE, Time Projection Chamber (TPC) was organized. TPC has an excellent capability for track finding of high-momentum particles and energy loss with the enormous volume. Commissioning in underground and calibration of the TPC using laser calibration system, cosmic rays and Kr gas system are on going. In this report, the status of the calibration related to field distortions using laser system and the data of cosmic run are described.

2. ALICE-TPC
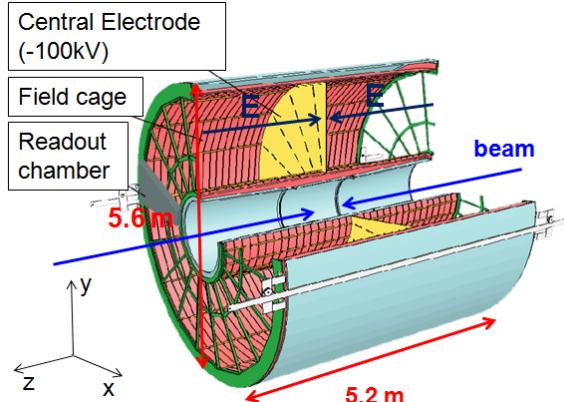
Figure 1. Overview of ALICE-TPC.

The maximal expected multiplicity ($dN_{ch}/dy \sim 8,000$ at mid-rapidity) was assumed for the design of the TPC, which results in 20,000 charged primary and secondary tracks in the TPC [2]. In order to accept the high multiplicity, the TPC has a enormous volume as shown in Fig. 1. The TPC is separated into two volumes with the Central Electrode (CE), and electrons generated by projected particles are read by pad-readout chambers located at both sides (A-side for positive-z side and C-side for negative-z side). Each side has 18 Inner Readout Chambers (IROCs) and 18 Outer Readout Chambers (OROCs) as shown in the lower panel of Fig. **??**. Some properties of the ALICE-TPC are summarized as follows.

- geometrical acceptance
  $|\eta| < 0.9$ in pseudorapidity , 2π in azimuthal angle
- pad size
  4×7.5 mm^2 for IROC

6×10 mm^2, 6×15 mm^2 for OROC
total number of channel: 557,568
- Gas: Ne-CO$_2$-N$_2$ [90:10:5] (atmospheric pressure)
- 400 V/cm of electric field of the drift
- 92 μs of total drift time

Ne was selected because the mobility of Ne$^+$ is a factor 2.5 higher than that of Ar$^+$. CO$_2$ is main quencher gas and N$_2$ improves the gain stability because N$_2$ has a larger photon absorption cross section than CO$_2$ at the main excitation state of Ne (16.8 eV).

3. Calibration with laser calibration system
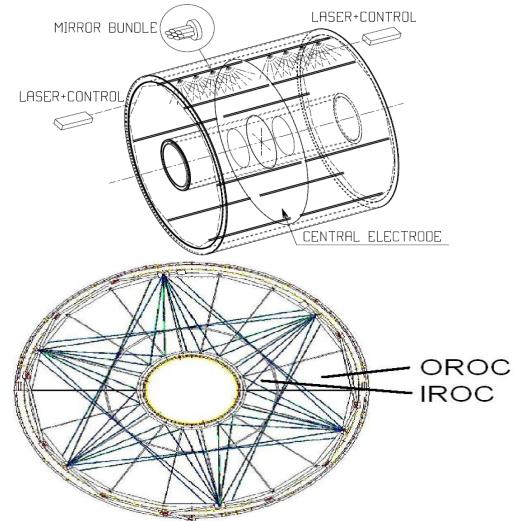
Figure 2. Overview of laser system (upper) and the position relation of chambers and laser tracks in xy direction. Each laser is pointing corners of chambers.

Calibration program for the ALICE-TPC is as follows.

- Noise, gain, and time equilibration of the readout electronics are checked using pulser system which induces charge on pads by injecting a signal pulse on the cathode wires.
- Drift velocity, drift-field distortions and distortions related to $\mathbf{E} \times \mathbf{B}$ effect are calibrated using laser calibration system or or cosmic rays.
- Gain of the gas amplification is calibrated using electrons emitted from the stable isotope ^{83}Kr filling the TPC.

The calibration and alignment data is stored in the Offline Conditions Database (OCDB), which is handled by the CDB access framework, an AliRoot-based package [3].

The upper panel of Fig. 2 shows the overall layout of the laser system. The main laser beam injected by the laser controller is separated and injected into 6 out of 18 rods supporting Mylar strips in which high voltages are applied to make the electric field. Part of laser beam in each rod is separated into 7 beams at mirror bundles and injected into the chamber in the direction perpendicular to the beam axis as shown in the upper panel of Fig. 2. The lower panel of Fig. 2 shows the position relation of chambers and laser tracks in xy direction. Each laser is pointing corners of chambers.
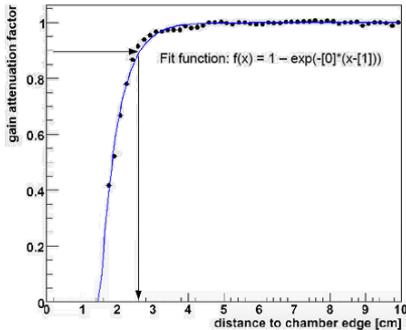
Figure 3. Modification factor of collected charge as a function of the distance from the edge of chambers. The value of y-axis is normalized with parabolic functions fitted in the charge distribution for each chamber.

Inefficiency of charge collection due to the distortion of the electric field near the edge of the chamber was checked using the photo electrons emitted from CE in laser run. Figure 3 shows the modification factor of collected charge as a function of the distance from the edge of chambers, which is integrated for all chambers of A-side. It can be seen that the gain collection is inefficient near the edge. The inverse of values on the fitting function shown in Fig. 3 were stored in OCDB as a correction factor.

Feasibility of calibration was checked with tracking of cosmic rays under the no-magnetic field. A new attempt for evaluation of the position transformation by calibration and alignment is under development using Kalman filter. Kalman filter is a recursive estimator where the state vector **x** is estimated by only the previous step [4] as shown in the following equation.

$$\mathbf{x}_k = \mathbf{x}_{k-1} + \mathbf{K}_k \mathbf{y}_k$$

In this investigation of the transformation, the state vector consists of two components, one is a vector of calibration parameters for rotation, translation, scaling, and tilting for each chamber, and another is that of linear-function parameters for tracks. $\mathbf{y}_k$ is the residual between the state estimated with the observation model and the observation, and $\mathbf{K}_k$ is the Kalman gain matrix optimizing the next estimation using $\mathbf{y}_k$, which is calculated with the transformation of the previous step. The step of the estimation is propagated along clusters belonging to the reconstructed track of the cosmic ray. Then the position of each cluster is corrected

among the propagation of the estimation. Circles and triangles on the upper panel of Fig. 4 show the dispersion of the cluster positions from tracks reconstructed with linear fit and Kalman filter, respectively.
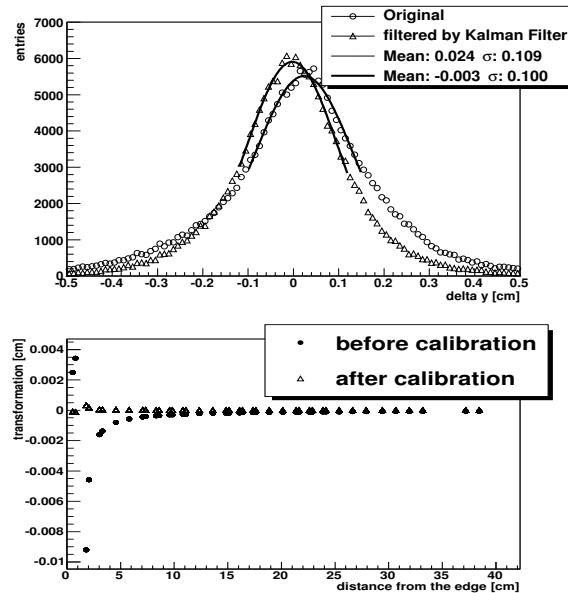
Figure 4. Circles and triangles of the upper panel show the dispersion of the cluster positions from tracks reconstructed with linear fit and Kalman filter, respectively. The lower panel shows the transformation as a function of the distance from the edge of chambers before and after applying (partial) calibration.

Visualization of the transformation was established such that the combination of calibration components were optimized to be able to visual the state of calibration easily. The lower panel of Fig. 4 shows the transformation which is a result of propagating of estimation with Kalman filter before and after applying (partial) calibration. This transformation is multiplied with a factor related with the distance from the edge of chambers.

4. summary and outlook

Calibration of ALICE-TPC is on going. Charge distortion near the edge of chambers was investigated. Transformation for calibration and alignment was calculated by using Kalman filter. The method for visualization of transformation was established.

References

[1] ALICE Collaboration "ALICE: Physics Performance Report, Volume I". Nucl. Part. Phys. 30 (2004) 1517-1763.

[2] ALICE Collaboration. "ALICE TPC Technical Resign Report". CERN/LHCC 2000-001.

[3] AliRoot and ALICE Offline Project.
http://aliceinfo.cern.ch/Offline

[4] R. E. Kalman, J. Basic Eng. 82 (1961) 34.

Simulation study for $dN/d\eta$ measurement in $\sqrt{s} = 10$ TeV proton-proton collisions at LHC-ALICE

S. Sano, H. Hamagaki, T. Gunji, and J.F. Grose-Oetringhaus[a]

Center for Nuclear Study, Graduate School of Science, University of Tokyo
[a]Gesellschaft fur Schwerionenforschung mbH, Darmstadt, Germany

1. Introduction

Parton density grows rapidly with decrease of fractional momentum x, but eventually tends to saturate, as a consequence of self-interaction of gluons, which is an intrinsic property of non-Abelian gauge theory. Such saturated state may be described with a classical field theory such as Color Glass Condensate (CGC) [1, 2].

The CGC hypothesis can describe the gluon distribution function obtained by HERA [3], and the BRAHMS data [4]. An investigation of gluon saturation is important to decide the initial condition for high-energy heavy-ion collisions.

At higher beam energy, gluons with smaller x can be probed and saturation scale Q_s is increased, where $1/Q_s$ corresponds to transverse size of gluons when the transverse plane of a hadron is filled with gluons. For the same p_t, Q_s at $\sqrt{s_{NN}} = 5.5$ TeV Pb+Pb collisions is three times larger than that at $\sqrt{s_{NN}} = 200$ GeV Au+Au collisions. At the LHC energy, CGC effects may be seen even at midrapidity [5]. Parton saturation will be investigated through the measurement of pseudo-rapidity distribution of charged particles $dN/d\eta$ in $\sqrt{s_{NN}} = 10$ TeV $p + p$ collisions and $\sqrt{s_{NN}} = 5.5$ TeV Pb+Pb collisions at LHC. This report describes the status of a preparation for the measurement of $dN/d\eta$.

2. Simulation and calculation

$dN/d\eta$ can be measured using the ALICE Time Projection Chamber (TPC), which is the main detector for tracking in the central barrel [6]. As the first step in the measurement of $dN/d\eta$, the detection efficiency of TPC for charged particles was evaluated using the simulation with AliRoot [7], the ALICE software package, which can provide event generation, simulation of the detector response, and reconstruction. The reconstructed tracks are recorded as ESD (Event Summary Data) tracks which have labels corresponding to the ID number of generated particles. Therefore, the reconstruction efficiency can be evaluated from the comparison between generated particles (MC particles) and ESD tracks using labels. PYTHIA 6 event generator [8] was adopted, and 277,500 events of minimum-bias $p + p$ collisions at $\sqrt{s} = 10$ TeV were used for this analysis. The detection efficiency depends on pseudo-rapidity, z position, and transverse momentum. Therefore, $dN/d\eta$ is calculated as

$$\frac{dN}{d\eta}\Big|_{\eta=\eta'} = \int_{V_{z_1}}^{V_{z_2}} \int_{p_T 1}^{p_T 2} C(\eta', z, p_T)$$
$$\times \left(\frac{dN}{dz dp_T d\eta}\right)_{\text{ESD}} dp_T dz \times C'_{p_T \text{cut}}(\eta') \quad (1)$$

where the integration is executed for the available region of the vertex z position and p_T. $C(\eta', z, p_T)$ is the correction factor obtained from the simulation as follows.

$$C(\eta, z, p_T) = \frac{N_{gen}(\eta, z, p_T)}{N_{acc}(\eta, z, p_T)} \quad (2)$$

$N_{acc}(\eta, z, p_T)$ and $N_{gen}(\eta, z, p_T)$ are the numbers of charged particles accepted and generated, respectively. $C'_{p_T \text{cut}}(\eta')$ is the correction factor due to the p_T cut [$p_T 1$, $p_T 2$].

3. Results on the simulation
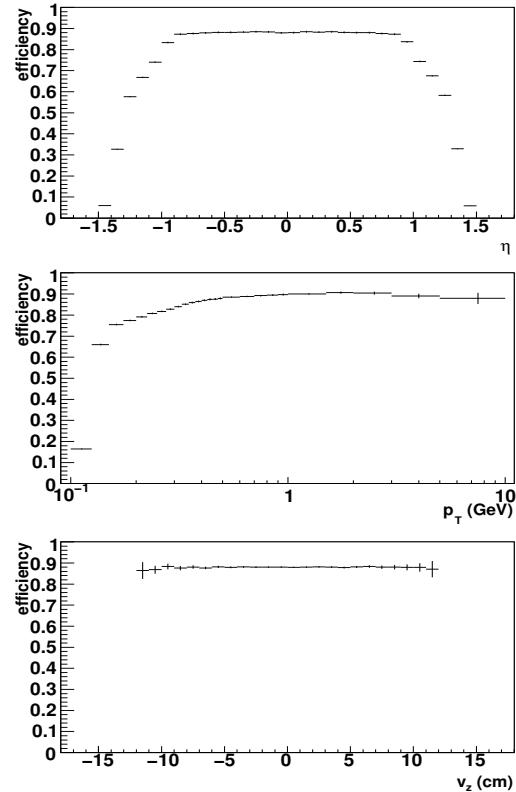
Figure 1. The reconstruction efficiencies for charged particles as a function of η, z, and p_T. These are the projections of $1/C(\eta, z, p_T)$ to η, z, and p_T.

Figure 1 shows the projections of $1/C(\eta, z, p_T)$ to η, z, and p_T, which corresponds to the reconstruction efficiency of the TPC for charged particles, where any feed-down correction is not applied. The cut parameter for each value was determined as $|\eta| < 0.9$, $|v_z| < 10$ cm.
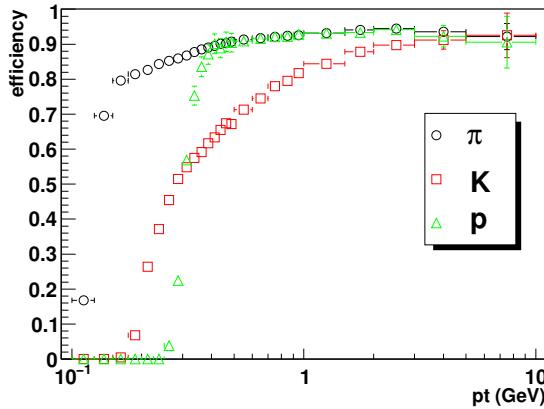
Figure 2. p_T distribution of the reconstruction efficiency for each particle in the TPC.

The reconstruction efficiencies for π K p were calculated to decide the p_T lower boundary. Figure 2 shows the reconstruction efficiencies as a function of p_T for each particle, where any feed-down correction is not also applied. The pseudo-rapidity and vertex cut determined from Fig. 1 are applied. The difference in the shape of the curve for π and K is due to the difference in the life time. Since β of protons is smaller and the energy loss in materials is larger than those of π and K, it is difficult for protons to reach the outer field cage of the TPC and the efficiency is small at $p_T < 0.3$ GeV. From this plot, p_T cutoff at 0.3 GeV was adopted. $C'_{p_T \, \text{cut}}$ is evaluated from the ratio of number of particles for $p_T > 0.3$ GeV and $p_T < 0.3$ GeV separately.
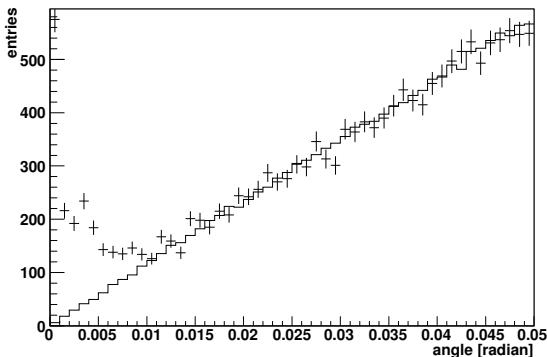
Figure 3. A histogram showing the opening angle distribution for pairs of particles. Crossing points and the solid line are plots for real pairs and mixing event, respectively.

Figure 3 shows the opening angle distribution between two tracks. Crossing points show the opening angle of real pairs and the solid line shows that from mixed events. A large number of entries is seen in the region below 0.01 radians for real pairs compared to the mixed pairs. The value of 0.01 radians correspond to the visual angle for phi direction of a cluster, a group of pads having charge, of TPC. Therefore a large portion of the entries below 0.01 radians seem to be fake tracks generated from the hit clusters be-

longing to one true track. The ratio of subtracted entries of real pairs with that of event mixing in the region below 0.01 rad to all track is about 0.08%.
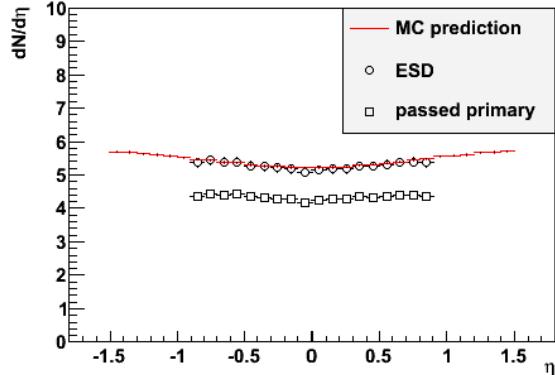
Figure 4. Comparison of $dN/d\eta$ between MC prediction and ESD. Circles show the result of ESD analysis and squares show the plots for only primary particles passed the cut of ESD analysis.

Figure 4 shows the comparison of $dN/d\eta$ between MC prediction (lines) and this analysis with the correction according to Eq. 1. (circles). The result of this analysis (circles) includes both primary particles and secondary particles which passed the cut of this analysis. Squares in Fig .4 show the plots for only primary particles. The ratio of the true primary particles to ESD plots (circles) of Fig. 4 is about 82±2% at $|\eta| < 0.5$.

4. Summary and outlook

The simulation study was performed for the measurement of $dN/d\eta$ of charged particles for $p + p$ collisions at $\sqrt{s_{NN}} = 10$ TeV with the ALICE TPC tracking system at LHC. Correction factors were evaluated in this study. In the next step, systematic errors will be estimated. The analysis of the first $p + p$ collisions planned in January 2010 will be done.

References

[1] L.V. Gribov, E.M. Levin, M.G. Ryskin, Phys. Rep.100 (1983) 1.

[2] L. McLerran, R. Venugopalan, Phys. Rev. D49 (1994) 2233.

[3] S. Eidelman *et al.*, [Particle Data Group], Phys. Lett. B 592 (2004) 1.

[4] D. Kharzeev, Y.V. Kovchegov, K. Tuchin, hep-ph/0405054 (2004).

[5] D. Kharzeev, E. Levin, M. Nardi, Nucl Phys A 747 (2005) 609.

[6] ALICE Collaboration. "ALICE TPC Technical Design Report". CERN/LHCC 2000-001.

[7] AliRoot and ALICE Offline Project. http://aliceinfo.cern.ch/Offline

[8] PYTHIA 6 http://projects.hepforge.org/pythia6/

Electron identification capability of ALICE-TRD studied by the beam test experiment at CERN-PS

A. Takahara, H. Hamagaki, T. Gunji, Y. Morino, S. Sano, for the ALICE collaboration

Center for Nuclear Study, Graduate School of Science, University of Tokyo

1. Introduction

ALICE-TRD (Transition Radiation detector) is one of the detectors for electron identification in ALICE experiment [1]. The AlICE's aim is to study the physics of Qurak Gluon Plasma at LHC enrgeies. For example, yield of J/ψ and Υ will be measured for Studying QGP thermodynamics. TRD will play a considerable role in these measurements. For this purpose PRF(pion rejection factor) $\geq$ 100 is required at electron efficiency 90% . Electron identification capabiliy of TRD super module was tested in CERN PS beam line at Nov 2007. This report will report its result.

2. TRD

Transition Radiation occurs when a charged particle crosses between two materials with different dielectric constants. The probability of emmission of TR has Lorentz factor, γ, dependence. In ALICE-TRD case, when an electron with over 1 GeV/c comes into the radiator, almost one transition radiation photon is liberated with 1-20 keV energy. The photon is emitted toward the moving direction of the electron. On the other hands, no TR photon is liberated from a pion less from 100 Gev/c, because of small γ value. Then. ALICE-TRD can can identify electrons. The TRD is wire drift chamber with radiator for transition radiation. In ALICE experiment, 18 TRD super modules are used. Each TRD super Module has 6 layers and 5 stacks. Then TRD super modules is composed of 30 TRDs. A TRD has a radiator, a drift region, an amplification region, and 12 or 14 set of 144 pads for read out. The thickness of the radiator is 4.8 cm , drift region is 3.0 cm and amplification region is 0.7 cm. Typical pad size is 0.725(azimuthal) $\times$ 8.75(longitudinal)cm. The gas in the chamber is 85% Xe and 15% CO_2. The drift velosity is 1.5 cm/μs. Then the drift time is typically 2 μs. Figure 1 shows average pulse shape shows that electron events have second peak.

The absorption length of Xe gas is 1-20 mm for 1-20 keV photons. The TR photons can make second peak.
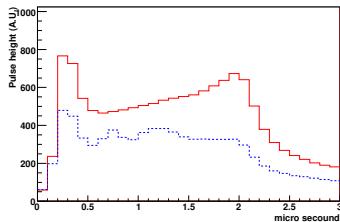
Figure 1. The average pulse shape of electron and pion events. Line corresponds to the pulse height of electron, dashed line corresponds to the pulse height of pion.

3. Experiment

The TRD super module was tested at 1, 2, 4, and 6 GeV/c beams. The beam was a mixture of electrons and pions. The spill of the beam is 0.5 s. One spill has 20000 particles. Figure 2 shows the setup.

Two double sided Si strip detectors are used for tracking and Lead-Glass Calorimeter (PbGl) and cherenkov was used to identify electrons and pions.

Table 1 shows count rate per spill. PbGl is added in trigger condition and about 98%(6 GeV) - 40%(1GeV) events are removed by requiring the coincidence of PbGl.

In this experiment, there is only two pile up rejection systems. One is INHIBIT signal. Another is Si's cut. In this trigger logic, INHIBIT signal required triggerd event. It means INHIBIT signal doesn't work in the case of pion event with under threshold value. Events which have over 2 tracks in the Si detector weren't used. However Si's gate time was set 350ns. Figure 1 shows the average pulse height at 3 and 0 μs isn't 0. Si can't rejection second tracks which enter before 0 ns or after 350 ns. It implies there were many double track events.
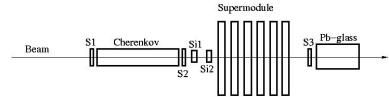
Figure 2. A schematic view of the beam test set up. S1 is not used. We used S2 and S3 to make trigger.

Table 1. counts per spill

	1 GeV/c	2 GeV/c	4 GeV/c	6 GeV/c
S2	11000	20000	25000	18500
S2+S3	5500	10000	10000	9500
S2+S3+Pbgl	3200	1400	438	193
accept	150	160	125	95

4. Analysys

Firstly, Pad Response Function (PaRF) was checked. The charge is shared by typical three or more adjacent pads. PaRF was calculated using a formula derived assuming a Gaussian PaRF

$$x = \frac{\ln(Q_{i+1}/Q_{i-1})}{\ln(Q_{2i}^2/Q_{i+1}Q_{i-1})} \quad (1)$$

$$\frac{Q_i}{Q_{i+1}+Q_i+Q_{i-1}} = A\exp(-x^2/2\sigma^2), \sigma = 0.5 - 0.6 \quad (2)$$

in ALICE-TRD [2, 3]. Here, i is the pad number, giuing the maximum charge. Q_i is the induced charge of the pad i. $x = 0$ is center of i pad and 1 is defined by pad width. Figure 3 shows scatter distribution of x and $Q_{i+1} + Q_i + Q_{i-1}$.
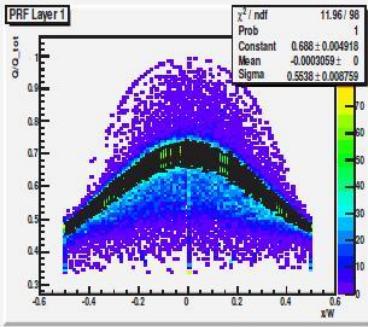
Figure 3. The scatters plot of x and Qtotal,$Q_{i+1} + Q_i + Q_{i-1}$

The figure shows σ is about 0.5. It implies about 96% charge is on center, left, and right pads. Then in this analysis $Q_{i+1} + Q_i + Q_{i-1}$ are used as total chage.

Test beam data was analyzed to evaluate the pion rejection factor with Neural Network (NN), where back propagation method is utilized as the training algorithm [4].

The test beam data was divided into two groups. One is for teaching, the other is for test. The data has the information on pulse height of each time bin where bin size is 0.1 μs and total number of time bins is 30 on the incident particle, where electron and pion are separated by Cherenkov and Pb-glass. Figure 4 shows PRF as function of momentum.

The PRF doesn't reach requirement. Figure 4 shows PRF as function of number of used layers at 2GeV/c.
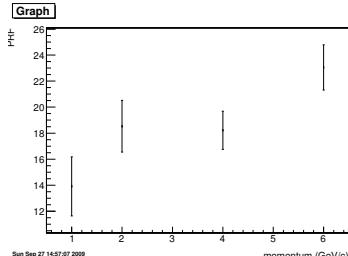
Figure 4. PRF as function of momentum.
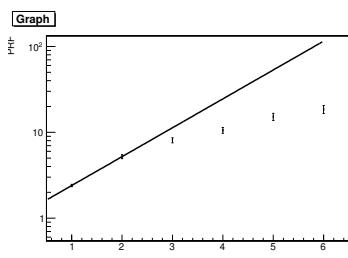
Figure 5. PRF as function of number of used layer at 2GeV/c.

Figure 6 shows PRF as function of number of used layer at 2GeV/c with layers "0,1,2,3" and "2,3,4,5" and "0,1,4,5", the 3 plots are basicaly same.

It shows the performance of 6 layers TRD were almost identical. The possible reason of low rejection factor is thought to be due to the double track events. Figure 7

shows the number of tracks reconstructed by TRD, where the tracks are not associated with SSD. According to the distribution shown in Fig. 7 and the difference in timing gate between SSD (350nsec) and TRD(3 μsec), 3.9% of the double tracks are accepted by SSD and TRD. By assuming that 3.9% of events contains double tracks in this analysis and this leads to the mis-identification of pions as electrons, PRF of 60% can be expected with this correction.

This figure has a vale at its center. The region was covered with the Si, but Si couldn't reject second tracks which entered before 0 ns or from 350 ns, and if second tracksentering Si were associated with the TRD, it can't be separate by TRD itself. According to the calculation from this distribution, 3.9 percent pion event will be miss identified as electron as might be expected. If there aren't 3.9 % miss identified events, the PRF be about 60. The result implies that high multiplicity intercepts electron identification. But The collision rate of LHC is about 7kHz. The time elapsing from collision to next is 100 μs. It is enough large as 3 μs. And maximum(Pb-Pb central collision) occupancy is 0.07 at one event [1].
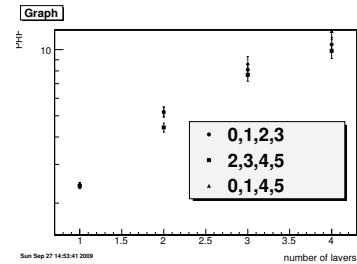
Figure 6. PRF as a function of number of used layer at 2GeV/c.
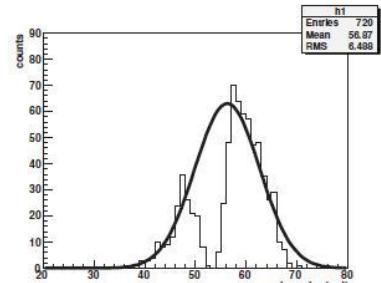
Figure 7. dstribution of center position of second tracks

5. Summary and Outlook

We got the best PRF 23. The reason of low performance might be double track event. The corrected value is PRF 60.

References

[1] ALICE TRD Techinical Design Report
[2] D.L.Fancher and A.C. Schaffer, IEEE Trans.Nucl.Sci.26(1979)150.
[3] S.R.Amendolia et al.,Nucl.Instr.Meth.217(1983)317.
[4] A.N.Kolmogorov,Dokl.Akad.Nauk.Nauk.USSR 114(1957935)

Accelerator and Instrumentation

SHARAQ Project – Progress in FY2008 –

T. Uesaka , S. Michimasa, K. Nakanishi, A. Saito[a], S. Ota , Y. Sasamoto, K. Miki[a,b], S. Noji[a],
H. Miya, H. Tokieda, S. Kawase, M. Sasano[a], S. Itoh[a], H. Kurei, T. Kawabata, N. Yamazaki,
A. Yoshino S. Shimoura, H. Sakai[a], T. Kubo[b], Y. Yanagisawa[b], K. Itahashi[b], H. Baba[b], G. P. Berg[c],
P. Roussel-Chomaz[d], D. Bazin[e], for the SHARAQ collaboration.

Center for Nuclear Study, Graduate School of Science, University of Tokyo
[a] Department of Physics, Graduate School of Science, University of Tokyo
[b] RIKEN Nishina Center
[c] Department of Physics, Notre Dame University
[d] GANIL
[e] National Superconducting Cyclotron Laboratory, Michigan State University

The first beam was successfully transported to the final focal plane of SHARAQ on 23 March 2009, the very end of FY2008. In the commissioning run, it was confirmed that the SHARAQ spectrometer [1] and the high-resolution beamline [2] work almost as designed. In this article, major progress in FY2008 and a part of results from the commissioning run are reported.

1. Spectrometer

Figure 1. Photograph of the SHARAQ spectrometer

The magnetic field distributions are key inputs in ion-optical calculations. Reliable determination of the transfer maps, up to higher-order aberrations, requires accurate and precise knowledge of magnetic field distributions. The magnetic field distributions for a large area of 1.3 m^2 each at the exit of D1 and the entrance and exit of D2 were measured in summer of 2008. In order to scan this large area within a reasonable time, we used the search coil method [4]. In addition to medium plane measurement, we also collected data for the off-medium plane of y=0–85 mm, where y denotes distance from the medium plane. The details of the measurement are described in Ref. [3]. Ion-optical calculation based on the measured field distributions was done to obtain transport maps of the SHARAQ spectrometer.

In the second half of this fiscal year, vacuum chambers and pumping systems were installed. With these equipment, the SHARAQ spectrometer was set ready to accept heavy ion beams from BigRIPS.

2. High-resolution beam line

The specifications of beamline devices have been finalized, based on the ion-optical design in Ref. [2]. In FY2008, two normal conducting dipole magnets with a 30° bending angle, vacuum chambers for beamline detectors, vacuum pumps, and DC power supplies were installed. Four normal conducting quadrupole magnets and one superconducting triplet quadrupole magnets (STQ) were recycled. One of the normal conducting quadrupoles was renovated by enlarging the bore radius from 75 mm to 90 mm to enable acceptance of large-emittance secondary beams. Construction of the beamline started in summer of 2008 and was completed in the end of February 2009 [5].

Ion-optical studies of the beam transport were continued in parallel to the construction, for versatile use of the SHARAQ spectrometer. We have investigated a new large momentum acceptance mode [6], in addition to dispersion matching and high-resolution achromatic modes for high-resolution missing mass measurements. In the large momentum acceptance mode, the beamline allows beam momentum spread of $\Delta p / p$ =2%, which is about 6 times larger than that in the dispersion matching mode. Experiments with low-intensity rare isotope beams can be efficiently conducted in the large acceptance mode.

3. Focal plane detectors

Cathode readout drift chambers with an effective area of 550 mm (H) $\times$300 mm (V) have been fabricated in collaboration with the GANIL group. They were installed to the SHARAQ final focal plane in the beginning of January 2009 and tested with α-rays from an Am source prior to the beam irradiation. Details of CRDCs are described in Ref. [7].

4. Beam-line detectors

Thin tracking detectors working under a beam intensity of higher than 1 MHz are key devices in high-resolution experiments with SHARAQ. They are used for tuning the beamline and tagging beam trajectories during measurements.

In 2008, the detectors were irradiated with an accelerated α-beam with an energy of 8.8A MeV. [8, 9, 10] The energy deposit of the alpha particles is same as that of a 200-MeV/A nitrogen beam which will be used in a future
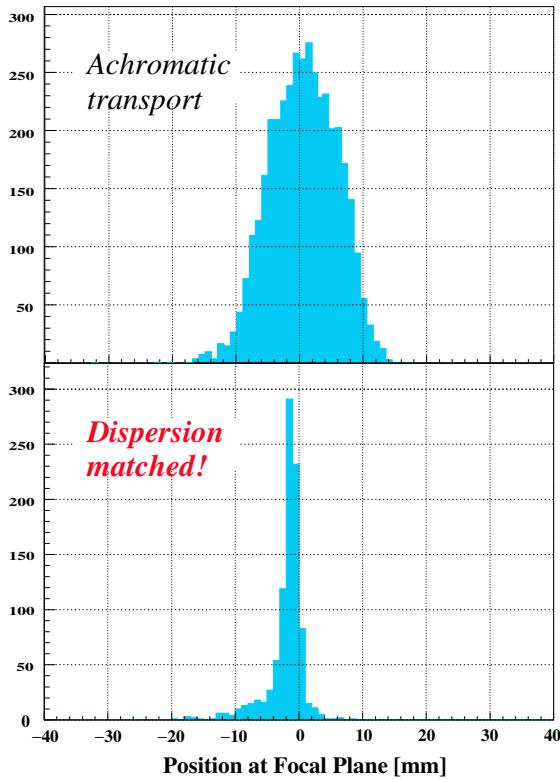
Figure 2. Horizontal beam images at the final focal plane in the achromatic (upper panel) and the dispersion matching transport (lower panel).

experiment at SHARAQ. The results clearly demonstrated that LP-MWDC with an isobuthane gas should work under a pressure as low as 10 kPa. It was also found that further improvements in the electronics are required for better determination of the energy loss of particles.

5. Commissioning run

A primary ^{14}N beam accelerated up to 250A MeV in SRC was transported from F0 of BigRIPS to the SHARAQ focal plane. The first beam fired plastic scintillation counters placed downstream of the focal plane at 22:37 on 23 March 2009. In the subsequent commissioning run, detector responses to the beam and ion-optical properties of the SHARAQ spectrometer and the beam-line were investigated.

First of all, almost all the detectors, except for one placed at F3, and the DAQ system were found to work well. Detection efficiencies of beam-line detectors were almost 100% at an anode high voltage of 1 kV and a gas pressure of 10 kPa. The position resolution was as good as 500 μm in FWHM. Focal plane CRDCs worked stably at an anode voltage of 800 V for an isobuthane gas of 2 kPa.

By using beam-trajectories deteremined by the track-

ing detectors, ion-optical properties of the magnetic system were investigated. Momentum dispersions $(x|\delta)$ at dispersive focal plane F6 and FH7, and the SHARAQ focal plane were measured to be 7.8 m, 7.5 m and 6.8 m, respectively. We tried to achieve a lateral dispersion matching condition by tuning beam-line quadrupoles, STQH15b and STQH19a. Figure 2 shows horizontal beam images at the SHARAQ focal plane. The beam image in achromatic transport (upper panel) is broad due to momentum spread of the beam itself and the beam spot size at the SHARAQ target position. On the other hand, the beam image after dispersion matching (lower panel) is as narrow as 2.6 mm (FWHM), which correspondes to a momentum resolution of $\delta p/p \sim$2500. Thus, lateral dispersion matching between the beamline and SHARAQ was, at least partially, achieved.

6. Summary

After 4-year construction, the SHARAQ spectrometer and the high-resolution beam-line have been put into operation. Data taken during the commissioning run should be useful for understanding ion-optical properties of the system and detector performances in detail. Future improvements will be embodied based on the results and will open a new opportunity of high-resolution experiments with variety of RI beams produced at RIBF.

References

[1] T. Uesaka et al., Nucl. Instrum. Methods B **266**, 4218 (2008).
[2] T. Kawabata et al.: Nucl. Instrum. Methods B **266**, 4201 (2008).
[3] K. Nakanishi et al.: CNS Annual Report 2008 (2010).
[4] J. A. Caggiano: Ph.D thesis, Michigan State University, (1999).
[5] T. Kubo, Y. Yanagisawa et al.: RIKEN Acc. Prog. Rep. **42** (2009).
[6] Y. Sasamoto et al.: CNS Annual Report 2008 (2010).
[7] H. Tokieda, S. Michimasa et al.: CNS Annual Report 2008 (2010).
[8] A. Saito et al.: CNS Annual Report 2008 (2010).
[9] H. Miya et al.: CNS Annual Report 2008 (2010).
[10] K. Miki et al.: RIKEN Acc. Prog. Rep. **42** (2009).

Studies of ion optics of the high resolution beam line for SHARAQ

Y. Sasamoto, K. Nakanishi, T. Uesaka, S. Shimoura, H. Sakai[a], T. Kubo[b], N. Yamazaki, A. Yoshino
and SHARAQ collaboration

Center for Nuclear Study, Graduate School of Science, University of Tokyo
[a]Department of Physics, University of Tokyo
[b]RIKEN (The institute of Physical and Chemical Research)

New missing mass spectroscopy with an RI beam is planned to be conducted at RIBF with the SHARAQ spectrometer [1]. The SHARAQ spectrometer is designed to achieve a resolving power of $p/\delta p = 1.5 \times 10^4$ and a high angular resolution of $\delta\theta \sim 1$ mrad for particles with a maximum magnetic rigidity of $B\rho = 6.8$ Tm.

To avoid loss of energy resolution due to the momentum spread of RI beams, the dispersion matching technique is applied to perform high resolution measurements [2]. The maximum resolving power of 15000 is expected to be achieved in the dispersion matching (DM) mode. However, in the DM mode, a large target is needed because the image size at the target is about as large as 10 cm. To be able to use small targets, high resolution achromatic (HA) mode is also prepared. In the HA mode, the beam size at the target is about a few cm with keeping the resolving power of 7500 by measuring beam trajectories at dispersive focal plane F6. The resolving power and acceptance of the DM and HA mode are summarized in Table 1.

Transport mode	DM	HA
Resolving power	15000	7500
		(at F6)
Momentum acceptance (%)		± 0.3
Angular acceptance		
horizontal (mrad)		± 10
vertical (mrad)		± 30

Table 1. Resolving power and acceptance for high resolution beam line. Transport mode of DM, HA indicate the dispersion matching mode, high resolution achromatic mode, respectively.

The high resolution beam line has been constructed [3]. Figure 1 shows the layout of the high resolution beam line. An RI beam emitted from the production target at F0 is achromatically focused at F3. F3 is the ion-optical starting point of the high resolution beam line. The beam line consists of 30 superconducting quadrupole magnets, 4 normal-conducting quadrupole magnets, and 5 dipoles. The magnets are set according to the central rigidity of the aimed radio-isotope in the experiment. For a reduction of the tuning time, each magnet was set according to the ion optical calculation based on the precise magnetic field measurement [4].

The field-map measurement had been performed for the dipoles and superconducting quadrupoles [5] [6], and for normal-conducting quadrupoles, which were used for

the SMART spectrograph [7], of QH16 and QH17 [8]. However, since there are little information available for the field-maps of QH18-a,b which are normal-conducting quadrupole magnets, we carried out the magnetic field mapping for QH18-a,b.

The magnetic field distribution in QH18-a,b were measured by using a hall probe. The distribution was measured at a radius of 25 mm which is inside of the bore radius of QH18-a,b of 90 mm. Hall probe voltages were measured with a digital multimeter (Keithley 2701 + 7702) linked to the PC with the Ethernet network communication. The hall probe were moved by hand at 20 mm interval along the beam axis, whereas the interval was reduced to be 10 mm where the distribution rapidly change along the axis. Integrating the distribution, the effective field lengths are obtained as shown in Fig. 2. The nominal effective lengths of QH18-a and QH18-b are 400 mm and 500 mm, respectively. The current settings were prepared for each $B\rho$ on the bases of the ion optical calculation results from the field-map measurement.

To achieve the performance listed in Table 1, the aberration effects should be corrected, for which precise knowledge of transfer matrix elements up to the higher order is necessary. Actually, the RI beams have a large emittance which causes the spread of beam image due to the higher order aberrations. For example, third order matrix element $(x|abb)$ causes a spread of 12 mm at the target from the ion-optical calculation. In the commissioning run in March 2009, ion-optical studies were conducted which include the measurements to determine the transfer matrix elements.
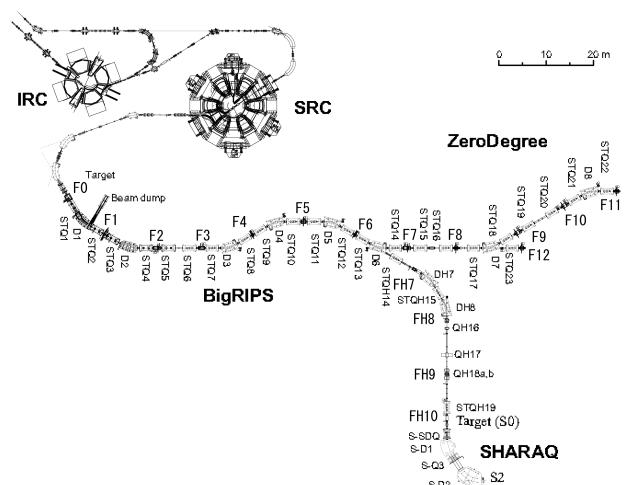
Figure 1. Layout of the high resolution beam line. It branches from BigRIPS after F6. F3 is the ion-optical starting point of the high resolution beam line.
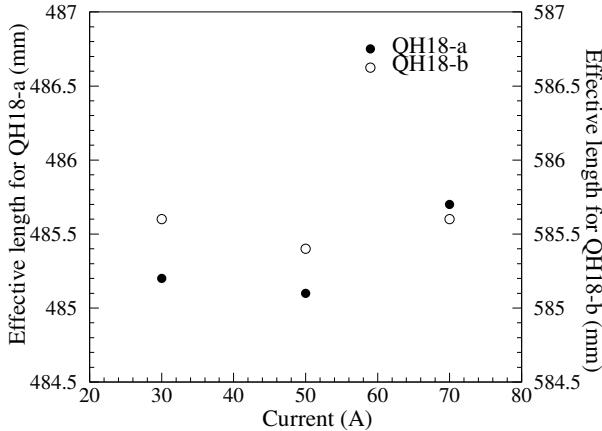
Figure 2. Effective field lengths of the QH18-a,b magnet.

In the commissioning, beam trajectories were obtained by using positions and angles of beams determined by beam-line detectors installed at each focal plane. To examine the fundamental optical properties, the dispersion was measured by using aluminium degraders installed at BigRIPS-F0 with primary ^{14}N beam. The measured $(x|\delta)$ at each focal plane for the DM mode is summarized in Table 2. It is shown in the table that the differences between the design and measured values for FH9 and FH10 are larger than ones for F6 and FH7. Those differences are considered to be caused by the focus condition which is mainly affected by the magnet settings. After the run it is found that the settings of the QH18-a,b were not correct. Measurements were also conducted using secondary beams. Other transfer matrix elements can be deduced from the data with primary and secondary ^{12}N beams. Such analysis is in progress.

Focal plane	F6	FH7	FH9	FH10
Measured value (mm/%)	77	−74	201	110
Design value (mm/%)	76.7	−73.7	229	150

Table 2. Measured $(x|\delta)$ for the DM mode.

One of the most important purpose of optical studies in the commissioning is to establish the method to tune the beam to the dispersion matching condition. When the matching condition between the beam line and spectrometer is completely realized, the horizontal positions at the focal plane of the spectrometer are independent of the spread of the beam. Therefore, the matching condition is expected to be experimentally diagnosed with the correlation between the beam momentum and horizontal position at the final focal plane. In the dispersion matching tuning, the primary beams were transported to the focal plane of SHARAQ. The beam momentum was obtained from the position at the dispersive focal plane FH7. Figure 3 shows correlation between the horizontal position at FH7 and that at the fo-

cal plane of SHARAQ. From the figure, the correlation between the beam momentum and position at the final focal plane was clearly seen. It is found that the diagnostic elements of the high-resolution beam line successfully worked.
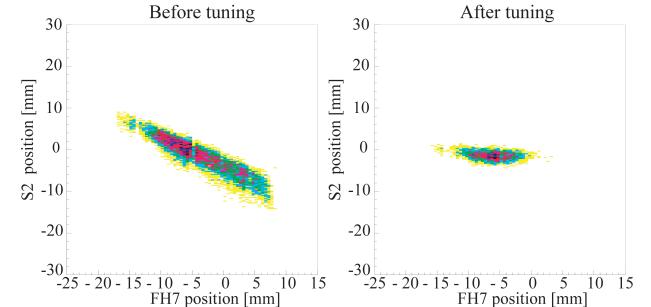
Figure 3. Horizontal-position correlation between at FH7 and at the focal plane of SHARAQ(S2). Left figure shows the correlation before the dispersion matching tuning, while the right one shows the correlation after the tuning.

It has been demonstrated in the commissioning that the dispersion matching condition has partially been achieved. To tune the beam to the dispersion matching condition, STQH15-b and STQH19-c were optimized to satisfy the matching condition using the diagnostic method described above. At present, the resolving power of ~ 2700 has been achieved when the magnification of F3-S0 and S0-S2 were assumed to be 1 and 0.5, respectively. The currently achieved resolving power was about six times smaller than the design value of 15000. At this moment during the commissioning run, the matching condition was achieved only for the lateral one, whereas the optimal resolution was designed to be achieved when both the lateral and angular dispersion matching are realized. Optimization for detectors to diagnose the beam transport are still not finalized. Therefore, when the tuning of the beam transport becomes possible with the finalized beam detectors, higher resolving power will be realized. Further evaluations with the refined diagnostic tools will be made in the next commissioning run.

References

[1] T. Uesaka *et al*., Nucl. Instrum. Meth. B **266** (2008) 4218.
[2] T. Kawabata *et al*., Nucl. Instrum. Meth. B **266** (2008) 4201.
[3] Y. Yanagisawa , Private communication.
[4] H. Takeda , Private communication.
[5] Y. Yanagisawa *et al*., RIKEN Accel. Prog. Rep. **41** (2008).
[6] H. Suzuki , Private communication.
[7] T. Ichihara *et al*., Nucl. Phys. A **569** (1994) 287c.
[8] Y. Tajima and S. Kato, *unpublished*.

Development of Beam Line Detectors for BigRIPS and High-Resolution Beam Line

A. Saito, S. Shimoura, K. Miki[a], H. Miya, T. Yoshida[b], T. Kawabata[c], S. Itoh[a], K. Itahashi[d],
M. Sasano[a], Y. Shimizu, S. Kawase, H. Kurei, S. Michimasa, K. Nakanishi, S. Noji[a], S. Ota,
Y. Sasamoto, H. Tokieda, T. Uesaka, and H. Sakai[a]

Center for Nuclear Study, Graduate School of Science, University of Tokyo
[a]Department of Physics, University of Tokyo
[b]Department of Physics, Rikkyo University
[c]Department of Physics, Kyoto University
[d]RIKEN (The Institute of Physical and Chemical Research)

1. Introduction

We are developing low-pressure multi-wire drift chambers (LP-MWDC's) and plastic scintillators which will be used in BigRIPS and the high-resolution beam line (HRBL), for the experiments using the SHARAQ spectrometer [1].

Figure 1 shows the BigRIPS, HRBL, and the SHARAQ spectrometer. The LP-MWDC's are used at F3, F6, F-H7, F-H9, and F-H10. A list of the LP-MWDC's is shown in Table 1. Plastic scintillators are installed in F3, F-H7, F-H9, and F-H10. We report here on developments of LP-MWDC's, plastic scintillators, and the commissioning performed in March 2009.
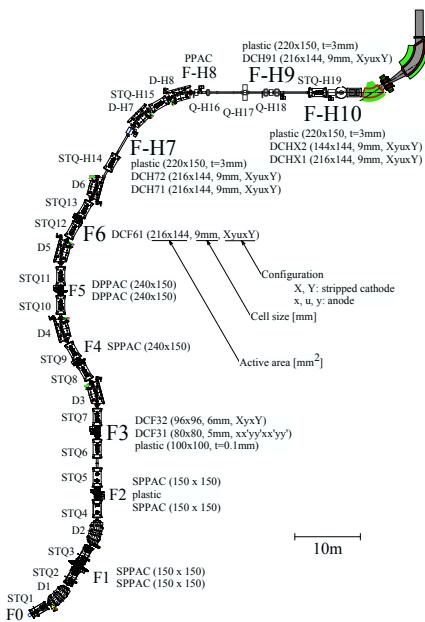
Figure 1. LP-MWDC's and plastic scintillators in BigRIPS and HRBL.

There are some requirements for the tracking detectors. The thickness of the detectors should be as small as $\sim10^{-4}$ of radiation length to reduce the effect of multiple scattering in the detectors to be ~0.1 mrad. The efficiency should be as large as possible even for light RI beams such as ^{8}He at 200 MeV/nucleon. The position resolution is required to be less than 300 μm in FWHM. The maximum counting rate should be 1 MHz for the dispersive beam transport. The energy loss information should be obtained by the tracking detectors for the particle identification of the RI beam to reject in-flight β-decay events.

The LP-MWDC's are being developed in order to realize the performance described above. A low-pressure operation at around 10 kPa is needed to reduce multiple scattering in the detector as small as 0.1 mrad.

Table 1. List of LP-MWDC's in BigRIPS and HRBL.

Focal Plane	Name	Active area [mm^2]	Cell size [mm]	Config- uration
F3	DCF31	80×80	5	xx'yy'xx'yy'
	DCF32	96×96	6	XyxY
F6	DCF61	216×144	9	XyuxY
F-H7	DCH71	216×144	9	XyuxY
	DCH72	216×144	9	XyuxY
F-H9	DCH91	216×144	9	XyuxY
F-H10	DCHX1	216×144	9	XyuxY
	DCHX2	144×144	9	XyuxY

X, Y: stripped cathode with delay-line readout
x, u, y: anode

2. MWDC's at F3

We measured gas gains of DCF32 using a 5.5-MeV α ray from ^{241}Am. The gas gain was calculated from the signals from the delay line (DL) readout, which was developed for the PPAC's [7], and from the energy loss calculations. The data were taken for five gas pressures by changing the bias voltages. Figure 2 shows the results. The closed circles, closed squares, closed triangles, open circles, and open squares are the data for 4, 5, 10, 15, and 20 kPa, respectively. The results roughly agree with the data in Ref. [5].

The performances of DCF31 and DCF32 were evaluated in experiments using an α beam at 8.8 MeV/nucleon which gives the same energy losses as ^{12}N at 200 MeV/nucleon, which will be used in the experiments using the SHARAQ spectrometer. Details of DCF31 and DCF32 are described in Refs. [3] and [4], respectively.
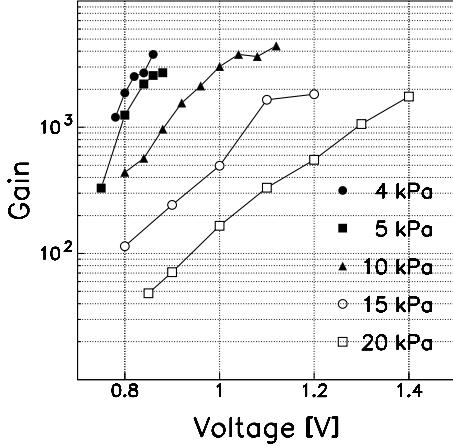
Figure 2. Gas gain of DCF32. The closed circles, closed squares, closed triangles, open circles, and open squares are the data for 4, 5, 10, 15, and 20 kPa, respectively.

3. MWDC's at F6, F-H7, F-H9, and F-H10

Figure 3 shows a schematic view of DCHX2. It includes three anode layers (x, u, and y) and two stripped cathodes (X and Y). The direction of the u wires are tilted by 30 degree with respect to the x wires. The cathodes at outside are stripped in horizontal and vertical directions (X and Y). The stripped cathodes give redundant position information, and the energy loss of the RI beam for the particle identification. The signals from the stripped cathodes are read out using DL's. Three high voltages can be supplied individually to the stripped cathodes, other cathodes, and the field wires. The signals from DL's are amplified by Kaizu 3356 preamplifier. The ones from the anode wires are amplified and discriminated by REPIC RPA-130/131 64-channel preamplifier and discriminator cards. The timing signals from RPA-130/131 are digitized by CAEN V1190A/B multi-hit TDC's.
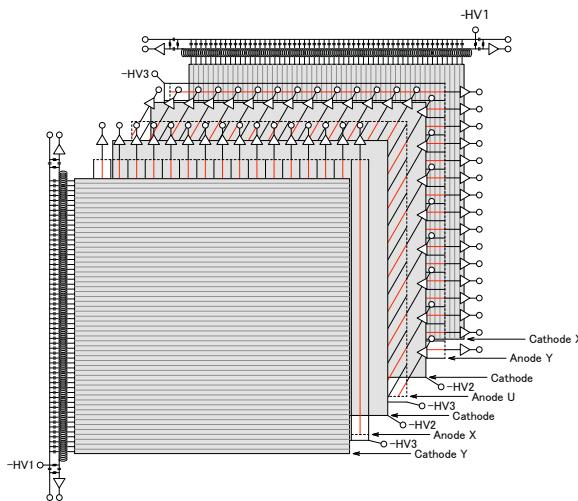
We performed an experiment to evaluate performances of DCF6, DCHX1, and DCHX2. Details of the experiment are described in Ref. [6].

4. Plastic scintillators

Plastic scintillators were installed in F3, F-H7, F-H9, and F-H10. The scintillators were Eljen Technology EJ-212. The geometry of SF3 and others are $100 \times 100 \times 1$ mm^3 and $220 \times 150 \times 3$ mm^3, respectively. The scintillation light was read out by two Hamamatsu R7600 photomultiplier tubes with light guides attached to both ends of the scintillator.

5. Commissioning

A commissioning of HRBL and SHARAQ spectrometer was performed in March 2009. Eight LP-MWDC's listed in Table 1 were used in the commissioning. We evaluated the tracking efficiencies and resolutions of LP-MWDC's at F6, F-H7, F-H9, and F-H10, at 10 kPa, for a ^{14}N beam at 250 MeV/nucleon [8]. The tracking efficiency of one LP-MWDC was around 97%, which is high enough for event-by-event tracking of the beam. The tracking resolutions are closed to the requirement, 300 μm. Further analyses are in progress to obtain higher resolution.

We have developed LP-MWDC's and plastic scintillators for BigRIPS and HRBL, for the experiments using SHARAQ spectrometer. Obtained performances of the anode layers are closed to the requirements. Further analyses are in progress to obtain higher resolution of anode layers and to evaluate the performances of the stripped cathodes with DL-readout.

References

[1] T. Uesaka et al.: Nucl. Instrum. Meth. in Phys. Res. **B266**, 4218 (2008).

[2] T. Kawabata et al.: Nucl. Instrum. Meth. in Phys. Res. **B266**, 4201 (2008).

[3] K. Miki et al.: RIKEN Accel. Prog. Rep. **42** (2009); K. Miki et al.: CNS Ann. Rep. 2008 (2010).

[4] H. Miya et al.: CNS Ann. Rep. 2007, 60 (2008); H. Miya et al.: RIKEN Accel. Prog. Rep. **42**, 173 (2009).

[5] Yu. I. Davydov et al.: Nucl. Instrum. Meth. in Phys. Res. **A545**, 194 (2005).

[6] T. Yoshida et al.: CNS Ann. Rep. 2008 (2010).

[7] H. Kumagai et al.: Nucl. Instrum. Meth. in Phys. Res. **A470**, 562 (2004).

[8] H. Miya et al.: CNS Ann. Rep. 2008 (2010).

Figure 3. Schematic view of DCHX2.

Performance of LP-MWDC for ^{14}N at 250 MeV/nucleon

H. Miya, S. Shimoura, A. Saito[a], K. Miki[a], T. Kawabata[c], K. Itahashi[b], S. Itoh[a], S. Ota,
M. Sasano[a], Y. Shimizu, H. Baba[b], H. Kurei, S. Michimasa, S. Noji[a], K. Nakanishi, Y. Sasamoto[b],
Y. Shimbara[d], H. Tokieda, T. Uesaka and H. Sakai[a]

Center for Nuclear Study, Graduate School of Science, University of Tokyo
[a]Department of Physics, University of Tokyo
[b]RIKEN (The institute of Physical and Chemical Research)
[c]Department of Physics, Kyoto University
[d]Department of Physics, Niigata University

1. Introduction

We are developing Low-Pressure Multiwire Drift Chambers (LP-MWDCs) [1, 2, 3, 4] for light heavy ions at 100–300 MeV/nucleon. The LP-MWDCs are used in BigRIPS and High-Resolution Beamline (HRBL) [5] in RI Beam Factory (RIBF).

The LP-MWDCs have 3 anode layers (x, u, and y). The u layer was tilted at $30°$ with respect to x. Pure isobutane is used as a counter gas at a pressure of 10 kPa. By using the gas at the low pressure, the effect of the multiple scattering can be reduced. The detail of the structures and specifications of the LP-MWDCs is described elsewhere [1, 2, 3, 4].

In March 2009, we performed a commissioning of HRBL [5] and SHARAQ spectrometer [6], and evaluated the performance of the LP-MWDCs for a ^{14}N beam at 250 MeV/nucleon. We report here the position resolutions and tracking efficiencies as a function of the applied voltage.

2. Experiment

A ^{14}N beam was accelerated up to 250 MeV/nucleon by AVF, RRC, and SRC cyclotrons and transported to HRBL. The LP-MWDCs and plastic scintillators were installed at the focal planes in BigRIPS and HRBL. The size of the scintillator at F3 was $100×100$ mm^2 and the thickness was 1 mm. This scintillator was used as a trigger counter. The size of the scintillators at F-H7, F-H9, and F-H10 was $220×150$ mm^2 and the thickness was 3 mm. The detail of the experimental setup at each focal plane is described in Ref. [2].

The anode signal of the LP-MWDCs was read out, amplified, and discriminated by REPIC RPA-130/131 cards. The timing of the leading edge and trailing edge were recorded by using CAEN V1190A/B multihit TDCs.

While the beam passes through the counter gas, it kicks electrons in the gas, called δ-rays. The δ-rays cause multiple hits in one anode layer. In order to prevent incorrect tracking, signals by δ-rays have to be rejected. In our experiment, pulse widths from the cards, which were related to the pulse height of the analog signals, were obtained [3]. These pulse widths enable us to separate the signals of the beam from those of the δ-rays by the pulse height.

3. Analysis and Results

The spectrum of the pulse width for all the hits in anode wires on x layer of DCH71, as one of beam line detectors,

at 1000 V is shown in Fig. 1 (a). Figure 1 (b) shows the relation between the pulse widths and the leading edge timing. The pulse width of the beam were separated from those of δ-rays. The spectrum of the leading-edge timing of input signals of the TDCs is shown in Fig. 1 (c). A drift time-to-distance calibration was carried out for each anode layer. The drift length was evaluated by assuming a uniform irradiation to each cell.
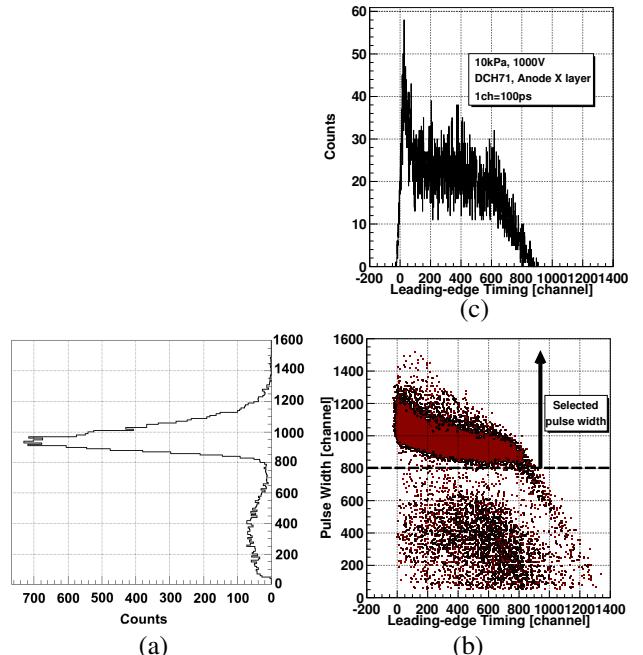
Figure 1. (a) A spectrum of the pulse width for all the hits in anode wires on x layer of DCH71 at 1000 V, (b) Relation between the pulse width and leading edge timing, (c) a spectrum of the leading edge timing by selecting the pulse width for the true pariçle.

We can compute the drift length from Anode wires, i.e., two candidates for x and y are obtained. As shown in Fig. 2 by circles, there remain four candidates, when we use position information of x and y. However, the hit position is uniquely determined by using the position information of u.

In order to estimate the position resolutions, the distributions of $u_u - u_{xy}$ were investigated. Here, u_u is a hit position
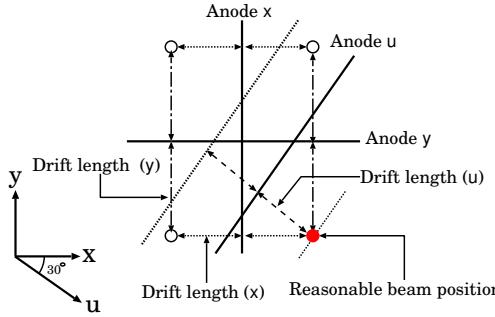
Figure 2. There remain 4 candidates, when we use position information of x and y. The hit position is determined by using the position information of u in addition.
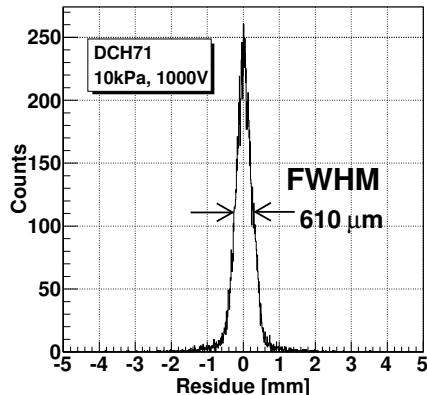
Figure 3. Residue distribution of $u_u - u_{xy}$ for DCH71 at 10 kPa and 1000 V.

of u and u_{xy} is a also hit position in u axis which is calculated from the hit positions in x and y. Figure 3 shows the distribution of $u_u - u_{xy}$ for DCH71 at 1000 V.

From the distribution of $u_u - u_{xy}$, the position resolution can be estimated. The position resolution is given by $\Delta_{u_u - u_{xy}}/\sqrt{2}$, where $\Delta_{u_u - u_{xy}}$ is FWHM of the distribution of $u_u - u_{xy}$. Figure 4 shows the position resolutions evaluated as a function of the applied voltage by using the means above. The position resolutions (FWHM) are obtained about 400 μm.

The tracking efficiencies were defined as the ratio of the number of the events satisfying $|u_u - u_{xy}| < 4.5$ mm, which is equal to the half cell size, to the counted number of the ^{14}N beam by using the plastic scintillator at F-H10. Since this scintillator was installed at the end of HRBL, particles detected at the scintillator surely passed through each LP-MWDC. Figure 5 shows the tracking efficiencies as a function of the applied voltage. Typically, the tracking efficiencies reached around 97% between 1000 V and 1100 V.
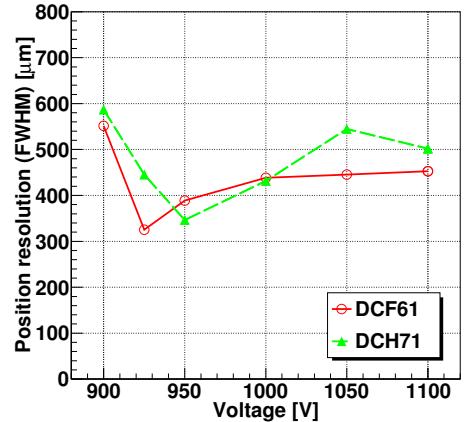
Figure 4. Position resolutions (FWHM) of DCF61 and DCH71 as a function of the applied voltage at 10 kPa. The Position resolutions are obtained from the distribution of $u_u - u_{xy}$.
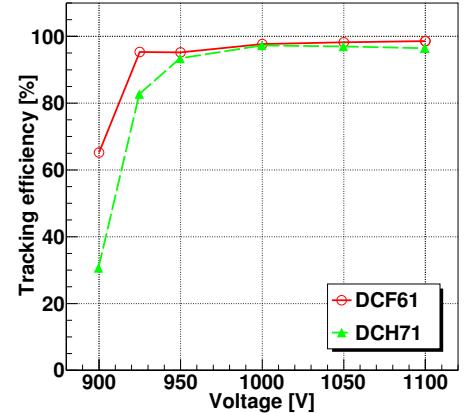
Figure 5. Tracking efficiencies of DCF61 and DCH71 as a function of the applied voltage at 10 kPa. The Tracking efficiencies are defined as the ratio of the number of the events satisfying $|u_u - u_{xy}| < 4.5$ mm to the counted number of the ^{14}N beam by using the plastic scintillator at F-H10.

4. Summary

The position resolutions and tracking efficiencies of the LP-MWDCs were evaluated as a function of the voltage at 10 kPa for the ^{14}N beam at 250 MeV/nucleon. The position resolutions (FWHM) were obtained around 400 μm. The tracking efficiencies reached around 97% between 1000 V and 1100 V.

References

[1] H. Miya *et al.*: CNS Ann. Rep. 2007 (2008).
[2] A. Saito *et al.*: CNS Ann. Rep. 2008 (2010).
[3] K. Miki *et al.*: CNS Ann. Rep. 2008 (2010).
[4] T. Yoshida *et al.*: CNS Ann. Rep. 2008 (2010).
[5] T. Kawabata *et al.*: Nucl. Instr. and Meth. *B* **266** (2008), 4201.
[6] T. Uesaka *et al.*: Nucl. Instr. and Meth. *B* **266** (2008), 4218.

Performance evaluation of low-pressure MWDC for BigRIPS-F3

K. Miki[a,d], A. Saito[a], H. Miya[b], S. Shimoura[b], T. Kawabata[b], H. Kurei[b], S. Michimasa[b],
K. Nakanishi[b], S. Noji[a], S. Ota[b], Y. Sasamoto[b,d], T. Tokieda[b], T. Yoshida[c], T. Uesaka[b], and
H. Sakai[a]

[a]*Department of Physics, University of Tokyo*
[b]*Center for Nuclear Study, Graduate School of Science, University of Tokyo*
[c]*Department of Physics, Rikkyo University*
[d]*RIKEN (The Institute of Physical and Chemical Research)*

1. LP-MWDC - DCF31

Low-pressure multiwire drift chambers (LP-MWDCs) have been developed [1] as beam line detectors (BLDs) for the high-resolution measurement using the newly constructed spectrometer SHARAQ [2] at RI Beam Factory (RIBF) in RIKEN. One of the largest physical motivations of SHARAQ is to explore the unknown region in nuclear physics via the exothermic charge exchange reaction using radioactive isotope (RI) beams. For the high-resolution measurement with RI beams, the following requirements are imposed on the BLDs:

1. the position resolution better than 300 μm (FWHM) for the precise ray tracing,

2. the gas pressure as low as possible for sufficiently small energy struggling and multiple scattering effects,

3. the efficiency close to 100% for the event-by-event tracking.

The performances of LP-MWDCs were tested by using an accelerated beam [3]. In this article, we report the performance evaluation for one of the LP-MWDCs, DCF31. DCF31 was built for the use at BigRIPS-F3, which is the start point of the high-resolution beam transport. The specifications and the schematic figure of DCF31 are shown in Table 1 and Fig. 1, respectively.

Among the developed LP-MWDCs, DCF31 has the smallest cell size of 5×4.8 mm^2, and therefore it can work at a relatively high rate. This feature is favorable for the use at F3, where the beam spot size is a few millimeter.

Table 1. Specifications of DCF31.

Number of planes	8 (X_1X_1'Y_1Y_1'X_2X_2'Y_2Y_2')
Number of cells	16 cells/plane
Cell size	5 mm^w $\times$ 4.8 mm^t
Sensitive Area	80 mm $\times$ 80 mm
Anode wire	Au-W 12.5 μm
Potential wire	Cu-W 75 μm
Cathode foil	Al-PET 2 μm
Operation Gas	pure isobutane
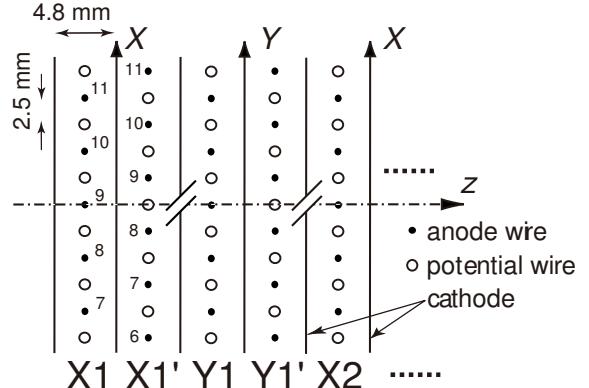
Figure 1. The schematic view of DCF31.

2. Experiment

The experiment was carried out at the E7 experimental hall in RIBF. The α beam was accelerated up to 8.8 MeV/nucleon by the AVF Cyclotron and was transported to the E7B course. The α beam at 8.8 MeV/nucleon gives the same energy loss in DCF31 as the ^{12}N beam at 250 MeV/nucleon, which is a major candidate for the RI beam used in SHARAQ experiments. The transported α beam was defocused around DCF31 so that the beam covered a large part of the sensitive area. The signals from anode wires were amplified and discriminated by the REPIC RPA-131 cards. Since the typical noise level was about 5 mV, the threshold of RPA-131 was set to 10 mV throughout the measurement. The timing information was digitized by the CAEN V1190A multi-hit TDC. The plastic scintillator with a thickness of 0.1 mm was installed about 60-cm upstream of DCF31. The signals from the photo multiplier tubes triggered the data acquisition system.

It is often problematic that the number of noise events, for instance such as δ-ray events, increases as the applied high voltage (HV) becomes higher. In our measurement, these events were successfully separated by gating on the pulse width of the anode signal. The pulse width was obtained as $t_{\text{trail}} - t_{\text{lead}}$, where t_{lead} and t_{trail} are the timing for the leading and trailing edges acquired by V1190A. Since noise events have small pulse widths, they are clearly separated from true signals as shown in Fig. 2. The events in the red colored region was used in the analysis.
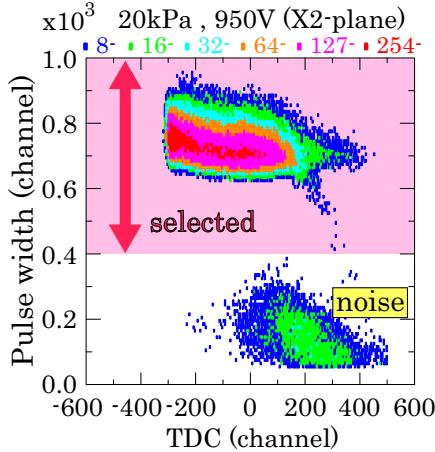
Figure 2. Event selection by gating on pulse widths. Noise events are clearly separated from true signals.

3. Result

The obtained TDC spectrum is shown in Fig. 3. The width of the spectrum, corresponding to the drift time in a half-cell size, was about 40 nsec. This is consistent with the simulated value of 43 nsec by the program Garfield [4].

Figure 4 shows the efficiency curve obtained at gas pressures of 5 kPa, 10 kPa and 20 kPa. The efficiency was estimated by $Y_{X2}/Y_{trigger}$, where Y_{X2} is the number of yields for X2 plane and $Y_{trigger}$ is the number of triggered events. At 5 kPa, the applied HV tripped before the efficiency reaches 100%. On the other hand, at 10 kPa and 20 kPa, it reaches about 100% with the applied HV above 800 V and 900 V, respectively. Therefore the requirements (2) and (3) are sufficiently met.

The position resolution for each anode plane is estimated by the variance (residue) of the ray fitting. The overall position resolution for DCF31 is given by the half of it. The obtained resolution is shown in Fig. 5. The requirement (1) is satisfied above 8 kPa.
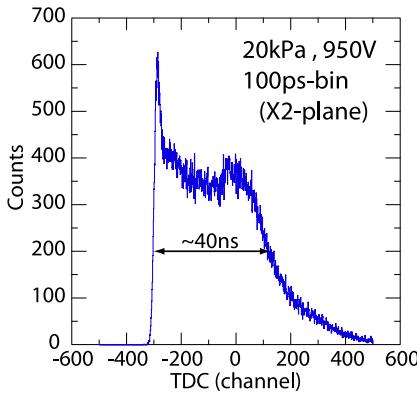
Figure 3. Typical TDC spectrum obtained at 20 kPa and 950 V.
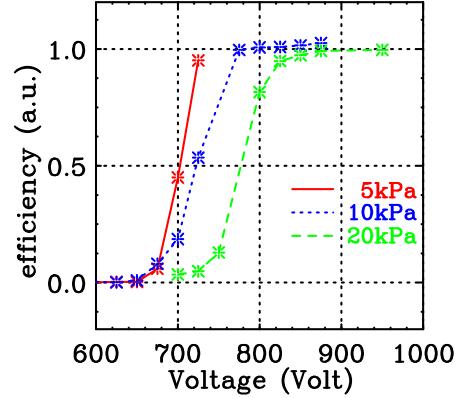
Figure 4. Efficiency curve at 5 kPa, 10 kPa and 20 kPa. The efficiency is sufficiently high above 800 V (900 V) at 10 kPa (20 kPa), respectively.
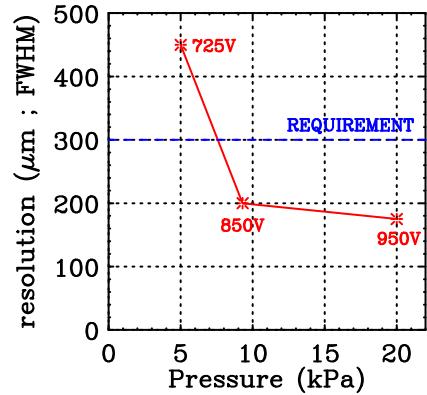
Figure 5. Position resolution obtained for each of gas pressures. The requirement is satisfied above 8 kPa.

In summary, it was confirmed that the performance of DCF31 is satisfactory as a BLD at F3. DCF31 will be operated at a gas pressure of 10 kPa in the SHARAQ commissioning and in the subsequent experiments.

References

[1] A. Saito *et al.*, RIKEN Accel. Prog. Rep. **40** (2007) 157.
[2] T. Uesaka *et al.*, Nucl. Inst. Meth. **B266** (2008) 4218.
[3] A. Saito *et al.*, in this report.
[4] R. Veenhof, program GARFIELD - simulation of gaseous detectors - http://garfield.web.cern.ch/garfield/.

Delay-line readout of Low-Pressure Multi-Wire Drift Chamber

T. Yoshida, S. Shimoura[a], A. Saito[a], K. Miki[b], H. Miya[a], S. Ota[a], H. Tokieda[a], K. Nakanishi[a],
Y. Sasamoto[a], S. Noji[b], H. Kurei[a], S. Michimasa[a], H. Kawabata[c], H. Sakai[b],

Department of Earth and Planetary Science, University of Tokyo
[a]Center for Nuclear Study, Graduate School of Science, University of Tokyo
[b]Department of Physics, University of Tokyo
[c]Department of Physics, Kyoto University

1. Intoroduction

We have been developing beamline detectors that used at the high resolution beamline for SHARAQ spectrometer in RI Beam Factory (RIBF). There are several requirements to be fulfilled for these detectors. Detection efficiency should be high even for light RI beams such as ^{12}N at 200 A MeV. The position resolution is required to be less than 300 μm at FWHM. The maximum counting rate should be 1 MHz for the dispersive beam transport. In order to realize the performance described above, we have developed Low-Pressure Multi-Wire Drift Chambers (LP-MWDCs).

We have developed LP-MWDC with stripped cathodes and delay-line readouts. Signals are obtained both from anode wires and segmented cathode strips. The cathode signals are read out with delay-line, as schematically shown in Fig. 1. LP-MWDC operated at the low pressure of less than 20 kPa to reduce the effect of the multiple scattering.

In December 2008, we performed a test experiment to study performances of the LP-MWDCs for an αbeam at 8.8 A MeV.

2. Structure of LP-MWDC

There are three LP-MWDC (MWDC2, 3 and 4) in this study. The active area of MWDC2 is 144 144 mm^2. That of MWDC3, 4 is 216 144 mm^2. The diameter of the sense wire is 12.5 μm, and that of the field wire is 75 μm. That of the cathode film is 1.5 μm for all the chambers. The cathode film is made of PET with aluminum evaporated on to both sides. MWDC2 has the channel of 16ch (X, Y) , and 22ch (U) . MWDC2, 3 have the channel of 24ch (X),16ch (Y) and 22ch (U) . Strip width of MWDC2 is 2.55 mm (X,Y) . Strip width of MWDC3, 4 is 2.55 mm (X) and 2.58 mm (Y). The striped cathode (CX, CY) are connected to delay-lines.

3. Delay-line readout

It is necessary to delay the signal in order to measure the signal from striped cathode by using TDC. Delay-line is the signal transmission line that consists of the coil and the capacitor to delay the signal as shown Fig. 1. Delay time (T) for each unit length of delay-line is evaluated as follows:

$$T = \sqrt{LC}, \tag{1}$$

where L and C are the values for each unit length. The position information is obtained by measuring the difference of the time of the signal that comes out from delay-line's both ends. The delay time for each unit length of these LP-MWDC is 0.8 ns/mm.
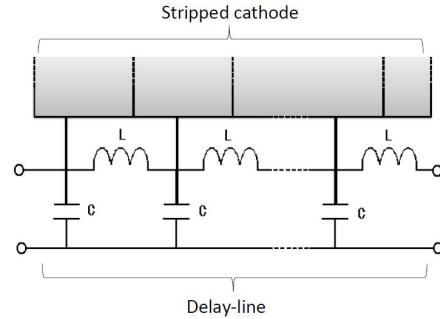
Figure 1. A schematic view of the LP-MWDC's delay-line.

4. Experiment

The LP-MWDCs were installed in the E7B beam line. Figure 2 shows a schematic view of the experimental setup.
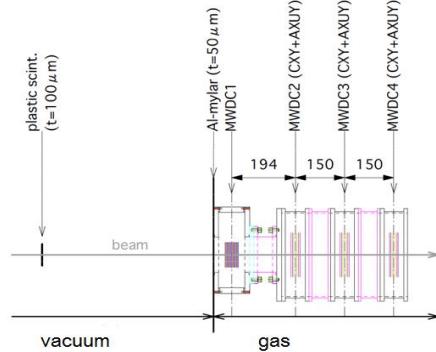
Figure 2. A schematic view of the experimental setup. LP-MWDCs that we report in this study are MWDC2, 3, and 4.

The distance between LP-MWDC2 and LP-MWDC3 is 150 mm. The LP-MWDCs were operated using an isobutane gas at 5, 10, and 20 kPa. An α beam at 8.8 MeV was provided from the AVF cyclotron accelerator. The energy deposition of the α beam in the LP-MWDCs is comparable to that of a ^{12}N ion at 200 A MeV, which will be used in the first experiment at SHARAQ.

5. Analysis and Result

Figure 4 shows coordinate plane that we thought in order to analyze. A vertical axis is the position, and a horizontal axis is distance from MWDC2. Both unit is mm. X_1, X_2, and X_3 is position of MWDC2,3 and 4.

X_1, X_2, and X_3 assumed to have equal resolution (δX). The resdual between X_2 actually obtained from test experiments and that obtained from the mean value of X_1 and X_3
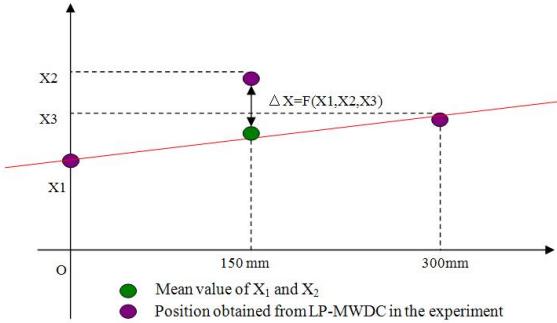
Figure 3. Coordinate plane that we thought in order to analyze. A horizontal axis is a distance from MWDC2. A vertical axis is a position obtained from each LP-MWDC. Both units are mm.
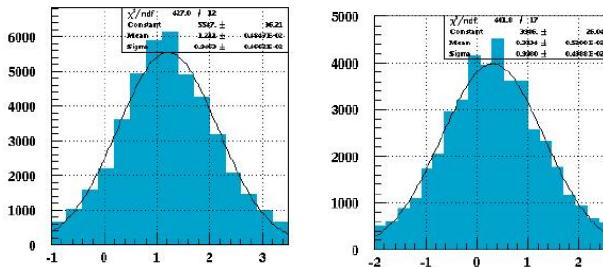
Figure 4. Histogram of ΔX. The unit of a horizontal axis is mm, a vertical axis is a number of counts.

Figure 5. Histogram of ΔY. The unit of a horizontal axis is mm, a vertical axis is a number of counts.

is assumed to be ΔX. ΔX is a function of X_1, X_2, and X_3. It is assumed ΔX=F(X_1,X_2,X_3), F is analytically determined from Fig. 3. F is evaluated as follows:
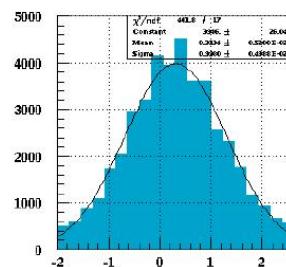
$$F = \frac{1}{2}X_1 - X_2 + \frac{1}{2}X_3, \qquad (2)$$

When the measurement frequency of ΔX increase, the histogram of ΔX is Gaussian distribution shown as Fig. 4,5.

The standard deviation of the Gaussian distribution is σ. By using the expression of a general error margin spread, the relation between resolution and standard deviation is evaluated as follows:

$$\{(\frac{\partial F}{\partial X1})^2 + (\frac{\partial F}{\partial X2})^2 + (\frac{\partial F}{\partial X3})^2\}, \delta X^2 = \sigma^2 \qquad (3)$$

When the resolution of Y is obtained, it only has to change X into Y. The resolution of X and Y is 1.40 mm and 1.56 mm at FWHM.

6. Summary

We performed a test experiment for the LP-MWDCs with stripped cathodes and delay-line readouts to study the performance using the α beam at 8.8 A MeV. We obtained position resolution of LP-MWDC's delay-line readout. Consequently, the position resolution of X and Y is 1.40 mm and 1.56 mm.

References

[1] A. Saito *et al.*, CNS Ann. Rep. 2008 (2010).
[2] H. Miya *et al.*, CNS Ann. Rep. 2008 (2010).
[3] T. Kawabata *et al.*, CNS Ann. Rep. 2006 (2007).
[4] H. Kumagai *et al.*, Instrum. and Meth. in Phys. Res. A **470** (2001) 562
[5] U. Lynen *et al.*, Instrum. and Meth. in Phys. Res. **162** (1979) 657

Focal-Plane Detector of SHARAQ Spectrometer

S. Michimasa, H. Tokieda, S. Noji[a], S. Ota, S. Shimoura, T. Uesaka, H. Sakai[a],
P. Roussel-Chomaz[b], J-F. Libin[b], P. Gangnant[b], and C. Spitaels[b]

Center for Nuclear Study, Graduate School of Science, University of Tokyo
[a]Department of Physics, University of Tokyo
[b]GANIL, France

The SHARAQ spectrometer [1] and the high-resolution beam line [2] have been constructed in the RI Beam Factory (RIBF) at RIKEN. In March, 2009, we performed the first beam study to examine dispersion-matching ion optics and to evaluate performances of detectors installed in the beam line and the spectrometer. Valuable information has been obtained on the basic performances of the high-resolution spectrometer system. This report describes basic performances of detectors installed at the dispersive focal plane of SHARAQ.

Figure 1 shows the detector setup used in the beam study. Two tracking detectors and two plastic scintillators were installed in the final focal plane of the SHARAQ spectrometer. The focal plane is located 3.04-m downstream from
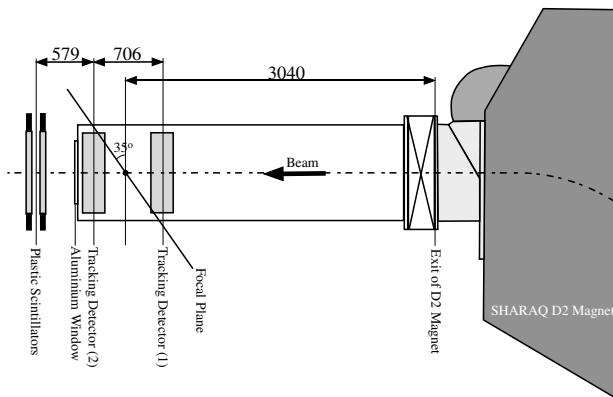
Figure 1. Detector setup for the dispersive focal plane of SHARAQ. Two tracking detectors and two plastic scintillators were installed in the first beam study.

the exit of the SHARAQ D2 magnet and inclined at 35 degrees relative to the central orbit. Beam passed through the tracking detectors installed in vacuum, and went out to the air through a 10 mm-thick aluminum window. The plastic scintillators were placed downstream of the aluminum window.

The plastic scintillators were used to measure the timings passing through the focal plane, and to measure energy deposits in them. The two-layer configuration of scintillators is efficient for rejecting cosmic-ray events. Each scintillator is read out by two photomultiplier tubes attached on both sides. The size of the plastic scintillator is $1110 \, (\text{H}) \times 300 \, (\text{V}) \times 5 \, (\text{T}) \, \text{mm}^3$. Charge and timing data of the scintillators were obtained by utilizing the charge-to-time conversion (QTC) technique and multi-hit TDC modules [3]. We could identify the atomic numbers of ^{12}N and ^{11}C particles with better than 5 σ separation.

Tracks of beam particles were measured by the tracking detectors, which are cathode-readout drift chambers

(CRDCs) [4]. The CRDCs have manufactured in the fiscal year of 2008 by collaboration with an experimental group of GANIL. Detailed structure of the CRDC is described in Ref. [5]. The CRDCs operated with isobutane gas at 15 or 30 torr in this study, because we detected various light particles at around 200A–250A MeV such as t, ^{6}He, ^{9}Li, ^{12}B, and ^{12,14}N.

The CRDC has 2 signals from the anode wires and 2 multiplexed signals from the cathode pads. The Anode signals were utilized to deduce drift time and charge amount of secondary electrons in the CRDC. Preamplifiers for anode signals were charge sensitive type and were set to be gain of 0.9 V/pC and time constant of 20 μs. Since the anode signal is generated when avalanche occurs around anode wires, the drift time are determined by difference between an anode timing signal and a timing signal of the plastic scintillator. We operated CRDCs with drift electric fields of 83.3 V/cm with 15-torr isobutane and 140 V/cm with 30-torr isobutane, respectively. The drift velocities of secondary electrons were 5.9 cm/μs at 15 torr and 5.3 cm/μs at 30 torr. These values are close to the ones evaluated by using the GARFIELD code [6]. Since vertical hit positions of CRDC is linearly related to the drift time, the time resolution of drift time determines the resolution of vertical position. In the present status, the vertical position resolution were approximately 1 mm FWHM and it is twice worse than the designed value. We are continuing data analysis to pin down the origin of such a bad resolution.

Figure 2 (a) shows avalanche gain measured at 30 torr of CRDCs as a function of voltage supplied to the anode wires. CRDC1 (CRDC2) indicates the upstream (down-
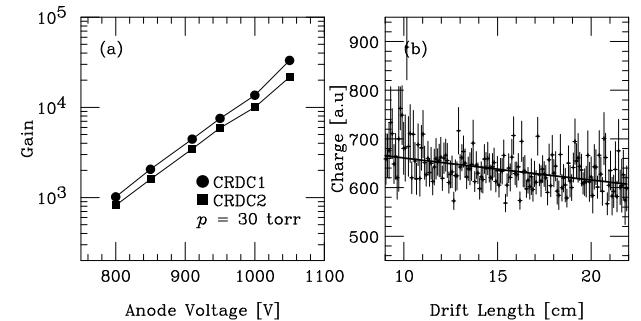
Figure 2. (a) Avalanche gain of CRDCs measured at 30 torr. The definitions of CRDC1 and CRDC2 are described in the text. (b) The correlation between charge amount of anode signal and drift length of secondary electron.

stream) tracking chamber. CRDC1 has potential wires lo-

cated between anode wires, and CRDC2 has no potential wires. (*See* Fig.2 in Ref. [5].) The difference of configurations is considered to cause difference of avalanche gains. However, we demonstrated that the both types of CRDCs achieve higher avalanche gain than the required gain of 10^4.

Figure 2 (b) shows a correlation between drift length of secondary electrons and charge amount obtained from anode wires. The data were obtained in 30-torr operation by 250A-MeV ^{14}N beam. The typical beam rate was 500 counts/sec. The flow rate of the counter gas was set to be 190 cc/min, and the counter gas in the detectors was replaced every 10 hours. This indicates that an amount of secondary electrons decreases during drift. The line in the figure was obtained by a linear fitting of the data. Based on the gradient of the line, 30% of secondary electrons is estimated to be lost by 30-cm electron drift. We can obtain clear signals from all the effective area of CRDC by control of its avalanche gain, though this effect is not so small.

The horizontal hit position is determined by a charge distribution induced on the cathode pads. The charge signals from the cathode pads were read out by using GASSIPLEX chips [7], developed at CERN for multiplexed readouts of pad chambers. The GASSIPLEX is mounted close to cathode pads inside the detector. With its capability of high multiplexing, the charge signals from 256 cathode pads can be transmitted through a single signal line and read out with a CAEN sequencer with a CRAM module [8]. The variation of pedestals in a GASSIPLEX chip is of 60–70 mV and the pedestals were not changed during the beam study (< 2 mV). In this study, the track-and-hold signals for GAS-SIPLEX chips were generated by the timing of anode signal of the CRDC under the condition that 2 plastic scintillators and the anode were coincident. Figure 3 (a) shows a charge distribution and an empirical distribution curve [9] fitted to the data. The curve is expressed as

$$q(x) = a_1 \cdot \mathrm{sech}^2\left[\pi(x - a_2)/a_3\right],$$

where a_i ($i = 1,2,3$) are fitting parameters. Typical resolution of horizontal position was estimated to be 500 μm FWHM in the case of 250A-MeV ^{14}N beam.

Figure 3 (b) shows the number of cathode pads from which induced charge signals were generated as the function of charge amount obtained by anode wires. The relation seems to be reproduced by a power function. When we operate CRDCs in the middle of the dynamic range of GAS-SIPLEX, induced charge is distributed in approximately 10 cathode pads. The data show that we are able to control the number of cathode signals by changing the voltage of anode wires. We continue to investigate the relation between the position resolution and the number of pad signals because this number is considered to be strongly coupled to achievable position resolution.

In the summary, we performed the first beam study using light radioactive isotopes at 200A–250A MeV and examined the detector system installed in the final focal-plane of the SHARAQ spectrometer. All the detectors operated successfully and we obtained basic data of their performance in order to optimize the detectors' parameters and to improve their data analysis algorithm. Further analysis is now in progress.

Figure 3. (a) Example of a charge distribution induced on the cathode pads. The curve shows the distribution curve obtained by fitting the data. The form of the distribution is described in the text. (b) The number of cathode pads where induced charge signals were generated as the function of charge amount obtained by anode wires.

References

[1] T. Uesaka *et al.*, Nucl. Instrum. Methods Phys. Res. B **266** (2008) 4218.

[2] T. Kawabata *et al.*, Nucl. Instrum. Methods Phys. Res. B **266** (2008) 4201.

[3] S. Ota *et al.*, described elsewhere in this report.

[4] M.H. Tanaka *et al.*, Nucl. Instrum. Methods Phys. Res. A **362** (1995) 521.

[5] S. Michimasa *et al.*, CNS-REP-80, (2009) 55.

[6] R. Veenhof, GARFIELD, CERN Program Library W5050.

[7] The GASSIPLEX is a re-designed chip of the AM-PLEX by J.C. -Santiard of CERN. The AMPLEX is described in E. Beuville *et al.*, Nucl. Instrum. Methods Phys. Res. A **288** (1990) 157.

[8] V551 C.A.E.N sequencer User Guide, V550 C.A.E.N CRAM User Guide.

[9] K. Lau and J. Pyrlik, Nucl. Instrum. Methods Phys. Res. A **366** (1995) 298.

Parallel Acquisition and Control Intelligent system for Femto-frontIer Collaboration (PACIFIC)

S. Ota, S. Shimoura, H. Baba[a], E. Ideguchi, M. Kurokawa[a], A. Saito[b], H. Tokieda, and T. Otsuka

Center for Nuclear Study, Graduate School of Science, University of Tokyo
[a]RIKEN Nishina Center for Accelerator-Based Schience
[b]Department of Physics, University of Tokyo

1. Introduction

Recent nuclear experiments to study the structures and properties of unstable nuclei become of large scale at the viewpoint of the number of detectors, of the reaction rate, and also of the geometry. A large amount of signals from each detector and the digitized data should be processed and recorded, respectively, with the smallest dead time. The data acquisition software named BABIRL [1] has been developed aiming at making the dead time of the data collection smaller. The signal processing, however, has not been optimized because of the significant dead time in analog-to-digital conversion. We developed, to resolve this problem, a new data-processing system called "Parallel Acquisition and Control Intelligent system for Femto-frontIer Collaboration (PACIFIC)" involving a couple of new modules. The PACIFIC consists of two categories, high-speed signal processing and parallel data acquisition. The former category has two components for charged particle detectors and γ-ray detectors. The latter category includes a event building. Three main parts are

1. Analog signal processing for fast signals (QTM),

2. Digital signal processing for slow signals (APU7110-P),

3. Asynchronous control and data collection (e-RT3) for monitoring the state of the experimental setup.

In this article, we report the concept and components of each part.

2. QTM module –analog signal processing for fast signals–

The QTM module is essentially a charge integrator, but it convert the amount of charge to the pulse width, it namely is a charge-to-time converter (QTC). The timing of the signal is picked off by leading-edge discrimination. This module is suitable for the fast signals, which have the rise-time of 5 to around 20 ns, such as plastic scintillators, cathode readout of Low Pressure Multi-Wire Drift Chamber (LPMWDC) and Parallel Plate Avalanche Counters (PPACs). Typical conversion time, *i.e.* dead time, is as short as 1 us, which enables us to perform fast signal processing in combination with the multi-event non-stop TDC module such as V1190/1290 module (CAEN).

The QTM module is a one-span NIM module involving six preamplifiers[2], and two QTC-chips, and a register controller. The QTC-chip has been made by IWATSU Test Instruments Corporation. This chip itself accepts the charge

up to around 50 pC and contains 3×3 QTCs. The input signal is divided into three same signals and two signals are attenuated by 1/7 and 1/49. Then the dynamic range of input charge is effectively enlarged up to about 2.5 nC. The QTM module have 6 inputs with 50 Ω termination and 18 LVDS outputs grouped into three categories by the dynamic range. The charge and time resolution is designed to be typically 1% and 0.1 ns, while they depends on the input charge.

Figure 1 shows the demonstration of the performance for light unstable beam particles such as ^{3}He, ^{6}He, and ^{9}Li in the SHARAQ commissioning run. The output pulse of QTM module was digitized by V1190 module. The horizontal and vertical axes show the time-of-flight from F3 to FH10 at SHARAQ beam line in RIBF and energy deposition in the plastic scintillator at the end of beam line. The beam particles are well discriminated from each other.

The further analysis to deduce the timing and energy resolution is in progress.
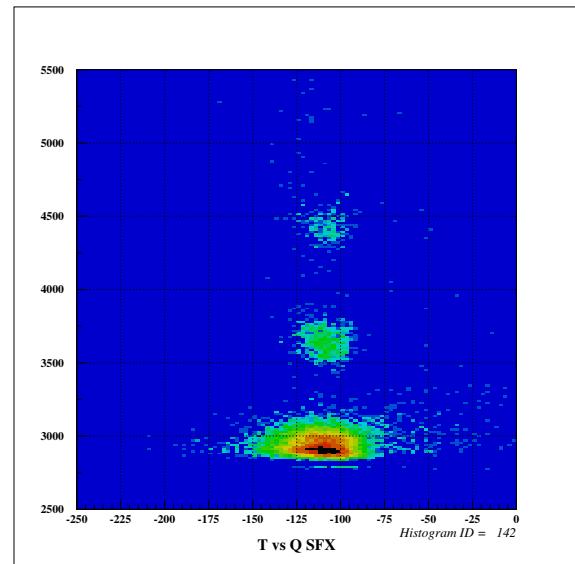
Figure 1. Particle identification of light neutron rich nuclei such as ^{3}H, ^{6}He, ^{9}Li. The vertical and horizontal axes are time-of-flight and energy deposition.

3. APU7110-P –digital signal processing for slow signals–

The APU7110-P modules has been developed for a γ-ray detector array GRAPE to extract the energy, timing and position of incident γ rays continuously. The pre-amplified

---

[2]The preamplifier is optional and can be bi-passed.

2×9 signals from a nine-fold segmented germanium detector are digitized in pipeline process by flash ADC (FADC). In addition, the digital signals are numerically processed by using FPGA to deduce the energy and timing by applying the trapezoidal shaping and constant-fraction discrimination method, respectively.

To extract three-dimensional position of incident γ rays, we are developing a new algorithm which is suitable for the pipeline processing.

4. Asynchronous monitoring and control of experimental devices

In order to perform the experiment safely and expeditiously, the parameters of each device, for example, the gas pressure and flow and the supplied high voltage of tracking detectors, the pressure in vacuum chambers, and the current of each magnet should be monitored and controlled during the experiment. Those values are also important to achieve better resolutions by correcting the effect due to the temporal change of the parameters in offline analysis. The devices are monitored and controlled by using Programmable Logic Controllers (PLC) for the beam-line detectors and Network IO controller (NIO) for the magnets.

Although general PLC are programed in the very specific and difficult language on sequence CPU, newly developed PLC module F3RP61 (Yokogawa Electric Corporation), which are available from since the summer in 2008, enable us to program in more familiar language, C, by using normal Linux operating system on PowerPC. For the control software, Experimental Physics and Industrial Control System (EPICS) is chosen because the EPICS is widely used and in the field of accelerator operation and is free software well developed in Argonne National Laboratory. The operating system and EPICS I/O controller are loaded from the main server via network boot protocol and the management of them is unified.

The NIO is a VME module produced by Hitachi Zohsen Corporation to control the power supplier of the magnets. We are developed a drivers and software in Linux system to drive NIO modules based on the software in VxWorks on PowerPC. The magnet control system consists of the VME CPU board, NIO-C, NIO-B and NIO-S. The operating system and control programs are loaded from the main server as well as those of PLC modules. The NIO-S board controls and monitors each power supply of a magnet directly and the NIO-C board controls all the NIO-B board sequentially via the NIO-B hub board.

The collected data of devices will be merged asynchronously into the physics data via BABIRL protocol to be used for the analysis and also stored in a database as one example of the experimental setup for the reference in the future experiments.

These developments are in progress.

References

[1] H. Baba *et al.*, to be submitted to Nucl. Instr. and Methods A

Measurement of basic performance of millimeter-scale Thick GEM

R. Akimoto, H. Hamagaki, T. Gunji and Y.L. Yamaguchi

Center for Nuclear Study, Graduate School of Science, University of Tokyo

1. Introduction

GEM is a micro pattern gaseous detector, made of a thin insulator film (a typical thickness is 50 μm), with metal electrode plates on both sides, and pieced holes (a typically 70 μm in diameter) in closely-packed array [1]. The GEM with such micro-scale is denoted as 'standard GEM' in this report. With voltage difference of several hundred volts applied between the both sides of the GEM film, electron multiplication occurs inside the holes.

GEM has many advantages; for example no degradation of performance is observed in high rate [2]. GEM has been applied to many detectors not only for physics [3], but also for medical research and nondestructive testing [4]. On the other hands, the standard GEM has some disadvantages; fragility against discharges and difficulty in obtaining enough gain at low pressure.

GEM with millimeter scale has been developed recently to overcome the disadvantages of the standard GEM [5]. It is called as Thick-GEM (TGEM). Since the electron density inside the holes becomes more rarefied due to the larger holes, discharge probability becomes small. Furthermore, TGEM with high resistive electrodes has also been developed. It is called as Resistive Electrode TGEM (RETGEM), originally developed at CERN [6]. Owing to the high resistivity, the voltage difference in the hole region is automatically reduced when large current is drawn due to discharges. Thus, discharges could be efficiently suppressed.

TGEM and RETGEM look very promising, but their basic properties have not yet been studied thoroughly. In the present report, TGEM and RETGEM with different geometries were made, and the basic properties such as the voltage dependence of gain, gain stability and energy resolution were investigated.

2. Geometrical configurations of TGEM and RETGEM

Figure 1 shows the plane view of TGEM. TGEM consists of a glass epoxy with 18 μm-thick copper electrodes. Two configurations were tried for hole geometry; with and without rim. Purpose of having rim of 75μm around a hole, as shown in Fig.1 (right), is to reduce frequency of discharge by suppressing the concentration of field flux on hole edges.

TGEMs with five different geometrical configurations and RETGEM were made (see Table 1). The resistance of electrode of RETGEM is about 100 kΩ/cm.

	TGEM					RETGEM
	#1	#2	#3	#4	#5	
Thickness (mm)	0.5				1.0	
Diameter of insulator (mm)	0.3	0.5	0.3	0.5	0.45	0.3
Rim	With					Without
Pitch of holes	Twice of the hole diameter of electrodes					

Table 1. The geometrical configurations of TGEM and RETGEM.
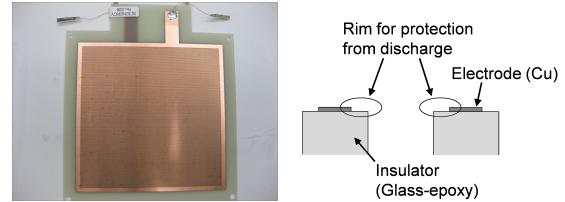
Figure 1. Left: The plane view of TGEM. Right: The cross sectional figure of TGEM.

3. Setup

Figure 2 shows the schematic view of the test setup. ^{55}Fe (X-ray: 5.9 keV) was used. The measurements were done with GEM in a single element. Distances between cathode mesh and GEM and between GEM and anode pad were 20 mm and 1.5 mm, respectively. The voltage supplied between cathode mesh and GEM, and between GEM and anode pad were 400 V. A signal was read from the pads with active region of 10×10 mm^2. Ar(90%) + CH$_4$(10%) gas mixture (P10) was used and gas flow was kept to be 300 cc/min. Measurements have been done at atmospheric pressure and at room temperature ($\sim$300 K).
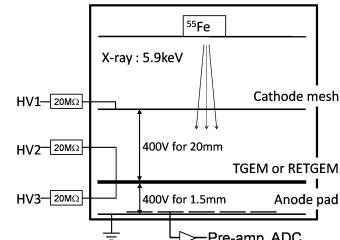
Figure 2. Setup of the measurements

4. Result

In the case of the TGEMs other than TGEM#3, a continuous discharge occurred before obtaining enough gain to separate the signal from the background. Thus, following measurements were done for only TGEM#3 and RETGEM.

4.1. Energy resolution

Figure 3 shows the charge distribution of TGEM#3 and RETGEM at gain of $\sim$2000. The higher peak corresponds to 5.9 keV and the escape peak (2.7 keV) was clearly seen in both cases. The energy resolution is shown in RMS of the Gaussian which is fitted to the higher peak. The energy resolution of TGEM#3 is about 16 %. It is significantly worse than that of the standard GEMs ($\sim$9 %) [7]. The energy resolution of RETGEM is about 9 %, comparable to that of the standard GEMs.

The difference of the energy resolution might be caused by discharges since discharges occur more frequently during the measurement for TGEM than RETGEM.
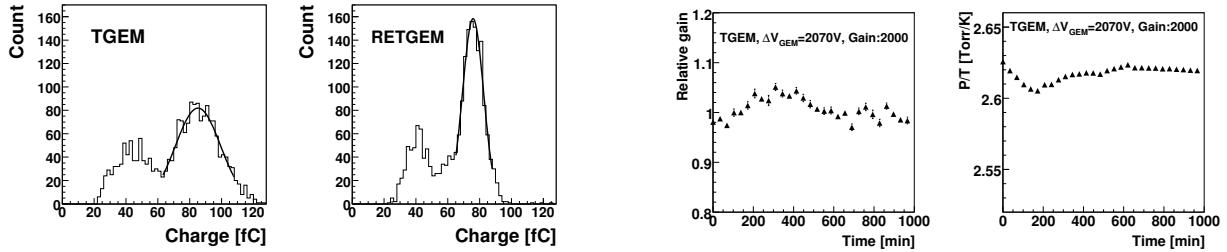
Figure 3. The charge distribution for TGEM and RETGEM.

4.2. Voltage dependence of gain

Figure 4 shows the voltage dependence of gain for TGEM#3 and RETGEM. The voltage supplied to GEM is called as ΔV_{GEM} in this report. A continuous discharge starts at ΔV_{GEM} = 2220 V (TGEM) and at ΔV_{GEM} = 1920 V (RETGEM) and the measurements could not be conducted further. The gain of TGEM#3 was obtained nearly 10^4, and that of RETGEM was obtained over 10^4.
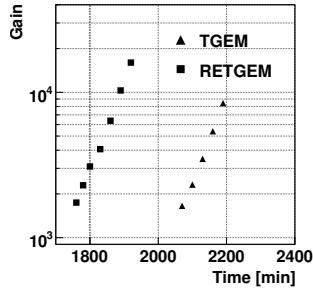
Figure 4. The voltage dependence of the gas gain.

4.3. Gain stability

The left figures in Figure 5 show the gain variation as a function of time of TGEM#3 and RETGEM. The top-left and middle-left shows the data of TGEM#3 with ΔV_{GEM} = 2070 V and 2150 V, which correspond to the gain $\simeq$ 2000 and 5000, respectively. Bottom-left shows the data of RETGEM with ΔV_{GEM} = 1780 V, which corresponds to the gain $\simeq$ 2000. The right figures show the time variation of pressure divided by temperature (P/T) during the corresponding time interval of the gain measurements.

The gain of GEM changes with the pressure(P) or the temperature(T) and the variation can be corrected by P/T in a narrow P/T region [7]. In both cases of TGEM, correlation between the gain and P/T was not seen clearly. Especially, more enormous gain variation was seen for the data with gain $\simeq$ 5000 than with gain $\simeq$ 2000. On the other hands, there seemed to be correlation between the gain and P/T for the data of RETGEM after 100 minutes.

Taken into consideration that the gain variation of TGEM becomes more enormously as the gain increases and that there seems to be the correlation for the data of RETGEM, the instability of the gain also might be explained by discharges. To ensure the gain stability of RETGEM, the gain variation as a function of time for longer time is needed. Furthermore, it is interesting to measure the gain stability of RETGEM with higher gain.
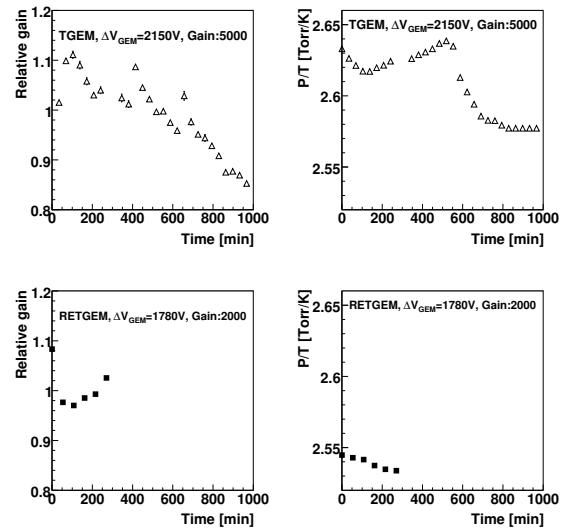
Figure 5. Left: Gain variation as a function of time of TGEM with ΔV_{GEM}=2070 V and 2150 V, and RETGEM with ΔV_{GEM}=1780 V. Right: P/T value during the measurement.

5. Summary and Outlook

TGEM with different geometries and RETGEM, which has high resistive electrode are made, and basic properties of them are investigated.

For all TGEMs but the TGEM#3, measurements could not be conducted due to discharges. The performance of RETGEM seems to be better than that of TGEM. Since the gain stability is a critical for stable operation, the gain stability of RETGEM for longer time and with high gain are our future task.

References

[1] F. Sauli, Nucl. Instr. and Meth. A **386** (1997) 531.

[2] M. Titov, Nucl. Instr. and Meth. A **581** (2007) 25.

[3] Z. Fraenkel, *et al.*, Nucl. Instr. and Meth. A **546** (2005) 1466.

[4] S. Bachmann, *et al.*, Nucl. Instr. and Meth. A **478** (2002) 104.

[5] L. Periale *et al.*, Nucl. Instr. and Meth. A **478** (2002) 377

[6] R. Oliveira *et al.*, Nucl. Instr. and Meth. A **576** (2007) 362

[7] Y.L. Yamaguchi, Master Thesis (2007).

Development of a Readout system for 2D-imaging using GEM

Y. Hori, H. Hamagaki, T. Gunji, S. Sano, Y. Tanaka[a] and T. Fusayasu[a]

Center for Nuclear Study, Graduate School of Science, University of Tokyo
[a]Graduate School of Technologies, Nagasaki Institute of Applied Science

1. Introduction

Gas Electron Multipulier (GEM) is one of the mirco pattern gas detectors, which is a metal-coated polymer foil with circular holes placed periodically [1]. The metal layers at both sides work as electrodes and a few hundred volts is applied between them. The thickness of GEM foil is typically $50\sim150\ \mu$m. When a drift electron passes through the holes, strong electric field inside the hole induces a cascade of electron multiplication.

GEM is suited for two-dimensional imaging applications because of its capability of flexible readout arrangement. Soft X-rays are converted to electrons by a reaction with Ar gas and can be effectively detected. An imaging of thermal neutrons is also possible by utilizing Boron-coated GEMs. Thermal neutrons can be efficiently detected through the reaction with Boron involving the emission of $\alpha-$rays.

We have been developing a 2D-imaging equipment using GEM. Readout system for 2D-imaging is developed and the progress is reported in this article.

2. Design

Figure 1 shows a schematic view of X-ray 2D-imaging prototype system. The drift length (between cathode and top of GEM layer) is about 1 cm and the gas chamber is filled with $ArCO_2$ at the atmospheric pressure. A size of GEM foil is 10 cm $\times$ 10 cm. To detect X-rays event by event, a gain of GEM

must be larger than 10^4 and this can be realized with triple $50\ \mu$m-GEMs or double $100\sim150\ \mu$m-GEM. In the case of the integrate type of the imaging instead of event by event detection, a single $50\ \mu$m-GEM is enough for electron multiplication.

Figure 2 shows the pixel board, where 16×16 pixels with square size of 2 mm $\times$ 2 mm are prepared for signal readout. On the back of the pixel board, 4 LSI chips and 4 ADC chips are mounted as shown in Fig. 3. Description of the LSI chip and the ADC chip will be provided in the following section.

Figure 2. 16×16 pixels in the center of the pixel board.
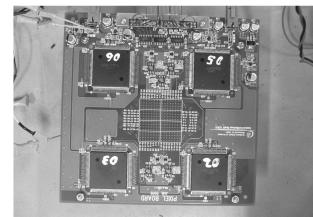
Figure 3. A back side of the pixel board with 4 LSIs.

2.1. LSI and pixel board

The LSI chip was designed and fabricated with 0.25 μm CMOS technology. The LSI has 64 channel integrators and multiplexers as shown in Fig. 4. The chip size is 5 mm $\times$ 2.5 mm. The designed specifications of the integrator are as follows; conversion gain is 1 V/pC, input range is 1 pC, slew rate is 50 V/μs, and Gain Band Width (GBW) is 30 MHz. The signals of 64 channel integrators are fed into the multiplexers and finally the serialized output goes to ADC. The charges induced on the pixels are integrated for at least 1 msec. A Correlated Double Sampling method is implemented, where an integrated signal is sampled first (pre-output) and a baseline is sampled after the discharge of the signal (post-output) for each channel.

Figure 1. A setup for X-ray 2D-imaging using GEM.
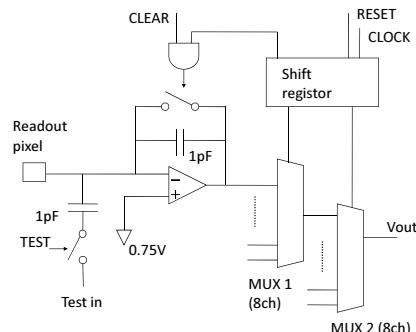
Figure 4. A schematic view of the LSI

A typical leak current is 0.1 pA, which is much smaller than that of typical FET input amplifiers ($\sim$1 pA). A noise level is less than 4 mV, which guarantees good S/N ratio (100/1) for the signal from GEM. The linearity is quite good and the difference in the conversion gain between channels

is less than 3% [2].

We choose 12 bits, 1 Msps (Mega Sampling Per Second), serial output ADC. This resolution is high and the noise level of the LSI is larger than 10 LSBs. The conversion process and data aquisition are controlled using two control signals, allowing the devices to interface with FPGA. A timing of the ADC sampling is synchronized with that of LSI sampling. Output rate of each ADCs is 2.5 Mbits/sec, which corresponds to the maximun imaging rate of 1 kfps (frame per second). An imaging above 1 kfps is possible, but the response of the LSI is nonlinear.

2.2. FPGA firmware

A Data AQuisition (DAQ) for the imaging is constructed using Feild Programmable Gate Array (FPGA). SiTCP is used in the front-end-system, which is FPGA-based firmware and enables to transfer data through 100 Mbps Ethernet using TCP/IP protocol. SiTCP has a possibility to construct DAQ easily compared to the convensional DAQ based on a bus architecture beacuse its interface is similar to FIFO and very simple.

There are two FPGAs (Xilinx Spartan-3A) on the SiTCP board, which is a product of BeeBeans Technologies. One is for the control of pixel board and the receipt of ADC output data from pixel board, the other is for the transfer of data to PC. The former is called USER-FPGA and the latter is called SiTCP. The USER-FPGA firmware has ten components as shown in Fig. 5; Finite state machine, Deserializer, Pre-post subtracter, Data-formatter, SiTCP-interface, PicoBlaze (micro processer), Programmable-ROM, RS232C-transmitter, RS232C-receiver and Control Signal Generator. The serial outputs of the four ADCs are deserialized at Deserializer and combined together with headers at Data-formatter. An online correction of the baseline shift is possible by Pre-post subtraction. PicoBlaze is a micro processer core based on 8-bit, RISC archtecture. Programming by its assembler language is possible. It is used for slow control. This processor receives commands through RS232C.

Utilization percentages of USER-FPGA components are listed in Table 1.
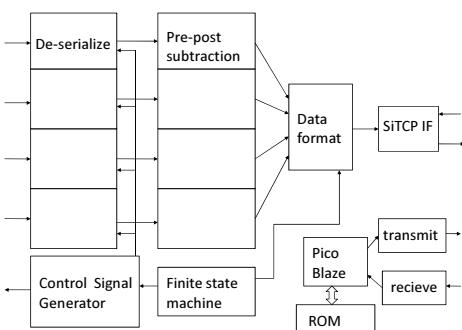
Figure 5. A schematic view of USER-FPGA firmware.

resource	Utilization
Occupied Slice	4%
Slice Flip Flop	3%
4 input LUTs	3%
bonbed IOBs	8%
BUFGMUXs	8%
RAMB16BWEs	5%

Table 1. Utilization percentages of USER-FPGA components.

3. Result of performance test

Basic perfomance was tested by taking pedestals. The Root Mean Square (RMS) of the pedestal data is lower than 30 channel even before pre-post subtraction. After pre-post subtraction, an offset of the pedestal data become lower than 3 channel and the RMS improves slightly. A uniformity over one LSI is quite good, but there are some differences among the chips. Figure 6 shows a linearity of the LSI.

Even though the readout seems to be working, there are a few problems to be solved. First, a connection realized using the flexible printed circuit between the pixel board and SiTCP board is unstable. Replacing the flexible printed circuit with conventional cable and connectors is planned. Second, ADC does not work properly for a while when voltage larger than the ADC dynamic range is input to ADC. It will be cured by adding diodes for over-voltage protection.
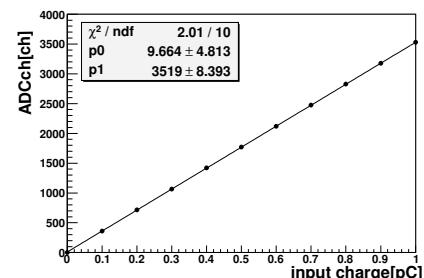
Figure 6. Linearity of the response of the LSI, which is tested with the fabricated DAQ.

4. Summary

We designed a 2D-imaging device using GEM and developed a prototype. SiTCP technique is chosen for the readout system. A basic performance of the readout electronics was investigated. This system seems to be working, but we found several issues such as cables and implementation of protection circuits in the pixel board to be fixed in the furture.

References

[1] F.Sauli, Nucl.Instr.and Meth. A **386** (1996) 531.

[2] S.Sano,Master Thesis(2008).

[3] T.Uchida and M.Tanaka, Development of TCP/IP processing hardware,IEEE NSS 2006 Conf.,pp1411-1414

Test of readout system of double-sided silicon-strip detector for decay spectroscopy

N. Uematsu, T. Sumikama, S. Nishimura[a], J. Chiba, T. Hashimoto[b], S. Hayakawa[b], C. Ishii,
S. Kubono[b], Y. Miyashita, Y. Shiraki, H. Watanabe[a], H. Yamaguchi[b], H. Yoshii and K. Yoshinaga

Department of Physics, Faculty of Science and Technology, Tokyo University of Science
[a] RIKEN Nishina Center
[b] Center for Nuclear Study, Graduate School of Science, University of Tokyo

Decay spectroscopy is a powerful tool to study nuclei far from stability line even with low production rate. Unstable nuclei with several hundreds MeV/nucleon provided by the in-flight fragment separator BigRIPS are stopped in an active stopper at the end of the beam line. β and γ rays emitted from stopped nuclei are detected using the double-sided silicon strip detectors (DSSDs) which serves as an active stopper as well, and Clover-type Ge detectors surrounding the stopper, respectively. The 2 dimensional position is obtained by the DSSD. The BigRIPS provides a cocktail beam, that is, the beam containing several nuclides, therefore the measurement of energy loss in DSSD at implantation process is needed for particle identification and capability of position correlation between an implanted nucleus and an emitted β ray is crucial to reduce contamination.

The energy loss in the DSSD ranges from 0 keV to several GeV, because the DSSD is used for the implantation of unstable nuclei and for the β ray detection. A new readout system of DSSD has been developed, which has a wide dynamic range from 20 keV to 4 GeV [1]. The signal is divided into two pre-amplifiers through two capacitors as shown in Fig. 3 of Ref. [1]. The two capacitors with different capacitance are used in order to change the charge-collection ratio. The capacitance was 33 pF for the high-gain part, and 10,000 pF for the low-gain part. The charge collection of the high-gain part was 250 times that of the low-gain part.

Here, we report the test of DSSD by using the unstable beam of ^{18}N at CNS Radio Isotope Beam separator (CRIB) [2]. ^{18}N ($T_{1/2} = 624$ ms) beam was produced through the reaction, ^{9}Be(^{18}O, ^{18}N)^{9}B. Target thickness was 2.62 mg/cm^2. The Mylar film with 10 μm thick was placed at F1 and was used as an energy degrader to purify the secondary beam. The purity of the ^{18}N beam was 14%. Main contaminant was ^{17}N ($T_{1/2} = 4.17$ s) and its fraction was 56%. The total production rate was restricted to less than 14 pps so as to measure the half life of ^{18}N. Three silicon detectors were placed at F2 of CRIB. First one is ΔE counter with 75 μm thick, second is the DSSD as a stopper with 1mm thick, and last is β counter with 1mm thick. The ^{18}N was implanted in the DSSD. The DSSD has a 16×16 strips and the size is 50×50×1 mm^3. The energy for implantation in DSSD was 50 MeV and the implantation depth was 43 μm. The implantation position was determined from a strip which had largest signal among strips.

The signal of junction side was divided to two pre-amplifiers, while the signal of ohmic side was connected to a single pre-pmplifier. The spectrum of the junction-side signal through the high-gain pre-amplifier is shown in Fig. 1. This spectrum was obtained by restricting the time of flight from RF signal of accelerator to PPAC at F2. Two distinct peaks were identified as ^{17}N and ^{17}O. The energy loss of ^{17}N and ^{17}O in the DSSD was 60.8 MeV and 43.7 MeV, respectively. The energy resolution was 11.9 % for ^{17}N and 16.1 % for ^{17}O in FWHM. The spectrum of the ohmic-side signal for one strip is shown in Fig. 2. The horizontal positions of ^{17}N and ^{17}O at F2 were different, thus only the ^{17}N was implanted in the strip shown in Fig. 2. The resolution was 12.2 % for ^{17}N. The resolution obtained from the single-preamplifier connected to the ohmic-side was comparable to that obtained from the high-gain preamplifier.
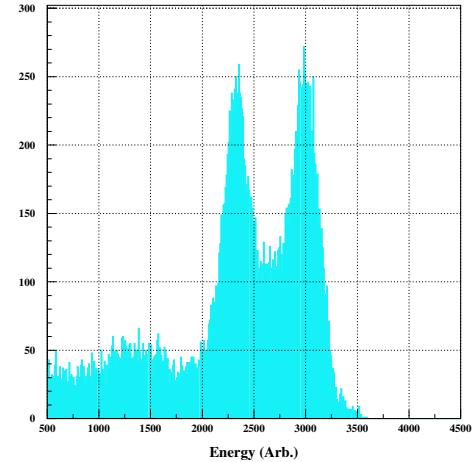
Figure 1. Energy loss of ^{17}N and ^{17}O in the DSSD. The spectrum was of the junction-side signal through the high-gain pre-amplifier.

The energy-loss spectrum of β ray in DSSD is shown in Fig. 3. The coincidence spectrum with the β counter is shown as the dashed line. The ^{18}N was implanted near the surface, therfore the β ray emitted to the direction of the surface was not detected. On the other hand, the β ray emitted to another surface was detected, because the passing length of beta-ray in DSSD was at least 1 mm, then the energy loss was larger than 300 keV. The energy loss of 300 keV around 400 ch and the noise less than 200 ch were clearly separated.

Other nuclei can be implanted before an implanted ^{18}N nucleus decays, because one nucleus was implanted per 70 ms on average while the half life is 624 ms. Therefore, position correlation between the implantation and the decay
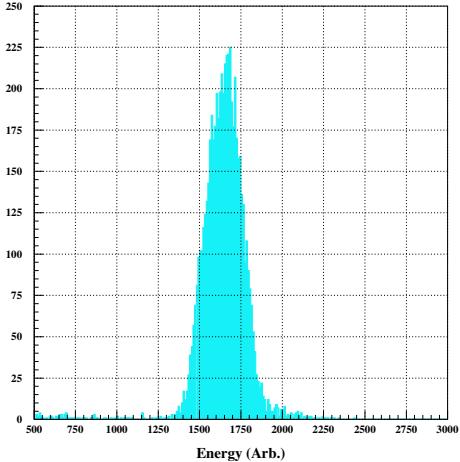
Figure 2. Energy loss of ^{17}N in the DSSD. The spectrum was of the ohmic-side signal. The ^{17}N was selected by the strip of DSSD, i.e. the horizontal position.
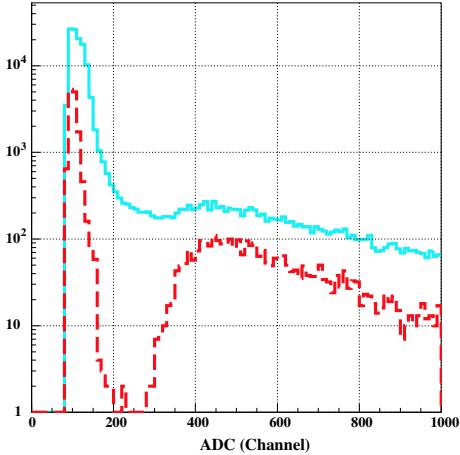
Figure 3. Energy loss of β ray in the first DSSD. The dased line shows the coincidence spectrum with the second DSSD. 400 ch was about 300 keV.

events is crucial to reduce the contamination and to determine precisely the half life of selected nuclear species. The analysis was performed for the single-hit event, that is, the event where β ray fired one strip on each side. The time spectrum of β decay after making position correlation is shown in Fig. 4.
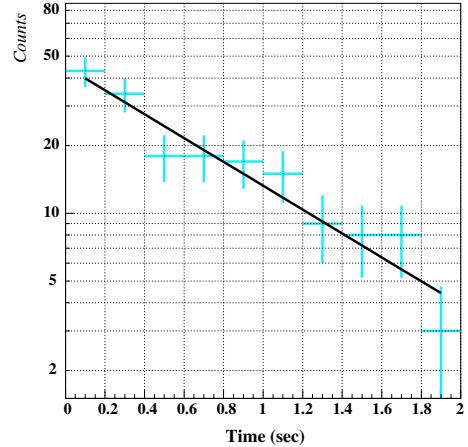
Figure 4. Time spectrum from the implantation of ^{18}N to the β-ray detection with the position correlation between the implantation and the β ray. The line shows the best fit of decay curve with no background component.

The half life was determined to be 560 ± 70 ms, which was consistent with the known value 624 ms [3]. The result shows that the decay of ^{18}N is successfully extracted.

The efficiency of β-ray detection was 42%. The fraction of β-ray emitted to the direction of the implanted surface was 50% and the β rays were not detected. In the analysis, the β ray was restricted to the single-hit event, therefore the events of 8% are expected to be the multi-hit event.

In summary, we tested the DSSD with the newly developed readout system using the unstable beam of ^{18}N at CRIB. The energy resolution of high-gain part in two pre-amplifier division was similar to the single pre-amplifier. The decay event was extracted by the position correlation between the implantation and the β ray. The performance satisfied the requirement of the decay spectroscopy.

References

[1] N. Uematsu and S. Nishimura, RIKEN Accel. Prog. Rep. **41** (2008) 151.

[2] Y. Yanagisawa *et al*., Nucl. Instr. Meth. A, **539** (2005) 74.

[3] R.B. Firestone *et al*., Table of Isotopes, 8th ed., A Wiley-Interscience Publication, (1996).

Pulse structure dependence of the proton polarization

T. Kawahara, T. Uesaka[a], Y. Shimizu[a], S. Sakaguchi[b], and T. Wakui[c]

Department of Physics, Toho University
[a]*Center for Nuclear Study, Graduate School of Science, University of Tokyo*
[b]*RIKEN (The Institute of Physical and Chemical Research)*
[c]*Cyclotron and Radioisotope Center, Tohoku University*

1. Introduction

A polarized proton solid target for RI beam experiments has been developed at Center for Nuclear Study, University of Tokyo [1]. The protons are polarized by transferring electron population difference in photo-excited triplet states of pentacene molecule. By this method, proton polarization of about 20% has been obtained at a low magnetic field of 0.1 T and in high temperature of 100 K. Although this target has been successfully applied to RI beam experiments [2, 3], further improvement in proton polarization is desirable for future applications. To pursue possible improvement in photo-excitation power, we examined pulse-structure dependence of proton polarization rate.

2. Optical system

For the optical excitation of pentacene molecules, an Arion laser (Coherent TSM25) with a wavelength range from 454.5 nm to 528.7 nm and a total maximum output power of 25 W is used. Since this laser is a continuous wave (CW) laser, we can be pulsed the light mechanically using an optical chopper (Fig. 1). The duty factor can be easily varied by shifting the overlap of two chopper blades. The frequency of laser pulse can be changed by changing the rotating speed of the optical chopper.

2 chopper blades   **slits**
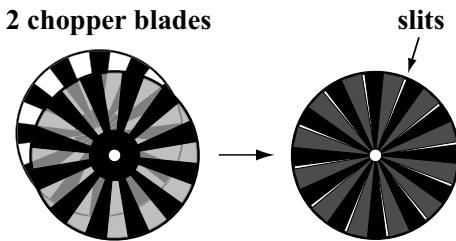
Figure 1. Optical chopper blades

This optical system enables us to change the duty factor from 5 to 50%, the repetition frequency from 0.75 to 7.5 kHz. The pulse width is determined by the duty factor and repetition frequency. The relation of the three parameter is expressed as

$$D = ft, \qquad (1)$$

where D, f, and t are the duty factor, the repetition frequency, and the pulse width, respectively.

3. Measurement

The measurement was carried out under following conditions. A crystal size was 14 mm in diameter and 3 mm in thickness. Protons were polarized at a temperature of 200 K and in magnetic field of about 60 mT.
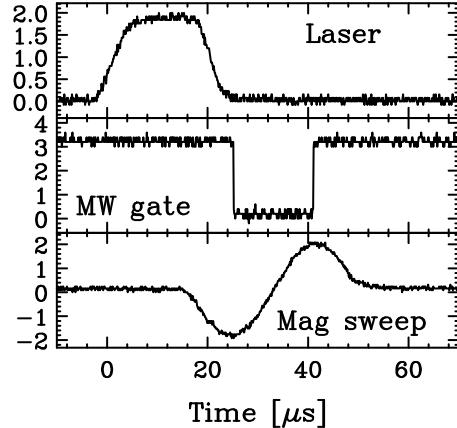
Figure 2. Timing chart during polarization. When the laser is irradiated with crystal, the electron polarization is made. Just after the irradiation of laser light, the microwave was irradiated and the magnetic field strength was swept in order to transfer the electron polarization to the protons.

Figure 2 shows the typical timing chart of polarization process. In the first step, the laser right was irradiated the crystal. Just after the irradiation of laser light, the microwave was irradiated and the magnetic field strength was swept in order to transfer the electron polarization to the protons. These steps were repeated at a certain repetition frequency. The magnitude of proton polarization after 5 minute. buildup is defined as the proton polarization rate, which is measured with the pulse NMR method.

The result is shown in Fig. 3 where the proton polarization rate is plotted as a function of the repetition frequency.
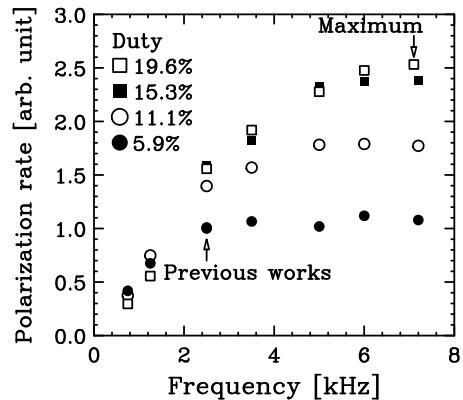
Figure 3. The polarization rate was measured by changing a duty factor and repetition frequency. The all measured data are normalized by the previous works value.
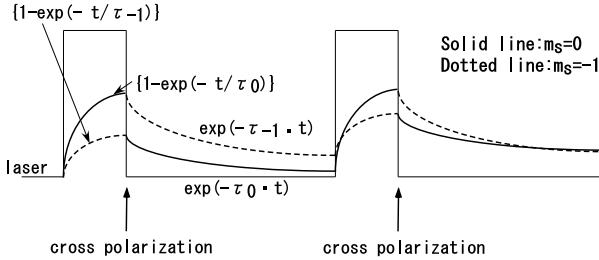
Figure 4. Time development electron population.
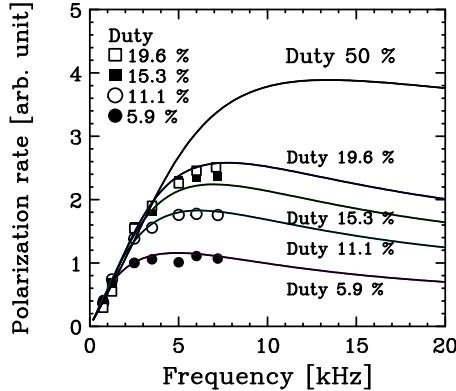
Figure 5. The polarization rate calculated from our simple model (solid curves) together with the measured polarization rate. The rates are calculated for the duty factor of 5.9%, 11.1%, 15.3%, 19.6%, and 50%.

In the previous works [1], the repetition frequency was 2.5 kHz and the duty factor was 5%. The all measured data are normalized by the previous data. At high frequency limit, the polarization rate is almost saturation and proportional to the duty factor. In the present works, we found that the proton polarization rate takes the maximum value when the repetition frequency is 7.3 kHz and the duty factor is 19.6%. The polarization rate was improved by a factor of 2.5 compared with the previous works.

4. Theoretical model

We built a simple theoretical model of the electron population in order to estimate the polarization rate.

There are three steps in the polarization process. The first is the electron polarization, the second is the polarization transfer from electron to proton, and the third is the electron relaxation. In this model, we assume that the electron polarization transfer to proton at 100%. The electron polarization is the electron population difference between the m=0 and m=-1 states which is magnetic sub-state of triplet state of pentacene molecule. Hereafter, the m=0 and m=−1 states are denoted as m_0 and m_- states, respectively.

In the first step, the electron population increases according to the build up function during laser irradiation. The build up function is given as

$$f_{b,i}(t) = A_i \tau_i \{1 - exp(-\frac{t}{\tau_i})\}, \tag{2}$$

where τ_i is the life time of the triplet state, A is the population rate and i is the magnetic sub-state of triplet state. After the laser irradiation, the electron population transfers to proton and decreases according to the relaxation function. When the electron polarization transfers, the number of the electrons in two magnetic sub-states turn over by a cross polarization [1]. The relaxation function is given as

$$f_{r,i}(t) = exp(-\frac{t}{\tau_i}). \tag{3}$$

Here, the life times of the two sub-states used in the model are τ_0=26 μsec and τ_-=83 μsec [4].

The solid and dotted line in Fig. 4 is time development of the electron population at m_0 state and m_- state, respectively.

The proton polarization rate is derived from

$$\frac{dP_p}{dt} \propto \rho_0 - \rho_-, \tag{4}$$

where ρ_0 and ρ_- are electron population in m_0 and m_- states. The proton polarization rate calculated by our simple model reproduces the measured data as shown in Fig. 5.

We found that the highest polarization rate can be obtained with a duty of 50% and a repetition frequency of 12 kHz.

5. Summary

To pursue possible improvement in photo-excitation power, we have examined the pulse structure dependence of proton polarization rate. The proton polarization rate was measured by changing the duty factor from 6% to 20% and the repetition frequency from 0.75 kHz to 7.5 kHz. At the duty factor of 19.6% and the repetition frequency 7.3 kHz, the polarization rate was improved by a factor of 2.5 compared with the previous works. We have found that the proton polarization rate depends strongly on the pulse structure. The pulse width dependences are reproduce with our simple model, using the life time of the triplet state is τ_0=26 μsec and τ_-=83μsec. Based on the calculation, the best performance is expected to be achieved with a duty factor of 50% and a repetition frequency of 10 kHz. The development at these parameters is in progress.

References

[1] T. Wakui *et al.*, Nucl. Instrum. Methods A **550** (2005) 521.

[2] M. Hatano *et al.*, Eur. Phys. J. A **25** (2005) 255.

[3] S. Sakaguchi *et al.* Proceedings of ISPUN07, World Scientific (2009) 245.

[4] M. Iinuma. Ph. D thesis, Kyoto University, (1997).

Developments of Cluster Ion Source as Magnetic-Field Calibrator of Rare RI Ring

Y. Ito, A. Ozawa, I. Arai, S. Kubono[a], S. Watanabe[a], Y. Ohshiro[a], and Y. Yamaguchi[b]

Department of Physics, University of Tsukuba
[a]*Center for Nuclear Study, Graduate School of Science, University of Tokyo*
[b]*RIKEN (The Institute of Physical and Chemical Research)*

1. Introduction

The construction of the Rare RI Ring, i.e., isochronous storage ring, is projected in RIKEN RI Beam Factory (RIBF) [1]. The Rare RI Ring will be used to measure the mass of radioactive isotopes (RI) with a precision of $\delta m/m \sim 10^{-6}$. The precision mass measurement of RI will play an important role in investigation of the r-process. Among the r-process nuclei, ^{78}Ni can be a good candidate of the "waiting point"due to its double-magicity. In order to achieve this precision, a magnetic field precision all over the ring must be calibrated in the same order. If it is revolving enough particles to calibrate in the ring, we will be able to calibrate the magnetic-field. However, the production rate of the RI is very low, for example, one particle per day for ^{78}Ni and only one particle is injected into the ring. In addition, it is difficult to calibrate using another particle from accelerator. Therefore, we consider an alternative method of calibration. By using an atomic cluster beam, it will be possible to calibrate the magnetic field precisely.

The magnetic rigidity $B\rho$ is given by

$$B\rho = \frac{(2mE_0)^{1/2}}{q} \tag{1}$$

where m is the mass of cluster, E_0 is the total energy and q is the charge of cluster. If we produce large-sized cluster and accelerate it by the precision acceleration voltage with a precision of 10^{-6}, then it can get the same rigidity as the RI which want to measure the mass. By measuring the time of flight of the cluster, we can monitor the magnetic field fluctuation of the ring. The parameters to make the same rigidity in case of the cluster Cu_n and the ^{78}Ni beam, are shown in Table 1.

The cluster ion source is able to produce the variable-sized clusters and accelerate them up to the desired energy. We have successfully achieved to produce the large-sized clusters enough to calibrate the magnetic field.

2. Experimental Setup

We have developed a magnetron-sputter-type gas aggregation cluster ion source. This type of cluster source can

	m	q	E_0
	[u]		
$Cu_{n=800}$	63×800	+1	~30keV
^{78}Ni	78	+28	200 MeV/u

Table 1. The parameter for Cu_n cluster and ^{78}Ni. The cluster energy E_0 is variable up to about 30 keV

generate clusters of high-melting point metal. The appara-tus is divided into three parts, i.e., a magnetron sputtering part, a gas aggregation cell and Time Of Flight Mass Spectrometer (TOF-MS) part. The schematic view of the cluster ion source is shown in Figure 1.
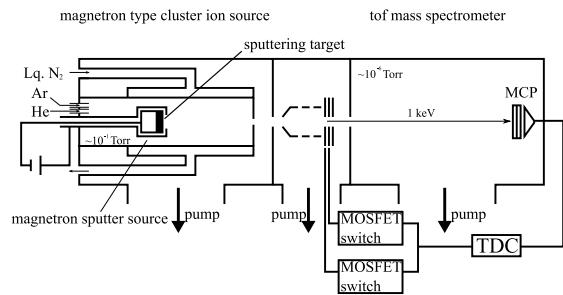
Figure 1. Schematics of magnetron-sputtering-type gas aggregation cluster ion source and TOF-MS.

In the magnetron sputtering part, ionized Ar atoms sputter the surface of the target mounted on the magnetron cathode. They produce a number of target atoms. The monomer atoms aggregate together into clusters in the gas aggregation cell, which is cooled by liquid nitrogen and is filled with Ar carrier gas. The masses of produced cluster ions are measured by TOF-MS. The distance L (cell length) between the magnetron and exit slit is changed by a calibrated sliding rod attached to the vacuum chamber. Note that the mass spectrum is also controlled by adjusting the flow rate of the Ar and He gases with a mass flow controller. Generally, the gas aggregation process is performed under the vapor pressure of 0.1-2 Torr to obtain a sufficient high collision rate.

TOF mass spectrometry has become popular in the cluster science since the first report by Stephens [2]. Several electrodes of ion optics driven with two MOSFET-switchs synchronized with the start pulse from pulse generator are used to accelerate the cluster ions. The total flight length is about 20 cm. The output signal from the Micro Channel Plate (MCP) is connected to the stop input of the multi-stop Time to Digital Converter (TDC).

3. Results

Figure 2 show a TOF spectrum of Cu_n cluster ions. According to the cluster growth model proposed by Smoluchowski [3], the cluster size distribution is expected to follow by a log-normal distribution. We calculated the mass of cluster from a TOF spectrum and converted a TOF spectrum to a cluster size spectrum. A cluster size spectrum fitted by log-normal distribution is shown in Figure 3. The result of

log-normal fitting reproduces the measured spectrum well. From this fitting curve, the $Cu_{n=800}$ is produced with the yield of about 0.07 s^{-1}. As a results, we have produced the large clusters up to the size of about eight hundreds.
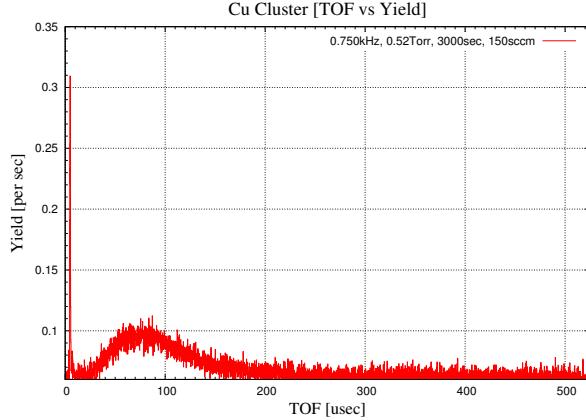
Figure 2. A TOF spectrum of Cu_n cluster ions.
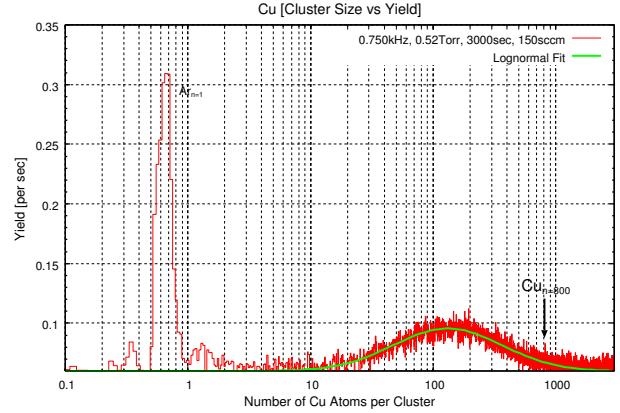
Figure 3. A cluster size spectrum of Cu_n cluster ions fitted by log-normal distribution.

4. Conclusion

We have succeeded to produce the $Cu_{n=800}$ clusters by using a magnetron-sputtering-type gas aggregation cluster ion source. We have achieved cluster the large size enough to calibrate the magnetic field of Rare RI Ring in RIKEN RIBF.

References

[1] Y. Yamaguchi, et al., Nucl. Instr. and Meth. B**266** (2008).
[2] W. E. Stephens, Phys. Rev. **69** (1946) 691.
[3] M. V. Smoluchowski, Z. Phys. Chem. **92** (1918) 129.

First observation of AVF bunched beam curent with a metal alloy core monitor

S. Watanabe, Y. Ohshiro, H. Yamaguchi, S. Kubono, M. Kase[a], and R. Koyama[ab]

Center for Nuclear Study, Graduate School of Science, University of Tokyo
[a]*RIKEN (The Institute of Physical and Chemical Research)*
[b]*SHI Accelerator Service Ltd.*

A low-energy in-flight type RI beam separator, called CRIB, for nuclear physics and nuclear astrophysics was constructed in 1999 on the Center for Nuclear Study, the University of Tokyo [1]. In CRIB experiments, a beam intensity should be known with a reasonable accuracy. At present, a detector to count elastically scattered particles from the target is used to monitor the beam intensity. Purpose of the present work is to develop a new beam current monitor which has features superior to the previous one; Firstly, it should enable a real-time diagnosis [2]. Second, it should work without destruction of the beam itself, namely without interrupting the user's experiment. As the beam current monitor possessing the features, we have developed a current transformer made of a magnetic alloy (MA) core [3] [4]. The dynamic range of measurable beam intensity is specified to be 0.01 to 100-eμA, which corresponds to the range of actual beam intensity used in experiments and to the range of a Farady cup, a destructive beam intensity monitor, in the AVF cyclotron beam-line. In particular, sensitivity at around several nano Ampeares is essentially important for CRIB experiments. A mechanical structure of the monitor is shown in Figure 1.
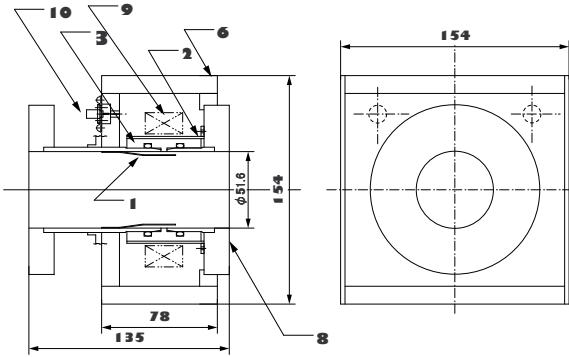
Figure 1. Cross section of the metal core monitor; 1=beam shield, 2=hoop (metal pipe supported by side wall of vacuum flange), 3=insulator (PEEK), 6=shield yoke, 8=vacuum flange (ICF114), 9=pick up core, 10=signal connector (SMA), 11= side panel.

The monitor comprises a current transformer with a secondary coil. The ion current I_{beam} passing through center of the monitor induces a magnetic flux in the toroidal core, and then it induces a current in the secondary coil with turn number N. The transformer yields nominal signal amplitude of

$$V_{sig} = \frac{I_{beam}}{N} Z_{in} \qquad (1)$$

The nominal sensitivity of 10 V/A is estimated where N, Z_{in} and I_{beam} are chosen at 5 turns, 50 Ω and 1-nA, respectively. Z_{in} is input impedance associate with burden resistor.

A current gain G_1 instead of I_{2nd}/I_{beam} was given by measurement of $(V_{sig}/Z_{in})/I_{beam}$. Consequently, G_1 of 0.126 was given by using a coaxial type beam current simulator. A cut off frequency (-3dB gain) was found at 100 MHz. The dummy current is fed to a test coil through a series resistor of 49.2 Ω. The test coil is wound around the current transformer to examine the monitor. This method gave G_1 of 0.172 within the frequency range of 1~100 MHz. The first trial of the signal detection was made successfully by using a low energy beam line composed of an ion source, magnetic analyzer, triplet Q magnets and RF buncher [8]. After the success of the beam test, the monitor was installed in the CRIB beam line. A flight pass length between an exit of AVF and target position of the primary beam, called F_0, is designed at 18.098m. The intensity of primary beam can be measured with the Faraday cup at 45 cm up stream of F_0. The monitor is installed at 1-m upstream of F_0. Preamplifier for the monitor is located near the metal box. A double shielded 50 Ω coaxial cable with a length of $\sim$ 60 m was installed to conduct the beam signal between the experimental room, called E7, and a counting room, called J1. Particular care was paid to isolate the cable from the high power AC line. Pierced ferrite cores to reduce a common mode noise are loaded on a small-sized coaxial cable adapted to extend the double-shielded coaxial cable. In the following, we call the new current monitor as the E7 core monitor.

A first measurement with the E7 core monitor was performed with a primary beam currents of $^{40}\text{Ar}^{q+}$. The current gain of the monitor was calibrated by passing $^{40}\text{Ar}^{7+}$ with kinetic energy of 3.6 MeV/u. Accelerating frequencies was set to 11.72 MHz.

Figure 2 shows time domain signal measured by E7 core monitor. A peak current I_{beam} passes through the monitor is estimated as

$$I_{beam} = V_{oscillo}/(Z_{in} G_{amp} G_{core}) \qquad (2)$$

where G_{amp} the preamplifier gain, G_{core} the coupling gain of the monitor.

Substituting the parameters, $V_{oscillo}$ = 3 mV, Z_{in} = 50 Ω, G_{amp} = 101.4, and $G_{core} \equiv G_1$ =0.126 to the above equation gives I_{beam} = 18.8-eμA. Measured pulse width τ and repetition time T were 4 ns (FWHM) and 85.3 ns (=1/11.72MHz), respectively. The difference of estimated τ of 2 ns and measured 4 ns is due to integration time constant of the monitor. So, equation $(\tau/T)I_{beam}$ gives averaged beam current I_{av} = $I_{beam}(\tau/T)$ = 0.88-eμA. The beam current I_{av} was compared with the Faraday cup current I_{dc} = 820-enA. Uncertainty of the measured current I_{av} and the I_{dc} is evaluated as $\varepsilon = (I_{av} - I_{dc})/I_{dc}$ and is found to be ε =0.073.
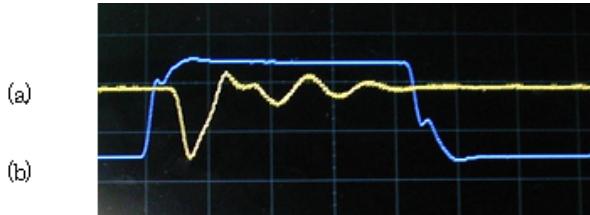
Figure 2. Time domain signals observed by 300 MHz oscilloscopes. (a): Single pulse of $^{40}Ar^{7+}$ with kinetic energy of 3.6 MeV/u when equivalent DC beams current I_{dc} = 820-enA Horizontal and Vertical scales correspond to 10 ns/div and 2 mV/div, respectively. Integrated charge per pulse corresponds 4.75E5 electrons (7.52×10^{-14} coulomb). (b): Square wave for the reference RF signal of the LIA, which corresponds time width of 42.66 ns and repetition frequency of 11.72 MHz.

For measuring an AVF cyclotron beam with a chain of short pulses with a width τ and a constant repetition rate T of $\sim$ 60 ns, synchronous detection with a spectrum analyzer or a lock-in-amplifier (LIA) is available [5] [6]. An equivalent signal waveform, $\phi(t)$, detected by the monitor is expressed by the formulae;

$$\phi(t) = \frac{1}{2\pi} \int_{-\infty}^{\infty} G(\omega) F(\omega) e^{jwt} d\omega \qquad (3)$$

where $G(\omega)$ the total gain of current transformer, $F(\omega)$ the Fourier components of the ion current. In order to measure $\phi(t)$ precisely, a large gain bandwidth (*GB* product) is required because an ideal bandwidth, B, deduced from $(T/\tau)(1/\tau)$ becomes very high, typically $\geq$ 1.68 THz. Practically, development of the large *GB* product is quite difficult. The toroidal core which bears a part of $G(\omega)$ is chosen with a viewpoint of large $\mu Q f$ product, where μ the magnetic permeability, Q the quality factor and f the frequency. The large $\mu Q f$ product promises the large gain bandwidth of the current transformer. An important feature of MA is a large magnetic permeability that makes the inductance of the pick up coil large. The MA core called FINEMET [7] is candidate of the toroidal core of the monitor. The FINEMET have varieties of mechanical sizes and ferromagnetic properties for the current transformer. The typical magnetic properties are B-H curve rectangular, high saturation field density and a small remnant field. A current transformer which built in Mn-Zn ferrite core has an impedance permeability which shows a large frequency dependence. The current transformer which built in the FINEMET core provides the constant impedance permeability compared with the ferrite loaded current trans-

former.

A noise reduction of the detected signal is very important in this system. An electromagnetic shielding of the pick-up core, cabling, and a selection of ground point are important issues to suppress the noise from the AVF cyclotron. The E7 beam line is electrically isolated from AVF cyclotron by the insulated vacuum flange. The noises originating from AVF was numerically eliminated by using a LIA (RF lock-in amplifier; model SR844, Stanford Research Systems). The measurement of the AVF beam intensities was made successfully with the current sensitivity of 10-enA. This performance was confirmed by using not only the spectrum analyzer but aloso the LIA to detect the Fourier components of a seriese of bunched beam. In order to evaluate the beam intensity precisely, width of a band pass filter used in the spectrum analyzer is chosen so as to correspond to the bandwidth of beam signal, because $\Delta\omega/\omega$ is proportional to $\Delta p/p$ of the AVF cyclotron beam.

The dynamic range of measurable beam intensity from 0.01 to 1-eμA was confirmed by the on-line test at the AVF beam line. The measurable beam intensity up to 100-eμA was confirmed by off-line test. This equipment is helpful not only to the CRIB experiments but to the AVF beam handling because it is capable of wide range beams intensity measurement.

References

[1] Y. Yanagisawa et al. "Low-energy radioisotope beam separator CRIB", Nucl. Instr. And Meth. A 539 (2005) 74-83.

[2] H. Yamaguchi et al. CNS-REP-77, March, 2008.

[3] S. Ninomiya et al. "Dual-mode beam current monitors", Proceedings of EPAC 2006, Edinburgh, Scotland, pp. 1145-1147.

[4] T. Toyama et al. "Beam instrumentations for the J-PARC RCS commissioning", Proceedings of EPAC08, Genoa, Italy, pp. 1125-1127.

[5] M. Wada et al. "Nondestructive intensity monitor for cyclotron beams", RIKEN Accel. Prog. Rep. 38 (2005)

[6] R. Koyama et al. Proceedings of the4th Annual Meeting of Particle Accelerator Society of Japan and the 32nd Linear Accelerator Meeting in Japan (August 1-3, 2007, Wako Japan) pp.318-320

[7] Hitach Metals Ltd. nanocrystalline soft magnetic material "FINEMET ®"

[8] T. Koseki et al. JJAP Vol. 45, No. 5A, 2006, pp. 4227-4231

Theoretical Nuclear Physics

$^1S_0$ pairing gap of low-density neutron matter near zero temperature in a pionless lattice effective field theory

T. Abe and R. Seki[a]

Department of Physics, University of Tokyo, Japan
[a]Department of Physics and Astronomy, California State University, Northridge, USA

We report a continuation of the investigation on thermal properties of low-density neutron matter by a lattice calculation with pionless *NN* effective field theory (EFT), which was previously reported in the CNS Annual Report 2007 [1]. Here, we focus on a $^1S_0$ pairing gap at $T \approx 0$, Δ, as it is one of our main results from the investigation. We show our Δ in the thermodynamic and continuum limits, and compare with other Δ's by various many-body and quantum Monte Carlo calculations. The full account of our investigation has been published [2,3,4].

Even though the investigations over many years provided much understanding of Δ, the reliable quantitative information has not been fully available [5]. For example, Δ had been firmly established *in the BCS approximation*, as evident in the fact that various conventional *NN* potentials have provided nearly the same Δ_{BCS} as a function of density [6]. Many-body calculations beyond the BCS approximation, however, have yielded Δ of various magnitudes, generally smaller than Δ_{BCS}. Quantum Monte Carlo calculations have also been used on the Δ determination. The Green's function Monte Carlo (GFMC) method has yielded Δ smaller than Δ_{BCS} [7] but not as small as those obtained by some of the many-body calculations beyond the BCS approximation. Another method closely related to GFMC, the auxiliary field diffusion Monte Carlo (AFDMC) method has given Δ quite close to Δ_{BCS} [8,9]. Our motivation is to determine Δ by a quantum Monte Carlo lattice calculation with *NN* EFT, which is motivated by the work of Ref. [10] and has been now started to applied to a few- and many-body systems [11] and also to the nuclear strucutre problems [12,13,14].

In this report, we present Δ by our determinantal quantum Monte Carlo calculation on the three-dimensional cubic lattice. Our calculation may be viewed, in a sense, as a nonrelativistic hadronic version of lattice QCD calculations, but it involves different aspects such as those associated with the large numbers of fermions on the lattice [11]. We also use a new ingredient, the *NN* interaction based on pionless *NN* EFT [15], in place of the conventional *NN* potentials. Our objective is twofold: (1) to apply the *NN* EFT interaction to the many-nucleon system of neutron matter by properly applying EFT counting rules, and (2) to determine reliably Δ by the *ab-initio* calculation. In the first attempt for achieving this objective, we have chosen a pionless *NN* EFT potential up to the next-to-leading order (NLO) [15]. The major consequence of this choice is that application of our calculation is limited to the low-density region ($k_F \lesssim 0.6$ fm^{-1}).

Table 1 lists our Δ in the thermodynamic and continuum limits. The table includes the ratio of Δ to Δ_{BCS}. Here, the Δ_{BCS}'s are taken from those tabulated in Ref. [16] as the representative BCS values, due to only quite small differences among the Δ_{BCS}'s calculated by various conventional *NN* potetials [6]. As seen in Table 1, our calculation yields Δ to be approximately 30% less than the BCS values.

Table 1. Our Δ in the thermodynamic and continuum limits, and the ratio to the Δ_{BCS}. Uncertainties are statistical only.

k_F (MeV)	ρ (ρ_0)	Δ (MeV)	Δ/Δ_{BCS}
15	9×10^{-5}	0.021(1)	0.69(3)
30	7×10^{-4}	0.13(1)	0.67(4)
60	6×10^{-3}	0.49(3)	0.56(5)
90	2×10^{-2}	1.10(7)	0.68(4)
120	5×10^{-2}	1.7(1)	0.74(4)

Figure 1 illustrates the density dependence of various Δ's reported in the literature. Δ's in the figure consist of those obtained by three types of calculations: (1) BCS (solid curve), (2) BCS or similar approximations, with higher order effects (dotted and dashed curves), and (3) quantum Monte Carlo (symbols with error bars).
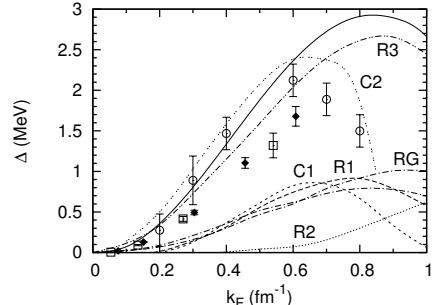
Figure 1. Comparison of our Δ to other calculations as a function of density (represented by the Fermi momentum k_F). The solid diamonds show our results, with statistical uncertainties. The other calculations consist of three types: quantum Monte Carlo (symbols with statistical uncertainties), BCS (solid curve), and BCS with higher-order effects (R's, C's, and RG; shown by dotted and dashed curves). See text for the description of each calculation shown.

(1) Below $k_F \approx 0.7$ fm^{-1}, there are few recognizable differences [6] among Δ_{BCS}'s calculated by various conventional *NN* potentials. Accordingly, Δ_{BCS}'s are represented by a single (solid) curve in Fig. 1.

(2) Figure 1 includes Δ's by the calculations beyond the BCS approximation. Calculations in the random phase approximation are by Wambach *et al.* [17] (denoted as R1),

by Schulze *et al.* [19] (R2), and by Cao *et al.* [19] (R3). Calculations using correlated-basis functions are by Chen *et al.* [20] (C1) and by Fabrocini *et al.* [8] (C2). A calculation based on a renormalization group approach is by Schwenk *et al.* [21] (RG). The curves for these Δ's are taken from similar figures in the recent literature: Figs. 1 and 2 of Ref. [9] and Fig. 4 of Ref. [7].

(3) Two types of quantum Monte Carlo calculations have been reported based on the GFMC [7] and AFDMC [8, 9] methods. They are applied for a fixed number of neutrons using the conventional *NN* potentials, while our work is based on a grand canonical ensemble formulation (for fixed chemical potentials) using the pionless EFT *NN* potentials up to the NLO. Figure 1 shows the most recent results of the GFMC [7] (open squares), the AFDMC [9] (open circles), and ours (solid diamonds).

In the figure, we see that all quantum Monte Carlo calculations are, overall, close to the Δ_{BCS}. The AFDMC Δ is quite close to the Δ_{BCS} in the density region examined in this work, while the GFMC Δ is smaller than the Δ_{BCS} and is similar to our Δ. It is difficult to assess the three quantum Monte Carlo calculations by comparing them because the intermediate steps of the calculations are all different. Here, however, we point out a possible issue closely tied to their basic formulations and setups: stemming from the neutron numbers being fixed, the GFMC and AFDMC Δ's are calculated using the odd-even staggering of the energy per neutron, while our Δ's are calculated directly from the correlation function. By physical arguments, the two ways of calculating Δ are expected to be the same for a large number of neutrons, but we are not aware of a rigorous proof for this expectation. While it might be caused by the different ways the nuclear potentials are applied in the two methods, the noticeable difference between the GFMC and AFDMC Δ's is puzzling to us.

In conclusion, we have reported a reliable calculation of the $^1S_0$ pairing gap at $T \approx 0$, Δ, of low-density neutron matter, using the determinantal quantum Monte Carlo lattice method with the pionless EFT *NN* potential up to the next-to-leading order. Δ was determined directly from the correlation function for the density of $(10^{-4}\text{-}10^{-1})\rho_0$. The thermodynamic limit was taken, and the continuum limit was examined in the determination. The Δ was found to be approximately 30% less than the BCS value.

References

[1] T. Abe and R. Seki, CNS-REP-77 Jun. 2009, pp72–73.

[2] T. Abe, R. Seki, and A. N. Kocharian, Phys. Rev. C **70** (2004) 014315 [Erratum-ibid. C **71** (2005) 059902].

[3] T. Abe and R. Seki, Phys. Rev. C **79** (2009) 054002.

[4] T. Abe and R. Seki, Phys. Rev. C **79** (2009) 054003.

[5] D. J. Dean and M. Hjorth-Jensen, Rev. Mod. Phys. **75** (2003) 607.

[6] Ø. Elgarøy and M. Hjorth-Jensen, Phys. Rev. C **57** (1998) 1174, K. Hebeler, A. Schwenk, and B. Friman, Phys. Lett. **B648** (2007) 176.

[7] A. Gezerlis and J. Carlson, Phys. Rev. C **77** (2008) 032801.

[8] A. Fabrocini, S. Fantoni, A. Yu. Illarionov, and K. E. Schmidt, Phys. Rev. Lett. **95** (2005) 192501.

[9] S. Gandolfi, A. Yu. Illarionov, S. Fantoni, F. Pederiva, and K. E. Schmidt, Phys. Rev. Lett. **101** (2008) 132501.

[10] H.-M. Müller, S. E. Koonin, R. Seki, and U. van Kolck, Phys. Rev. C **61** (2000) 044320.

[11] D. Lee, arXiv:0804.3501 [nucl-th].

[12] I. Stetcu, B. R. Barrett and U. van Kolck, Phys. Lett. B **653** (2007) 358.

[13] T. Otsuka, T. Suzuki, and Y. Akaishi AIP Conf. Proc. **1011** (2008) 153; T. Otsuka, T. Suzuki and Y. Akaishi, Mod. Phys. Lett. A **23** (2008) 2568.

[14] A. Schwenk and J. D. Holt, AIP Conf. Proc. **1011** (2008) 159, A. Schwenk, arXiv:0902.2585 [nucl-th].

[15] R. Seki and U. van Kolck, Phys. Rev. C **73** (2006) 044006.

[16] Ø. Elgarøy, L. Engvik, M. Hjorth-Jensen, and E. Osnes, Nucl. Phys. **A604** (1996) 466.

[17] J. Wambach, T. L. Ainsworth, and D. Pines, Nucl. Phys. **A555** (1993) 128.

[18] H. J. Schulze, J. Cugnon, A. Lejeune, M. Baldo, and U. Lombardo, Phys. Lett. **B375** (1996) 1.

[19] L. G. Cao, U. Lombardo, and P. Schuck, Phys. Rev. C **74** (2006) 064301.

[20] J. M. C. Chen, J. W. Clark, R. D. Davé, and V. V. Khodel, Nucl. Phys. **A555** (1993) 59.

[21] A. Schwenk, B. Friman, and G. E. Brown, Nucl. Phys. **A713** (2003) 191.

Other Activities

The Seven-th CNS-EFES Summer School (CNS-EFES08)

T. Kawabata, H. Hamagaki, N. Itagaki[a], S. Kubono, T. Nakatsukasa[b], T. Otsuka[a], H. Sakai[a],
S. Shimoura, T. Suzuki[c], and H. Yamaguchi

Center for Nuclear Study, Graduate School of Science, University of Tokyo
[a]Department of Physics, Graduate School of Science, University of Tokyo
[b]RIKEN (The Institute of Physical and Chemical Research)
[c]Department of Physics, Nihon University

The 7th CNS-EFES International Summer School (CNS-EFES08) was organized jointly by the Center for Nuclear Study (CNS), the University of Tokyo, and the Japan Society for the Promotion of Science (JSPS) Core-to-Core Program "International Research Network for Exotic Femto Systems (EFES)", in the period of August 26–September 1, 2008. The summer school was held at the Nishina hall in the Wako campus of RIKEN and at the Koshiba hall in the Hongo campus, the University of Tokyo.

This summer school was the seventh one in the series which aimed at providing graduate students and post docs with basic knowledge and perspectives of nuclear physics. It consisted of lectures by leading scientists in the fields of both experimental and theoretical nuclear physics. Each lecture started with an introductory talk from the fundamental point of view and ended with up-to-date topics in the relevant field.

The list of lecturers and the title of lectures are shown below.

P. Van Isacker (GANIL, France)
    "Dynamical Symmetries in Nuclei"
U.-G. Meissner (Bonn, Germany)
    "Nuclear Force and Chiral Effective Field Theory"
T. Nakamura (Tokyo Institute of Technology)
    "Invariant Mass Spectroscopy of Neutron Halo Nuclei"
T. Nakatsukasa (RIKEN Nishina Center)
    "Time-Dependent-Density-Functional Theory"
A. Ohnishi (Yukawa Institute of Theoretical Physics)
    "Nuclear Matter Equation of State"
T. Otsuka (The University of Tokyo)
    "Structure of Exotic Nuclei"
A. Richter (Darmstadt, Germany)
    "Collective Excitations and Superfluidity in Nuclei"
    "Fine Structure of Pygmy and Giant Resonances, Scales and Level Densities"
    "Nuclear Structure in Astrophysics"
    "Quantum Chaos in Billiards and Nuclei"
J. P. Schiffer (Argonne National Labolatory, USA)
    "Nuclear Reactions for Nuclear Structure"
M. Wakasugi (RIKEN Nishina Center)
    "SCRIT -New Technique for Electron-RI Collision"

This year, 9 lecturers and 115 participants attended from fourteen countries. Four lectures and twenty-eight participants were from foreign institutes, and ten participants were foreign researchers belonging to domestic institutes. Attendances communicated each other in the free discussion time between the lectures and in the welcome and farewell parties with a relaxed atmosphere.

Five lectures on Aug. 28 were held at the Koshiba hall in the Hongo campus and were broadcasted via Internet for the first time. There were constantly 20-25 audiences from all over the world, and 686 connections were eventually made in total.

The Student and Post Doc sessions were also held in the school. Twenty talks and twenty-seven posters were presented by graduate students and post docs.

All information concerning the summer school is open for access at the following URL:

http://www.cns.s.u-tokyo.ac.jp/summerschool/cns-efes08

Laboratory Exercise for Undergraduate Students

T. Kawabata[a], K. Yako[b], S. Hayakawa[a], H. Sakai[b], and S. Shimoura[a]

[a]*Center for Nuclear Study, Graduate School of Science, University of Tokyo*
[b]*Department of Physics, University of Tokyo, Tokyo*

Nuclear scattering experiments were performed as a laboratory exercise for undergraduate students of the University of Tokyo. This program was aiming at providing undergraduate students with an opportunity to learn how to study subatomic physics by using an ion beam from an accelerator. In 2008, 32 students joined this program.

The four beam times were scheduled in the second semester for third-year students, and 8 students participated in each beam time. The experiment was performed at the RIKEN accelerator research facility (RARF) using a 26-MeV alpha beam accelerated by the AVF cyclotron. The alpha beam extracted from the AVF cyclotron was transported to the CRIB beam line in the E7 experimental hall. In each beam time, the students were divided into two groups and took one of the following two subjects:

1. Measurement of elastic scattering of α particles from ^{197}Au.

2. Measurement of gamma rays emitted in the cascade decay of the rotational bands in ^{154}Gd and ^{184}Os.

Before the experiment, the students learned the basic handling of the semiconductor detectors and electronic circuits at the Hongo campus, and attended a radiation safety lecture at RIKEN. They also joined a tour to the RI beam factory at RIKEN.

In the $\alpha + ^{197}$Au measurement, α particles scattered from the Au target with a thickness of 1.42 mg/cm^2 were detected by a silicon PIN-diode located 11 cm away from the target. A collimator with a diameter of 6 mm was attached on the silicon detector. The energy spectrum of the scattered α particles was recorded by a multi-channel analyzer (MCA) system. The beam was stopped by a Faraday cup in the scattering chamber. The cross section for the alpha elastic scattering was measured in the angular range of $\theta_{lab} = 25$–$150°$. The measured cross section was compared with the calculated cross section for the Rutherford scattering as shown in Fig. 1. The cross section was also analyzed by the potential-model calculation, and the radius of the gold nucleus was discussed. Some students obtained the radius of $\sim$10 fm by using a classical model where the trajectory of the α particle in the nuclear potential is obtained by the Runge-Kutta method. Others tried to understand the scattering process by calculating the angular distribution by the distorted wave Born approximation with a Coulomb wave function and a realistic nuclear potential.

In the measurement of the rotational bands, excited states in ^{154}Gd and ^{184}Os nuclei were populated by the ^{152}Sm$(\alpha, 2n)$ and ^{182}W$(\alpha, 2n)$ reactions, respectively. The gamma rays emitted from the cascade decay of the rotational bands were measured by a high purity germanium detector located 50 cm away from the target. The energies of the gamma rays were recorded by the MCA system. The gain and the efficiency of the detector system had been calibrated with standard gamma-ray sources of ^{22}Na, ^{60}Co, ^{133}Ba, and ^{137}Cs. The typical spectra of the gamma rays from the cascade decay of the rotational bands in ^{154}Gd and ^{184}Os are shown in Fig. 2. The gamma rays from the $12^+ \rightarrow 10^+$ and $10^+ \rightarrow 8^+$ decay in ^{154}Gd and ^{184}Os were successfully identified. Based on the energies of the gamma rays, the moment of inertia and the deformation parameters of the excited states were discussed by using a classical rigid rotor model and a irrotational fluid model. The students found that the reality lies between the two extreme models. The initial population among the levels in the rotational band was also discussed by taking the effect of the internal conversion into account.
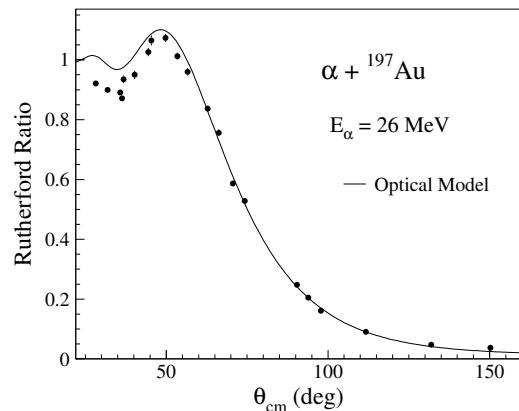
Figure 1. Ratio of the measured cross section for the $\alpha + ^{197}$Au elastic scattering to the Rutherford scattering cross sections. The solid line shows a result from an optical-model analysis by a student.
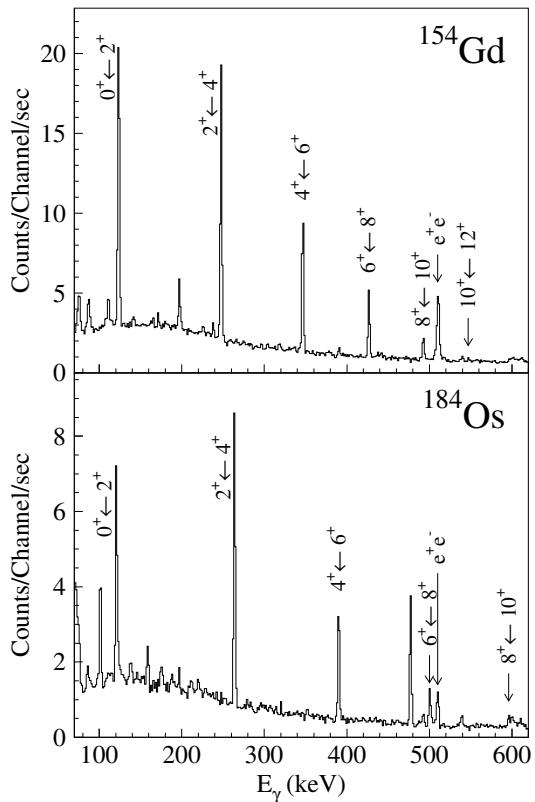
Figure 2. Typical spectra of the gamma rays from $\alpha + {}^{152}$Sm and ^{182}W reactions.

We believe this program was very impressive for the students. It was the first time for most of the students to use large experimental equipments. They learned basic things about the experimental nuclear physics and how to extract physics from the data.

Appendices

Symposium, Workshop, Seminar, and PAC
CNS Reports
Publication List
Talks and Presentations
Personnel

Symposium, Workshop, Seminar, and PAC

A. Symposium

1. The CNS-RIKEN Joint International Symposium on "Frontier of gamma-ray spectroscopy and Perspectives for Nuclear Structure Studies" (gamma08)
   Apr. 3 – 5 2008, Wako campus of RIKEN, Japan.

   Recent progress and future perspectives of gamma-ray spectroscopy and recent development of advanced gamma-ray detectors were discussed.

   The organizers were, E. Ideguchi (CNS), N. Aoi (RIKEN), S. Michimasa (CNS), H. Scheit (RIKEN), A. Odahara (Osaka), T. Koike (Tohoku), T. Ishii (JAEA), T. Nakatsukasa (RIKEN), S. Shimoura (CNS), T. Motobayashi (RIKEN), T. Otsuka (CNS/Tokyo).

   The symposium was hosted by CNS University of Tokyo and RIKEN.

2. Japanese-French conference "New Paradigms in Nuclear Physics"
   Sep. 29 – Oct. 2 2008, Paris, France.

   The year 2008 was the 150th anniversary year of Japan-France relationship, and the present symposium was regarded as a part of the 150th anniversary project of the Ministry of Foreign Affairs of Japan. About 100 participants discussed the new paradigms in nuclear physics. EFES was one of the co-hosts. The workshop was organized by Hiroshi Toki (RCNP: Co-chair), Sydney Gales (GANIL: Co-chair), Mamoru Fujiwara (RCNP: scientific secretary), David Boilley (GANIL: scientific secretary), Kouichi Hagino (Tohoku: scientific secretary), Marcella Grasso (IPN Orsay: scientific secretary), Toru Motobayashi (RIKEN), Nguyen Van Giai (IPN Orsay), Takaharu Otsuka (Tokyo), Valerie Frois (IPN Orsay: Symposium secretary), Hiroaki Utsunomiya (Konan), Christine Lemaitre (GANIL: Symposium secretary)

3. The ICHOR-EFES International Symposium on "New Facet of Spin-Isospin Responses"
   Oct. 29 – 31, 2008, RIBF Conference Hall, RIKEN, Japan.

   At RIKEN the Radio-Isotope Beam Factory (RIBF) has started working. The University of Tokyo has taken an initiative to construct the magnetic spectrometer called 'SHARAQ' dedicated to the high energy-resolution measurements in the experimental hall of RIBF under the Isospin-spin responses in CHarge-exchange exOthermic Reactions (ICHOR) program. Commissioning of SHARAQ was planned to start at March 2009. Thus this was a good opportunity to discuss physics which will be opened up by SHARAQ, placing particular emphasis on the spin-isospin responses. The symposium was organized by H. Sakai (UT) Chair, H. Sakurai (RIKEN), T. Otsuka (CNS,UT), S. Shimoura (CNS,UT, Secretary), R. G. T. Zegers (NSCL), and K. Langanke (GSI). and was hosted by RIKEN, ICHOR program, EFES, RIKEN, and CNS University of Tokyo.

4. The 6th Japan-Italy symposium on Heavy Ion Physics Nov. 11 – 15, 2008. Tokai, Japan.

   The aim of this symposium was to discuss the recent studies in nuclear and hadron physics and future projects. The topics of this symposium were Nuclear structure (shell structure, nuclear mass, symmetry energy, hyper nuclei), Nuclear dynamics (Superheavy element, nuclear fusion, direct reaction, nuclear fission), Innovative instrumentation and future facilities (RNB-development, detectors and electronics, J-PARC, RIBF, TRIAC, SPES), and Applications of nuclear physics (life science, material science, nuclear energy). EFES was one of the co-hosts. The workshop was organized by H. Ikezoe (JAEA, Chair), T. Kajino (NAOJ/Tokyo), H. Miyatake (KEK, Scientific secretary), T. Motobayashi (RIKEN, Vice Chair), T. Nakatsukasa (RIKEN), T. Otsuka (Tokyo/CNS/RIKEN), A. Bracco (Milano), G. Fortuna (INFN Headquarters), M. Lattuada (LNS), C. Signorini (Padova), A. Vitturi (Padova).

B. Workshop

1. Hokudai-TORIJIN JUSTIPEN-EFES workshop "Perspective in Resonances and Continua on nuclei" & "JUSTIPEN-EFES-Hokkaido-UNEDF meeting"
   Jul. 21 – 25 2008, Onuma, Japan.

   The workshop was under the activities of JUSTIPEN and EFES. JUSTIPEN is the DOE project in USA to send nuclear physicists to Japan to promote the nuclear theory collaborations. This time 20 scientists have visited Japan from USA and discussed with 50 Japanese participants. The main focus was on resonance behavior of unstable nuclei, large scale calculation etc. "Hokudai-EFES-TORIJIN-JUSTIPEN meeting on Resonances and Continua" was organized by K. Kato (Hokkaido), M. Kimura(Hokkaido), T. Otsuka (Tokyo), N. Itagaki (Tokyo), S. Shimoura (CNS, Tokyo), T. Motobayashi (RIKEN), T. Nakatsukasa (RIKEN), and "JUSTIPEN-EFES-Hokudai-UNEDF meeting" was organized by B. Balantekin (Wisconsin), B. Barrett (Arizona), W. Nazarewicz (Oak Ridge), J. Vary (Iowa), N. Itagaki (Tokyo), T. Otsuka (Tokyo), K. Kato (Hokkaido), M. Kimura (Hokkaido).

2. The Joint ANL-EFES Workshop for a Compton-Suppressed Ge Clover Array for Stopped and Energy Degraded Exotic Beams
   Dec. 4 – 5, 2008, Argonne National Laboratory, USA.

   The workshop was hosted by Argonne National Lab., USA, EFES, and Argonne National Lab.

3. First EMMI-EFES workshop on neutron-rich exotic nuclei "Realistic effective nuclear forces for neutron-rich nuclei"
   Feb. 9 – 11 2009, GSI Darmstadt, Germany.

   The workshop focused on the transformation of realistic forces to realistic effective forces that retain the phase-shifts and deuteron properties ("realistic") but are adapted ("effective") to low-momentum many-body Hilbert spaces that cannot represent short-range correlations. About 50 people have participated (15 from Japan). The workshop was organized by H. Feldmeier (GSI) and T. Otsuka (Tokyo).

4. The Workshop on "Competition of hydrogen burning with νp-process and r-process in explosive nucleosynthesis"
   Feb. 19 – 20, 2009, Nishina Hall, RIKEN, Japan.

   43 persons were attended. High-temperature hydrogen burning, in relation with recent hot topics such as νp-process in supernovae, p-nuclei and metal-poor stars were extensively discussed from experimental and theoretical points of view.

   The organizers were, S. Kubono (CNS), T. Kajino (NAO), S. Nishimura (RIKEN), H. Yamaguchi (CNS), T. Yoshida (NAO), T. Teranishi (Kyushu), N. Iwasa (Tohoku), S. Wanajo (Tokyo), K. Maeda (Tokyo), H. Ishiyama (KEK) and K. Yoneda (RIKEN).

   The workshop was financially supported by CNS, RIKEN and JSPS.

5. The 3rd LACM-EFES-JUSTIPEN workshop
   Feb. 23 – 25 2008, Oak Ridge National Laboratory, USA.

   The purpose of the meeting was to bring together scientists (theorists and experimentalists) with interests in physics of radioactive nuclei, large amplitude collective motion, and theoretical approaches related to the SciDAC-2 UNEDF project. As in the preceding Joint JUSTIPEN-LACM Meetings (2007, 2008), one emphasis of the meeting was on topics related to future collaborations between US and Japanese groups (under JUSTIPEN). About 70 scientists (20 were from Japan) have participated in. This workshop was organized by Takaharu Otsuka (Tokyo), Takashi Nakatsukasa (RIKEN), Susumu Shimoura (CNS, Tokyo), David Dean (Oak Ridge), Witek Nazarewicz (Oak Ridge), Thomas Papenbrock (Oak Ridge, Lead Organizer) Nicolas Schunck (Oak Ridge).

6. Fist LIA-EFES workshop "Low-energy collective motion of exotic nuclei"
   Mar. 2 – 4 2009, GANIL, Cean, France.

   There were 30 participants and the workshop was organized in order to conduct informal discussions. The aim of the workshop was to discuss possible developments of various models and theories on the structure of heavier exotic nuclei, which will become a frontier of the next generation of radioactive-ion beams. The workshop was organized by Takaharu Otsuka (Tokyo), Nori Aoi (RIKEN), Navin Alahari (GANIL), Piet Van Isacker (GANIL).

C. CNS Seminar

1. "Status of the SPIRAL2 Project at GANIL",
   P. Roussel-Chomaz (GANIL) Apr. 2nd, 2008.

2. "Lattice Calculation of Thermal properties of Low-Density Neutron Matter with NN Effective Field Theory",
   T. Abe (CNS, University of Tokyo) Jun. 24th, 2008.

3. "Alpha-particle condensation in nuclei",
   P. Schuck (Orsay) Oct. 8th, 2008.

4. "Direct measurement of the astrophysical nuclear reaction rate with radioactive nuclear beams",
   T. Hashimoto (CNS, University of Tokyo) Oct. 28th, 2008.

5. "The Thick Gas Electron Multiplier: its performance and applications",
   J. Miyamoto (Weizmann Institute) Jan. 30th, 2009.

6. "Some Results and Progress in Nuclear Astrophysics Research",
   J.J. He (IMP, Lanzhou, China) Mar. 12th, 2009.

D. Program Advisory Committee for Nuclear-Physics Experiments at RI Beam Factory

1. The 4th NP-PAC meeting
   Date: November 20–21, 2008
   Place: Conference room, 2F RIBF building

   Four experimental proposals for CRIB were examined in the 4th NP-PAC meeting.

CNS Reports

#78 "Low-lying Proton Intruder State in ^{13}B",

S. Ota, S. Shimoura, H. Iwasaki, M. Kurokawa, S. Michimasa, N. Aoi, H. Baba, K. Demichi, Z. Elekes, T. Fukuchi, T. Gomi, S. Kanno, S. Kubono, K. Kurita, H. Hasegawa, E. Ideguchi, N. Iwasa, Y.U. Matsuyama, K.L. Yurkewicz, T. Minemura, T. Motobayashi, T. Murakami, M. Notani, A. Odahara, A. Saito, H. Sakurai, E. Takeshita, S. Takeuchi, M. Tamaki, T. Teranishi, Y. Yanagisawa, K. Yamada, M. Ishihara, July. 2008.

#81 "Low-lying non-normal parity states in ^{8}B measured by proton elastic scattering on ^{7}Be",

H. Yamaguchi, Y. Wakabayashi, S. Kubono, G. Amadio, H. Fujikawa, T. Teranishi, A. Saito, J.J. He, S. Nishimura, Y. Togano, Y.K. Kwon, M. Niikura, N. Iwasa, K. Inafuku, L.H. Khirm, Feb. 2009.

Publication List

A. Original Papers

1. A. Adare, *et al*, for the PHENIX Collaboration: "Inclusive cross section and double helicity asymmetry for π^0 production in $p + p$ collisions at $\sqrt{s}$ = 62.4 GeV", Phys. Rev. D 79 (2009) 012003.

2. A. Adare, *et al*, for the PHENIX Collaboration: "Dilepton mass spectra in $p + p$ collisions at and the contribution from open charm", Phys. Lett. B 670 (2009) 313.

3. A. Adare, *et al*, for the PHENIX Collaboration: "Charged hadron multiplicity fluctuations in Au+Au and Cu+Cu collisions from $\sqrt{s_{NN}}$ = 22.5 to 200 GeV", Phys. Rev. C 78 (2008) 044902.

4. A. Adare, *et al*, for the PHENIX Collaboration: "Dihadron azimuthal correlations in Au+Au collisions at $\sqrt{s_{NN}}$ =200 GeV", Phys. Rev. C 78 (2008) 014901.

5. A. Adare, *et al*, for the PHENIX Collaboration: "Onset of π^0 Suppression Studied in Cu+Cu collisions at $\sqrt{s_{NN}}$ = 22.4, 62.4, and 200 GeV", Phys. Rev. Lett. 101 (2008) 162301.

6. A. Adare, *et al*, for the PHENIX Collaboration: "Suppression Pattern of Neutral Pions at High Transverse Momentum in Au+Au Collisions at $\sqrt{s_{NN}}$ =200 GeV and Constraints on Medium Transport Coefficients", Phys. Rev. Lett. 101 (2008) 232301.

7. A. Adare, *et al*, for the PHENIX Collaboration: "Quantitative constraints on the transport properties of hot partonic matter from semi-inclusive single high transverse momentum pion suppression in Au+Au collisions at $\sqrt{s_{NN}}$ =200 GeV", Phys. Rev. C 77 (2008) 064907.

8. A. Adare, *et al*, for the PHENIX Collaboration: "J/ψ Production in $\sqrt{s_{NN}}$ =200 GeV Cu+Cu Collisions", Phys. Rev. Lett. 101 (2008) 122301.

9. S. Afanasiev, *et al*, for the PHENIX Collaboration: "Particle-Species Dependent Modification of Jet-Induced Correlations in Au+Au Collisions at $\sqrt{s_{NN}}$ = 200 GeV", Phys. Rev. Lett. 101 (2008) 082301.

10. S. Afanasiev, *et al*, for the PHENIX Collaboration: "Source Breakup Dynamics in Au+Au Collisions at $\sqrt{s_{NN}}$ = 200 GeV via Three-Dimensional Two-Pion Source Imaging", Phys. Rev. Lett. 100 (2008) 232301.

11. N. Aoi, E. Takeshita, H. Suzuki, S. Takeuchi, S. Ota, H. Baba, S. Bishop, T. Fukui, Y. Hashimoto, H.J. Ong, E. Ideguchi, K. Ieki, N. Imai, M. Ishihara, H. Iwasaki, S. Kanno, Y. Kondo, T. Kubo, K. Kurita, K. Kusaka, T. Minemura, T. Motobayashi, T. Nakabayashi, T. Nakamura, T. Nakao, M. Niikura, T. Okumura, T.K. Ohnishi, H. Sakurai, S. Shimoura, R. Sugo, D. Suzuki, M.K. Suzuki, M. Tamaki, K. Tanaka, Y. Togano, K. Yamada: "Development of Large Deformation in ^{62}Cr", Phys. Rev. Lett. **102** (2009) 012502 (4 pages).

12. S. Cherubini, C. Spitaleri, V. Crucilla, M. Gulino, M. La Cognata, L. Lamia, R.G. Pizzone, S. Romano, S. Kubono, H. Yamaguchi, Y. Wakabayashi, S. Hayakawa, N. Iwasa, S. Kato, H. Komatsubara, T. Teranishi, A. Coc, N. De Sereville, F. Hammache: "The study of ^{18}F+p reaction at astrophysical energies", Proceedings of the 6th Japan-Italy Symposium on Heavy-Ion Physics, AIP Conf. Proc. 1120 (2009) 294–297.

13. Z. Elekes, Z. Dombradi, N. Aoi, H. Baba, S. Bishop, K. Demichi, Z. Fulop, J. Gibelin, T. Gomi, H. Hasegawa, Y. Hashimoto, N. Imai, M. Ishihara, N. Iwasa, H. Iwasaki, G. Kalinka, S. Kanno, S. Kawai, T. Kishida, Y. Kondo, A.A. Korsheninnikov, T. Kubo, K. Kurita, M. Kurokawa, N. Matsui, Y. Matsuyama, S. Michimasa, T. Minemura, T. Motobayashi, T. Nakamura, T. Nakao, E.Y. Nikolskii, M. Notani, T.K. Ohnishi, T. Okumura, H.J. Ong, S. Ota, A. Ozawa, A. Perera, A. Saito, H.K. Sakai, H. Sakurai, Y. Satou, S. Shimoura, D. Sohler, T. Sumikama, D. Suzuki, M. Suzuki, H. Takeda, E. Takeshita, S. Takeuchi, M. Tamaki, Y. Togano, K. Yamada, Y. Yanagisawa, K. Yoneda: "The study of shell closures in light neutron-rich nuclei", J.Phys.(London) **G35** (2008) 014038.

14. J.J. He, S. Kubono, T. Teranishi, M. Notani, H. Baba, S. Nishimura, J.Y. Moon, M. Nishimura, S. Michimasa, H. Iwasaki, Y. Yanagisawa, N. Hokoiwa, M. Kibe, J.H. Lee, S. Kato, Y. Gono, C.S. Lee: "A study of the proton resonant property in ^{22}Mg by elastic scattering of ^{21}Na + p and its astrophysical implication in the ^{18}Ne(α, p)^{21}Na reaction rate", Eur. Phys. J. A **36** (2008) 1–5.

15. N. Imai, N. Aoi, H.J. Ong, H. Sakurai, K. Demichi, H. Kawasaki, H. Baba, Zs. Dombradi, Z. Elekes, N. Fukuda, Zs. Fulop, A. Gelberg, T. Gomi, H. Hasegawa, K. Ishikawa, M. Ishihara, H. Iwasaki, E. Kaneko, S. Kanno, T. Kishida, Y. Kondo, T. Kubo, K. Kurita, S. Michimasa, T. Minemura, M. Miura, T. Motobayashi, T. Nakamura, M. Notani, T.K. Ohnishi, A. Saito, S. Shimoura, T. Sugimoto, M.K. Suzuki, E. Takeshita, S. Takeuchi, M. Tamaki, H. Watanabe, K. Yoneda: "First lifetime measurement of 2_1^+ state in ^{12}Be", Phys. Lett. B **673** (2004) 179–182.

16. N. Iwasa, T. Motobayashi, S. Bishop, Z. Elekes, J. Gibelin, M. Hosoi, K. Ieki, K. Ishikawa, H. Iwasaki, S. Kawai, S. Kubono, K. Kurita, M. Kurokawa, N. Matsui, T. Minemura, H. Morikawa, T. Nakamura, M. Niikura, M. Notani, S. Ota, A. Saito, H. Sakurai, S. Shimoura, K. Sugawara, T. Sugimoto, H. Suzuki, T. Suzuki, I. Tanihata, E. Takeshita, T. Teranishi, Y. Togano, K. Yamada, K. Yamaguchi, Y. Yanagisawa: "Large proton contribution to the 2^+ excitation in ^{20}Mg studied by intermediate energy inelastic scattering", Phys. Rev. C **78** (2008) 024306.

17. H. Iwasaki, S. Michimasa, M. Niikura, M. Tamaki, N. Aoi, H. Sakurai, S. Shimoura, S. Takeuchi, S. Ota, M. Honma, T. K. Onishi, E. Takeshita, H. J. Ong, H. Baba, Z. Elekes, T. Fukuchi, Y. Ichikawa, M. Ishihara, N. Iwasa, S. Kanno, R. Kanungo, S. Kawai, T. Kubo, K. Kurita, T. Motobayashi, A. Saito, Y. Satou, H. Suzuki, M. K. Suzuki, Y. Togano, Y. Yanagisawa: "Persistence of the *N*=50 shell closure in the neutron-rich isotope ^{80}Ge", Phys. Rev. C **78** (2008) 021304(R).

18. D. Kaji, K. Morimoto, N. Sato, T. Ichikawa, E. Ideguchi, K. Ozeki, H. Haba, H. Koura, Y. Kudou, A. Ozawa, T. Sumita, T. Yamaguchi, A. Yoneda, A. Yoshida, K. Morita: "Production and Decay Properties of ^{263}Hs", J. Phys. Soc. Jpn. **78** (2009) 035003 (2 pages).

19. T. Kawabata, G.P.A. Berg, T. Kubo, H. Sakai, S. Shimoura, T. Uesaka: "High resolution beam line for the SHARAQ spectrometer", Nucl.Instrum. Methods Phys. Res. B **266** (2008) 4201.

20. Y. Kondo, T. Nakamura, Y. Satou, T. Matsumoto, N. Aoi, N. Endo, N. Fukuda, T. Gomi, Y. Hashimoto, M. Ishihara, S. Kawai, M. Kitayama, T. Kobayashi, Y. Matsuda, N. Matsui, T. Motobayashi, T. Nakabayashi, K. Ogata, T. Okumura, H.J. Ong, T.K. Onishi, H. Otsu, H. Sakurai, S. Shimoura, M. Shinohara, T. Sugimoto, S. Takeuchi, M. Tamaki, Y. Togano, Y. Yanagisawa, "One-neutron removal reactions of ^{18}C and ^{19}C on a proton target", Phys. Rev. C **79** (2009) 014602 (7 pages).

21. Y.K. Kwon, C.S. Lee, J.Y. Moon, J.H. Lee, J.Y. Kim, M.K. Cheoun, S. Kubono, N. Iwasa, K. Inafuku, H. Yamaguchi, J.J. He, A. Saito, Y. Wakabayashi, H. Fujikawa, G. Amadio, L.H. Khiem, M. Tanaka, A.A. Chen, S. Kato, Y. Fuchi, N. Fukunishi: "Astrophysically Important ^{26}Si States Studied with the ^{28}Si(^{4}He,^{6}He)^{26}Si Reaction", J. Korean Phys. Soc. **53** (2008) 1141.

22. T. Nakamura, N. Fukuda, N. Aoi, N. Imai, M. Ishihara, H. Iwasaki, T. Kobayashi, T. Kubo, A. Mengoni, T. Motobayashi, M. Notani, H. Otsu, H. Sakurai, S. Shimoura, T. Teranishi, Y.X. Watanabe, K. Yoneda: "Neutron capture cross section of ^{14}C of astrophysical interest studied by Coulomb breakup of ^{15}C", Phys. Rev. C **79** (2009) 035805 (6 pages).

23. S. Ota, S. Shimoura, H. Iwasaki, M. Kurokawa, S. Michimasa, N. Aoi, H. Baba, K. Demichi, Z. Elekes, T. Fukuchi, T. Gomi, S. Kanno, S. Kubono, K. Kurita, H. Hasegawa, E. Ideguchi, N. Iwasa, Y.U. Matsuyama, K.L. Yurkewicz, T. Minemura, T. Motobayashi, T. Murakami, M. Notani, A. Odahara, A. Saito, H. Sakurai, E. Takeshita, S. Takeuchi, M. Tamaki, T. Teranishi, Y. Yanagisawa, K. Yamada, M. Ishihara: "Low-lying proton intruder state in ^{13}B", Phys. Lett. B **666** (2008) 311–314.

24. H. Sagawa, X.R. Zhou, T. Suzuki, N. Yoshida: "Possible shape coexistence and magnetic dipole transitions in ^{17}C and ^{21}Ne", Physical Review C **78** (2008) 041304 (R) 1–5.

25. T. Shizuma, T. Ishii, H. Makii, T. Hayakawa, M. Matsuda, S. Shigematsu, E. Ideguchi, Y. Zheng, M. Liu, T. Morikawa, M. Oi: "One-quasiparticle bands in neutron-rich ^{187}W", Phys. Rev. C **77** (2008) 047303 (4 pages).

26. C. Spitaleri, S. Romano, L. Lamia, S.M.R. Puglia, M.G. Del Szanto, N. Carlin, M.G. Munhoz, V. Kroha, S. Kubono, E. Somoryai, A. Szanto de Toledo, S. Cherubini, V. Crucilla, M. Gulino, G. Kiss, M.La Cognata, Chengbo Li, R. Liguori Neto, M.M. De Moura, R.G. Pizzone, G.G. Rapisarda, M.L. Sergi, F.A. Souza, A.A.P. Suaide, E. Szanto, G. Tabacaru, S. Tudisco, A. Tumino, Y. Wakabayashi, Qungang Wen, H. Yamaguchi: "New results on the Trojan Horse Method applied to the ^{10,11}B+p reactions", Proceedings of the 6th Japan-Italy Symposium on Heavy-Ion Physics, AIP Conf. Proc. 1120 (2009) 171–176.

27. T. Suda, T. Nozawa, A. Ohnishi, K. Kato, M.Y. Fujimoto, T. Kajino, S. Kubono: "The Proceedings of the International Symposium on Origin of Matter and Evolution of Galaxies 2007", AIP Conference Proc. No. 1016 (2008).

28. T. Suzuki, T. Otsuka: "Exotic magnetic properties in ^{17}C", Phys. Rev. C **78** (2008) 061301(R)/1-5.

29. T. Uesaka, S. Shimoura, H. Sakai, G.P.A. Berg, K. Nakanishi, Y. Sasamoto, A. Saito, S. Michimasa, T. Kawabata, T. Kubo: "The high resolution SHARAQ spectrometer", Nucl. Instrum. Meth. in Phys. Res. B **266** (2008) 4218.

30. H. Yamaguchi, Y. Wakabayashi, G. Amadio, S. Hayakawa, H. Fujikawa, S. Kubono, J.J. He, A. Kim, D.N. Binh: "Development of a cryogenic gas target system for intense radioisotope beam production at CRIB", Nucl. Instr. and Meth. in Phys. Res. A **589** (2008) 150–156.

31. H. Yamaguchi, Y. Wakabayashi, S. Kubono, G. Amadio, H. Fujikawa, T. Teranishi, A. Saito, J.J. He, S. Nishimura, Y. Togano, Y.K. Kwon, M. Niikura, N. Iwasa, K. Inafuku, L.H. Khiem: "Low-lying non-normal parity states in ^{8}B measured by proton elastic scattering on ^{7}Be", Phys. Lett. B **672** (2009) 230–234.

32. T. Yoshida, T. Suzuki, S. Chiba, T. Kajino, H. Yokomura, K. Kimura, A. Takamura, D.H. Hartmann: "Neutrino-nucleus reaction cross sections for light element synthesis in supernova explosions",   The Astrophysical Journal. **686** (2008) 448-466.

B. Proceedings

1. N. Aoi, H. Suzuki, E. Takeshita, S. Takeuchi, S. Ota, H. Baba, S. Bishop, T. Fukui, Y. Hashimoto, H.J. Ong, E. Ideguchi, K. Ieki, N. Imai, H. Iwasaki, S. Kanno, Y. Kondo, T. Kubo, K. Kurita, K. Kusaka, T. Minemura, T. Motobayashi, T. Nakabayashi, T. Nakamura, T. Nakao, M. Niikura, T. Okumura, T.K. Ohnishi, H. Sakurai, S. Shimoura, R. Sugo, D. Suzuki, M.K. Suzuki, M. Tamaki, K. Tanaka, Y. Togano, K. Yamada: "Shape transition observed in neutron-rich pf-shell isotopes studied via proton inelastic scattering", Proc. of the 23rd International Nuclear Physics Conference (INPC07), June 3–8, 2007, Tokyo, Japan, Nucl. Phys. A **805** (2008) 400c–407c.

2. N. Imai, N. Aoi, H.J. Ong, H. Sakurai, K. Demichi, H. Kawasaki, H. Baba, Zs. Dombrádi, Z. Elekes, N. Fukuda, Zs. Fülöp, A. Gelberg, T. Gomi, H. Hasegawa, K. Ishikawa, H. Iwasaki, E. Kaneko, S. Kanno, T. Kishida, Y. Kondo, T. Kubo, K. Kurita, S. Michimasa, T. Minemura, M. Miura, T. Motobayashi, T. Nakamura, M. Notani, T.K. Ohnishi, A. Saito, S. Shimoura, T. Sugimoto, M.K. Suzuki, E. Takeshita, S. Takeuchi, M. Tamaki, H. Watanabe, K. Yoneda, M. Ishihara: "The lifetime measurement of the first 2^+ state of ^{12}Be", Proceedings of the 23rd International Nuclear Physics Conference (INPC07), June 3–8, 2007, Tokyo, Japan, Volume 2, (2008) pp.245–247.

3. N. Imai, N. Aoi, H.J. Ong, H. Sakurai, K. Demichi, H. Kawasaki, H. Baba, Zs. Dombrádi, Z. Elekes, N. Fukuda, Zs. Fülöp, A. Gelberg, T. Gomi, H. Hasegawa, K. Ishikawa, M. Ishihara, H. Iwasaki, E. Kaneko, S. Kanno, T. Kishida, Y. Kondo, T. Kubo, K. Kurita, S. Michimasa, T. Minemura, M. Miura, T. Motobayashi, T. Nakamura, M. Notani, T.K. Ohnishi, A. Saito, S. Shimoura, T. Sugimoto, M.K. Suzuki, E. Takeshita, S. Takeuchi, M. Tamaki, H. Watanabe, K. Yoneda: "Application of Doppler-shift attenuation method to the de-excitation γ rays from the in-flight ^{12}Be beam", Proc. of the 6th Japan-Italy Symposium on Heavy-Ion Physics, November 11–15, 2008, Tokai, Japan, AIP Conf. Proc. **1120** (2009) 265–269.

4. M. Janek, V.P. Ladygin, L.S. Azhgirey, T. Uesaka, Yu.V. Gurchin, M. Hatano, K. Itoh, A.Yu. Isupov, J.-T.Karachuk, H.Kato, T.Kawabata, V.A.Krasnov, A.N.Khrenov, A.S. Kiselev, V.A. Kizka, J. Kliman, A.K. Kurilkin, P.K. Kurilkin, N.B. Ladygina, A.N. Livanov, Y. Maeda, A.I. Malakhov, V. Matousek, M. Morhach, J. Nishikawa, Yu.K. Pilipenko, T. Ohnishi, H. Okamura, S.M. Piyadin, S.G. Reznikov, T. Saito, S. Sakaguchi, H. Sakai, N. Sakamoto, S. Sakoda, Y. Sasamoto, Y. Satou, K. Sekiguchi, K. Suda, M.A. Shikhalev, A. Tamii, I. Turzo, N. Uchigashima, T.A. Vasiliev, K. Yako, L.S. Zolin "Status of the investigation of the spin structure of d, 3H, and 3He at VBLHE using polarized and unpolarized deuteron beam", Phys.Atomic Nuclei **71**, 1495 (2008).

5. T. Kawabata, G.P.A. Berg, T. Kubo, H. Sakai, S. Shimoura, T. Uesaka: "High resolution beam line for the SHARAQ spectrometer", Proc. the XVth International Conference on Electromagnetic Isotope Separators and Techniques Related to their Applications, 24–29, 2007, Deauville, France, Nucl. Instr. Meth. in Phys. Res. B **266** (2008) 4201–4204.

6. A.S.Kiselev, V.P.Ladygin, T.Uesaka, T.A.Vasiliev, M.Janek, T.Saito, M.Hatano, A.Yu.Isupov, H.Kato, N.B.Ladygina, Y.Maeda, A.I.Malakhov, J.Nishikawa, T.Ohnishi, H.Okamura, S.G.Reznikov, H.Sakai, N.Sakamoto, S.Sakoda, Y.Satou, K.Sekiguchi, K.Suda, A.Tamii, N.Uchigashima, K.Yako "Analyzing powers in the ^{12}C($\vec{d}$,p)^{13}C reaction at the energy $T_d = 270$ MeV", Eur.Phys.J. Special Topics **162**, 143 (2008).

7. A.K.Kurilkin, T.Saito, V.P.Ladygin, T.Uesaka, T.A.Vasiliev, M.Janek, M.Hatano, A.Yu.Isupov, H.Kato, N.B.Ladygina, Y.Maeda, A.I.Malakhov, J.Nishikawa,T.Ohnishi, H.Okamura, S.G.Reznikov, H.Sakai, N.Sakamoto, S.Sakoda, Y.Satou, K.Sekiguchi, K.Suda, A.Tamii, N.Uchigashima, K.Yako " Measurement of the vector A_y and tensor A_{yy}, A_{xx}, A_{xz} analyzing powers for the $dd \to ^3$Hp reaction at 200 MeV", Eur.Phys.J. Special Topics **162**, 133 (2008).

8. P.K.Kurilkin, K.Suda, T.Uesaka, V.P.Ladygin, Yu.V.Gurchin, A.Yu.Isupov, K.Itoh, M.Janek, J.-T.Karachuk, T.Kawabata, A.N.Khrenov, A.S.Kiselev, V.A.Kizka, J.Kliman, V.A.Krasnov, N.B.Ladygina, A.N.Livanov, Y.Maeda, A.I.Malakhov, V.Matoucek, M.Morhac, S.G.Reznikov, S.Sakaguchi, H.Sakai, Y.Sasamoto, K.Sekiguchi, M.A.Shikhalev, I.Turzo, T.A.Vasiliev, H.Witala "Measurement of the vector and tensor analyzing powers in dp elastic scattering at the energy of 880 MeV" Eur.Phys.J. Special Topics **162**, 137 (2008).

9. Y.K. Kwon, C.S. Lee, J.Y. Moon, J.H. Lee, J.Y. Kim, M.K. Cheoun, S. Kubono, N. Iwasa, K. Inafuku, H. Yamaguchi, J.J. He, A. Saito, Y. Wakabayashi, H. Fujikawa, G. Amadio, L.H. Khiem, M. Tanaka, A.A. Chen, S. Kato, Y. Fuchi, N. Fukunishi: "Astrophysically Important ^{26}Si States Studied with the ^{28}Si(^{4}He,^{6}He)^{26}Si Reaction", J. Korean Phys. Soc. **53** (2008) 1141–1145.

10. Y. Morino, for the PHENIX Collaboration: "Measurement of charm and bottom production in p+p collisions at $\sqrt{s}$ = 200 GeV at RHIC-PHENIX", Proc. of the 20th International Conference on Ultra-Relativistic Nucleus-Nucleus Collisions (QM2008), February 4–10, 2008, Jaipur, India, J. Phys. G **35** (2008) 104116–104119.

11. S. Sakaguchi, T. Uesaka, T. Wakui, T. Kawabata, N. Aoi, Y. Hashimoto, M. Ichikawa, Y. Ichikawa, K. Itoh, M. Itoh, H. Iwasaki, T. Kawahara, H. Kuboki, Y. Maeda, R. Matsuo, T. Nakao, H. Okamura, H. Sakai, N. Sakamoto, Y. Sasamoto, M. Sasano, Y. Satou, K. Sekiguchi, M. Shinohara, K. Suda, D. Suzuki, Y. Takahashi, A. Tamii, K. Yako, M. Yamaguchi: "Spin-orbit potential in ^{6}He studied with polarized proton target", Proc. of International Nuclear Physics Conference 2007 (INPC2007), June 3–8, 2007, Tokyo, Japan, Nucl. Phys. A **805** (2008) 467–469.

12. S. Sakaguchi, T. Uesaka, T. Wakui, T. Kawabata, N. Aoi, Y. Hashimoto, M. Ichikawa, Y. Ichikawa, K. Itoh, M. Itoh, H. Iwasaki, T. Kawahara, H. Kuboki, Y. Maeda, R. Matsuo, T. Nakao, H. Okamura, H. Sakai, N. Sakamoto, Y. Sasamoto, M. Sasano, Y. Satou, K. Sekiguchi, M. Shinohara, K. Suda, D. Suzuki, Y. Takahashi, A. Tamii, K. Yako, M. Yamaguchi: "Analyzing power measurement for proton elastic scattering on ^{6}He", Proc. of the International Symposium on Physics of Unstable Nuclei (ISPUN07), July 3–7, 2007, Hoi An, Vietnam, World Scientific (2008) 245–248.

13. Y. Satou, T. Nakamura, N. Fukuda, T. Sugimoto, Y. Kondo, N. Matsui, Y. Hashimoto, T. Nakabayashi, T. Okumura, M. Shinohara, T. Motobayashi, Y. Yanagisawa, N. Aoi, S. Takeuchi, T. Gomi, Y. Togano, S. Kawai, H. Sakurai, H.J. Ong, T.K. Ohnishi, S. Shimoura, M. Tamaki, T. Kobayashi, H. Otsu, Y. Matsuda, N. Endo, M. Kitayama, M. Ishihara: "Unbound excited states in ^{19,17}C", Proc. of the 23rd International Nuclear Physics Conference (INPC07), June 3–8, 2007, Tokyo, Japan, Volume 2 (2008) pp. 248–250.

14. S. Shimoura: "Light Neutron-Rich Nuclei Studied by Alpha-Induced Reactions", Proc. of the International Symposium on Physics of Unstable Nuclei (ISPUN07), July 3–7, 2007, Hoi An, Vietnam, ed. D.T. Khoa, P. Egelhof, S. Gales, N.Van Giai, T. Motobayashi, World Scientific, pp. 230–237.

15. S. Shimoura, S. Ota, H. Iwasaki, M. Kurokawa, S. Michimasa, S. Kubono, T. Teranishi, M. Notani, M. Tamaki, T. Murakami, N. Iwasa, T. Motobayashi, Y. Yanagisawa, T. Minemura, S. Takeuchi, T. Gomi, K. Yamada, A. Saito, H. Baba, Y.U. Matsuyama, S. Kanno, E. Takeshita, K. Demichi, K. Hasegawa, K. Kurita, H. Sakurai, N. Aoi, E. Ideguchi, A. Odahara, T. Fukuchi, K. Miller, Z. Elekes, M. Ishihara: "Lifetime of the low-lying isomeric 0^+ state in ^{12}Be", Proc. of the 23rd International Nuclear Physics Conference (INPC07), June 3–8, 2007, Tokyo, Japan, Volume 2 (2008) pp.365–367.

16. S. Shimoura: "SHARAQ spectrometer and GRAPE", Proc. the XVth International Conference on Electromagnetic Isotope Separators and Techniques Related to their Applications, 24–29, 2007, Deauville, France, Nucl. Instr. Meth. in Phys. Res. B **266** (2008) 4131–4136.

17. S. Shimoura: "High-resolution spectroscopy using direct reactions of RI beams", Proc. of the 6th Japan-Italy Symposium on Heavy-Ion Physics, November 11–15, 2008, Tokai, Japan, AIP Conf. Proc. **1120** (2009) 59–63.

18. T. Suzuki, S. Chiba, M. Honma, K. Higahiyama, T. Yoshida, H. Umeda, K. Nomoto, T. Kajono, T. Otsuka: "Spin-Dependent Transitions in Nuclei and Neutrino-Nucleus Reactions", Proc. of Frontiers in Nuclear Structure, Astrophysics, and Reactions (FINUSTAR2), September 10–14, 2007, Crete, Greece, AIP Conf. Proc. **1012** (2008) 51–54.

19. T. Suzuki, S. Chiba, T. Yoshida, M. Honma, K. Higashiyama, H. Umeda, K. Nomoto, T. Kajino, T. Otsuka: "Neutrino-Nucleus Reactions and Nucleosynthesis", Proc. of 10th International Symposium on Origin of Matter and Evolution of Galaxies: From the Dawn of Universe to the Formation of Solar System, December 4–7, 2007, Sapporo, Japan, AIP Conf. Proc. **1016** (2008) 321–326.

20. T. Suzuki, T. Otsuka, M. Honma, K. Higashiyama: "Spin Modes, Neutrino-Induced Reactions and Nucleosynthesis in Stars", Proc. of the International Conference on Nuclear Physics and Astrophysics: From Stable Beams to Exotic Nuclei, June 25–30, 2008, Cappadocia, Turkey, AIP Conf. Proc. **1072** (2008) 112–117.

21. T. Suzuki, T. Otsuka: "Magnetic Properties of Light Neutron-Rich Nuclei and Shell Evolution", Proc. of the International Symposium on Physics of Unstable Nuclei, July 3–7, 2007, Hoi An, Vietnam, eds. by D.T. Khoa, P.E. Egelhof, S. Gales, N. Van Giai and T. Motobayashi, World Scientific (2008) pp.318-325.

22. T. Teranishi, S. Kubono, H. Yamaguchi, J.J. He, A. Saito, H. Fujikawa, G. Amadio, M. Niikura, S. Shimoura, Y. Wakabayashi, S. Nishimura, M. Nishimura, J.Y. Moon, C.S. Lee, A. Odahara, D. Sohler, L.H. Khiem, Z.H. Li, G. Lian, W.P. Liu: "Spectroscopy of resonance levels in ^{14}O by ^{13}N+p", Proc. of the 23rd International Nuclear Physics Conference (INPC07), June 3–8, 2007, Tokyo, Japan, Volume 2 (2008) pp. 305–307.

23. Y. Togano, T. Gomi, T. Motobayashi, Y. Ando, N. Aoi, H. Baba, K. Demichi, Z. Elekes, N. Fukuda, Zs. Fulop, U. Futakami, H. Hasegawa, Y. Higurashi, K. Ieki, N. Imai, M. Ishihara, K. Ishikawa, N. Iwasa, H. Iwasaki, S. Kanno, Y. Kondo, T. Kubo, S. Kubono, M. Kunibu, K. Kurita, Y.U. Matsuyama, S. Michimasa, T. Minemura, M. Miura, H. Murakami, T. Nakamura, M. Notani, S. Ota, A. Saito, H. Sakurai, M. Serata, S. Shimoura, T. Sugimoto, E. Takeshita, S. Takeuchi, K. Ue, K. Yamada, Y. Yanagisawa, K. Yoneda, A. Yoshida: "Investigation of Stellar ^{26}Si(p,γ)^{27}P Reaction via Coulomb Dissociation", Proc. 10th, Int. Sym. on Origin of Matter and Evolution of Galaxies 2007 (OMEG07): December 4–7, 2007, Sapporo, Japan, AIP Conf. Proc. **1016** (2008) 193–198.

24. T. Uesaka, S. Shimoura, H. Sakai, G.P.A. Berg, K. Nakanishi, Y. Sasamoto, A. Saito, S. Michimasa, T. Kawabata, T. Kubo: "The high resolution SHARAQ spectrometer", Proc. the XVth International Conference on Electromagnetic Isotope Separators and Techniques Related to their Applications, 24–29, 2007, Deauville, France, Nucl. Instr. Meth. in Phys. Res. B **266** (2008) 4218–4222.

25. H. Yamaguchi, Y. Wakabayashi, S. Hayakawa, G. Amadio, S. Kubono, H. Fujikawa, A. Saito, J.J. He, T. Teranishi, Y.K. Kwon, S. Nishimura, Y. Togano, N. Iwasa, K. Inafuku, M. Niikura, D.N. Binh, L.H. Khiem: "Nuclear Structure of 8B Studied by Proton Resonance Scatterings on 7Be", *Origin of Matter and Evolution of Galaxies*, AIP conference proceeding **1016** (2008) 307–312.

26. H. Yamaguchi, Y. Wakabayashi, G. Amadio, S. Hayakawa, H. Fujikawa, S. Kubono, T. Teranishi, J.J. He, A. Saito, S. Nishimura, Y. Togano, Y.K. Kwon, A. Kim, M. Niikura, N. Iwasa, K. Inafuku, L.H. Khiem, D.N. Binh: "Nuclear astrophysics studies using low-energy 7Be beams at CRIB", Nucl. Phys. A. **805** (2008) 546–548.

27. H. Yamaguchi, Y. Wakabayashi, S. Hayakawa, D.N. Binh, D. Kahl, Y. Kurihara, S. Kubono, T. Teranishi, J.J. He, Y.K. Kwon, S. Nishimura, Y. Togano, N. Iwasa, M. Niikura, L.H. Khiem: "Nuclear Astrophysical studies using low-energy RI beams at CRIB", Proc. of the 6th Japan-Italy Symposium on Heavy-Ion Physics, November 11–15, 2008, Tokai, Japan, AIP Conf. Proc. **1120** (2009) 189–193.

28. Y.L. Yamaguchi, for the PHENIX collaboration: "Di-electron Continuum at PHENIX", Proc. of the 43th Recontres de Moriond, March 8–15, 2008, La Thuile, Italy, Conference Record, (2008) pp. 317–320.

29. Y.L. Yamaguchi, for the PHENIX collaboration: "Measurements of low pT direct photons in PHENIX", Proc. of the 24th Winter Workshop on Nuclear Dynamics, April 5–Apr. 12, 2008, South Padre Island, Texas, USA, Conference Record, (2008) pp. 249–254.

C. Theses

1. D.H. Kahl: "^{30}S Beam Development and the ^{30}S Wating Point in Type I X-Ray Bursts", Mater thesis, McMaster University, Canada, (2008).

2. T. Kawahara: "Process of proton polarization under low magnetic field at high temperature", Master Thesis, Toho University, September (2008).

3. Y. Kurihara:" Development of High-Energy Resolution Ion Chamber for Low-Energy Heavy Ions ", Mater thesis, University of Tokyo, March (2008).

4. Y.K. Kwon:" Study of Astrophysically Important Resonant States in ^{26}Si by the ^{28}Si(^{4}He,^{6}He) Reaction ", Doctor thesis of Chung Ang University, Korea, (2007).

5. Y. Morino: "Production of charm and bottom quarks in $p+p$ collisions at 200 GeV", Doctor Thesis, the University of Tokyo, March (2009).

6. M. Niikura: "High-spin Spectroscopy of $^{49-51}$Ti by Fusion Reaction of RI Beam", Doctor Thesis, University of Tokyo, March (2009).

7. S. Ota: "Low-lying proton intruder state in ^{13}B via ^{4}He(^{12}Be,^{13}Bγ) reaction", Doctor Thesis, Kyoto University, March (2009).

8. S. Sakaguchi: "Elastic Scattering of Polarized Protons from Neutron-rich Helium Isotopes at 71 MeV/A", PhD. Thesis, University of Tokyo, March (2008).

9.   : "LHC-ALICE   TRD   ", Master Thesis, the University of Tokyo, March (2009).

D. Other Publications

1.   "J/ψ Production in High Energy Heavy Ion Collisions at RHIC",   vol. 53-2 (2009) 29–39

2.   : "
   ",   vol. 53-2 (2009) 62–73

Talks and Presentations

A. Conferences

1. T. Abe, R. Seki (Oral): "Hadronic lattice calculation of thermal properties of low–density neutron matter with pionless *NN* effective field theory", Hokudai–TORJIN–EFES Workshop "Perspectives in Resonances and Continua on Nuclei" & JUSTIPEN–EFES–Hokudai–UNEDF Meeting, July 21–25, 2008, Onuma, Hokkaido, Japan.

2. T. Abe, R. Seki (Poster): "Lattice calculation of thermal properties of low-density neutron matter with pionless effective field theory", RIKEN Nishina Center Workshop on Perspectives in Nuclear Physics, November 26–27, Nishina Center, RIKEN, Japan.

3. T. Abe, R. Seki (Oral): "Lattice calculation of thermal properties of low-density neutron matter with pionless effective field theory", EENEN 09, First EMMI–EFES Workshop on Neutron–Rich Nuclei, February 9–11, 2009, GSI, Germany.

4. T. Abe, R. Seki (Oral): "Lattice calculation of thermal properties of low-density neutron matter with pionless effective field theory", The 2nd LACM–EFES Workshop, February 23–25, 2009, Joint Institute for Heavy Ion Research, Oak Ridge National Laboratory, Oak Ridge, Tennessee, USA.

5. R. Akimoto, H. Hamagaki, T. Gunji, Y.L. Yamaguchi (Oral): "Recent study and development of MPGD at CNS", The 5th Micro Pattern Gas Detector Workshop, December 12–13, RIKEN, Saitama, Japan.

6. R. Akimoto, H. Hamagaki, T. Gunji, Y.L. Yamaguchi (Poster): "P/T dependence of the multiplication factor for Gas Electron Multiplier(GEM)", at the 1st International Conference on Technology and Instrumentation in Particle Physics, March 12–17, Tsukuba, Japan.

7. Y. Aramaki, for the PHENIX Collaboration (Poster): "Measurement of azimuthal anisotropy of high p_T neutral pion in $\sqrt{s_{NN}} = 200$ GeV Au+Au collisions at RHIC-PHENIX", Annual RHIC and AGS Users Meeting, May 27–30, BNL, NY, USA.

8. Y. Aramaki, for the PHENIX Collaboration (Oral): "Reaction plane dependence of neutral pion production in center-of-mass energy of 200 GeV Au+Au collisions at RHIC-PHENIX", The International Conference on Particles And Nuclei (PANIC08), November 9–14, Eilat, Israel.

9. Y. Aramaki, for the PHENIX Collaboration (Oral): "Electromagnetic Particle Production at PHENIX", RENCONTRES DE MORIOND, March 7–14, La Thuile, Italy.

10. Y. Aramaki, for the PHENIX Collaboration (Poster): "Neutral pion production with respect to reaction plane at $\sqrt{s_{NN}} = 200$ GeV Au+Au collisions at RHIC-PHENIX", The 21th International Conference on Ultra-Relativistic Nucleus-Nucleus Collisions (Quark Matter 2008), March 29–Apr.4, Knoxville, Tennessee, USA.

11. T. Gunji (Oral): "Heavy Quark and Quarkonia Production at RHIC", The 2nd Asian Triangle Heavy Ion Conference (ATHIC2008), October 13–15, 2008, University of Tsukuba, Japan.

12. T. Gunji (Oral): "Quarkonia Production in High Energy Heavy Ion Collisions at RHIC ", International Conference on Strangeness in Quark Matter 2008, October 06–10, 2008, Tsinghua University, Beijing, China.

13. T. Gunji (Oral): "Heavy Quark and Quarkonia Measurement at RHIC & LHC", The workshop on Photons and Jets with ALICE, December 4–6, Central China Normal University , Wuhan, China.

14. H. Hamagaki (Oral): "Heavy Ion Physics at RHIC", Workshop on Ultra high-energy cosmic-rays and hadron structure (2008), April 25–26, 2008, KEK, Japan.

15. H. Hamagaki (Oral): "Charmonium and Heavy Quarks – experimental overview –", 10th Tamura Symposium on Heavy Ion Physics, November 20–22, 2008, University of Texas, Austin, USA.

16. H. Hamagaki (Oral): "Gluon PDF at LHC", The workshop on Photons and Jets with ALICE, December 4–6, 2008, Central China Normal University, Wuhan, China.

17. H. Hamagaki (Oral): "A Forward Electromagnetic Calorimeter (F-CAL) for the ALICE Experiment", The workshop on Photons and Jets with ALICE, December 4–6, 2008, Central China Normal University, Wuhan, China.

18. S. Hayakawa (Oral): "Breakout from the pp-chain region through an alternative path $^{11}C(\alpha, p)^{14}N$", Hidrogen burning and competition between the νp-process and the r-process in explosive nucleosyntheses, February 19–20, 2009, Nishina Hall, RIKEN, Wako, Japan.

19. Y. Hori, S. Sano, T. Gunji, H. Hamagaki, Y. Tanaka, T. Fusayasu (Poster): "Readout electronics for 2D-imaging using GEM(Gas Electron Multiplier)", The 1st international conference on Technology and Instrumentation in Particle Physics(TIPP09), March 12–17, 2009, Tsukuba, Japan.

20. E. Ideguchi (Invited), S. Shimoura, H. Baba, T. Fukuchi, M. Kurokawa, S. Michimasa, M. Niikura, S. Ota: "Development of CNS GRAPE and experiments at RIBF", CNS-RIKEN Joint Int. Symp. on Frontier of gamma-ray spectroscopy and Perspectives for Nuclear Structure Studies (gamma08), April 3–5, 2008, Wako, Saitama, Japan.

21. E. Ideguchi (Invited): "Gamma-ray spectroscopy instruments in Japan (Present status and future perspectives)", 7th AGATA Week, July 8–11, 2008, Uppsala, Sweden.

22. E. Ideguchi: "Study of High-Spin States by Using Degraded RI Beam at RIBF", Joint ANL-EFES Workshop for a Compton-Suppressed Ge Clover Array for Stopped and Energy Degraded Exotic Beams at RIKEN, December 4–5, ANL, Argonne, IL, USA.

23. E. Ideguchi: "Study of high-spin states in mass 30 region", JAEA tandem accelerator workshop, January 6–7, JAEA, Japan.

24. E. Ideguchi (Invited): "Collective band structure in ^{40}Ar", The 3rd LACM-EFES-JUSTIPEN Workshop, February 23–25, 2009, Oak Ridge National Laboratory, Tennessee, USA.

25. S. Kubono: "Study of Explosive Burning Process with RI Beams", Invited talk at the 2008 APCTP-BLTP-RIKEN Joint Workshop on Quarks and Mesons in Nuclear Physics, April 21–24, 2008, Pohang, Korea.

26. S. Kubono: " The Low Energy RI Beam Facility CRIB and the Activities", Invited talk at the Workshop on Low-energy RI beam facility at MSU, August 2, 2008, East Lansing, USA.

27. S. Kubono: "Nuclear Astrophysics with RI Beams", Invited talk at the workshop on Frontiers in Nuclear Astrophysics, January 8, 2008, Osaka, Japan.

28. S. Kubono: "Nuclear Astrophysics with Low Energy RI Beams at CRIB", Invited talk at the workshop on the strategic approach to the r-process, September 25–26, 2008, Wako, Japan.

29. S. Kubono: "Nuclear Astrophysics Programs with Low Energy RI Beams at CRIB", Invited talk at the SSRI workshop, December 24–25, 2008, Osaka, Japan.

30. S. Kubono: "Future of the JAEA Tandem Accelerator Facility", Invited talk at the memorial workshop on the 100 thousand-our operation of the JAEA tandem operation, January 6–7, 2009, Tokai, Ibaraki, Japan.

31. S. Kubono: "vp-process in Type II Supernovae", Invited talk at the workshop on r-process, March 9–10, 2009, Tsukuba, Japan.

32. S. Michimasa (Oral): "Search for two-proton correlation in unbound nuclei", RIKEN mini Workshop on Di-neutron correlation, September 3, 2008, RIKEN, Wako, Japan.

33. S. Michimasa, P. Gangnant, T. Kawabata, H. Kurei, J-F. Libin, K. Miki, H. Miya, K. Nakanishi, S. Ota, P. Roussel-Chomaz, A. Saito, H. Sakai, Y. Sasamoto, S. Shimoura, C. Spitaels, H. Tokieda, T. Uesaka (Oral): "Low-pressure tracking detectors for SHARAQ spectrometer", ICHOR-EFES International Symposium on New Facet of Spin-Isospin Responses (SIR08), October 29–31, 2008, RIKEN, Wako, Japan.

34. Y. Morino, for the PHENIX Collaboration: "Measurements of charm and bottom production at RHIC-PHENIX", International Conference on Strangeness in Quark Matter 2008, October 06–10, 2008, Tsinghua University, Beijing, China.

35. Y. Morino, for the PHENIX Collaboration (Oral): "Measurement of charm and bottom production in pp collisions at $\sqrt{s} = 200$ GeV at RHIC-PHENIX", 20th International Conference Quark Matter, February 4–10, 2008, Jaipur, India.

36. Y. Morino, for the PHENIX Collaboration (Oral): "Measurements of charm and bottom production in pp collisions in PHENIX", 24th Winter Workshop on Nuclear Dynamics, April 5–12, 2008, South Padre Island, USA.

37. K. Nakanishi: "Ion optical design and current status of SHARAQ spectrometer", ICHOR-EFES International Symposium on New Facet of Spin-Isospin Responses - Toward the Commissioning of SHARAQ Spectrometer - (SIR2008), October 29–31, 2008, RIKEN, Wako, Japan.

38. M. Niikura (Oral), E. Ideguchi, S. Michimasa, T. Ohnishi, T.K. Onishi, S. Ota, S. Shimoura, H. Suzuki, D. Suzuki, Y. Wakabayashi, K. Yoshida, Y. Zheng, N. Aoi, H. Baba, T. Fukuchi, Y. Ichikawa, H. Iwasaki, T. Kubo, M. Kurokawa, M. Liu: "Study of High-spin States in $^{49-51}$Ti", CNS-RIKEN Joint Int. Symp. on Frontier of gamma-ray spectroscopy and Perspectives for Nuclear Structure Studies (gamma08), April 3–5, 2008, Wako, Saitama, Japan.

39. M. Niikura (Invited): "In-beam Spectroscopy in $^{49-51}$Ti via Fusion Reaction of RI Beam", LIA-EFES Workshop on Low-energy collective excitations in exotic nuclei, March 2–4, GANIL, Caen, France.

40. S. Ota (Oral): "Proton intruder state in the neutron-rich nucleus ^{13}B", Conference on Nuclear Structure 2008 (NS2008), June 3–6, 2008, East Lansing, Michigan, USA.

41. S. Ota (Oral): "Study of neutron correlation in low density nuclear matter via charge exchange reaction", RIKEN mini Workshop on Di-neutron correlation, September 3, 2008, RIKEN, Wako, Japan.

A. Saito (Oral): "Alpha+^{8}He cluster states in ^{12}Be *via* α-inelastic scattering", Frontier in Unstable Nuclear Physics, July 18–19, 2008, Hokkaido University, Sapporo, Japan.

42. S. Sakaguchi, T. Uesaka, T. Wakui, T. Kawabata, N. Aoi, Y. Hashimoto, M. Ichikawa, Y. Ichikawa, K. Itoh, M. Itoh, H. Iwasaki, T. Kawahara, Y. Kondo, H. Kuboki, Y. Maeda, R. Matsuo, K. Miki, T. Nakamura, T. Nakao, Y. Nakayama, S. Noji, H. Okamura, H. Sakai, Y. Sasamoto, M. Sasano, Y. Satou, K. Sekiguchi, M. Shinohara, K. Suda, D. Suzuki, Y. Takahashi, A. Tamii, K. Yako, M. Yamaguchi (Oral): "Analyzing Power Measurement for Proton Elastic Scattering on Neutron-rich Helium Isotopes", Future of Nuclear Reaction Studies, February 21, 2009, Miyazaki, Japan.

43. S. Sano, H. Hamagaki, Y. Tanaka, T. Fusayasu, T. Gunji (Oral): "Development of a Readout Circuit for 2D-Imaging Using GEM", IEEE 2008 Nuclear Science Symposium, Medical Imaging Conference and 16th Room Temperature Semiconductor Detector Workshop, N23-4, August 19–25, 2008, Dresden, Germany.

44. Y. Sasamoto (Oral): "High resolution beam   line for SHARAQ", ICHOR-EFES International Symposium on New Facet of Spin-Isospin Responses, October 29–31, 2008, RIKEN, Saitama, Japan.

45. S. Shimoura (Invited): "High-resolution spectroscopy using RI beams ? SHARAQ project", Japanese French Symposium on New paradigms in Nuclear Physics, September 29–October 2, 2008, Institut Henri Poincarè, Paris, France.

46. S. Shimoura (Invited): "High-resolution spectroscopy using direct reactions of RI beams", 6th Italy-Japan Symposium on Heavy Ion Physics, November 11–15, 2008, Tokai, Ibaraki, Japan.

47. S. Shimoura: "Digital electronics for GRAPE", Joint ANL-EFES Workshop for a Compton-Suppressed Ge Clover Array for Stopped and Energy Degraded Exotic Beams at RIKEN, December 4–5, ANL, Argonne, IL, USA.

48. S. Shimoura (Invited): "Proton single-particle states in neutron-rich nuclei", The 3rd LACM-EFES-JUSTIPEN Workshop, February 23–25, 2009, Oak Ridge National Laboratory, Tennessee, USA.

49. T. Suzuki (Oral): "Structure of Light Exotic Nuclei", The 3rd LACM-EFES-JUSTIPEN Workshop, February 2009, Oak Ridge, USA.

50. T. Suzuki, T. Otsuka (Oral): "Exotic Electromagnetic Transitions in Neutron-Rich Cabon Isotopes", Franco-Japanese Symposium on New Paradigms in Nuclear Physics, September 2008, Paris, France.

51. T. Suzuki, T. Otsuka (Poster and Short Oral): "Electromagnetic Properties of Neutron-Rich Li and C Isotopes", The 5th International Conference on Exotic Nuclei and Atomic Masses (ENAM08), September 2008, Ryn, Poland.

52. T. Suzuki (Invited): "Spin Modes, Neutrino-induced Reactions and Nucleosynthesis in Stars", International Conference on Nuclear Physics and Astrophysics: From Stable Beams to Exotic Nuclei, June 2008, Cappadocia, Turkey.

53. T. Suzuki (Oral): ”Nuclear Structure and Nucleosynthesis”, Theoretical Issues in Nuclear Astrophysics, April 2008, Orsay, France.

54. T. Uesaka: "Spin Polarization in QFS experiments with RI beams", 1st International Workshop on Quasi-free Scattering with Radioactive Ion Beams, April 7–11, 2008, ECT* Trento, Italy.

55. T. Uesaka: ”New facets of nuclear spin-isospin responses: challenge with the SHARAQ spectrometer”, ICHOR-EFES International Symposium on New Facet of Spin-Isospin Responses, October 29–31, 2008, RIKEN, Saitama, Japan.

56. H. Yamaguchi, Y. Wakabayashi, S. Hayakawa, D.N. Binh, D. Kahl, Y. Kurihara, S. Kubono(Oral): "Nuclear Astrophysical Studies Using Low-energy RI Beams at CRIB", JAEA Techno Community Square "RICOTTI", Ibaraki, Japan.

57. H. Yamaguchi, Y. Wakabayashi, T. Hashimoto, S. Hayakawa, D.N. Binh, D. Kahl, Y. Kurihara, S. Kubono (Oral): "Measurement of proton and alpha resonance scattering using ^{7}Be beam, at CRIB", Workshop on Competition of hydrogen burning with νp-process and r-process in explosive nucleosynthesis, February 19–20, 2009, Nishina Hall, RIKEN, Saitama, Japan.

58. H. Yamaguchi, Y. Wakabayashi, T. Hashimoto, S. Hayakawa, D.N. Binh, D. Kahl, Y. Kurihara, S. Kubono (Oral): "Current status of nuclear astrophysical studies using RI beams at CRIB", Workshop on studies of isotope abundances and origin of elements, by means of astronomical observation, analysis on meteorites, and nuclear astrophysics, February 23–25, 2009, National Astronomical Observatory of Japan, Tokyo, Japan.

59. Y.L. Yamaguchi, for the PHENIX collaboration (Oral): "Measurements of low pT direct photons in PHENIX", The 24th Winter Workshop on Nuclear Dynamics (WWND2008), April 5–12, 2008, South Padre Island, Texas, USA.

60. Y.L. Yamaguchi, for the PHENIX collaboration (Oral): "Soft photons in PHENIX", The RHIC-AGS User's Meeting, May 27–30, 2008, Brookhaven National Laboratory, New York, USA.

61. Y.L. Yamaguchi, for the PHENIX collaboration (Oral): "Direct photon in PHENIX", The 2nd Asian Triangle Heavy Ion Conference (ATHIC2008), October 13–15, 2008, University of Tsukuba, Japan.

62. Y.L. Yamaguchi, for the PHENIX collaboration (Oral): "Measurements of Soft and Intermediate pT Photons from Hot and Dense Matter at RHIC-PHENIX", at the 21st International Conference on Ultra-Relativistic Nucleus Nucleus Collisions (Quark Matter 2009), March 30–April 5, 2009, Knoxville, Tennessee, USA.

B. JPS Meetings

1. Y. Aramaki, for the PHENIX Collaboration (Oral): "Measurement of neutral pion production at $\sqrt{s_{NN}}$ =200 GeV Au+Au collisions at RHIC-PHENIX", JPS Autumn Meeting, September 20–23, Yamagata University, Yamagata, Japan.

2. T. Gunji, for the ALICE Collaboration: "ALICE Performance for the Measurent of Heavy Quarkonia via dielectron decays ", JPS Autumn Meeting, September 20–23, Yamagata University, Yamagata, Japan

3. H. Hamagaki: "High-Energy Heavy-Ion Collisions – Yet another new decade is about to begin", , September 21, 2008, Yamagata University, Yamagata, Japan.

4. S. Hayakawa, H. Yamaguchi, Y. Wakabayashi, Y. Kurihara, S. Kubono, S. Nishimura, D. Kaji, K. Morimoto (Oral): "Performance Assessments of a Position-sensitive MCP Beam Monitor", JPS Autumn Meeting, September 20–23, 2008, Yamagata University, Yamagata, Japan.

5. S. Shimoura: "Status of SHARAQ Spectrometer and Charge Exchange Reactions induced by Unstable Nuclei", Symposium on New Facet in Spin-Isospin Responses, JPS Fall Meeting, September 20–23, 2008, Yamagata University, Yamagata, Japan.

6. A. Takahara, for the ALICE collaboration: "Momentum dependence of the electron identification capability of the ALICE-TRD", JPS Autumn Meeting, September 20–23, Yamagata University, Yamagata, Japan

7. R. Akimoto, H. Hamagaki, T. Gunji, Y.L. Yamaguchi: "The basic performance of Thick GEM", JPS Spring Meeting, March 27–30, Rikkyo University, Tokyo, Japan.

8. Y. Hori. S. Sano, T. Gunji, H. Hamagaki, Y. Tanaka, T. Fusayasu (Oral): "Development of a Readout system for 2D-imaging using GEM(Gas Electron Multiplier)", JPS Spring Meeting, March 27–30, 2009, Rikkyo University, Tokyo, Japan.

9. E. Ideguchi, S. Ota, T. Morikawa, T. Shizuma, M. Ohshima, M. Koizumi, Y. Tou, Y. Hatsukawa, A. Kimura, K. Furutaka, S. Nakamura, F. Kitatani, H. Harada, M. Sugawara, Y. Watanabe, Y. Hirayama, H. Miyatake: "Study of High-Spin States in ^{40}Ar", JPS Spring Meeting, March 27–30, 2009, Rikkyo University, Tokyo, Japan.

10. H. Miya, S. Shimoura, A. Saito, T. Kawabata, S. Michimasa, K. Miki, K. Nakanishi, S. Ota, Y. Sasamoto, H. Kurei, T. Uesaka, H. Sakai (Oral): "Performance evaluation of Low-Pressure Multi-Wire Drift Chamber", JPS Spring Meeting, March 27–30, 2009, Rikkyo University, Tokyo, Japan.

11. M. Niikura, E. Ideguchi, N. Aoi, H. Baba, T. Fukuchi, Y. Ichikawa, H. Iwasaki, T. Kubo, M. Kurokawa, M. Liu, S. Michimasa, T. Ohnishi, T.K. Onishi, S. Ota, S. Shimoura, H. Suzuki, D. Suzuki, Y. Wakabayashi, K. Yoshida, Y. Zheng: "High-Spin Spectroscopy of $^{49-51}$Ti via Fusion Reaction of RI Beam", JPS Spring Meeting, March 27–30, 2009, Rikkyo University, Tokyo, Japan.

12. S. Sakaguchi, T. Uesaka, T. Wakui, T. Kawabata, N. Aoi, Y. Hashimoto, M. Ichikawa, Y. Ichikawa, K. Itoh, M. Itoh, H. Iwasaki, T. Kawahara, Y. Kondo, H. Kuboki, Y. Maeda, R. Matsuo, K. Miki, T. Nakamura, T. Nakao, Y. Nakayama, S. Noji, H. Okamura, H. Sakai, Y. Sasamoto, M. Sasano, Y. Satou, K. Sekiguchi, M. Shinohara, K. Suda, D. Suzuki, Y. Takahashi, A. Tamii, K. Yako, M. Yamaguchi (Oral): "Spin-orbit Potential between Proton and Neutron-rich Helium Isotopes", JPS Spring Meeting, March 27–30, 2009, Rikkyo University, Tokyo, Japan.

13. S. Sano, H. Hamagaki, T. Gunji, M. Ivanov, J. Wiechula (Oral): "Multiplicity measurement using TPC at LHC", JPS Spring Meeting, March 27–30, 2009, Rikkyo University, Tokyo, Japan.

14. Y. Shimizu, T. Uesaka, T, Kawabata, M. Dozono, K. Hatanaka, K. Itho, T. Kawahara, Y. Maeda, H. Matsubara, T. Noro, H. Okamura, S. Sakaguchi, H. Sakai, Y. Sasamoto, M. Sasano, A. Tamii, H. Tokieda, T. Wakasa, T. Wakui, K. Yako, Y. Yamada, H.P. Yoshida (Oral): "Spin dependent momentum distribution of proton in ^{3}He studied via proton induced exclusive knockout reaction", JPS Spring Meeting, March 27–30, 2009, Rikkyo University, Tokyo, Japan.

C. Lectures

1. S. Shimoura: "3rd Lecture on Practical Nuclear Reaction Theory for Experimentalists", Lecture Series on Nuclear Physics, Course IV, May 27, 2008, RIKEN, Wako, Japan

2. T. Uesaka: "Spin Physics at RI Beam Factory", , 19–24 August 2008, ,

3. : KEK 2009 1 20

D. Seminars

1. T. Abe: "Lattice calculation of thermal properties of neutron matter with *NN* effective field theory", Nuclear Theory Group Seminar, July 10, 2008, University of Tokyo, Hongo, Japn.

2. H. Hamagaki: "Electro-Magnetic Measurements at RHIC PHENIX", Colloquium at the Cyclotron Institute, November 25, 2008, Texas A & M University, College Station, USA.

3. E. Ideguchi: "Overview and status of RIBF", December 5, 2008, ANL, Argonne, IL, USA.

4. S. Shimoura: "Structure of light exotic nuclei via α-induced direct reaction", February 13, 2009, RCNP, Osaka University, Osaka, Japan.

5. S. Shimoura: "In-beam spectroscopy of exotic nuclei via direct reactions of RI beams", February 27, 2009, LBNL, Berkeley, USA.

Personnel

Director

    OTSUKA, Takaharu   *Professor, Department of Physics,*
                                                  Graduate School of Science

Scientific Staff

1. Heavy-Ion Collisions

    SHIMOURA, Susumu   *Professor*

    UESAKA, Tomohiro   *Associate Professor*

    IDEGUCHI, Eiji   *Lecturer*

    IWASAKI, Hironori   *Assistant Professor* (– December 2008)

    KAWABATA, Takahiro   *Assistant Professor* (– January 2009)

    MICHIMASA, Shin'ichiro   *Assistant Professor*

2. Nuclear Structure in Extreme States

    KUBONO, Shigeru   *Professor*

    HAMAGAKI, Hideki   *Associate Professor*

    YAMAGUCHI, Hidetoshi   *Assistant Professor*

    GUNJI, Taku   *Assistant Professor*

Guest Professors

    SUZUKI, Toshio   *Nihon University*

    MITSUMOTO, Toshinori   *Sumitomo Heavy Industries, Ltd.*

Technical Staff

    OHSHIRO, Yukimitsu   YAMAZAKI, Norio

Technical Assistants

WATANABE, Shin-ichi

YAMAKA, Shoichi

NINOMIYA, Hideaki

KUREI, Hiroshi

YOSHINO, Akira

Post Doctoral Associates

SHIMIZU, Yohei

OTA, Shinsuke

NAKANISHI, Kosuke

TSUCHIMOTO, Yuji (March 2009 –)

ABE, Takashi

WAKABAYASHI, Yasuo

HASHIMOTO, Takashi

Graduate Students

NIIKURA, Megumi

SAKAGUCHI, Satoshi

YAMAGUCHI, Yorito

BINH, Dam Nguyen

HAYAKAWA, Seiya

TAKAHARA, Akihisa

MIYA, Hiroyuki

OKADA, Kenshi

TOKIEDA, Hiroshi

MORINO, Yuhei

SASAMOTO, Yoshiko

ARAMAKI, Yoki

SANO, Satoshi

KAHL, David M (October 2008 –)

KURIHARA, Yuzo

AKIMOTO, Ryohji

HORI, Yasuto

Administration Staff

HIRANO, Midori

YAMAMOTO, Ikuko

ENDO, Takako

SOMA, Yuko (July 2008 –)

KISHI, Yukino

ITAGAKI, Toshiko

ICHINOHE, Ikuko (– June 2008)

Committees

Council

YAMAMOTO, Masayuki (chair)	*Dean, Graduate School of Science*
SAKAI, Hideyuki	*Department of Physics, Graduate School of Science*
YAMAGATA, Toshio	*Department of Earth and Planetary Science, Graduate School of Science*
OTSUKA, Takaharu	*Department of Physics, Graduate School of Science*
HAYANO, Ryugo	*Department of Physics, Graduate School of Science*
KUBONO, Shigeru	*Center for Nuclear Study, Graduate School of Science*
SHIMOURA, Susumu	*Center for Nuclear Study, Graduate School of Science*
NAGAMIYA, Shoji	*J-PARC Project Office, High Energy Accelerator Research Organization*

Steering Committee

HAYANO, Ryugo (chair)	*Department of Physics, Graduate School of Science*
OTSUKA, Takaharu	*Department of Physics, Graduate School of Science*
SHIMOURA, Susumu	*Center for Nuclear Study, Graduate School of Science*
KUBONO, Shigeru	*Center for Nuclear Study, Graduate School of Science*
HAMAGAKI, Hideki	*Center for Nuclear Study, Graduate School of Science*
SAKAI, Hideyuki	*Department of Physics, Graduate School of Science*
AIHARA, Hiroaki	*Department of Physics, Graduate School of Science*
HAMAGUCHI, Hiroo	*Department of Chemistry, Graduate School of Science*
KOBAYASHI, Tomio	*International Center for Elementary Particle Physics*
YAMAZAKI, Yasunori	*Department of Basic Science, Graduate School of Arts and Sciences*
MADARAME, Haruki	*Nuclear Professional School, School of Engineering*

Program Advisory Committee

HATANAKA, Kichiji (chair)	*Research Center for Nuclear Physics, Osaka University*
EN'YO, Hideto	*RIKEN Nishina Center*
YABANA, Kazuhiro	*University of Tsukuba*
ODAHARA, Atsuko	*Osaka University*
HAMAMOTO, Ikuko	*University of Lund, Sweden*
MITTIG, Wolfgang	*National Superconducting Cyclotron Laboratory, Michigan State University, USA*